Journal of
Mechanics of
Materials and Structures

JOURNAL OF MECHANICS OF MATERIALS AND STRUCTURES

msp.org/jomms

Founded by Charles R. Steele and Marie-Louise Steele

Cover photo: Mando Gomez, www.mandolux.com

■msp

WHAT DISCRETE MODEL CORRESPONDS EXACTLY
TO A GRADIENT ELASTICITY EQUATION?

Vasily E. Tarasov

In this paper, we obtain exact discrete analogs of the gradient elasticity equations. The suggested discrete equations have differences represented by infinite series. Physically, these equations describe models of lattices with long-range interactions. Mathematically, unique difference equations correspond exactly to continuum gradient elasticity equations.

1. Introduction

There are two basic approaches to describe elasticity of solid states: a microscopic approach based on the classical and quantum theory of crystal lattices and solids [Born and Huang 1998; Böttger 1983; Kittel 1987] and a macroscopic phenomenological approach based on the classical mechanics of continua [Sedov 1971]. On the one hand, continuum equations can be considered as a limit case of discrete (lattice) equations when the primitive lattice vectors tend to zero. On the other hand, different discretizations of the continuum equations can be used to get discrete (difference) equations, which allow us to apply computer simulations. Usually discretization of differential equations is realized by using the standard difference operators. In some cases, the corresponding difference equations are similar to the lattice equations. For example, the standard finite difference of second order corresponds to the nearest-neighbor interaction of lattice particles. The standard finite difference of fourth order describes the next-nearest-neighbor interaction [Tarasov 2014a; 2015b].

In this paper, we are not trying to find out which type of equation is primary and which is secondary. We do not try to argue that discrete or continuous equations are primary. The main goal of our paper is to define an exact correspondence between continuum and discrete (lattice) equations. We would like to describe the correspondence without using approximations and limit passages that discard some terms. The mathematical basis of our consideration is the following correspondence principle: the correspondence between the discrete (lattice) theory and the continuum theory lies not so much in the limiting condition when the steps (or primitive lattice vectors) tend to zero as in the fact that mathematical operations on these theories should obey the same laws in many cases. We will use a new type of difference operator, which can be considered an exact discretization of partial derivatives and a lattice operator on physical lattices with long-range interactions [Tarasov 2015a]. The proposed T-differences satisfy the same algebraic relations as the corresponding derivatives. The suggested difference operators allow us to have difference (lattice) equations, whose solutions are equal to the solutions of corresponding continuum differential equations.

This article focuses on gradient elasticity models first suggested by Mindlin [1964; 1965; 1968; Eringen 1983]. These models can be considered a special type of theory of nonlocal elastic continua and continuous media with internal degrees of freedom [Carcaterra et al. 2015; Auffray et al. 2015; dell'Isola et al. 2016b; Sedov 1968; Eringen 1972; 2002; Rogula 1982]. The theory of nonlocal continuum mechanics was initiated by Piola [dell'Isola et al. 2015; 2016a; Rahali et al. 2015]. Nonlocal elasticity theory is based on the assumption that the forces between particles are long-range types that correspond to the long-range character of interatomic forces.

There are three main approaches to derive equations of gradient elasticity: a phenomenological continuum approach based on the postulation of equations, an approach based on homogenization of discrete models, and an approach based on continuum limit of lattice models.

The first approach to derive equations of gradient elasticity in the framework of phenomenological consideration was suggested by [Mindlin 1964; 1965; 1968], which suggest an elasticity theory of materials with microstructure, where two different types of quantities are used for the micro- and macroscales. In the phenomenological approach, the gradient elasticity models differ in the assumed relation between the microscopic deformation and the macroscopic displacement. It is important to note that, despite the theoretical differences between these models, the equations for displacements of these models are identical [Mindlin 1964]. Using the phenomenology approach, the simplest equation of the one-dimensional gradient elasticity has the form

$$\frac{\partial^2 u(x,t)}{\partial t^2} = c^2 \frac{\partial^2 u(x,t)}{\partial x^2} + l^2 \frac{\partial^4 u(x,t)}{\partial x^4}, \tag{1-1}$$

where l^2 is the scale parameter.

The second approach to obtain equations of gradient elasticity is the continualization (homogenization) of a lattice with nearest-neighbor interactions [Mindlin 1968]. Usually a basis of this approach is models of systems of particles and springs. In the simplest case of one-dimensional system of particles and springs, where all particles have mass M and all springs have spring stiffness K, the equations of motion have the form

$$M \frac{d^2 u_n(t)}{dt^2} = K(u_{n+1}(t) - 2u_n(t) + u_{n-1}(t)). \tag{1-2}$$

In the homogenization procedure, it is assumed that the continuum displacement $u(x,t)$ is equal to the lattice displacement $u_n(t)$ of particle n by $u_n(t) = u(nh,t)$, where h is the particle spacing. In this case, the displacements $u_{n\pm1}(t)$ are expressed in terms of the continuum displacement $u(x \pm h, t)$. Then the Taylor series is used in the form

$$u_{n\pm1}(t) = u(x \pm h, t) = \sum_{m=0}^{\infty} \frac{(\pm h)^m}{m!} \frac{\partial^m u(x,t)}{\partial x^m} \tag{1-3}$$

to substitute (1-3) into (1-2). Note that all odd-order derivatives of $u(x,t)$ have canceled. As a result, the division by the cross-section area A of the medium and the interparticle distance h gives the equation

$$\frac{\partial^2 u(x,t)}{\partial t^2} = \frac{c^2}{h^2} \sum_{m=0}^{\infty} \frac{2h^{2m}}{(2m)!} \frac{\partial^{2m} u(x,t)}{\partial x^{2m}}, \tag{1-4}$$

where $\rho = M/(Ah)$ is the mass density and $E = (Kh)/A$ is the Young's modulus, where $c = \sqrt{E/\rho}$ is the elastic bar velocity. Equation (1-1) is obtained by deleting all terms $O(h^6)$, and we get the equation of the gradient elasticity

$$\frac{\partial^2 u(x,t)}{\partial t^2} = c^2 \frac{\partial^2 u(x,t)}{\partial x^2} + \frac{h^2 c^2}{12} \frac{\partial^4 u(x,t)}{\partial x^4}. \tag{1-5}$$

It is easy to see that continualization (homogenization) by Taylor series cannot give the equation of the gradient elasticity exactly. Therefore, the discrete equation (1-1) cannot be considered as an exact analog to (1-2) of the gradient elasticity.

The third approach for obtaining the gradient elasticity equations has been suggested in [Tarasov 2014a; 2015b]. This approach is based on the models of lattices with the nearest-neighbor and next-nearest-neighbor interactions, instead of the case (1-2) that corresponds to the lattice with the nearest-neighbor interactions only. It was proved that two classes of the gradient models (with positive and negative signs in front of the gradient term) can have a general lattice model as a microstructural basis. To obtain the gradient elasticity equations, we consider a lattice model with the nearest-neighbor and next-nearest-neighbor interactions with two different coupling constants. A generalization of this approach to lattice models with long-range interactions has been suggested in recent papers [Tarasov 2013; 2014b; 2014c; 2016b] to describe the fractional nonlocal elastic materials. Note that the models of lattices with the nearest-neighbor and next-nearest-neighbor interactions also cannot be considered as exact discrete models of gradient elasticity.

In this paper, we do not plan to discuss these approaches of obtaining the gradient elasticity equations in detail. Some aspects of this question have been discussed in the cited articles and in [Tarasov 2006a; 2006b; 2014d; 2015a]. We will solve an inverse problem. Considering these continuum equations as already specified, we would like to get an exact discrete analog to the equations. In this paper, we get discrete (lattice) equations that correspond exactly to the continuum gradient elasticity equation (1-1). Physically, these discrete equations describe lattice models with long-range interactions [Tarasov 2006a; 2006b]. Mathematically, unique difference equations correspond exactly to the continuum gradient elasticity equations. Note that exact correspondence means also that the difference equations have the same general solutions as the associated differential equations. In the beginning, we will consider one-dimensional gradient elasticity equations for simplification. Then we suggest a generalization for the three-dimensional case by using an approach proposed in [Tarasov 2014d; 2015a].

2. Transformation of a discrete equation into a continuum gradient elasticity equation

Let us describe in details a transform of a discrete equation into a continuum gradient elasticity equation to fix notation for further consideration.

Usually a discrete analog to the gradient elasticity equation (1-1) is considered in the form of the equation with finite difference of second order

$$\frac{d^2 u_n(t)}{dt^2} = \frac{c^2}{h^2} (u_{n+1}(t) - 2u_n(t) + u_{n-1}(t)). \tag{2-1}$$

Another discrete analog to the gradient elasticity equation (1-1) is considered in the form of the equation with finite difference of second and fourth orders [Tarasov 2014a; 2015b]. As we shortly describe in

Section 1, the discrete equation (2-1) cannot be an exact analog to the gradient elasticity equation (1-1).
Let us give some details to explain a connection between (1-1) and (2-1). The Fourier series transform $F_{h,\Delta}$, which is defined by

$$\hat{u}(k,t) = \sum_{n=-\infty}^{+\infty} u_n(t)e^{-iknh} = F_{h,\Delta}\{u_n(t)\}, \tag{2-2}$$

maps the difference equation (2-1) to

$$\frac{\partial^2 \hat{u}(k,t)}{\partial t^2} = -\frac{2c^2}{h^2} \sum_{m=1}^{\infty} \frac{(-1)^m}{(2m)!}(kh)^{2m}\hat{u}(k,t). \tag{2-3}$$

The inverse Fourier integral transform F^{-1}, which is defined by

$$u(x,t) = \frac{1}{2\pi} \int_{-\infty}^{+\infty} dk\, \hat{u}(k,t)e^{ikx} = F^{-1}\{\hat{u}(k,t)\}, \tag{2-4}$$

gives

$$\frac{\partial^2 u(x,t)}{\partial t^2} = \frac{2c^2}{h^2} \sum_{m=1}^{\infty} \frac{h^{2m}}{(2m)!} \frac{\partial^{2m} u(x,t)}{\partial x^{2m}}. \tag{2-5}$$

Equation (2-5) also can be obtained (for details, see Section 8 of [Maslov 1976]) by using the well-known relation

$$\exp\left(h\frac{\partial}{\partial x}\right)f(x) = f(x+h).$$

It is easy to see that (1-1) can be obtained only in approximation of (2-5) by deleting all $O(h^6)$ terms. It is important to note that the limit $h \to 0$ of (2-5) gives only the wave equation since

$$\lim_{h \to 0} \frac{2}{h^2} \sum_{m=1}^{\infty} \frac{h^{2m}}{(2m)!} \frac{\partial^{2m} u(x,t)}{\partial x^{2m}} = \frac{\partial^2 u(x,t)}{\partial x^2}. \tag{2-6}$$

It is important to emphasize that the gradient elasticity equation (1-1) cannot be obtained by the limit $h \to 0$ [Tarasov 2014a]. Equation (2-5) gives (1-1) only by deleting all $O(h^6)$ terms. Therefore, (2-1) cannot be considered as an exact discretization of (1-1) or its microstructural basis to derive equations of gradient elasticity.

It should be noted that approaches based on models of lattices with the nearest-neighbor and next-nearest-neighbor interactions [Tarasov 2014a; 2015b] can give (1-1) in the limit $h \to 0$ in contrast to approaches based on lattice equation (2-1) with the nearest-neighbor interactions. At the same time, the lattice equations with nearest-neighbor and next-nearest-neighbor interactions have infinite series of even-order derivatives similar to (2-5) before taking the limit.

3. Exact difference analogs of derivatives

To have an exact discrete analog to the gradient elasticity equations, we should consider a problem of discretization of these equations. Let us consider a problem of derivation of an exact discrete analog to the gradient elasticity equation (1-1). To solve this problem, we should find new types of differences,

which will be denoted by $^T\Delta^{2n}$, that correspond exactly to the derivatives $\partial^{2n}/\partial x^{2n}$ with $n = 1$ and $n = 2$. In order for the difference $^T\Delta^{2n}$ of even orders $2n$ ($n \in \mathbb{N}$) to not correspond to the derivatives $\partial^{2n}/\partial x^{2n}$ approximately, these differences should satisfy the condition

$$\frac{1}{h^{2n}} F^{-1}(F_{h,\Delta}(^T\Delta^{2n} u_n(t))) = \frac{\partial^{2n} u(x,t)}{\partial x^{2n}} \tag{3-1}$$

in contrast to the usual finite differences that are represented by infinite series of derivatives (see (2-5)).

Condition (3-1) can be realized if the difference $^T\Delta^{2n}$ has the Fourier series transform in the form

$$F_{h,\Delta}\{^T\boldsymbol{\Delta}^{2n} u_m(t)\} := \sum_{m=-\infty}^{+\infty} e^{-ikm} {}^T\boldsymbol{\Delta}^{2n} u_m(t) = (-1)^n (kh)^{2n} \hat{u}(k,t). \tag{3-2}$$

In order to get (3-2), the differences $^T\Delta^{2n}$ should be represented by the convolution

$$^T\boldsymbol{\Delta}^{2n} u_m(t) := \sum_{j=-\infty}^{+\infty} K_{2n}(j) u_{m-j}(t), \tag{3-3}$$

where

$$F_{1,\Delta}\{K_{2n}(j)\} = (-1)^n k^{2n} \tag{3-4}$$

and $K_{2n}(-m) = K_{2n}(m)$ hold for all $m \in \mathbb{N}$ and $n \in \mathbb{N}$.

In order to apply $F_{1,\Delta}$ to the differences (3-3), we assume that u_m and $K_{2n}(m)$ are the real-valued functions of discrete variable $m \in \mathbb{Z}$ such that $u_m \in l^2$ and $K_{2n}(m) \in l^1$.

Using $K_{2n}(-m) = K_{2n}(m)$, the kernels $K_{2n}(m)$ can be defined by

$$K_{2n}(m) = F_{1,\Delta}^{-1}\{(-1)^n k^{2n}\} = (-1)^n \frac{1}{\pi} \int_0^\pi k^{2n} \cos(km) \, dk. \tag{3-5}$$

For $m = 2$ and $m = 4$, we get

$$K_2(n) = -\frac{2(-1)^n}{n^2} \qquad (n \neq 0), \qquad K_2(0) = -\frac{\pi^2}{3}, \tag{3-6}$$

$$K_4(n) = +\frac{4\pi^2(-1)^n}{n^2} - \frac{24(-1)^n}{n^4} \quad (n \neq 0, \ n \in \mathbb{Z}), \qquad K_4(0) = +\frac{\pi^4}{5}. \tag{3-7}$$

As a result, the differences (3-3) of second and fourth orders are defined by

$$^T\boldsymbol{\Delta}^2 u_n := -\sum_{\substack{m=-\infty \\ m \neq 0}}^{+\infty} \frac{2(-1)^m}{m^2} u_{n-m} - \frac{\pi^2}{3} u_n, \tag{3-8}$$

$$^T\boldsymbol{\Delta}^4 u_n := \sum_{\substack{m=-\infty \\ m \neq 0}}^{+\infty} \left(\frac{4\pi^2(-1)^m}{m^2} - \frac{24(-1)^m}{m^4} \right) u_{n-m} + \frac{\pi^4}{5} u_n. \tag{3-9}$$

In the general case, we can use Equation 2.5.3.5 of [Prudnikov et al. 1986], which gives

$$K_{2n}(m) = \sum_{k=0}^{n-1} \frac{(-1)^{m+k+n}(2n)! \, \pi^{2n-2k-2}}{(2n-2k-1)!} \frac{1}{m^{2k+2}} \quad (m \in \mathbb{Z}, \ m \neq 0). \tag{3-10}$$

For $m = 0$, we have

$$K_{2n}(0) = \frac{(-1)^n \pi^{2n}}{2n+1}. \tag{3-11}$$

These kernels define the differences $^T\mathbf{\Delta}^{2n}$ of even orders $2n$ for all $n \in \mathbb{N}$ by (3-3).

4. Transformation of a gradient elasticity equation into a discrete equation

In Section 2, we demonstrate that discrete equation (2-1) cannot be considered as an exact discrete analog to (1-1).

Using the differences (3-8) and (3-9), we can consider an inverse problem. We will start with the equation of gradient elasticity and then try to get an exact discrete analog to this continuum equation without approximation by deleting terms. We would like to answer the questions: what do the gradient elasticity equations describe exactly at discrete (lattice) level and what is an exact analog to the gradient elasticity equations?

Let us consider the Fourier integral transform F, which is defined by

$$\hat{u}(k, t) = \int_{-\infty}^{+\infty} dx\, u(x, t) e^{-ikx} = F\{u(x, t)\}. \tag{4-1}$$

Applying this Fourier transform F to (1-1), we get

$$\frac{d^2\hat{u}(k, t)}{dt^2} = -c^2 k^2 \hat{u}(k, t) + l^2 k^4 \hat{u}(k, t). \tag{4-2}$$

Using the inverse Fourier series transform $F_{h,\Delta}^{-1}$ such that

$$u_n(t) = \frac{h}{2\pi} \int_{-\pi/h}^{+\pi/h} dk\, \hat{u}(k, t) e^{ikhn} = F_{h,\Delta}^{-1}\{\hat{u}(k, t)\}, \tag{4-3}$$

(4-2) gives

$$\frac{d^2 u_n(t)}{dt^2} = \frac{c^2}{h^2}\,^T\mathbf{\Delta}^2 u_n(t) + \frac{l^2}{h^4}\,^T\mathbf{\Delta}^4 u_n(t), \tag{4-4}$$

where $^T\mathbf{\Delta}^2$ and $^T\mathbf{\Delta}^4$ are the differences that are defined by (3-8) and (3-9). Substitution of (3-8) and (3-9) into (4-4) gives

$$\frac{d^2 u_n(t)}{dt^2} = \sum_{\substack{m=-\infty \\ m \neq 0}}^{+\infty} \left(\frac{4\pi^2 l^2 - 2c^2 h^2}{h^4} \frac{(-1)^m}{m^2} - \frac{24 l^2}{h^4} \frac{(-1)^m}{m^4} \right) u_{n-m}(t) + \left(\frac{\pi^4 l^2}{5h^4} - \frac{\pi^2 c^2}{3h^2} \right) u_n(t) \quad (n \in \mathbb{Z}). \tag{4-5}$$

These equations are an exact discrete analog to the equation of gradient elasticity (1-1).

Let us give some mathematical remarks about suggested difference equations. To use the Fourier series transform, we assume that the function $u_n(t)$ belongs to the Hilbert space l^2 of square-summable sequences, where the norm on the l^p-space is defined by

$$\|u\|_p := \left(\sum_{n=-\infty}^{+\infty} |u_n|^p \right)^{1/p}.$$

It is easy to see that the differences (3-8) and (3-9) are defined by convolutions of $u_m \in l^2$ and the functions

$$a_{2n}(m) = \frac{(-1)^m}{m^{2n}} \quad (m \neq 0, \ m \in \mathbb{Z})$$

that belong to the space l^1. Using the Young's inequality for convolutions [Young 1912a; 1912b; Hardy et al. 1952, Theorem 276] in the form

$$\|{}^T\mathbf{\Delta}^{2n} u\|_r = \|a_{2n} * u\|_r \leq \|a_{2n}\|_p \|u\|_q, \tag{4-6}$$

where

$$\frac{1}{r} + 1 = \frac{1}{p} + \frac{1}{q}, \tag{4-7}$$

we get that the result of the action of operators ${}^T\mathbf{\Delta}^{2n}$ also belongs to the Hilbert space l^2 of square-summable sequences, i.e.,

$$g_m := {}^T\mathbf{\Delta}^{2n} u_m \in l^2 \tag{4-8}$$

since condition (4-7) holds.

As a result, the T-differences are the operators ${}^T\mathbf{\Delta}^{2n} : l^2 \rightarrow l^2$.

Note that, using Equation 5.1.2.3 of [Prudnikov et al. 1986], we can get

$$\sum_{m=1}^{\infty} K_{2n}(m) = \sum_{m=1}^{\infty} \frac{(-1)^m}{m^{2n}} = (2^{1-2n} - 1)\zeta(2n) = -\frac{1}{\Gamma(2n)} \int_0^{\infty} \frac{x^{2n-1}}{e^x + 1} \, dx = T_{2n}, \tag{4-9}$$

where $\zeta(z)$ is the Riemann zeta function, $\Gamma(z)$ is the gamma function, and

$$T_2 = -\frac{\pi^2}{12}, \qquad T_4 = -\frac{7\pi^4}{720}.$$

As a result, the T-differences acting on $u_m = 1$ converge.

The main property of the suggested differences (3-8) and (3-9) are that the Fourier series transform $F_{h,\Delta}$ of these differences is represented by

$$F_{h,\Delta}({}^T\mathbf{\Delta}^{2n} u_m(t)) = (ikh)^{2n} \hat{u}(k,t). \tag{4-10}$$

This equation leads us to the corresponding equality

$$\frac{1}{h^{2n}} F^{-1}(F_{h,\Delta}({}^T\mathbf{\Delta}^{2n} u_m(t))) = \frac{1}{h^{2n}} F^{-1}((ikh)^{2n} \hat{u}(k,t)) = \frac{\partial^{2n} u(x,t)}{\partial x^{2n}}, \tag{4-11}$$

which means that this difference of order $2n$ gives the derivative $\partial^{2n}/\partial x^{2n}$ exactly. The T-differences of orders $2n$ are connected with the derivatives $\partial^{2n}/\partial x^{2n}$ not only asymptotically by the limit $h \rightarrow 0$. It's obvious that the limit $h \rightarrow 0$ also gives this derivatives

$$\lim_{h \rightarrow 0} \frac{F^{-1}(F_{h,\Delta}({}^T\mathbf{\Delta}^{2n}))}{h^{2n}} = \frac{\partial^{2n}}{\partial x^{2n}}. \tag{4-12}$$

As a result, the suggested equations (4-5) with T-difference can be considered not only as approximations of the gradient elasticity equations. The suggested discrete equations (4-5) are exact discrete analogs to the continuum gradient elasticity equation (1-1).

5. Exact difference equations for three-dimensional gradient elasticity

In this section, we propose discrete equations of three-dimensional gradient elasticity by using the approach suggested in [Tarasov 2014d; 2015a].

The Mindlin equations [1964; 1965; 1968] of three-dimensional gradient elasticity have the form

$$
\rho \frac{\partial^2 u_i(\boldsymbol{r}, t)}{\partial t^2} - \rho l_1^2 \sum_{j=1}^{3} \frac{\partial^4 u_i(\boldsymbol{r}, t)}{\partial x_j^2 \partial t^2} = (\lambda + \mu) \sum_{j=1}^{3} \frac{\partial^2 u_j(\boldsymbol{r}, t)}{\partial x_i \, \partial x_j} + \mu \sum_{j=1}^{3} \frac{\partial^2 u_i(\boldsymbol{r}, t)}{\partial x_j^2}
$$

$$
- (\lambda + \mu) l_2^2 \sum_{k=1}^{3} \sum_{j=1}^{3} \frac{\partial^4 u_j(\boldsymbol{r}, t)}{\partial x_k^2 \, \partial x_i \, \partial x_j} - \mu l_3^2 \sum_{k=1}^{3} \sum_{j=1}^{3} \frac{\partial^4 u_i(\boldsymbol{r}, t)}{\partial x_k^2 \, \partial x_j^2} + f_i(\boldsymbol{r}, t), \quad (5\text{-}1)
$$

where the $u_i(\boldsymbol{r}, t)$ are components of the displacement field for the continuum, $f_i(\boldsymbol{r}, t)$ are the components of the body force, λ and μ are the Lame constants, l_i ($i = 1, 2, 3$) are the Mindlin scale parameters, ρ is the mass density, $\boldsymbol{r} = \sum_{j=1}^{3} x_j \boldsymbol{e}_j$, and $\boldsymbol{e}_j$ ($j = 1, 2, 3$) are the basis vectors of the Cartesian coordinate system of $\mathbb{R}^3$.

Using the Fourier transforms $F_{h,\Delta}^{-1} \circ F$, the equations with T-differences for (5-1) have the form

$$
\rho \frac{\partial^2 u_i[\boldsymbol{n}, t]}{\partial t^2} - \frac{\rho l_1^2}{h^2} \sum_{j=1}^{3} {}^T\!\boldsymbol{\Delta}_j^2 \frac{\partial^2 u_i[\boldsymbol{n}, t]}{\partial t^2} = \frac{\lambda + \mu}{h^2} \sum_{j=1}^{3} {}^T\!\boldsymbol{\Delta}_i^1 {}^T\!\boldsymbol{\Delta}_j^1 u_j[\boldsymbol{n}, t] + \frac{\mu}{h^2} \sum_{j=1}^{3} {}^T\!\boldsymbol{\Delta}_j^2 u_i[\boldsymbol{n}, t]
$$

$$
- \frac{(\lambda + \mu) l_2^2}{h^4} \sum_{k=1}^{3} \sum_{j=1}^{3} {}^T\!\boldsymbol{\Delta}_k^{2T}\!\boldsymbol{\Delta}_i^1 {}^T\!\boldsymbol{\Delta}_j^1 u_j[\boldsymbol{n}, t] - \frac{\mu l_3^2}{h^4} \sum_{k=1}^{3} \sum_{j=1}^{3} {}^T\!\boldsymbol{\Delta}_k^{2T}\!\boldsymbol{\Delta}_j^2 u_i[\boldsymbol{n}, t] + f_i[\boldsymbol{n}, t], \quad (5\text{-}2)
$$

where we assume $h_1 = h_2 = h_3 = h$ and $u_j[\boldsymbol{n}, t] := F_{h,\Delta}^{-1} \circ F u_j(\boldsymbol{r}, t)$ are discrete fields such that $u_j[\boldsymbol{n}, t] = h u_j(h\boldsymbol{n}, t)$. In (5-2), we use ${}^T\!\boldsymbol{\Delta}_j^1$ and ${}^T\!\boldsymbol{\Delta}_j^2$, which are the partial T-differences of first and second orders. The partial T-difference of first order is defined by

$$
{}^T\!\boldsymbol{\Delta}_j^1 u_i[\boldsymbol{n}, t] := \sum_{\substack{m_j = -\infty \\ m_j \neq 0}}^{+\infty} \frac{(-1)^{m_j}}{m_j} u_i[\boldsymbol{n} - m_j \boldsymbol{e}_j, t]. \tag{5-3}
$$

The partial T-difference of second order has the form

$$
{}^T\!\boldsymbol{\Delta}_j^2 u_i[\boldsymbol{n}, t] := \sum_{\substack{m_j = -\infty \\ m_j \neq 0}}^{+\infty} \frac{2(-1)^{m_j + 1}}{m_j^2} u_i[\boldsymbol{n} - m_j \boldsymbol{e}_j, t] - \frac{\pi^2}{3} u_i[\boldsymbol{n}, t]. \tag{5-4}
$$

Here $\boldsymbol{e}_j$ ($j = 1, 2, 3$) are the basis vectors of the Cartesian coordinate system of $\mathbb{R}^3$, and $\boldsymbol{n} = \sum_{j=1}^{3} n_j \boldsymbol{e}_j$, where $n_j \in \mathbb{Z}$.

Note that it is easy to generalize these difference equation to the case of various h_j ($j = 1, 2, 3$). For example, in this case, we should use $u_j[\boldsymbol{n}, t] = h_j u_j(\boldsymbol{x}(\boldsymbol{n}), t)$, where $\boldsymbol{x}(\boldsymbol{n}) = \sum_{i=1}^{3} h_j n_j \boldsymbol{e}_j$.

For the three-dimensional case, the simplified continuum equations of gradient elasticity have the form

$$
\rho \frac{\partial^2 u_i(\boldsymbol{r}, t)}{\partial t^2} = \sum_{j,k,l=1}^{3} C_{ijkl} \frac{\partial^2}{\partial x_j \, \partial x_l} \left(1 + l^2 \sum_{m=1}^{3} \frac{\partial^2}{\partial x_m^2} \right) u_k(\boldsymbol{r}, t) + f_i(\boldsymbol{r}, t), \tag{5-5}
$$

where $u_i(\boldsymbol{r}, t)$ are components of the displacement field for the continuum, $f_i(\boldsymbol{r}, t)$ are the components of the body force, and C_{ijkl} is the fourth-order elastic stiffness tensor. For isotropic materials, C_{ijkl} are expressed in terms of the Lame constants λ and μ by

$$C_{ijkl} = \lambda \delta_{ij}\delta_{kl} + \mu(\delta_{ik}\delta_{jl} + \delta_{il}\delta_{jk}), \tag{5-6}$$

where λ and μ are the usual Lame constants.

The equations with T-differences for (5-5) of the three-dimensional gradient elasticity have the form

$$\rho \frac{\partial^2 u_i[\boldsymbol{n}, t]}{\partial t^2} = \frac{1}{h^2} \sum_{j,k,l=1}^{3} C_{ijkl}{}^T\boldsymbol{\Delta}_j^1{}^T\boldsymbol{\Delta}_l^1 \left(1 + \frac{l^2}{h^2} \sum_{m=1}^{3} {}^T\boldsymbol{\Delta}_m^2\right) u_k[\boldsymbol{n}, t] + f_i[\boldsymbol{n}, t]. \tag{5-7}$$

If we consider the case with $u_x(\boldsymbol{r}, t) = u(x, t)$ and $f_x(\boldsymbol{r}, t) = f(x, t)$, where the other components, u_y, u_z, f_y, and f_z, are equal to zero, then we get the considered one-dimensional gradient elasticity equations.

Equations (5-2) and (5-7) are equations of exact discretization of the three-dimensional gradient elasticity equations. These equations with T-differences are connected with the partial differential equation of gradient elasticity without approximations.

To solve linear partial differential and difference equations of the gradient elasticity, we can use the method of separation of variables. For simplification, we will consider (1-1) and (4-4). For these equations, the fields $u(x, t)$ and $u_n(t)$ are represented in the forms

$$u(x, t) = u(x)T(t), \qquad u_n(t) = u[n]T(t). \tag{5-8}$$

Substitution of (5-8) into (1-1) and (4-4) gives equations of $u(x)$ and $u[n]$ that can be represented as

$$l^2 \frac{\partial^4 u(x)}{\partial x^4} + c^2 \frac{\partial^2 u(x)}{\partial x^2} + \omega^2 u(x) = 0, \tag{5-9}$$

$$\frac{l^2}{h^4}{}^T\boldsymbol{\Delta}^4 u[n] + \frac{c^2}{h^2}{}^T\boldsymbol{\Delta}^2 u[n] + \omega^2 u[n] = 0, \tag{5-10}$$

where ${}^T\boldsymbol{\Delta}^m$ is the T-difference of order m with respect to n. The equations for $T(t)$ are the same for (1-1) and (4-4).

To solve (5-10), we assume that the solution of (5-10) is proportional to $\exp(\lambda n)$ for some constant λ. Substitute $u[n] = \exp(\lambda n)$ into difference equation (5-10), and use the relation

$$^T\boldsymbol{\Delta}^1 \exp(\lambda n) = \lambda \exp(\lambda n), \tag{5-11}$$

which is proved by the Poisson–Abel technique in [Tarasov 2016a]. Then we get a general solution of difference equation (5-10) in the form

$$u[n] = C_1 e^{\lambda_+ \cdot hn} + C_2 e^{-\lambda_+ \cdot hn} + C_3 e^{\lambda_- \cdot hn} + C_4 e^{-\lambda_- \cdot hn}, \tag{5-12}$$

where

$$\lambda_\pm := \sqrt{\pm \frac{1}{2l^2}\sqrt{c^4 - 4l^2\omega^2} - \frac{c^2}{2l^2}}. \tag{5-13}$$

Differential equation (5-9) has the general solution

$$u(x) = c_1 e^{\lambda_+ \cdot x} + c_2 e^{-\lambda_+ \cdot x} + c_3 e^{\lambda_- v x} + c_4 e^{-\lambda_- \cdot x}. \qquad (5\text{-}14)$$

It is easy to see that solutions (5-12) and (5-14) are connected by the relation $u[n] = hu(hn)$ for all $n \in \mathbb{Z}$ and $h > 0$, where $C_k = hc_k$ ($k = 1, 2, 3, 4$).

Equation (5-10) can be considered as an exact discretization of differential equation (5-9). The exact discretization means that the difference equation has the same general solution as the associated differential equation. The criterion of exact discretization of differential equations can be formulated in the following form [Potts 1982; Mickens 2000; Tarasov 2016a].

An exact discretization is a map from a differential equation to a discrete (difference) equation, for which the solution $u[n]$ of the discrete equation and the solution $u(x)$ of the associated differential equation are the same, i.e., if and only if the discrete function $u[n]$ is exactly equal to the function $u(x)$ for $x = hn$, i.e., $u[n] = hu(hn)$ ($n \in \mathbb{Z}$) for arbitrary values of $h > 0$.

It should be noted that discretization of an equation by standard finite differences (5-9) cannot be considered as an exact discretization since $^f\Delta^1 \exp(\lambda n) \neq \lambda \exp(\lambda n)$ and (5-12) is not the solution of the corresponding finite difference equation.

In elasticity theory, the boundary conditions play an important role. The boundary conditions for T-difference equations have a form that is similar to the boundary conditions of the corresponding differential equations. In these boundary conditions, the function $u_i[n]$ should be used instead of the function $u_i(x)$ and the T-differences $^T\mathbf{\Delta}_j^m$ instead of the partial derivatives $\partial^m/\partial x_j^m$ of order $m \in \mathbb{N}$. For a simple example, the exact discrete analog to the boundary conditions

$$\left(\frac{\partial^m u(x)}{\partial x^m} \right)_{x=0} = 0, \qquad \left(\frac{\partial^m u(x)}{\partial x^m} \right)_{x=L} = 0, \qquad (5\text{-}15)$$

for some values $m \in \{0, 1, 2, 3\}$, where $\partial^0 u(x)/\partial x^0 := u(x)$, have the form

$$^T\mathbf{\Delta}^m u[0] = 0, \qquad ^T\mathbf{\Delta}^m u[N] = 0, \qquad (5\text{-}16)$$

where $hN = L$, $N \in \mathbb{N}$, $u[n] = hu(hn)$, and $^T\mathbf{\Delta}^0 u[n] = u[n]$. For example, the discrete analog to the periodic boundary condition $u(x + L) = u(x)$ takes the form $u[n + N] = u[n]$. The boundary conditions for the difference equations define the constants of the corresponding general solution.

As a result, we can see that discrete (lattice) equations with T-differences can be solved analytically. Thus, obtained solutions of these discrete equations are the same as those of the associated differential equations of continuum models.

6. Physical interpretation of the difference equations

In this section, we describe a direct connection between the proposed T-differences and lattice models with long-range interactions. We prove that the discrete (lattice) equations with T-differences, which are suggested for the gradient elasticity models, correspond to lattice models with long-range interactions of power-law type.

From a mathematical point of view, the previous discrete (lattice) models of the gradient elasticity are based on the standard (forward, backward, and central) finite differences. These models assume that we

consider nearest-neighbor and next-nearest-neighbor interactions only, which do not correspond exactly to real physical properties of interactions of particles. The characteristic properties of the underlying physical interactions, which are electromagnetic interactions, are of a long-range nature. The models will more adequately describe elastic materials and media, if these models take into account the long-range character of interatomic forces. One of the most widely used long-range interactions is the interaction of the type $1/|n|^\alpha$, or equivalently $1/|n-m|^\alpha$. The integer values of α correspond to the well-known physical cases that correspond to the Coulomb potential for $\alpha = 1$ and the dipole-dipole interaction for $\alpha = 3$. Moreover, in various cases, these interactions are crucial. For example, the excitation transfer in molecular crystals and the vibron energy transport in polymers are due to the transition dipole-dipole interaction of the type $1/|n|^3$. Polyatomic molecules contain charged groups with a long-range Coulomb interaction $1/|n|^1$ between them. For excitons and phonons in semiconductors and molecular crystals, the dispersion curves of two elementary excitations intersect or are close, which leads to an effective long-range transfer.

It should be noted that classical and quantum descriptions of media with long-range interactions are the subject of continued interest in physics. The long-range interactions have been studied in discrete systems as well as in their continuous analogs. For example, discrete and lattice models with long-range interactions have been studied in the references below. An infinite one-dimensional model with long-range interactions is described in [Dyson 1969a; 1969b; 1971]. Two-dimensional and three-dimensional classical models with long-range interactions are considered in [Joyce 1969], and their quantum generalization has been suggested in [Nakano and Takahashi 1994a; 1994b; 1995; Sousa 2005]. Kinks, solitons, breathers, dynamical chaos, and synchronization in lattice models with long-range particle interactions are studied in different papers (for example, see [Gaididei et al. 1995; Mingaleev et al. 1998; Rasmussen et al. 1998; Gorbach and Flach 2005; Korabel and Zaslavsky 2007; Korabel et al. 2007; Zaslavsky et al. 2007] and references therein).

It should be noted that the kernels (3-10), (3-8), (5-3), and (5-4) of the suggested T-differences can be considered linear combinations of kernels of the type $1/|n|^\alpha$, with integer $\alpha \in \mathbb{N}$. We can assume that the suggested T-differences (3-8) of second and fourth orders in gradient elasticity equations correspond to the well-known underlying interatomic and intermolecular forces such as the Coulomb force of the type $1/|n|^2$ and the dipole-dipole force of the type $1/|n|^4$. From a mathematical point of view, these linear combinations are selected from the set of other combinations by the fact that they exactly correspond to the continuum models, which are described by differential equations of integer orders. The suggested type of long-range interactions, which are described by the kernels of the suggested T-differences, is distinguished from other interactions by exact correspondence to continuum differential equations and by preservation of the main characteristic properties of differential equations and corresponding solutions.

7. Conclusion

In this paper, we focused our consideration on gradient elasticity models that were suggested by Mindlin [1964; 1965; 1968; Eringen 1983]. It should be noted that the proposed approach can also be applied to the gradient elasticity models suggested by Aifantis [1994; 1992; 2011; Metrikine and Askes 2002; Askes and Aifantis 2011]. The standard approach has certain disadvantages compared to the proposed approach of obtaining exact discrete (lattice) analogs of continuum equations. Let us explain this point in more detail. From a mathematical point of view, the standard discrete (lattice) models of the gradient

elasticity are based on a mathematical approach that uses the forward, backward, and central finite differences. From the physical point of view, these models assume nearest-neighbor and next-nearest-neighbor interactions in the media [Tarasov 2014a; 2015b; Askes and Aifantis 2011]. These models are not quite adequate for the following reasons. From a mathematical point of view, it is well-known that the finite differences of cannot be considered an exact discretization of the derivatives: solutions of equations with standard finite differences do not coincide with solutions of the corresponding differential equations, and the standard finite differences do not satisfy the same algebraic relations as the operators of differentiation. The correspondence between the discrete (lattice) theory and the continuum theory lies not so much in the limiting condition of the steps (or primitive lattice vectors) as in the fact that mathematical operations on these theories should obey the same laws in many cases. From a physical point of view, the standard discrete (lattice) models, which are based on an assumption of nearest-neighbor and next-nearest-neighbor interactions only, do not fully reflect the physical reality. The characteristic properties of the underlying physical interactions, which are electromagnetic interactions, are of a long-range nature. The models will more adequately describe elastic materials and media, when these models will take into account the long-range character of interatomic forces that can be characterized as $1/|n|^{\alpha}$. The integer values of α correspond to the well-known physical cases that correspond to the Coulomb force for $\alpha = 1$ and the dipole-dipole force for $\alpha = 4$. Moreover, in various cases, these interactions are crucial.

In this paper, we propose discrete (lattice) equations that correspond exactly to the gradient elasticity equations. From a mathematical point of view, these discrete equations are uniquely equations with differences that correspond exactly to the continuum equations. From a physical point of view, these equations describe microstructural models of lattices with long-range interactions of the type $1/|n|^{\alpha}$ with integer α.

The main advantage of the suggested discrete (lattice) equations is the connection with continuum equations without any approximation. Moreover, these discrete (difference) equations have the same general solutions as the associated differential equations. The exact discretization means that the difference equation has the same general solution as the associated differential equation. It should also be emphasized that these discrete equations allow us to obtain analytical solutions. This is based on the fact that the proposed T-differences satisfy the same algebraic relations as the operators of differentiation.

The computer simulations of discrete systems with long-range interactions of the form $1/|n|^{\alpha}$ are actively used for integer and noninteger values of α (for example, see [Gaididei et al. 1995; Mingaleev et al. 1998; Rasmussen et al. 1998; Gorbach and Flach 2005; Korabel and Zaslavsky 2007; Korabel et al. 2007; Zaslavsky et al. 2007]). The suggested T-differences can be considered linear combinations of interactions of the type $1/|n|^{\alpha}$ with integer α. Therefore, we assume that computer simulations of the suggested T-difference (lattice) equations, which are exact discretizations of corresponding differential equations of continua, can be successfully realized.

We assume that the suggested equations with T-differences can be important in application since they allow us to reflect characteristic properties of complex elastic materials and media at the microscale and nanoscale, where long-range interactions play a crucial role in determining the properties of these materials and media (see [Ostoja-Starzewski 2002; Tarasov 2010] and references therein).

References

[Aifantis 1992] E. C. Aifantis, "On the role of gradients in the localization of deformation and fracture", *Int. J. Eng. Sci.* **30**:10 (1992), 1279–1299.

[Aifantis 1994] E. C. Aifantis, "Gradient effects at macro, micro, and nano scales", *J. Mech. Behav. Mater.* **5**:3 (1994), 355–375.

[Aifantis 2011] E. C. Aifantis, "Gradient nanomechanics: applications to deformation, fracture, and diffusion in nanopolycrystals", *Metall. Mater. Trans. A* **42**:10 (2011), 2985–2998.

[Askes and Aifantis 2011] H. Askes and E. C. Aifantis, "Gradient elasticity in statics and dynamics: an overview of formulations, length scale identification procedures, finite element implementations and new results", *Int. J. Solids Struct.* **48**:13 (2011), 1962–1990.

[Auffray et al. 2015] N. Auffray, F. dell'Isola, V. A. Eremeyev, A. Madeo, and G. Rosi, "Analytical continuum mechanics *à la* Hamilton–Piola least action principle for second gradient continua and capillary fluids", *Math. Mech. Solids* **20**:4 (2015), 375–417.

[Born and Huang 1998] M. Born and K. Huang, *Dynamical theory of crystal lattices*, Clarendon, Oxford, 1998.

[Böttger 1983] H. Böttger, *Principles of the theory of lattice dynamics*, Physik-Verlag, Weinheim, Germany, 1983.

[Carcaterra et al. 2015] A. Carcaterra, F. dell'Isola, R. Esposito, and M. Pulvirenti, "Macroscopic description of microscopically strongly inhomogenous systems: a mathematical basis for the synthesis of higher gradients metamaterials", *Arch. Ration. Mech. Anal.* **218**:3 (2015), 1239–1262.

[dell'Isola et al. 2015] F. dell'Isola, U. Andreaus, and L. Placidi, "At the origins and in the vanguard of peridynamics, nonlocal and higher-gradient continuum mechanics: an underestimated and still topical contribution of Gabrio Piola", *Math. Mech. Solids* **20**:8 (2015), 887–928.

[dell'Isola et al. 2016a] F. dell'Isola, A. Della Corte, and I. Giorgio, "Higher-gradient continua: the legacy of Piola, Mindlin, Sedov and Toupin and some future research perspectives", *Math. Mech. Solids* (online publication January 2016).

[dell'Isola et al. 2016b] F. dell'Isola, I. Giorgio, M. Pawlikowski, and N. L. Rizzi, "Large deformations of planar extensible beams and pantographic lattices: heuristic homogenization, experimental and numerical examples of equilibrium", *Proc. R. Soc. Lond. A* **472**:2185 (2016), article 20150790.

[Dyson 1969a] F. J. Dyson, "Existence of a phase-transition in a one-dimensional Ising ferromagnet", *Commun. Math. Phys.* **12**:2 (1969), 91–107.

[Dyson 1969b] F. J. Dyson, "Non-existence of spontaneous magnetization in a one-dimensional Ising ferromagnet", *Commun. Math. Phys.* **12**:3 (1969), 212–215.

[Dyson 1971] F. J. Dyson, "An Ising ferromagnet with discontinuous long-range order", *Commun. Math. Phys.* **21** (1971), 269–283.

[Eringen 1972] A. C. Eringen, "Nonlocal polar elastic continua", *Int. J. Eng. Sci.* **10**:1 (1972), 1–16.

[Eringen 1983] A. C. Eringen, "On differential-equations of nonlocal elasticity and solutions of screw dislocation and surface-waves", *J. Appl. Phys.* **54**:9 (1983), 4703–4710.

[Eringen 2002] A. C. Eringen, *Nonlocal continuum field theories*, Springer, New York, 2002.

[Gaididei et al. 1995] Yu. B. Gaididei, N. Flytzanis, A. Neuper, and F. G. Mertens, "Effect of nonlocal interactions on soliton dynamics in anharmonic lattices", *Phys. Rev. Lett.* **75**:11 (1995), 2240–2243.

[Gorbach and Flach 2005] A. V. Gorbach and S. Flach, "Compactlike discrete breathers in systems with nonlinear and nonlocal dispersive terms", *Phys. Rev. E* **72**:5 (2005), 056607.

[Hardy et al. 1952] G. H. Hardy, J. E. Littlewood, and G. Pólya, *Inequalities*, 2nd ed., Cambridge University Press, 1952.

[Joyce 1969] G. S. Joyce, "Absence of ferromagnetism or antiferromagnetism in the isotropic Heisenberg model with long-range interactions", *J. Phys. C Solid State Phys.* **2**:8 (1969), 1531–1533.

[Kittel 1987] C. Kittel, *Quantum theory of solids*, 2nd ed., Wiley, New York, 1987.

[Korabel and Zaslavsky 2007] N. Korabel and G. M. Zaslavsky, "Transition to chaos in discrete nonlinear Schrödinger equation with long-range interaction", *Physica A* **378**:2 (2007), 223–237.

[Korabel et al. 2007] N. Korabel, G. M. Zaslavsky, and V. E. Tarasov, "Coupled oscillators with power-law interaction and their fractional dynamics analogues", *Commun. Nonlinear Sci. Numer. Simul.* **12**:8 (2007), 1405–1417.

[Maslov 1976] V. P. Maslov, *Operational methods*, Mir, Moscow, 1976.

[Metrikine and Askes 2002] A. V. Metrikine and H. Askes, "One-dimensional dynamically consistent gradient elasticity models derived from a discrete microstructure, 1: Generic formulation", *Eur. J. Mech. A Solids* **21**:4 (2002), 555–572.

[Mickens 2000] R. E. Mickens, "Nonstandard finite difference schemes", Chapter 1, pp. 1–54 in *Applications of nonstandard finite difference schemes* (Atlanta, 1999), edited by R. E. Mickens, World Scientific, River Edge, NJ, 2000.

[Mindlin 1964] R. D. Mindlin, "Micro-structure in linear elasticity", *Arch. Ration. Mech. Anal.* **16**:1 (1964), 51–78.

[Mindlin 1965] R. D. Mindlin, "Second gradient of strain and surface-tension in linear elasticity", *Int. J. Solids Struct.* **1**:4 (1965), 417–438.

[Mindlin 1968] R. D. Mindlin, "Theories of elastic continua and crystal lattice theories", Chapter 3, pp. 312–320 in *Mechanics of generalized continua* (Stuttgart, 1967), edited by E. Kröner, Springer, Berlin, 1968.

[Mingaleev et al. 1998] S. F. Mingaleev, Yu. B. Gaididei, and F. G. Mertens, "Solitons in anharmonic chains with power-law long range interactions", *Phys. Rev. E* **58**:3 (1998), 3833–3842.

[Nakano and Takahashi 1994a] H. Nakano and M. Takahashi, "Quantum Heisenberg chain with long-range ferromagnetic interactions at low temperature", *J. Phys. Soc. Japan* **63**:3 (1994), 926–933.

[Nakano and Takahashi 1994b] H. Nakano and M. Takahashi, "Quantum Heisenberg model with long-range ferromagnetic interactions", *Phys. Rev. B* **50**:14 (1994), 10331–10334.

[Nakano and Takahashi 1995] H. Nakano and M. Takahashi, "Magnetic-properties of quantum Heisenberg ferromagnets with long-range interactions", *Phys. Rev. B* **52**:9 (1995), 6606–6610.

[Ostoja-Starzewski 2002] M. Ostoja-Starzewski, "Lattice models in micromechanics", *Appl. Mech. Rev. (ASME)* **55**:1 (2002), 35–60.

[Potts 1982] R. B. Potts, "Differential and difference equations", *Amer. Math. Monthly* **89**:6 (1982), 402–407.

[Prudnikov et al. 1986] A. P. Prudnikov, Yu. A. Brychkov, and O. I. Marichev, *Integrals and series*, vol. 1: Elementary functions, Gordon and Breach Science, New York, 1986.

[Rahali et al. 2015] Y. Rahali, I. Giorgio, J. F. Ganghoffer, and F. dell'Isola, "Homogenization à la Piola produces second gradient continuum models for linear pantographic lattices", *Int. J. Eng. Sci.* **97** (2015), 148–172.

[Rasmussen et al. 1998] K. Ø. Rasmussen, P. L. Christiansen, M. Johansson, Yu. B. Gaididei, and S. F. Mingaleev, "Localized excitations in discrete nonlinear Schrödinger systems: effects of nonlocal dispersive interactions and noise", *Physica D* **113**:2–4 (1998), 134–151.

[Rogula 1982] D. Rogula, *Nonlocal theory of material media*, International Centre for Mechanical Sciences **268**, Springer, Vienna, 1982.

[Sedov 1968] L. I. Sedov, "Модели сплошных сред с внутренними степенями свободы", *Prikl. Mat. Mekh.* **32**:5 (1968), 771–785. Translated as Models of continuous media with internal degrees of freedom in *Journal of Applied Mathematics and Mechanics* **32**:5 (1968), 803–819.

[Sedov 1971] L. I. Sedov, *A course in continuum mechanics*, vol. 1–4, Wolters-Noordhoff, Groningen, 1971.

[Sousa 2005] J. R. Sousa, "Phase diagram in the quantum XY model with long-range interactions", *Eur. Phys. J. B* **43**:1 (2005), 93–96.

[Tarasov 2006a] V. E. Tarasov, "Continuous limit of discrete systems with long-range interaction", *J. Phys. A Math. Gen.* **39**:48 (2006), 14895–14910.

[Tarasov 2006b] V. E. Tarasov, "Map of discrete system into continuous", *J. Math. Phys.* **47**:9 (2006), article 092901.

[Tarasov 2010] V. E. Tarasov, *Fractional dynamics: applications of fractional calculus to dynamics of particles, fields and media*, Springer, Heidelberg, 2010.

[Tarasov 2013] V. E. Tarasov, "Lattice model with power-law spatial dispersion for fractional elasticity", *Cent. Eur. J. Phys.* **11**:11 (2013), 1580–1588.

[Tarasov 2014a] V. E. Tarasov, "General lattice model of gradient elasticity", *Mod. Phys. Lett. B* **28**:7 (2014), article 1450054.

[Tarasov 2014b] V. E. Tarasov, "Lattice model of fractional gradient and integral elasticity: long-range interaction of Grünwald–Letnikov–Riesz type", *Mech. Mater.* **70** (2014), 106–114.

[Tarasov 2014c] V. E. Tarasov, "Lattice with long-range interaction of power-law type for fractional non-local elasticity", *Int. J. Solids Struct.* **51**:15–16 (2014), 2900–2907.

[Tarasov 2014d] V. E. Tarasov, "Toward lattice fractional vector calculus", *J. Phys. A Math. Gen.* **47**:35 (2014), article 355204.

[Tarasov 2015a] V. E. Tarasov, "Lattice fractional calculus", *Appl. Math. Comput.* **257** (2015), 12–33.

[Tarasov 2015b] V. E. Tarasov, "Lattice model with nearest-neighbor and next-nearest-neighbor interactions for gradient elasticity", *Discontin. Nonlinearity Complex.* **4**:1 (2015), 11–23.

[Tarasov 2016a] V. E. Tarasov, "Exact discretization by Fourier transforms", *Commun. Nonlinear Sci. Numer. Simul.* **37** (2016), 31–61.

[Tarasov 2016b] V. E. Tarasov, "Three-dimensional lattice models with long-range interactions of Grünwald–Letnikov type for fractional generalization of gradient elasticity", *Meccanica* (*Milano*) **51**:1 (2016), 125–138.

[Young 1912a] W. H. Young, "On classes of summable functions and their Fourier series", *Proc. R. Soc. Lond. A* **87**:594 (1912), 225–229.

[Young 1912b] W. H. Young, "On the multiplication of successions of Fourier constants", *Proc. R. Soc. Lond. A* **87**:596 (1912), 331–339.

[Zaslavsky et al. 2007] G. M. Zaslavsky, M. Edelman, and V. E. Tarasov, "Dynamics of the chain of forced oscillators with long-range interaction: from synchronization to chaos", *Chaos* **17**:4 (2007), 043124.

VASILY E. TARASOV: tarasov@theory.sinp.msu.ru

Skobeltsyn Institute of Nuclear Physics, Lomonosov Moscow State University, Leninskie gory, GSP-1, Moscow, 119991, Russia

msp

A REFINED 1D BEAM THEORY BUILT ON 3D SAINT-VENANT'S SOLUTION TO COMPUTE HOMOGENEOUS AND COMPOSITE BEAMS

RACHED EL FATMI

This paper proposes a refined 1D beam theory (RBT) built on the 3D Saint-Venant (SV) solution established for arbitrary composite cross-section. In this theory (RBT/SV), the displacement model introduces sectional out-of-plane warpings, Poisson's effects and distortions. For a given cross-section, the sectional displacement modes are extracted from the computation of the correspondent 3D SV's solution. These sectional modes, which reflect the mechanical behavior of the cross-section, lead to a beam theory that really fits the section nature (shape and material(s)). As a result, RBT/SV allows to recover a more realistic spatial behavior for the beam, to catch a significant part of the edge effects, and hence to compute a relatively short beam. In order to apply RBT/SV, a package (named CSB) of two complementary numerical Matlab tools have been developed: CSection and CBeam. CSection computes by 2D-FEM the deformation modes of the cross-section, and CBeam uses these sectional modes to generate the correspondent beam theory and compute by 1D-FEM the beam. A significant set of homogeneous/composite beams have been computed and, to show the efficiency of such a theory, 3D RBT/SV results have been systematically compared with those provided by full 3D-FEM computations.

1. Introduction

Nowadays, the design of homogeneous beams is well understood and the calculation methods available for engineers are sufficient to meet the requirements of current mechanical engineering, even if walled profiles are not completely under control (especially when thin/thick and open/closed multicellular sections are involved).

In contrast, composite beams are not so easy to design. Their mechanical behavior is much more difficult to understand and to predict. Laminated composite beams are known to exhibit complex phenomena such as coupled deformations arising from the anisotropic nature of the layers and from the stacking sequences. And the situation is more complex when, to reduce cost and weight, thin-walled open/closed composite sections are involved. Detailed structural models are then essential in order to fully exploit such specific effects in the design phase. In addition to the structural level, detailed 3D stress analysis is of practical relevance for laminated composites and especially the interlaminar stresses which may result in delamination and failure of the laminates.

Today, using composite beams is a real trend in many engineering applications but the use of 3D finite element (3D-FEM) analysis to facilitate design is costly. This trend calls for the development of a realistic general beam theory and efficient numerical tools, suitable for the analysis of beams exhibiting 3D effects, for which the classical beam theory (CBT) assumptions are no longer valid. In CBT, a beam

is practically reduced to a 1D body; nowadays, a beam must be considered as a 3D *slim* body whose cross-section can warp in and out-of its plane. Furthermore, a general beam theory has to account for the shape of the cross-section, the spatial arrangement of the materials and their anisotropy and must, at least, lead to an acceptable approximation of the 3D stress state in each material, which is fundamental for a composite beam.

This is the objective of the present beam theory which refers to the extended 3D SV's solution established by Iesan [1976] for an arbitrary composite cross-section. This theory is the result of a work initiated more than 10 years ago. It started offering low cost numerical methods [El Fatmi and Zenzri 2002; 2004] to compute the extended 3D SV's solution as expressed by Ladevèze and Simmonds [1998] in the framework of the *exact* beam theory. More recently a first formulation of a composite beam theory based on SV's results have been proposed [El Fatmi and Ghazouani 2011a; 2011b] but it was limited to symmetric section and particular orthotropic materials. The present work, which could be seen as a large extension of this first formulation, deals with an arbitrary homogeneous/composite cross-section. It is worth noting that this beam theory is free from all the classical assumptions and no homogenization step is needed for the composite case.

The accuracy of a beam model depends on its aptitude to capture the behavior associated with the two small dimensions eliminated in the final 1D beam analysis. From the literature surrounding the development of (1D) beam theories, three important approaches can be identified:

- beam theories based on kinematic (and static) assumptions using some engineering experience or intuition;

- beam theories based on the asymptotic expansion of the 3D solution, using small parameter(s) inherent to the beam features;

- the so-called one-dimensional beam-like theory which derives from the 3D Saint-Venant (SV) solution of SV's problem.

These different approaches have been discussed in [El Fatmi and Ghazouani 2011a] and we will not take the same (one can also see the interesting review on classical and advanced beam theories of [Carrera et al. 2011]). However, the beam theory proposed here being completely based on 3D SV's solution, this approach deserves some attention again.

Established first for homogeneous and isotropic section, SV's solution have been extended by Iesan [1976] to any composite section wherein each material is anisotropic and where the beam is also subjected to any uniform lateral loading. 3D SV's solution has always been a reference for the development of beam theories, and now even more since its extension to any composite sections [Giavotto et al. 1983; Ladevèze and Simmonds 1998; Dong et al. 2001; El Fatmi and Ghazouani 2011a; Yu et al. 2012; Genoese et al. 2014a]. This is due to the status and the asymptotic nature of SV's solution, as well as to the sectional mechanical characteristics it provides [Ladevèze and Simmonds 1998; El Fatmi and Zenzri 2002; Yu et al. 2012; Blasques 2012; El Fatmi 2012; Genoese et al. 2014a]. SV's solution, SV's principle, and SV's end-effects are redundant key-words in the literature around SV's problem for which the main results need here to be recalled.

Because it describes the exact 3D solution in the interior area of the beam, 3D SV's solution (also called central solution) reflects the real mechanical behavior of the section that results from its shape

and its materials. It is worth noting that an important set of sectional quantities can be extracted from the computation of 3D SV's solution [El Fatmi and Ghazouani 2011a; 2011b; Yu et al. 2012; Blasques 2012; El Fatmi 2012]; these quantities are:

- the canonical sectional stress fields $\boldsymbol{\sigma}_{\text{sv}}^i$, that correspond to each one of the six cross-sectional stresses (the shear forces, the axial force, the torsional moment, the bending moments);

- the sectional out-of plane warping $\boldsymbol{W}_{\text{sv}}^i$, and the sectional Poisson's effects $\boldsymbol{\Pi}_{\text{sv}}^i$ related to each one the 6 cross-sectional stresses;

- the structural sectional stiffness 6×6 matrix $\boldsymbol{\Gamma}_{\text{sv}}$ wherein the off-diagonal terms reflect the *coupling effects* (between bending, torsion and tension) that can occur for an arbitrary composite section.

The existence of the sectional properties are mainly due to two important mathematical properties of SV's solution; this one is polynomial with respect to the beam axis and is a linear function of the (six) cross-sectional stresses. Using these properties, Berdichevsky [1979] has shown that 3D SV's solution can be split[1] into a set of 2D problems on the cross-section and a set of 1D equations that defines a beam-like theory (denoted here by SVBT). This splitting has been later used in several works to compute SV's solution using a 2D finite element technique, where only the section has to be discretized [Giavotto et al. 1983; El Fatmi and Zenzri 2002; 2004; Alpdogan et al. 2010; Blasques 2012; El Fatmi 2012; Genoese et al. 2014b]. Recently, using different numerical methods, software has even been developed as variational asymptotic beam section analysis (VABS) [Yu et al. 2012], beam cross-section analysis software (BECAS) [Blasques 2012], or composite section and beam analysis (CSection, a part of CSB) [El Fatmi 2012] to provide, for any section defined by its 2D geometry and its material(s), all its sectional characteristics ($\boldsymbol{\sigma}_{\text{sv}}^i$, $\boldsymbol{W}_{\text{sv}}^i$, $\boldsymbol{\Pi}_{\text{sv}}^i$, $\boldsymbol{\Gamma}_{\text{sv}}$).

Besides, concerning the end-effects, SV's Principle is usually taken to mean that these effects vanish closely to the loaded ends. In many cases, this is not true; see [Toupin 1965] for counter examples, and also the end-effects analysis of [Horgan and Simmonds 1991; 1994] and [Volovoi et al. 1999] when strongly anisotropic materials and/or thin-walled open profiles are involved. For such beams, end-effects can persist over distances comparable to the beam length, and even dominate the structural beam behavior; in that case SV's solution may no longer be valid to describe the elastic solution in the interior part of the beam.

The most famous case deals with the torsion of a cantilever open thin-walled profile (Figure 1(a)) for which the built-in effects (characterized here by a distance d) can reach the loaded end. In that case, SV's solution is no longer valid to describe the solution in the interior part of the beam. This leads to a structural mechanical behavior for the beam significantly different from that predicted by (1D) SVBT's torsion; in that case one has to resort to the nonuniform torsion of [Vlasov 1959] which accounts for the restrained warping right to the built-in section.

Let's use this example to also show that, unlike conventional beam theories that distinguish compact and walled (and even thin or thick, open or closed) sections, no distinction should be done for a composite section. Indeed, consider the rectangular *compact* composite section shown in (Figure 1(c)), where both materials are isotropic but with different elastic Young's moduli E_1 and E_2. When $E_1 = E_2$, the section

---

[1]One could find a link with the proper generalized decomposition (PGD) method [Polit et al. 2015], but it is worth noting that this decomposition is here an exact mathematical property of 3D SV's solution.
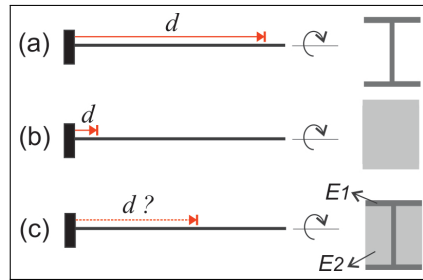
Figure 1. Built-in effects for cantilever beams subjected to tip torsion.

becomes a compact homogeneous section, and one can show that the built-in effect (d) remains close to the built-in section (Figure 1(b)), SV's solution is valid in the interior area of the beam and SVBT's torsion correctly describes the structural behavior of the beam. In contrast, when $E_1 \gg E_2$, the beam behavior becomes similar to that of an open profile. It is here clear that the built-in effect, for this composite section, may spread over a distance d that depends on the material contrast E_1/E_2 which may significantly influence the structural behavior of the beam.

What to learn from this example? Moving away from the end sections, the 3D solution tends asymptotically towards SV's solution. The *end-effects* depend on the whole nature of the cross-section and the boundary conditions, and are not necessary *confined* close to the end sections but can significantly *spread* in the interior area of the beam. In particular, for open profile or/and strongly anisotropic composite section, such end-effects may dominate the global elastic behavior of the beam. For such beams, it is then important to refine classical beam theories (and even SVBT) by incorporating, at least, the most influential end-effects. Thus, for a really general beam theory, no distinction about the kind of section has to be done. The behavior of a section is due to its whole *nature*: shape and material(s).

To improve the prediction of the classical beam theories which assume a rigid body motion of the cross-section, the so-called *higher order beam theories* are built on displacement models that allow some deformation of the section. In literature, some refined beam theories are based on a mathematical modeling of the displacement field and others, more physical, are based on a modeling that account for the cross-section nature.

As mathematical modeling, a significant contribution is the Carrera unified formulation (CUF) proposed in [Carrera and Giunta 2010]. In CUF, different N-order beam models can be developed using the same unified displacement field expression. Let (x, y) and z be the coordinates of the cross-section and the beam axis, respectively. The displacement model is written as an expansion of generic functions, F_τ,

$$\boldsymbol{u}(x, y, z) = \sum_{\tau=1}^{M} F_\tau(x, y)\boldsymbol{u}_\tau(z), \qquad (1)$$

where M is the number of terms of the expansion, F_τ the base functions that model the kinematic of the cross-section and $\boldsymbol{u}_\tau$ the displacement vector. A common choice is the use of a Taylor-like $x^i y^j$-polynomial expansion (where i and j are integer such as $0 \le (i + j) \le N$); in that case, one can show that the total number of displacement variables (or degrees of freedom) is given by $[3(N + 1)(N + 2)/2]$ for an N-order beam theory. CUF, allows, a priori, to deal with an arbitrary cross-section. However, this

approach remains N-dependent and, in practice, the choice of N is not so evident because it depends on the cross-section complexity and the beam problem to solve. One can find a CUF presentation and several applications in [Carrera et al. 2015] and also a software using CUF, named MUL2, on the website mul2.com.

In the other modeling way, more physical, the displacement field is written as

$$
\boldsymbol{\xi}(\boldsymbol{u}, \boldsymbol{\omega}, \{\eta\}) = \overbrace{\boldsymbol{u}(z) + \boldsymbol{\omega}(z) \wedge \boldsymbol{X}}^{\text{rigid motion of the section}} + \sum_{k=1}^{n} \overbrace{\eta_k(z) \boldsymbol{M}^k(x, y)}^{\text{enrichment}}, \tag{2}
$$

where $(\boldsymbol{u}, \boldsymbol{\omega})$ are the cross-sectional displacement (translation and rotation), $\boldsymbol{X}$ the in-section vector position, and $\{\eta\}$ a set of η_k control parameters of the sectional displacement modes $\boldsymbol{M}^k$ which are supposed to be known. The objective of such models is to allow and control some sectional displacement modes to better satisfy the boundary conditions, which *could capture* some *end-effects*. This approach requires, as a first step, a *cross-section analysis* to determine the set $\{\boldsymbol{M}^k\}$ of sectional modes to be used in the enrichment part of the displacement model. However, this way leads to a beam theory that *really fit* the cross-section, and hence the beam problem, if the set $\{\boldsymbol{M}^k\}$ is sufficiently representative of the cross-section mechanics.

The pioneers of such theories are Benscoter [1954] and Vlasov [1959], who deal with the torsion of thin-walled profiles using as sectional mode an approximation of the SV-torsional out-of plane warping of the section. Later, both theories have been extended (or generalized) to different shapes of homogeneous sections and also adapted to some composite sections [Loughlan and Ata 1998; Kim and White 1997; Roberts and Al-Ubaidi 2001; Ferrero et al. 2001; Lee and Lee 2004; Yu et al. 2005; Kim et al. 2006; Pluzsik and Kollar 2006; Jung et al. 2007; Sapountzakis and Mokos 2007].

A significant contribution, even if limited to thin open/closed profiles, is given by the generalized beam theory (GBT) initiated by Schardt [1994] and currently developed by Camotim, Silvestre and their colleagues [Camotim et al. 2006; Silvestre et al. 2011; Bebiano et al. 2015]. GBT is a beam theory including, as sectional modes, out-of plane warpings and distortions. In GBT cross-section analysis step, the section is reduced to a piecewise description of its contour from which the computation of the sectional modes is done; one can find a description of this procedure in [Camotim et al. 2007] or in the manual of the software GBTUL (http://www.civil.ist.utl.pt/gbt/) based on GBT computations.

Another solution, available for an arbitrary cross-section, is to refer to the extended 3D SV's solution. Indeed, the set of sectional modes $\{\boldsymbol{W}_{\text{sv}}^i, \boldsymbol{\Pi}_{\text{sv}}^i\}$ introduced above and that can be extracted from the computation of the correspondent SV's solution is particularly indicated[2] to reflect the cross-section mechanics, taking into account its shape and material(s). Using this way that refers to 3D SV's solution I proposed in [El Fatmi 2007a; 2007b; 2007c] for homogeneous beams a general nonuniform warping theory including as sectional modes the three SV out-of plane warpings $\{\boldsymbol{W}_{\text{sv}}^k, i = 1, \ldots, 3)\}$ related to the two shear forces and the torsional moment; its enrichment displacement part is written $\sum_{k=1}^{3} \eta_k(z) \boldsymbol{W}_{\text{sv}}^k(x, y)$. Later this work has been extended in [El Fatmi and Ghazouani 2011a] to composite beams, including also, as in

---

[2]Vlasov and Benscoter models constitute examples that refer to SV's solution, using as its unique sectional mode an approximation of the SV-torsional out-of plane warping.

plane deformation, the SV sectional Poisson's effects leading to the following displacement model

$$\xi(u, \omega, \{\alpha\}, \{\beta\}) = u(z) + \omega(z) \wedge X + \sum_{i=1}^{3} \alpha_i(z) \Pi_{sv}^{i}(x, y) + \sum_{j=1}^{3} \beta_j(z) W_{sv}^{j}(x, y), \qquad (3)$$

where Π_{sv}^{i} are the sectional Poisson's effects related to the axial force and the two bending moments. However, the correspondent beam theory was limited to x-y-symmetric sections made of orthotropic materials for which the principal material coordinates coincide with those of the beam (this kind of cross-section will be denoted by *so*-CS). Except the limitation[3] to *so*-CS, the displacement model (Equation (3)) has the advantage to lead to a refined beam theory (RBT) adapted to the section nature. This RBT built on SV's solution has been applied [El Fatmi and Ghazouani 2011b] to analyze the built-in effects influence on the structural behavior of end-loaded cantilever beams. The results, obtained for a representative set of *so*-CS, showed that the beam theory is able to describe the built-in effects, and hence their influence on the structural behavior of the beam. Moreover, moving away from the built-in section, the results (3D displacements and stresses) tend towards 3D SV's solution in the interior part of the beam, which is expected for a beam model built on 3D SV's solution.

In contrast with this beam model (Equation (3)) where the unknowns are only the kinematic parameters η_k (or α_k and β_k), an alternative way has been proposed by [Genoese et al. 2014a; 2014b] where the beam theory is obtained on the basis of a mixed Hellinger–Reissner principle by defining the static and the kinematics on the basis of stresses and displacements that refers to SV's solution: the kinematic description uses the six SV's sectional modes (as in (3)) and the stress field is evaluated as the sum of the contribution due to the central solution (or SV's solution) and to the six sectional modes.

The present refined beam theory (denoted RBT/SV) is a large extension of the RBT proposed in [El Fatmi and Ghazouani 2011a], also built on SV's solution, but valid for an arbitrary cross-section: compact or walled, mono or multicellular, thin or thick, symmetric or not, homogeneous or composite and each material may be fully anisotropic and free oriented. For that aim, the enrichment of the displacement model will not be limited to the (SV) sectional out-of plane warpings and the (SV) sectional Poisson's effects but introduces also some sectional distortion modes (denoted by D^j, $j = (1, \ldots, p)$); these latter are fundamental to help describe the mechanical behavior of thin/thick-walled profiles (Figure 2), but also some strongly contrasted composite beams (see the example of Figure 1(c)). There are different ways to choose the sectional distortions [Silvestre et al. 2011; Basaglia et al. 2011; Genoese et al. 2014b]; in the present RBT/SV, D^j are also be derived from SV's solution. RBT/SV displacement model is then defined by (2) where all the sectional modes M^k that express the enrichment part are extracted from SV's solution: $M^k = \{\Pi_{sv}^{i}, W_{sv}^{i}, D_{sv}^{j}; i = (1, \ldots, 6) \text{ and } j = (1, \ldots, p)\}$.

To solve a beam problem using RBT/SV, two steps are needed. The first step (the cross-section analysis) has to determine the sectional modes; this is achieved using an upgraded version of the numerical

---

[3]It is shown in [El Fatmi and Zenzri 2002], for this particular case of cross section, that the Poisson's effects are only due to the axial force and the bending moments, the out-of-plane warpings are only due to the torsional moment and the shear forces, and no elastic coupling is present in the structural behavior of the correspondent beam. For arbitrary composite beam, several elastic couplings between extensional, flexural and torsional deformations may occur [Chandra et al. 1990; Chandra and Chopra 1991; Rand 1998; 2000; Rappel and Rand 2000; Volovoi et al. 2001; El Fatmi and Zenzri 2002; 2004] and one can show that each one of the six cross-sectional stresses may lead to a Poisson's effect and an out-of plane warping (see the case the laminated section in Figure 12). Therefore, the choice of *so*-CS makes it possible to avoid the elastic couplings.
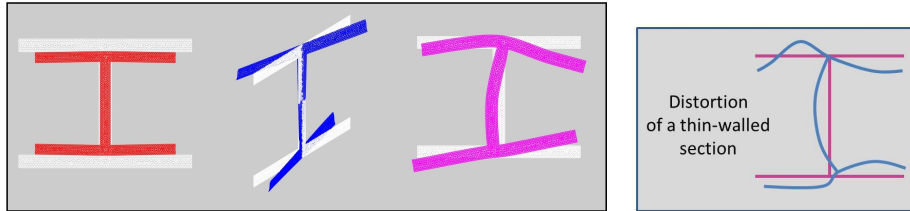
Figure 2. Left side: examples of a Poisson's effect, an out-of-plane warping and a distortion for an **I**-section. Right side: an arbitrary distortion.

Matlab tool, named CSection, I recently developed [El Fatmi 2012]. The second step uses these sectional modes to generate the correspondent beam theory and to solve the beam problem; for this step a second numerical Matlab tool, named CBeam, has been developed.

In the present paper, the first section recalls the main properties of 3D SV's solution needed for the development of the beam theory. The second section describes how the (SV) sectional modes can be extracted from SV's solution. Then, in the third section, starting from the displacement model, the corresponding beam theory is established and discussed. The numerical implementation of RBT/SV and the numerical tools CSection and CBeam are presented in the fourth section. Finally, using RBT/SV, the last section is devoted to the computations of a significant set of homogeneous and composite beams. To clearly show the accuracy of the beam model and the numerical tools[4] CSection and CBeam that come with it, the 1D/3D results focus on the critical points as the shear force effect in the 1D structural behavior of the beam and the 3D stress fields in the interior area of the beam and close to the ends. 1D/3D RBT/SV results are compared to 1D/3D SV's solution and to the those provided by full 3D-FEM computations, using the finite element code Abaqus.
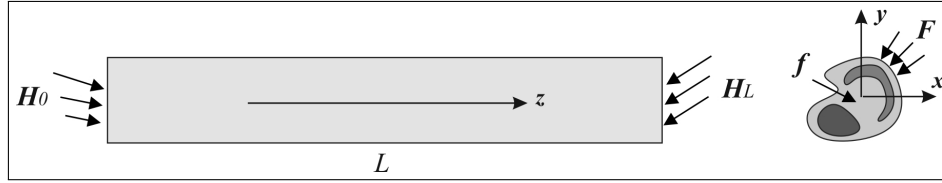
2. The extended Saint-Venant's problem and solution

One can find in [El Fatmi and Zenzri 2002; 2004; El Fatmi and Ghazouani 2011a; El Fatmi 2012] details about the 3D SV's solution and its properties; in this section we just recall the reference problem and the general expression of the correspondent 3D SV's solution[5] and some important properties. Indeed, this solution is here fundamental to extract the sectional displacement modes that will be used to formulate the beam theory.

2A. *The reference beam problem.* SV's problem is a 3D equilibrium elastic problem Figure 3. The composite beam is along the z axis and occupies a prismatic domain Ω of cross-section S independent of z and length L. S_{lat} is the lateral surface, S_0 and S_L are the end sections. A point of the beam is marked $P = zz + X$ where X belongs to S. The materials constituting the beam are linear elastic, anisotropic and perfectly bonded together; the elastic tensor field denoted by K is z-constant (vectors and tensors are noted in boldface characters).

---

[4]CSection and CBeam can be used as Matlab tools. An evaluation version of CSection and CBeam can be obtained from the author upon email.

[5]Here, the SV problem is not the original one established for homogeneous and isotropic section and due to Saint-Venant, but that of [Iesan 1976] extended to composite section and a lateral uniform loading.

Figure 3. The extended Saint-Venant's problem.

The beam is in equilibrium under a body force density f on Ω, and surface force densities F, H_0 and H_L on S_{lat}, S_0 and S_L, respectively; the densities f and F are supposed z-constant. The equations of the linearized equilibrium are

$$
\begin{aligned}
\text{div}\boldsymbol{\sigma} + \boldsymbol{f} &= \mathbf{0} && \text{in } \Omega, \\
\boldsymbol{\varepsilon}(\boldsymbol{\xi}) &= \tfrac{1}{2}(\nabla^t \boldsymbol{\xi} + \nabla \boldsymbol{\xi}) && \text{in } \Omega, \\
\boldsymbol{\sigma} &= \boldsymbol{K} : \boldsymbol{\varepsilon}(\boldsymbol{\xi}) && \text{in } \Omega, \\
\boldsymbol{\sigma} \cdot \boldsymbol{n} &= \boldsymbol{F} && \text{on } S_{\text{lat}},
\end{aligned}
\tag{4}
$$

$$
\begin{aligned}
\boldsymbol{\sigma} \cdot (-\boldsymbol{z}) &= \boldsymbol{H}_0 && \text{on } S_0, \\
\boldsymbol{\sigma} \cdot \boldsymbol{z} &= \boldsymbol{H}_L && \text{on } S_L,
\end{aligned}
\tag{5}
$$

where $\boldsymbol{\varepsilon}(\boldsymbol{\xi})$ is the strain tensor associated to the displacement field $\boldsymbol{\xi}$; ∇, $(\cdot)^t$ and $(:)$ denote the gradient, the transpose and the double contraction operators, respectively; $\boldsymbol{\sigma}$ is the stress tensor and $\boldsymbol{n}$ is the unit vector that is normal and external to S_{lat}.

2B. ***3D SV's solution.*** 3D SV's solution is the unique (z-polynomial) solution that exactly satisfies (4) and satisfies the boundary conditions (5) only in term of resultant (force and moment). To express hereafter SV's solution, we introduce the forces and moments related to $\boldsymbol{H}_0$ and $\boldsymbol{H}_L$:

$$
[\boldsymbol{F}_0, \boldsymbol{C}_0] = \int_{S_0} [\boldsymbol{H}_0, \boldsymbol{X} \wedge \boldsymbol{H}_0]\, dS, \quad [\boldsymbol{F}_L, \boldsymbol{C}_L] = \int_{S_L} [\boldsymbol{H}_L, \boldsymbol{X} \wedge \boldsymbol{H}_L]\, dS,
\tag{6}
$$

and the classical cross-sectional stresses $[\boldsymbol{R}, \boldsymbol{M}]$ defined by

$$
\boldsymbol{R} = \int_S (\boldsymbol{\sigma} \cdot \boldsymbol{z})\, dS = \begin{bmatrix} T_x \\ T_y \\ N \end{bmatrix}, \quad \boldsymbol{M} = \int_S (\boldsymbol{X} \wedge \boldsymbol{\sigma} \cdot \boldsymbol{z})\, dS = \begin{bmatrix} M_x \\ M_y \\ M_t \end{bmatrix},
\tag{7}
$$

where the six components are the 6 classical internal forces $[T_x, T_y, N, M_x, M_y, M_t]$: the shear forces, the axial force, the bending moments and the torsional moment, respectively.

2B1. *Case without a lateral loading.* In this case, the loading is reduced to $[H_0, H_L]$ and 3D SV's solution is given by

$$\boldsymbol{\xi}_{sv}(x, y, z) = \boldsymbol{u}(z) + \boldsymbol{\omega}(z) \wedge \boldsymbol{X} + \sum_{i=1}^{6} F_i(z) \boldsymbol{U}_{sv}^i(x, y), \tag{8}$$

$$\boldsymbol{\sigma}_{sv}(x, y, z) = \sum_{i=1}^{6} F_i(z) \boldsymbol{\sigma}_{sv}^i(x, y), \tag{9}$$

where F_i is one of the six internal forces $\{T_x, T_y, N, M_x, M_y, M_t\}$. In these expressions, the cross-sectional displacement $[\boldsymbol{u}, \boldsymbol{\omega}]$ and the cross-sectional stresses $[\boldsymbol{R}, \boldsymbol{M}]$ are solution of the following set[6] of 1D equations:

$$\boldsymbol{R}' = \boldsymbol{0},$$

$$\boldsymbol{M}' + z \wedge \boldsymbol{R} = \boldsymbol{0},$$

$$\begin{bmatrix} \boldsymbol{\gamma} \\ \boldsymbol{\chi} \end{bmatrix} = \begin{bmatrix} \boldsymbol{u}' + z \wedge \boldsymbol{\omega} \\ \boldsymbol{\omega}' \end{bmatrix} = \boldsymbol{\Lambda}_{sv} \begin{bmatrix} \boldsymbol{R} \\ \boldsymbol{M} \end{bmatrix}, \tag{10}$$

$$[\boldsymbol{R}, \boldsymbol{M}]_{z=0} = [-\boldsymbol{F}_0, -\boldsymbol{C}_0],$$

$$[\boldsymbol{R}, \boldsymbol{M}]_{z=L} = [\boldsymbol{F}_L, \boldsymbol{C}_L],$$

where $(\cdot)'$ denotes the derivative with respect to z. Besides, the 6×6 compliance matrix $\boldsymbol{\Lambda}_{sv}$, which defines the structural 1D behavior of the beam, is related to the elasticity tensor $\boldsymbol{K}$ by

$$\boldsymbol{\Lambda}_{sv} = [\lambda_{ij}], \quad \lambda_{ij} = \int_S \boldsymbol{\sigma}_{sv}^i(x, y) : \boldsymbol{K}^{-1}(x, y) : \boldsymbol{\sigma}_{sv}^j(x, y) \, dS. \tag{11}$$

Remark 2.1. In 3D SV's solution, $\boldsymbol{U}_{sv}^i$, $\boldsymbol{\sigma}_{sv}^i$ and $\boldsymbol{\Lambda}_{sv}$ don't depend on the beam problem, but only on the section nature (shape and materials). For a given cross-section defined by its 2D geometry and its material(s), these (SV) sectional quantities can be determined once and for all. In that case, for a given beam problem, they can be used to easily obtain the correspondent 3D SV solution; for that aim, two steps are needed:

(i) $\boldsymbol{\Lambda}_{sv}$ is used to solve the 1D problem (10) to obtain the correspondent 1D solution $[\boldsymbol{u}, \boldsymbol{\omega}, \boldsymbol{R}, \boldsymbol{M}]$;

(ii) then, $[\boldsymbol{U}_{sv}^i, \boldsymbol{\sigma}_{sv}^i]$ are used to immediately express the 3D SV's solution according to (8) and (9).

2B2. *Case with a lateral loading.* If a z-uniform lateral loading $[\boldsymbol{f}, \boldsymbol{F}]$ is added to $[H_0, H_L]$, the expression of SV's changes[7] and, in particular, the expression of the displacement becomes

$$\boldsymbol{\xi}_{sv}(x, y, z) = \boldsymbol{u}(z) + \boldsymbol{\omega}(z) \wedge \boldsymbol{X} + \sum_{i=1}^{6} F_i(z) \boldsymbol{U}_{sv}^i(x, y) + \boldsymbol{D}_{sv}(x, y), \tag{12}$$

---

[6]These 1D equations define the SV beam-like theory (SVBT).

[7]For more details, see [Ladevèze and Simmonds 1998; El Fatmi and Zenzri 2002; 2004].

Distortion of the profile
(simple distortional mode)
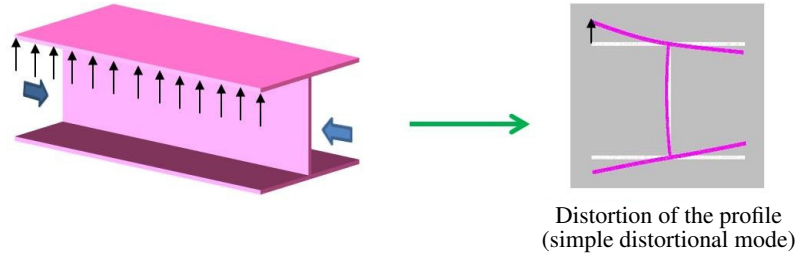
Figure 4. The sectional distortion D_{sv} related to the uniform lateral load.

where the vector D_{sv}, which is proportional to $[f, F]$, depends only on the section nature (shape and materials) and the kind of $[f, F]$ loading. Therefore, for a given uniform lateral loading $[f, F]$, D_{sv} can be determined once and for all [El Fatmi 2012].

3. The sectional displacement modes

Three kinds of sectional modes are extracted from the SV displacement expressions (8) and (12): the Poisson's effects and the out of plane warpings related to each one of the six internal forces and several sectional distortions. An example of each kind of mode is given left side of Figure 2. For a given section (shape and materials), all these SV sectional modes will be provided by the numerical tool CSection [El Fatmi 2012] which has been upgraded for the present work (a quick presentation of CSection is done in section-5A).

3A. *Sectional Poisson's effects and out-of plane warpings.* The expression of the 3D SV displacement (Equation (8)) may be seen as the contribution of two parts:

- $[u(z) + \omega(z) \wedge X]$, which reflects the rigid motion of the section,
- $\left[\sum_{i=1}^{6} F_i(z) U_{sv}^i(x, y)\right]$, which reflects the contribution of each internal forces to the deformation of the section.

Because U_{sv}^i depend only on the section nature (shape and materials), they are viewed as sectional deformation modes. Moreover, each U_{sv}^i can be split into two parts:

- $W_{sv}^i = (U_{sv}^i \cdot z)\, z$, the out of plane warping,
- $\Pi_{sv}^i = U_{sv}^i - W_{sv}^i$, the in plane warping that can be related to the Poisson's effect.

The set of $\{\Pi_{sv}^i, W_{sv}^i; i = 1, \ldots, 6\}$ define a first set of deformation modes for the section.

Remark 3.1. For homogeneous and isotropic sections and even for *so*-CS introduced above, Poisson's effects are only due to the axial force and the bending moments, and the out-of plane warpings are only due to the shear forces and the torsional moment. However, for an arbitrary composite section each one of the six internal forces may contribute[8] to the Poisson's effects and to the out-of-plane warpings; Figure 12 shows these sectional modes for a laminated section (symmetric or antisymmetric) using anisotropic layers.

---

[8]This is intimately associated to the elastic couplings between extensional, flexural and torsional deformations that can occur for an arbitrary cross-section.
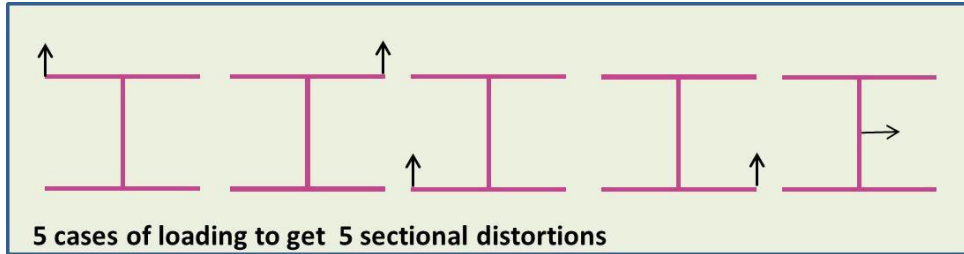
**Figure 5.** Example of uniform lateral loads for the **I**-section.
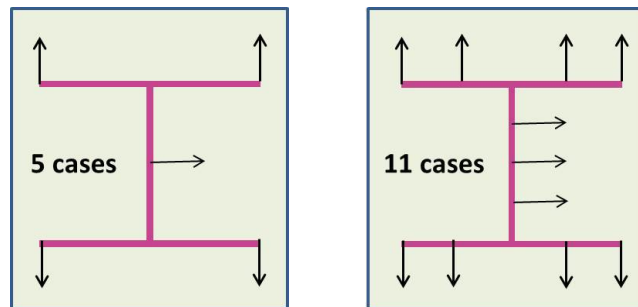
Figure 6. Different load cases (5 and 11) for the **I**-section.

3B. *Sectional distortions.* An arbitrary sectional distortion (right side of Figure 2) may be approximated by the combination of p simple distortional modes. The way used to identify a simple distortional mode is the following (Figure 4): we consider a SV problem with a particular uniform and lateral load F and we extract from the corresponding displacement SV solution (Equation (12)), the vector D_{sv}. The later which contributes to the displacement and which is due to the presence (and the location) of the lateral load is viewed as a distortional mode; for instance, see the result obtained for D_{sv} in the right-side of Figure 4. To obtain p simple distortional modes, one has to consider (separately) p cases of lateral loads. For example, five uniform lateral loads[9] may be considered to compute (separately) five simple distortion modes for the **I**-section (Figure 5), each case is related to a uniform lateral load. These five cases can be summarized on the cross-section (left side of Figure 6). However, one could choose a larger number of cases, for example the 11 cases presented in the right side of Figure 6. Figure 7 shows the 11 simple sectional distortion modes (computed by CSection) that correspond to the 11 load cases. This procedure is not automatic and need a little experience: dealing with a thin-walled section, each case of load is chosen to *cause the local bending* of a branch, or a part of the section contour easy to deform.

Remark 3.2. Other sectional modes are being investigated:

- The procedure to generate the distortions is not automatic and requires some experience. An alternative solution (more systematic) is to choose the first natural in-plane modes of vibration of the section.

---

[9]For this particular section, thanks to the symmetries, these loads can of course be theoretically reduced to one vertical load and the horizontal one. However this example is here given only to show how the loads can be chosen.
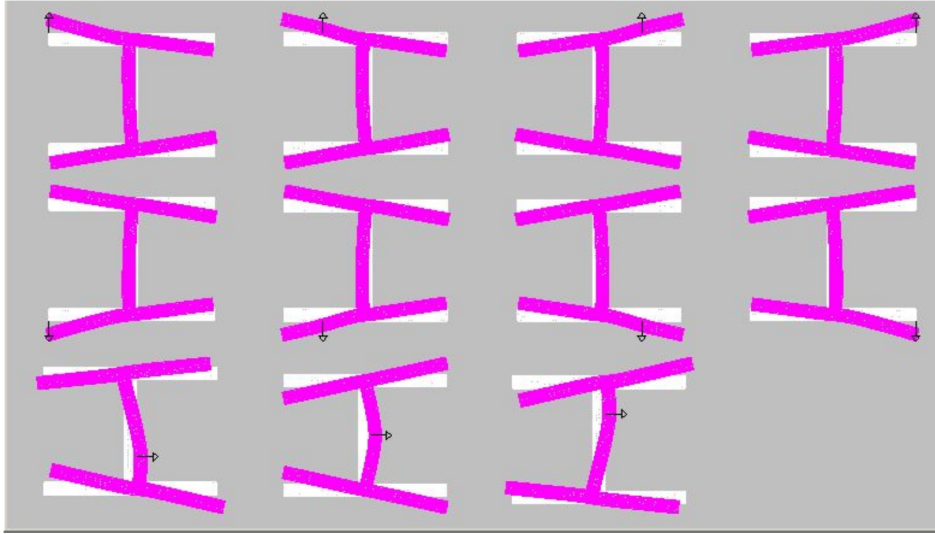
Figure 7. The 11 sectional distortions of the **I**-section.
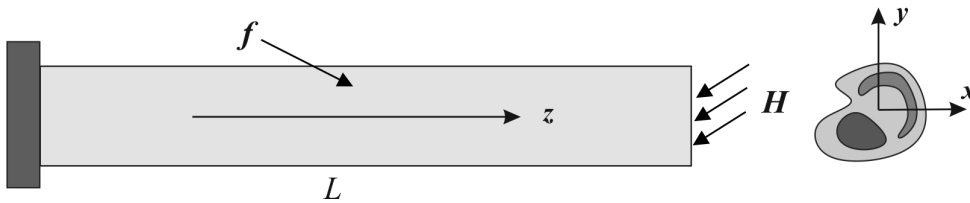
Figure 8. Cantilever composite beam subjected to a body force and a tip traction.

- Concerning the out of plane warpings, they are here limited to those extracted from SV's solution and they might be considered as the most important ones. However, for the case which cannot be described with SV's modes, an enrichment may also be done using the first out-of plane natural vibrations of the section.

To allow these investigations, the software CBeam presented in Section 5B has been designed to run regardless of the number of sectional modes provided for the section.

4. The refined beam theory built on SV's solution

To derive the equations that govern the beam theory (RBT/SV), we consider just for convenience, the cantilever composite beam (Figure 8) subjected to a body loading f and a traction H acting on S_L.

4A. *Kinematical modeling.* The RBT/SV displacement model is given by

$$\boldsymbol{\xi}_{\text{RBT/SV}}(x, y, z) = \boldsymbol{\xi}(\boldsymbol{u}, \boldsymbol{\omega}, \{\eta\}) = \boldsymbol{u}(z) + \boldsymbol{\omega}(z) \wedge \boldsymbol{X} + \eta_k(z) \boldsymbol{M}^k(x, y), \tag{13}$$

where $(\eta_k(z)\boldsymbol{M}^k(x, y))$ is here a sum using the repeated indices convention with $k \in \{1, \ldots, n\}$. In RBT/SV model, the sectional modes $\boldsymbol{M}^k$ are the *own* modes of the section that *derive* from the correspondent 3D SV's solution. The set of sectional modes $\boldsymbol{M}^k$ is given by all the available sectional modes for the cross-section:

- $\boldsymbol{W}_{\mathrm{sv}}^i$, the sectional out of plane warping ($i \in \{1, \ldots, 6\}$),

- $\boldsymbol{\Pi}_{\mathrm{sv}}^i$, the sectional Poisson's effects ($i \in \{1, \ldots, 6\}$),

- $\boldsymbol{D}_{\mathrm{sv}}^j$, a set of sectional distortion modes ($j \in \{1, \ldots, p\}$).

The beam theory associated with this displacement model, parametrized by $(\boldsymbol{u}, \boldsymbol{\omega}, \{\eta\})$, is derived below thanks to the virtual work principle; however, this way being classical, only the main equations are specified and commented (for more details see, for example, [El Fatmi and Ghazouani 2011a]).

Using the matrix notation, the strain tensor components corresponding to this displacement model are

$$
[\boldsymbol{\varepsilon}] = \begin{bmatrix} \varepsilon_{xx} \\ \varepsilon_{yy} \\ 2\varepsilon_{xy} \\ 2\varepsilon_{xz} \\ 2\varepsilon_{yz} \\ \varepsilon_{zz} \end{bmatrix} = \begin{bmatrix} 0 \\ 0 \\ 0 \\ \gamma_x - y\chi_z \\ \gamma_y + x\chi_z \\ \gamma_z + y\chi_x - x\chi_y \end{bmatrix} + \begin{bmatrix} \eta_k M_{x,x}^k \\ \eta_k M_{y,y}^k \\ \eta_k (M_{x,y}^k + M_{y,x}^k) \\ \eta_k M_{z,x}^k + \eta_k' M_x^k \\ \eta_k M_{z,y}^k + \eta_k' M_y^k \\ \eta_k' M_z^k \end{bmatrix}, \tag{14}
$$

where $\boldsymbol{\gamma} = \boldsymbol{u}' + \boldsymbol{z} \wedge \boldsymbol{\omega}$, $\boldsymbol{\chi} = \boldsymbol{\omega}'$, and $(\cdot)_{,x}$ or $(\cdot)_{,y}$ denote the derivative with respect to x or y, respectively; $\boldsymbol{z}$ is the unit vector along the beam axis, as already mentioned.

4B. *Internal forces, external forces and equilibrium equations.* Let us denote by $\hat{\boldsymbol{\xi}} = \boldsymbol{\xi}(\hat{\boldsymbol{u}}, \hat{\boldsymbol{\omega}}, \{\hat{\eta}\})$ a virtual displacement that satisfies the boundary conditions $(\hat{\boldsymbol{u}}, \hat{\boldsymbol{\omega}}, \{\hat{\eta}\}) = (\boldsymbol{0}, \boldsymbol{0}, \{0\})$ at $z = 0$ and $\hat{\boldsymbol{\varepsilon}} = \boldsymbol{\varepsilon}(\hat{\boldsymbol{\xi}})$ the corresponding virtual strain tensor. The internal virtual work is

$$
W_i = - \int_L \int_S \boldsymbol{\sigma} : \hat{\boldsymbol{\varepsilon}} \, dS \, dz. \tag{15}
$$

Using (14), W_i takes the form

$$
\begin{aligned}
W_i &= - \int_L (\boldsymbol{R} \cdot \hat{\boldsymbol{\gamma}} + \boldsymbol{M} \cdot \hat{\boldsymbol{\omega}} + A^k \hat{\eta_k}' + A_s^k \hat{\eta_k}) \, dz \\
&= \int_L [\boldsymbol{R}' \cdot \hat{\boldsymbol{u}} + (\boldsymbol{M}' + \boldsymbol{x} \wedge \boldsymbol{R}) \cdot \hat{\boldsymbol{\omega}} + (A^{k'} - A_s^k)\hat{\eta_k}] \, dz - [\boldsymbol{R} \cdot \hat{\boldsymbol{u}} + \boldsymbol{M} \cdot \hat{\boldsymbol{\omega}} + A^k \hat{\eta_k}]_L,
\end{aligned} \tag{16}
$$

where $(\boldsymbol{R}, \boldsymbol{M})$, the classical cross sectional stresses, and the new (or additional) ones (A^k, A_s^k) are related to the stress tensor by

$$
\boldsymbol{R} = \int_S \boldsymbol{\sigma}.\boldsymbol{z} \, dS, \tag{17}
$$

$$
\boldsymbol{M} = \int_S (\boldsymbol{X} \wedge \boldsymbol{\sigma}.\boldsymbol{z}) \, dS, \tag{18}
$$

$$A^k = \int_S (\tau_{xz} M_x^k + \tau_{yz} M_y^k + \sigma_{zz} M_z^k) \, dS, \tag{19}$$

$$A_s^k = \int_S (\sigma_{xx} M_{x,x}^k + \sigma_{yy} M_{y,y}^k + \tau_{xy}(M_{x,y}^k + M_{y,x}^i) + \tau_{xz} M_{z,x}^k + \tau_{yz} M_{z,y}^k) \, dS, \tag{20}$$

where

$$[\sigma_{xx}, \sigma_{yy}, \tau_{xy}, \tau_{xz}, \tau_{yz}, \sigma_{zz}]$$

are the components of the stress tensor. The external virtual work is

$$W_e = \int_L \int_S \boldsymbol{f} \cdot \hat{\boldsymbol{\xi}} \, dS \, dz + \int_{S_L} \boldsymbol{H} \cdot \hat{\boldsymbol{\xi}} \, dS. \tag{21}$$

Using the expression of $\hat{\boldsymbol{\xi}}$, W_e takes the form

$$W_e = \int_L (\boldsymbol{p} \cdot \hat{\boldsymbol{u}} + \boldsymbol{\mu} \cdot \hat{\boldsymbol{\omega}} + \kappa^k \widehat{\eta_k}) \, dz + \boldsymbol{P} \cdot \hat{\boldsymbol{u}}_L + \boldsymbol{C} \cdot \hat{\boldsymbol{\omega}}_L + Q^k \widehat{\eta^k}_L, \tag{22}$$

where the (1D) generalized external forces $(\boldsymbol{p}, \boldsymbol{\mu}, \kappa^k, \boldsymbol{P}, \boldsymbol{C}, Q^k)$ are defined by

$$\begin{aligned} \boldsymbol{p} &= \int_S \boldsymbol{f} \, dS, & \boldsymbol{P} &= \int_{S_L} \boldsymbol{H} \, dS, \\ \boldsymbol{\mu} &= \int_S \boldsymbol{X} \wedge \boldsymbol{f} \, dS, & \boldsymbol{C} &= \int_{S_L} \boldsymbol{X} \wedge \boldsymbol{H} \, dS, \\ \kappa^k &= \int_S \boldsymbol{f} \cdot \boldsymbol{M}^k, & Q^k &= \int_{S_L} \boldsymbol{H} \cdot \boldsymbol{M}^k \, dS, \end{aligned} \tag{23}$$

where $(\boldsymbol{p}, \boldsymbol{\mu}, \boldsymbol{P}, \boldsymbol{C})$ are classical and (κ^k, Q^k) are new (or additional) generalized external forces related to the sectional deformation modes $\boldsymbol{M}^k$. Thanks to the principle of virtual work, Equations (16) and (22) are used to provide the equilibrium equations

$$\begin{aligned} \boldsymbol{R}' + \boldsymbol{p} &= 0, \\ \boldsymbol{M}' + \boldsymbol{x} \wedge \boldsymbol{R} + \boldsymbol{\mu} &= 0, \\ A^{k'} - A_s^k + \kappa^k &= 0 \quad \text{(for all } k), \end{aligned} \tag{24}$$

and the boundary conditions

$$x = L, \quad (\boldsymbol{R}, \boldsymbol{M}) = (\boldsymbol{P}, \boldsymbol{C}) \quad \text{and} \quad A^k = Q^k \quad \text{(for all } k). \tag{25}$$

4C. *Structural behavior.* Using matrix notation, the strain tensor can be written $\mathscr{D}$:

$$[\boldsymbol{\varepsilon}](x, y, z) = \mathbf{B}(x, y)\mathscr{D}(z), \tag{26}$$

with

$$
\mathbf{B} =
\begin{bmatrix}
0 & 0 & 0 & 0 & 0 & 0 & \ldots & M_{x,x}^k & 0 & \ldots \\
0 & 0 & 0 & 0 & 0 & 0 & \ldots & M_{y,y}^k & 0 & \ldots \\
0 & 0 & 0 & 0 & 0 & 0 & \ldots & M_{x,y}^k + M_{y,x}^k & 0 & \ldots \\
1 & 0 & 0 & 0 & 0 & -y & \ldots & M_{z,x}^k & M_x^k & \ldots \\
0 & 1 & 0 & 0 & 0 & x & \ldots & M_{z,y}^k & M_y^k & \ldots \\
0 & 0 & 1 & y & -x & 0 & \ldots & 0 & M_z^k & \ldots
\end{bmatrix},
\qquad
\mathscr{D} =
\begin{bmatrix}
\gamma_x \\ \gamma_y \\ \gamma_z \\ \chi_x \\ \chi_y \\ \chi_z \\ \vdots \\ \eta_k \\ \eta_k' \\ \vdots
\end{bmatrix},
\tag{27}
$$

where $\mathscr{D}$ represents the generalized 1D strain vector. If $\mathscr{T}$ denotes the corresponding generalized cross-sectional stress vector, the 1D elastic constitutive relation can be written $\mathscr{T} = \mathbf{\Gamma}\,\mathscr{D}$ where $\mathbf{\Gamma}$ defines the 1D structural rigidity operator

$$
\begin{bmatrix}
\boldsymbol{R} \\ \boldsymbol{M} \\ \vdots \\ A_s^k \\ A_k \\ \vdots
\end{bmatrix}
= \mathbf{\Gamma}
\begin{bmatrix}
\boldsymbol{\gamma} \\ \boldsymbol{\chi} \\ \vdots \\ \eta_k \\ \eta_k' \\ \vdots
\end{bmatrix}.
\tag{28}
$$

The operator $\mathbf{\Gamma}$ may be derived from the identification

$$
\int_S ([\boldsymbol{\varepsilon}_I]^t [\,\mathbf{K}][\boldsymbol{\varepsilon}_J])\, dS = [\mathscr{D}_I]^t \mathbf{\Gamma}[\mathscr{D}_J],
\tag{29}
$$

where $(\boldsymbol{\varepsilon}_I, \mathscr{D}_I)$ and $(\boldsymbol{\varepsilon}_J, \mathscr{D}_J)$ are any virtual strains. Introducing the expression of the deformations (Equation (26)), we obtain the following results for $\mathbf{\Gamma}$:

$$
\mathbf{\Gamma} = \int_S \boldsymbol{B}^t(x, y)[\mathbf{K}](x, y)\boldsymbol{B}(x, y)\, dS.
\tag{30}
$$

4D. *The RBT/SV equations.* To summarize, the displacement model $\boldsymbol{\xi}(\boldsymbol{u}, \boldsymbol{\omega}, \{\eta\})$ has led to a beam theory governed by the set of 1D equations

$$
\begin{aligned}
\boldsymbol{R}' + \boldsymbol{p} &= 0, \\
\boldsymbol{M}' + \boldsymbol{x} \wedge \boldsymbol{R} + \boldsymbol{\mu} &= 0, \\
A^{k'} - A_s^k + \kappa^k &= 0 \quad \text{(for all } k\text{)}, \\
\mathscr{T} &= \mathbf{\Gamma}\,\mathscr{D},
\end{aligned}
\tag{31}
$$

and, for the cantilever reference problem (Figure 8), the 1D boundary conditions are

$$
\begin{aligned}
x = 0, &\qquad\qquad (\boldsymbol{u}, \boldsymbol{\omega}, \{\eta\}) = (\boldsymbol{O}, \boldsymbol{O}, \{O\}), \\
x = L(\boldsymbol{R}, \boldsymbol{M}) = (\boldsymbol{P}, \boldsymbol{C}), &\qquad\qquad A^k = Q^k \quad \text{(for all } k\text{)}.
\end{aligned}
\tag{32}
$$

4E. *The correspondent 3D solution.* Let $\boldsymbol{u}^e$, $\boldsymbol{\omega}^e$, $\{\eta^e\}$ be the 1D equilibrium solution of a beam problem using RBT/SV. Conforming to the displacement model, the correspondent 3D solution is given by the 3D displacement field

$$\boldsymbol{\xi}_{\text{RBT/SV}}^e(x, y, z) = \boldsymbol{\xi}(\boldsymbol{u}^e, \boldsymbol{\omega}^e, \{\eta\}^e) = \boldsymbol{u}^e(z) + \boldsymbol{\omega}^e(z) \wedge \boldsymbol{X} + \eta_k^e(z)\boldsymbol{M}^k(x, y), \qquad (33)$$

which leads to the 3D stress tensor field

$$\boldsymbol{\sigma}_{\text{RBT/SV}}^e(x, y, z) = \boldsymbol{K}(x, y) : \boldsymbol{\varepsilon}(\boldsymbol{\xi}^e(x, y, z)) = [\boldsymbol{K}](x, y)\mathbf{B}(x, y)\mathcal{D}^e(z). \qquad (34)$$

The 3D stress field may also be given with respect to the internal forces:

$$\boldsymbol{\sigma}_{\text{RBT/SV}}^e = [\boldsymbol{K}](x, y)\mathbf{B}(x, y)\boldsymbol{\Gamma}^{-1}\mathcal{T}^e(z). \qquad (35)$$

4F. *Comments.* RBT/SV displacement model (Equation (13)), which is built on 3D SV's solution, may be seen as a model which starts from the exact 3D SV displacement form (Equation (8)), where the sectional stresses F_i are relaxed in favor of independent in-and-out warping parameters (η_k). These new kinematical parameters (η_k) lead, by duality, to enrich the static ones (the internal and external generalized forces) which could better satisfy the boundary conditions. Therefore, if the beam length is sufficiently large, it is expected that 3D RBT/SV solution coincide with 3D SV's solution in the interior area of the beam, and better describes the end effects (see the examples presented in Section 6C).

5. Numerical implementation and numerical tools

To solve a beam problem using RBT/SV, two steps are needed; each one of them is associated to a numerical tool: CSection and CBeam. CSection computes by 2D-FEM the sectional modes of the cross-section; then, CBeam, uses these sectional modes to generate systematically the correspondent beam theory (RBT/SV) and to compute by 1D-FEM the beam problem. Developed on Matlab platform as any Matlab-tool, CSection and CBeam are complementary and constitute a package named CSB (composite section and beam analysis). These numerical tools are quickly presented hereafter.

5A. *CSection to compute the sectional characteristics.* CSection [El Fatmi 2012] is a numerical tool devoted to the computation of all the sectional characteristics of an arbitrary cross-section

$$\{\boldsymbol{\Gamma}_{\text{sv}}, \boldsymbol{\sigma}_{\text{sv}}^i, \boldsymbol{\Pi}_{\text{sv}}^i, \boldsymbol{W}_{\text{sv}}^i (i = 1 \cdots 6), \boldsymbol{D}_{\text{sv}}^j (j = 1 \cdots p)\}.$$

CSection is developed conforming to the numerical method proposed by El Fatmi and Zenzri [2002]. This method consists in solving, by 2D finite elements, a set of elastic problems on the section from which all the above sectional characteristics are deduced. In the first version, the sectional modes provided by CSection were limited to the Poisson's effects and the out-of-plane warpings. For the present work, CSection has been upgraded in order to provide also a set of sectional distortions. For a given cross-section, $n = 6 + p$ linear 2D problems are solved and the numerical cost is low considering that the n problems use the same rigidity matrix. The time needed to compute a section with 1000 elements (six-node triangles) is about a few seconds on a common PC; however, for a composite section as a laminated one, the discretization can be more important and need a little more time (for instance, the laminated cross-section presented in Section 6B has 5230 elements and its computation is about 20 seconds).

Remark 5.1. It is worth noting that all the characteristics provided for a section constitute a relevant set of information about the *section Mechanics* that can help section design and even predict the mechanical behavior of the beam that will result.

5B. *CBeam to compute the beam.* CBeam computes the equilibrium of a straight beam subjected to any loading and boundary conditions. CBeam solves by 1D-FEM the beam problem according to RBT/SV equations *regardless of the number*[10] *of sectional modes* available for the cross-section.

RBT/SV displacement model (13) uses a set of kinematical parameters $\{\boldsymbol{u}, \boldsymbol{\omega}, \{\eta\}\}$ which represent $m = 6+n$ independent degrees of freedom (DOF) for the displacement field: three translations $[u_x, u_y, u_z]$, three rotations $[\omega_x, \omega_y, \omega_z]$ and the η_k associated to the sectional modes available for the cross-section. In CBeam, RBT/SV equations are solved by 1D-FEM using cubic (Hermite type) interpolation (shape) functions for each one of the m DOF.

In CBeam, the loading has to be introduced in a 3D way, as it is applied and localized on the beam. The computation of the 1D sectional forces (or generalized external forces) needed by the 1D-FEM computation (as κ^k or Q^k in (23)) are ensured automatically by CBeam.

The displacement boundary conditions may act on each sectional parameter of the displacement model (or each DOF). For instance, for a built-in section, one has to block not only the cross-sectional displacement ($\boldsymbol{u}, \boldsymbol{\omega}$) but also $\{\eta\}$ to restrain the deformation right to the built-in section. Another interesting use is the simulation of a diaphragm placed inside a closed thin-walled profile: one may block just the in plane deformation right to the cross-section where the diaphragm is located.

In CBeam, just for comparison, two solvers are proposed: RBT/SV solver and SVBT solver. RBT/SV solver solves the beam problem using RBT/SV and SVBT solver solves the beam problem to get the correspondent 3D SV's solution[11] according to (8)–(10) (see Remark 2.1). Using RBT/SV solver or SVBT solver, the resolution being by 1D-FEM, the time required to solve any beam problem is really insignificant (less of one second on a common PC).

6. Numerical applications and results

To illustrate the efficiency of RBT/SV and the numerical tools CSection and CBeam that come with, a significant set of homogeneous and composite beams are computed, using different loads and displacement conditions. The panel of the different cross-sections and beam problems to be analyzed have been chosen to clearly show that RBT/SV is able to describe the different kinds of 3D effects related to the section nature (shape and materials), to take for account a significant part of the end effects (as those related to the restrained warpings) and to provide a good description of the structural beam behavior, even if the beam slenderness is relatively small.

The most important 1D/3D results are presented focusing on the 3D stress fields, in the interior area of the beam and close to the ends. RBT/SV results are compared to 3D SV's solution (also computed by

---

[10]For the present work, the sectional modes are those deriving from 3D SV's solution, but (in CBeam) the user is free to introduce any additional sectional mode he wants to consider, as an analytic closed form function of the section coordinates x and y. Each additional mode is associated systematically to an additional parameter (η) which is viewed as a new degree of freedom for the section deformation. In CBeam, the independence of the sectional modes is systematically checked and the current solver uses a simple diagonal preconditioning to avoid the singularities of the operators.

[11]Of course, for SVBT solver the displacement boundary conditions act (as in classical beam theory) only on $\boldsymbol{u}$ and $\boldsymbol{\omega}$.

Mats	$E_s = 200\,\text{GPa}$	$\nu = 0.25$	
Matc	$E_c = \{200, 100, 10, 4, 1\}\,\text{GPa}$	$\nu = 0.25$	
Mat33	$E_Z = 148.00\,\text{GPa}$	$E_X = 8.37\,\text{GPa}$	$E_Y = 8.37\,\text{GPa}$
	$G_{XZ} = 4.40\,\text{GPa}$	$G_{YZ} = 4.40\,\text{GPa}$	$G_{XY} = 2.72\,\text{GPa}$
	$\nu_{XZ} = 0.33$	$\nu_{YZ} = 0.33$	$\nu_{XY} = 0.54$

Table 1. The materials.

CBeam but using SVBT-solver) and to those provided by a full 3D-FEM computation, using the finite element code Abaqus.

6A. *The materials, the sections and the beam problems.*

6A1. *The materials.* The materials are given in Table 1 where E, G and ν denote the Young modulus, the shear modulus and the Poisson's ratio, respectively. Mats (s as skin) and Matc (c as core) are two contrasted isotropic materials for which E_s/E_c can reach 200; Mat33 is an orthotropic[12] material used in [El Fatmi and Ghazouani 2011b] and chosen because its ratio $E/G \approx 33$ is important which can significantly influence the amount of the restrained warping effect in case of torsion, even if the beam is not an open-walled profile.

6A2. *The sections.* Three homogeneous sections (H1, H2 and H3) and three composite sections (C1, C2 and C3) are considered; their dimensions are specified in Figure 9:

H1: h=100mm; t=20mm
H2: h=50mm; b=150mm
H3: h=50; b=150mm; t=10mm

C1: h2=2xh1=50mm; b=50mm;
C2: h=b/2=100mm; c=75mm; t=5mm
C3: h=8mm; b=30mm; t=1mm
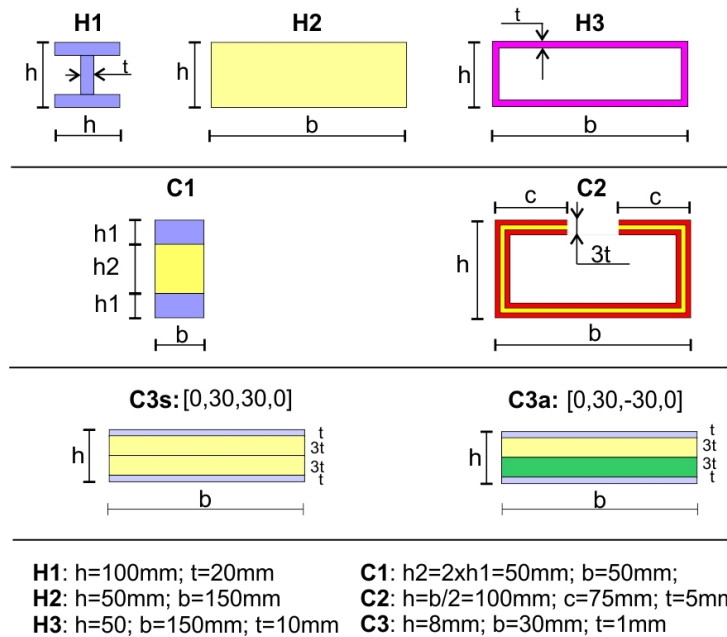
Figure 9. The different cross-sections and their dimensions.

---

[12] Mat33 is in fact a transversely isotropic material.

- H1 is a thick isotropic (Mats) I-section;

- H2 is a compact rectangular orthotropic (Mat33) section;

- H3 is a thin orthotropic (Mat33) box section;

- C1 is a sandwich section where the materials are isotropic (Mats, Matc) and strongly contrasted $E_s/E_c = 200$;

- C2 is a nonsymmetric open-walled and sandwich section where the materials (Mats, Matc) are isotropic with $E_s/E_c = 50$;

- C3 is a symmetric (C3s) or antisymmetric (C3a) laminated section using the same layers (Mat33) with $[0, +30, +30, 0]$ and $[0, -30, +30, 0]$ orientations, respectively.

6A3. *The beam problems.* Using the above sections, six equilibrium beam problems (Figure 10) are analyzed:

- P1: the bending-torsion of a cantilever H1-beam of length $L = 10h$; the end loads are applied as indicated in Figure 10 where the magnitude of the force is $F = 1000\,\mathrm{N}$;

- P2: the torsion of a cantilever H2-beam of length $L = 10h$; the end loads are applied as indicated in Figure 10 where the magnitude of the force is $F = 1000\,\mathrm{N}$;

- P3: the bending of a clamped-clamped H3-beam of length $L = 10h$; the upper face of the beam is subjected to a pressure $q = 10000\,\mathrm{Nm}^{-2}$;

- P4: the bending of a clamped-clamped composite C1-beam of length $L = 20h$; the beam is subjected to the body force $\boldsymbol{f} = \rho \boldsymbol{g}$ with $g = 10\,\mathrm{ms}^{-2}$, $\rho_s = 7500\,\mathrm{kgm}^{-3}$, $\rho_c = 250\,\mathrm{kgm}^{-3}$;

- P5: the bending-torsion of a short ($L/h = 7$) cantilever composite C2-beam subjected to a lateral traction $q = 10000\,\mathrm{Nm}^{-2}$;

- P6: a cantilever laminated C3-beam of length $L = 10h$ (symmetric or antisymmetric) subjected to a tension $q = 10000\,\mathrm{Nm}^{-2}$.

6B. *Cross-section analyses.*

6B1. *Sectional constants.* Tables 2 and 3 provide, for each section, the (nonzero) components of the 6×6 rigidity matrix $\boldsymbol{\Gamma}_{\mathrm{sv}}$ related to the structural 1D behavior. Note that, as expected: no elastic coupling is present for the sections H1, H2, H3 and C1; for C2, the only off-diagonal term (Γ_{16}) is due to the nonsymmetry[13] of the section; however the laminated composite sections C3a and C3s exhibit 2 and 3 off-diagonal terms, respectively, which reflect different elastic couplings (between extensional, flexural and torsional deformation) arising from the anisotropic nature of the layers and their stacking sequences.

Remark 6.1. For the sandwich section C1, one can deduce from $\boldsymbol{\Gamma}_{\mathrm{sv}}$ (computed for different ratios $r = E_s/E_c$) the values of the shear coefficients k_y with respect to r. The reults, given in Table 4, clearly show how much k_y can be affected when the sandwich is strongly contrasted. In such a case, it is expected to get an important shear force effect for an x-flexure of the correspondent beam (see the solution to problem P4).

---

[13]For C2, the position of the shear center C, given by CSection, is $y_C = \boldsymbol{GC} \cdot \boldsymbol{y} = -9.37\,\mathrm{mm}$.
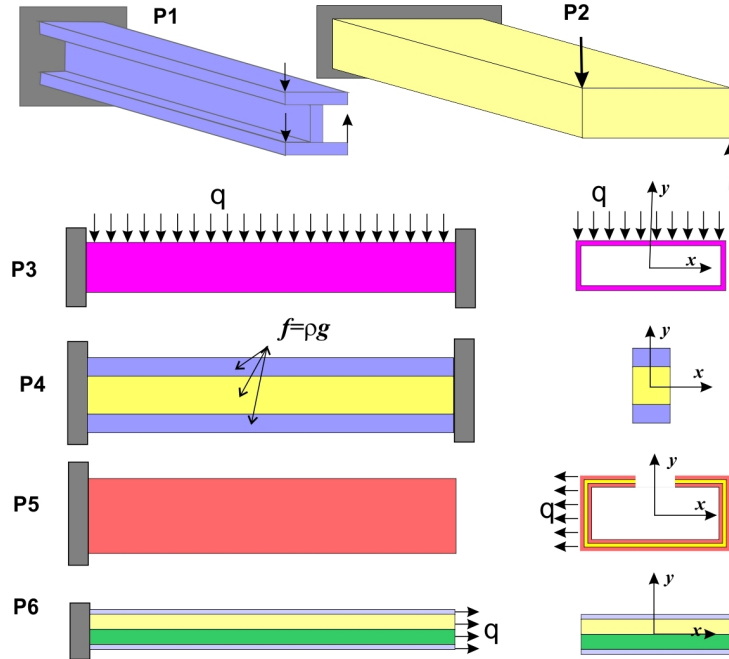
Figure 10. The equilibrium beam problems.

Sect.	H1	H2	H3	C1
Γ_{11}	$2.8788 \cdot 10^8$	$2.7500 \cdot 10^7$	$2.1254 \cdot 10^8$	$1.6117 \cdot 10^8$
Γ_{22}	$1.3211 \cdot 10^8$	$2.7460 \cdot 10^7$	$3.8106 \cdot 10^7$	$2.4131 \cdot 10^6$
Γ_{33}	$1.0400 \cdot 10^9$	$1.1100 \cdot 10^9$	$7.2000 \cdot 10^8$	$5.0250 \cdot 10^8$
Γ_{44}	$1.3787 \cdot 10^6$	$2.3125 \cdot 10^5$	$2.5400 \cdot 10^5$	$7.2969 \cdot 10^5$
Γ_{55}	$6.7467 \cdot 10^5$	$2.0813 \cdot 10^6$	$1.7140 \cdot 10^6$	$1.0469 \cdot 10^5$
Γ_{66}	$5.7766 \cdot 10^4$	$2.1724 \cdot 10^4$	$2.9900 \cdot 10^5$	$3.0352 \cdot 10^4$

Table 2. The nonzero components of the (6×6) rigidity matrix for the sections H1, H2, H3 and C1.

6B2. *Sectional modes.* For the sections H1, H2, H3, C1 and C2, Figure 11 presents the Poisson's effects (associated to the axial force and the bending moments) and the out of plane warpings (associated to the shear forces and the torsional moment). However, these sectional modes are given by Figure 12 for the laminated sections C3s and C3a; note that for these sections, each one of the six internal forces contribute to a Poisson's effect and an out-of plane warping. Besides, some additional sectional distortions are considered for the walled sections H3 and C2 and presented in Figure 13.

6C. *Beam problems: 1D/3D results.* Each beam problem has been computed using the numerical tool CBeam to get the 1D/3D RBT/SV solution and the correspondent 1D/3D SV solution. The 3D results are compared with a full 3D-FEM computation using Abaqus.

Sect.	C2	C3s	C3a
Γ_{11}	$1.0070 \cdot 10^8$	$2.5017 \cdot 10^6$	$3.7185 \cdot 10^6$
Γ_{22}	$1.0252 \cdot 10^8$	$7.1272 \cdot 10^5$	$8.2449 \cdot 10^5$
Γ_{33}	$9.8980 \cdot 10^8$	$1.6309 \cdot 10^7$	$1.6515 \cdot 10^7$
Γ_{44}	$1.4007 \cdot 10^6$	134.1989	139.7267
Γ_{55}	$5.1182 \cdot 10^6$	946.9796	$1.1268 \cdot 10^3$
Γ_{66}	$3.9179 \cdot 10^4$	40.2305	40.0723
Γ_{13}		$3.0162 \cdot 10^6$	
Γ_{14}			$-7.1338 \cdot 10^3$
Γ_{16}	$9.4318 \cdot 10^6$		
Γ_{25}			-40.9738
Γ_{36}			$8.4477 \cdot 10^3$
Γ_{46}		-20.3360	

Table 3. The nonzero components of the (6×6) rigidity matrix for the sections C2 and C3.

r	1	10	50	100	200
k_y	0.8330	0.2087	0.0469	0.0238	0.0120

Table 4. The shear coefficient k_y with respect to the ratios $r = E_s/E_c$ for the sandwich section C1.

Starting with the same $[x, y]$-discretization for the section (used in CSection), the beam is obtained in Abaqus by extrusion (with respect to the beam axis) and the z-discretization along the span is chosen in line with the $[x, y]$-discretization (i.e., in terms of size elements). As finite element, the computations are achieved with the C3D15 nodes quadratic triangular prism.

The comparison between RBT/SV, SV and 3D-FEM results are systematically done for the most important components of the stresses: the axial stresses σ_{zz} and the shear $\tau = \sqrt{\tau_{xz}^2 + \tau_{yz}^2}$, at the midspan ($z = L/2$) of the beam and very close to the built-in section ($0 < z < h/20$) simply denoted by z_0 which should read $z/L \approx 0$.

6D. _P1: Bending-torsion of a cantilever thick-walled beam._ Figure 14 presents the sectional stress fields for σ_{zz} and τ at the midspan and very close to the built-in section. On can note that RBT/SV and 3D-FEM results are in agreement and coincide with those of SV at midspan. Besides, Figure 15 shows the z-variation of the axial stress σ_{zz} along the span for two point A and B belonging to the extremities of the upper flange of the section. Note that, as expected SV results are the same for both points (for which the axial stresses are due only to the bending), but RBT/SV and 3D-FEM results, which are quite comparable in the major interior area of the beam, show how much the restrained warping (due to the torsion) affects the axial stresses. One can deduce from Figure 15 that the built-in effect spreads over a distance of about $d \approx 5h = L/2$.
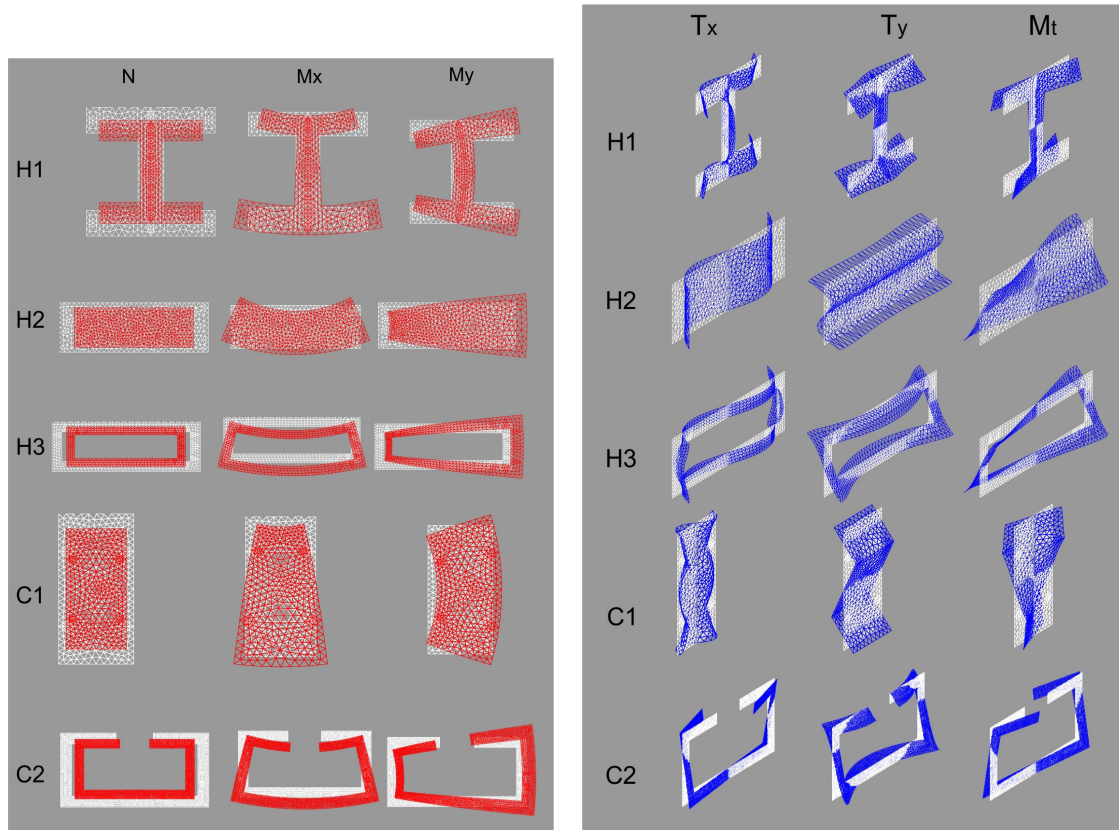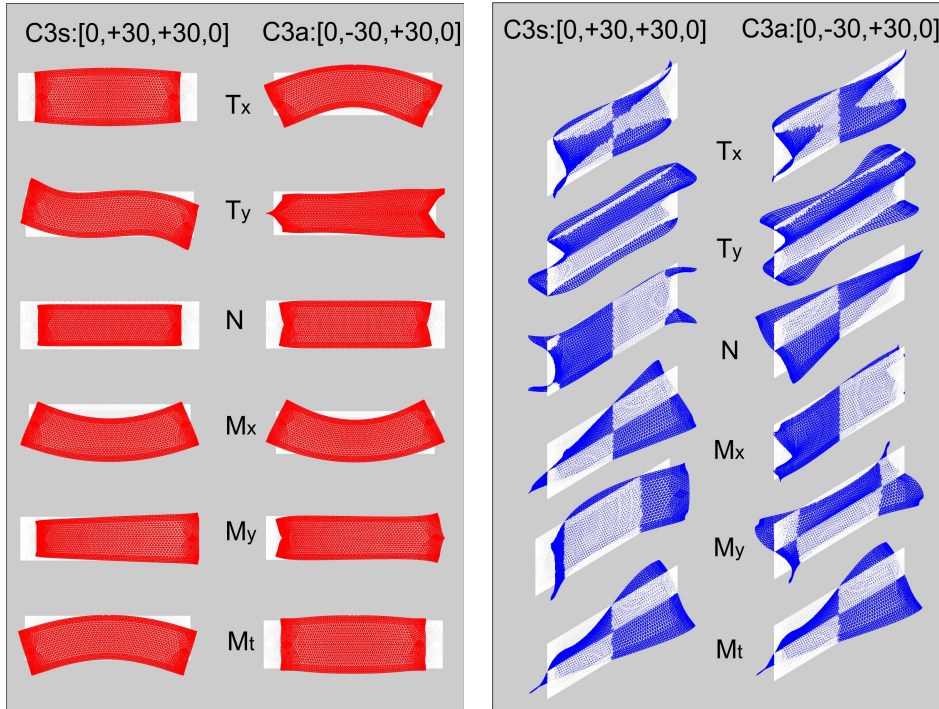
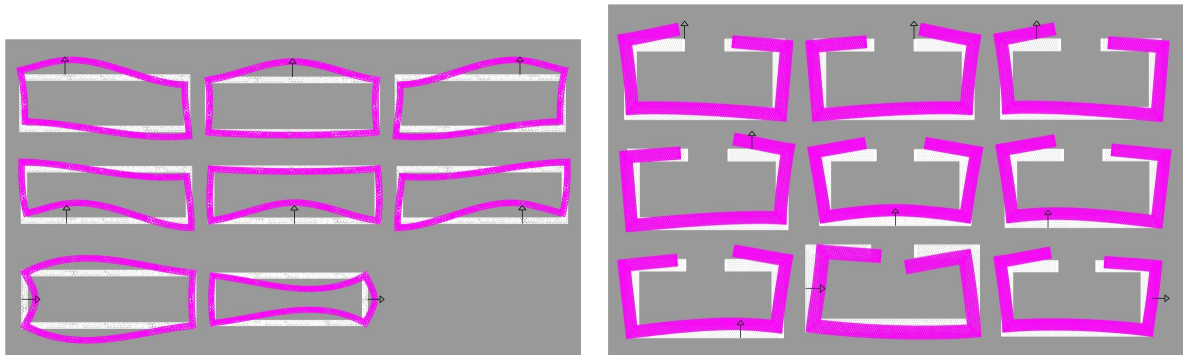**Figure 11.** Sectional deformations: Poisson's effects and out-of plane warpings.

6E. *P2: Torsion of a cantilever orthotropic beam.* It is known that the restrained warping effect is important for a walled open section subjected to torsion. However this effect can also be important for a compact section when the ratio E/G is large [El Fatmi and Ghazouani 2011b]. This ratio is about 2.5 for an isotropic material and its value for the present (Mat33) material is about 33. In Figure 16 the stresses provided by RBT/SV and 3D-FEM results are in agreement (in the major part of the beam). Moreover, Figure 17 depicts the z-variations of the axial stress σ_{zz} for a point A close to a section corner, and the z-variation of the shear τ for the point[14] B in the middle of the big side of the section. Note that, moving from the free end, the shear τ vanishes in favor of the axial stress σ_{zz}. RBT/SV and 3D-FEM results are really comparable and show that the built-in effect (related to the restrained torsional warping) spreads over a distance $d \approx L$ for this compact section; in this case SV's solution is no longer valid to represent the *central* solution.

6F. *P3: Bending of a thin orthotropic box beam.* Figure 18 depicts the 3D deformed shapes obtained by RBT/SV and the 3D-FEM computations. Note the (local) bending of the upper face of the beam due to the loading. To achieve this result, which reflects the location of the load, 8 distortional modes (see

---

[14]This point B is chosen because it is the point where the shear is maximum for SV's torsion.

**Figure 12.** Sectional deformations: Poisson's effects and warpings for the laminated sections.

Figure 13. Sectional deformations: distortions for the walled sections H3 and C2.

the left side of Figure 13) have been added to the sectional Poisson's effects and out-of plane warping modes to be used in RBT/SV.

Figure 19 shows that RBT/SV and 3D-FEM results are mainly in agreement for the axial stress σ_{zz} and the shear τ in the midspan and close to the built-in section. Instead of the shear, which is nil in the midspan, the bottom of the right side of Figure 19 compares, the σ_{xx}-field due to the local bending of the upper face of the beam: the results are qualitatively comparable but the magnitude of RBT/SV results are about 50% less than 3D-FEM ones. Thus, using some distortional modes, RBT/SV seems able to
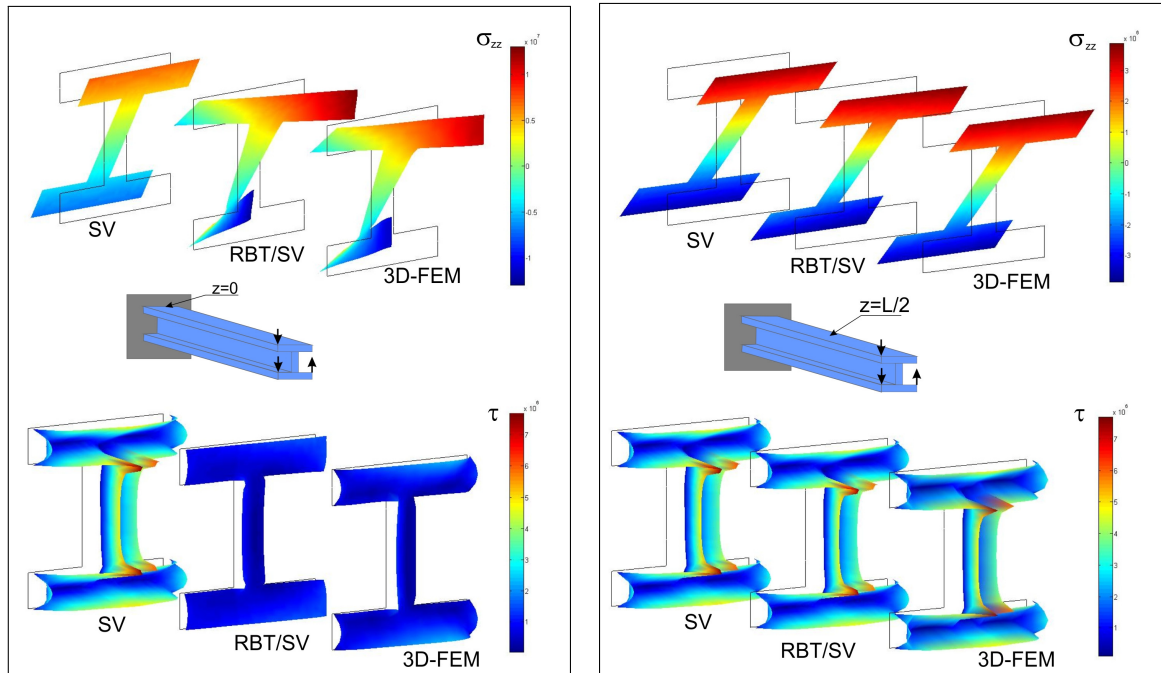
Figure 14. σ_{zz} and τ fields at $z0$ and midspan. Comparison of SV, RBT/SV and 3D-FEM results.
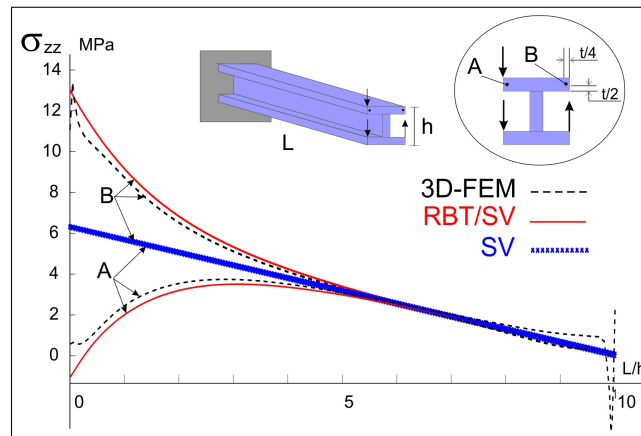
**Figure 15.** σ_{zz}-variations along the span for two points A and B belonging to the upper flange. Comparison of SV, RBT/SV and 3D-FEM results.

account for the location of the loading, which leads in this case to the bending of the upper face of the beam, but the σ_{xx} stress level is underestimated.
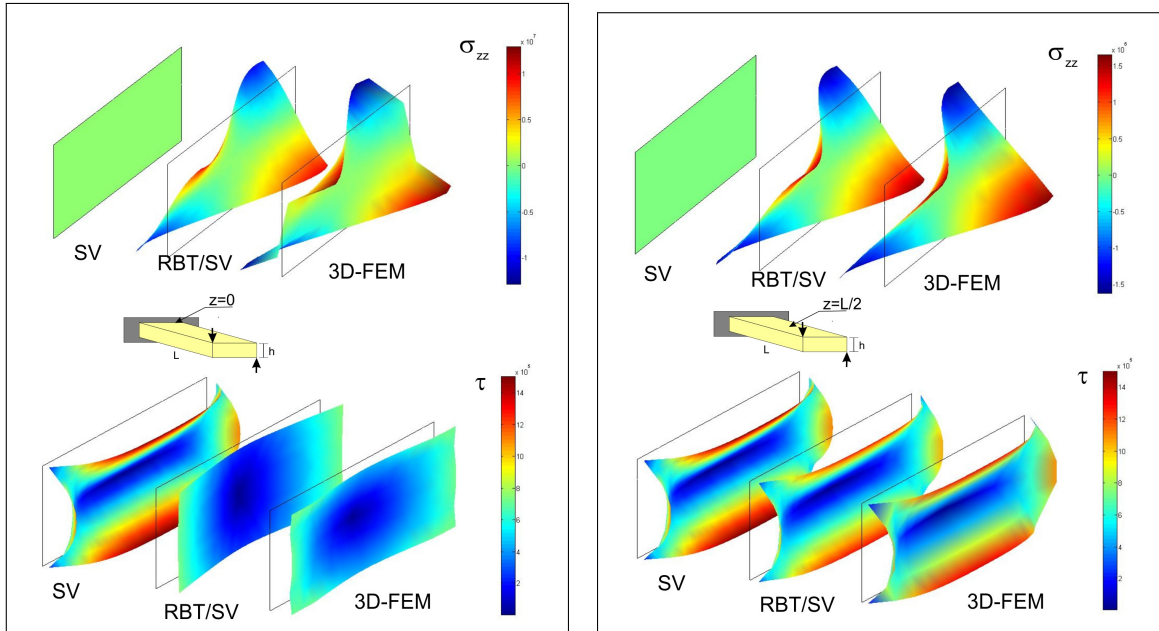
Figure 16. σ_{zz} and τ fields at $z0$ and midspan. Comparison of SV, RBT/SV and 3D-FEM results.
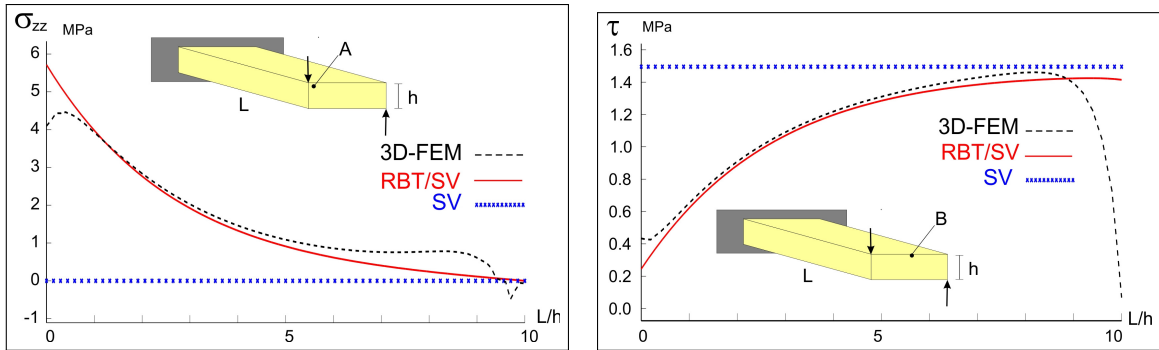
Figure 17. σ_{zz}- and τ-variation along the span for the points A and B. Comparison of SV, RBT/SV and 3D-FEM results.

6G. P4: Bending of a sandwich beam strongly contrasted. The 1D deflection due to the present x-bending is given by $u_y(z)$. Figure 20 compares SV, RBT/SV and 3D-FEM results.[15] The shear force effect is here important and taken into account by TPSV. However, for TPSV, the out-of plane warpings due to the shear force are free at the ends which leads to a more flexible beam behavior. In fact these warpings are restrained right the built-in sections and the deflection appears notably less pronounced as depicted by RBT/SV and 3D-FEM results. It is clear for this example, that these end effects are

---

[15]For the 3D-FEM results, right to a cross-section at a z abscissa, $u_y(z)$ is taken as the average of the 3D displacement with respect to y axis.
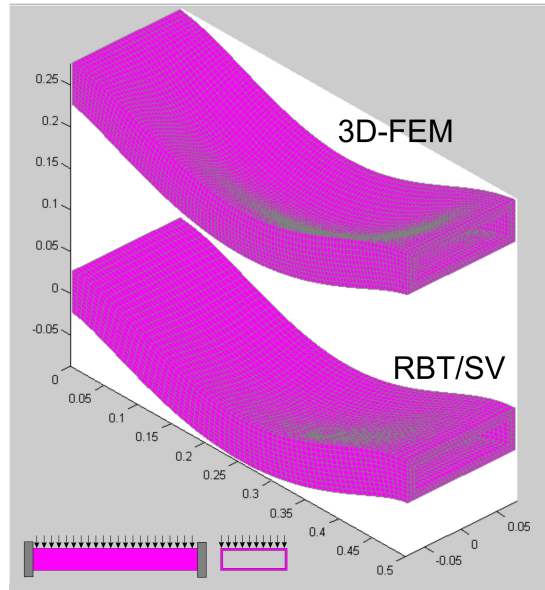
**Figure 18.** 3D deformed shape of the box beam.
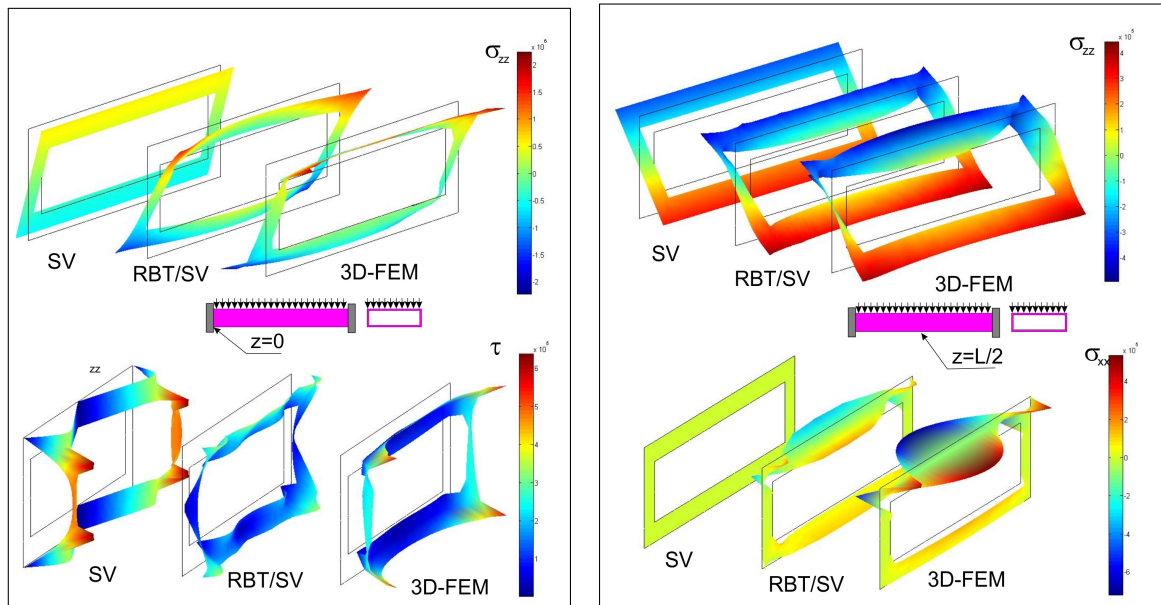
Figure 19. σ_{zz}, τ and σ_{xx} fields at $z0$ and midspan. Comparison of SV, RBT/SV and 3D-FEM results.

important and dominate the structural behavior of this (strongly contrasted) sandwich beam. For the stresses, Figure 21 shows that RBT/SV and 3D-FEM results are in agreement for the axial stress σ_{zz}, but this is not so true for the shear τ even if it is qualitatively acceptable.
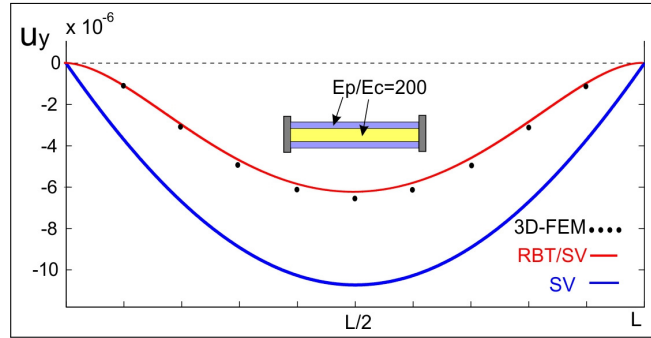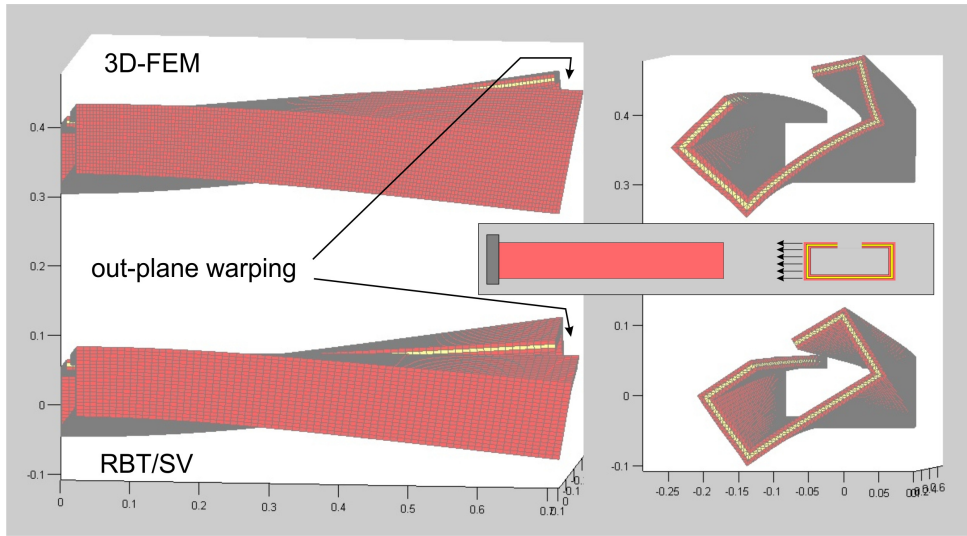
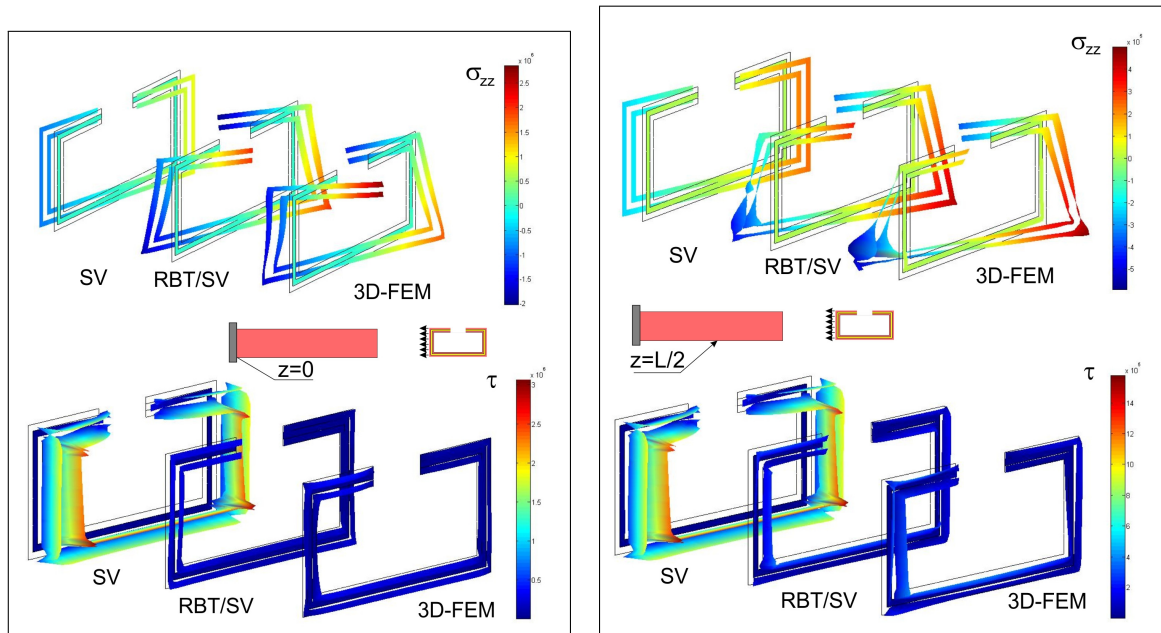**Figure 20.** Deflection u_y along the span: SV, RBT/SV and 3D-FEM results.
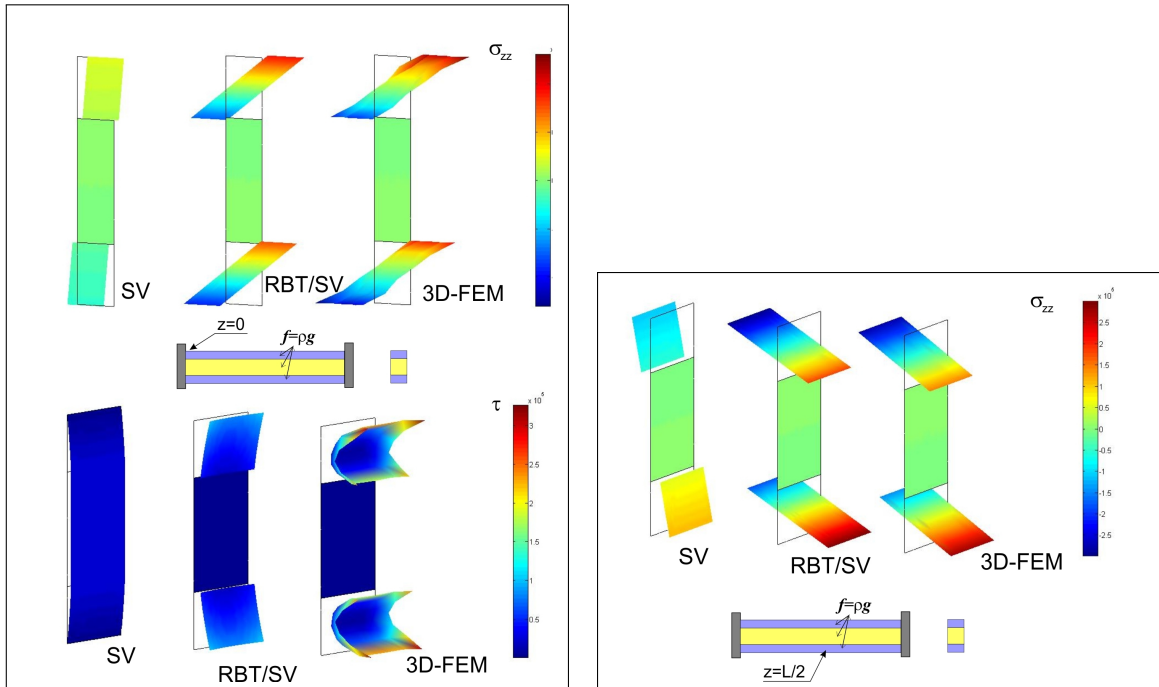
Figure 21. σ_{zz} and τ fields at $z0$ and midspan. Comparison of SV, RBT/SV and 3D-FEM results.

6H. *P5: Bending and torsion of a short unsymmetric open-walled sandwich profile.* For this unsymmetrical section, it is expected that the lateral loading leads to the bending and torsion of the beam as it is shown by the 3D deformed shape given by RBT/SV and 3D-FEM results in Figure 22: note, at the free end, that the out-of plane warping of the section and its shape are relatively well described by RBT/SV result. To obtain this result nine distortional modes (see the right side of Figure 13 have been computed by CSection to be used in RBT/SV. Figure 23 shows that RBT/SV and 3D-FEM results are also in agreement for the axial stress σ_{zz} and the shear τ in the midspan and close to the built-in section even if the beam slenderness is here relatively small ($L/h = 7$). For more details, Figure 24 depicts the
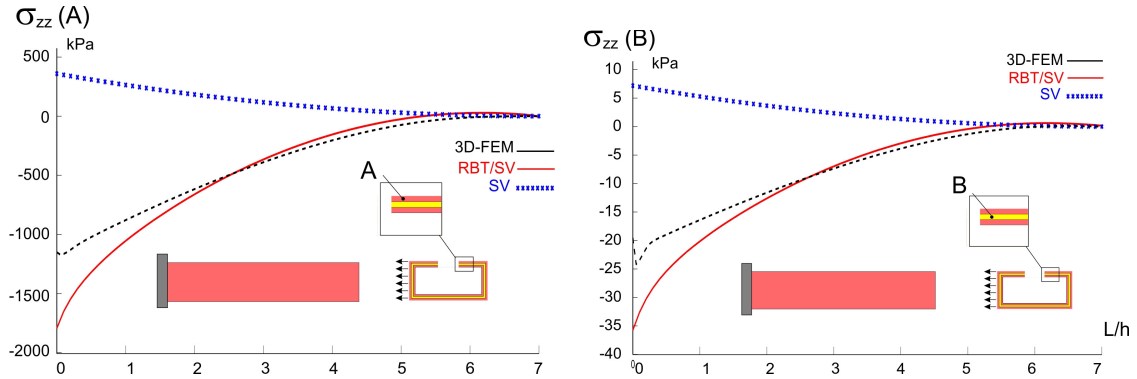
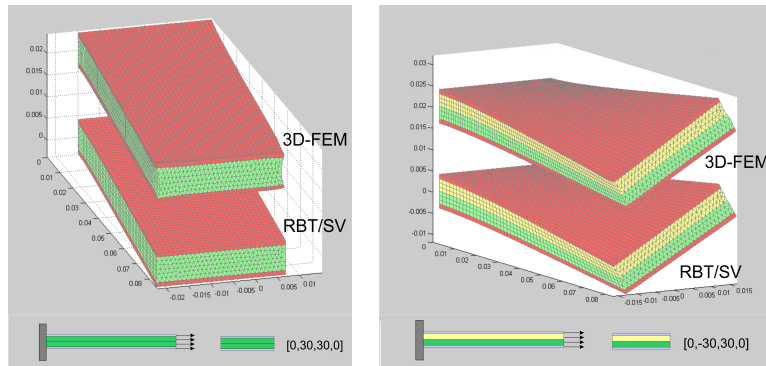**Figure 22.** 3D deformed shape for the sandwich profile: RBT/SV and 3D-FEM results.

Figure 23. σ_{zz} and τ fields at $z0$ and midspan. Comparison of SV, RBT/SV and 3D-FEM results.

σ_{zz}-variations along the span for two points A and B belonging to the skin and the core, respectively; RBT/SV and 3D-FEM results are relatively in agreement and clearly different from that of SV. This is due to the built-in effect (or the restrained warping) which spreads over a distance comparable to the beam length, and dominates the structural beam behavior.

Figure 24. σ_{zz}-variations along the span for two points A and B belonging to the skin and the core, respectively. RBT/SV and 3D-FEM results.


Figure 25. 3D deformed shape for the symmetric and antisymmetric laminated beam: RBT/SV and 3D-FEM results.

6I. *P6: Tension of a symmetric/antisymmetric laminated beam.* As expected for these laminate beams the tension leads to a lateral y-bending for the symmetric case and a torsion for the antisymmetric one, as it is shown by the 3D deformed shapes obtained by both RBT/SV and 3D-FEM computations. In terms of stresses, Figures 26 and 27 show that RBT/SV results are in agreement with the 3D-FEM ones, for both cases, symmetric and unsymmetric. For these cases, the end effects are not important and remain confined close to the ends and SV results appear valid to describe the solution in the major interior area of the beam; thus SV's solution (and hence TPSV) may be used to solve these beam problems, at least for this loading.

7. Conclusion

The present refined (1D) beam theory (RBT/SV) is free from all the classical beam assumptions and valid for an arbitrary cross-section. For a composite section, it is worth noting that no homogenization step is needed, and RBT/SV is able to predict the 3D local stresses (the six components of the stress tensor) in each material, which is fundamental for a composite beam.
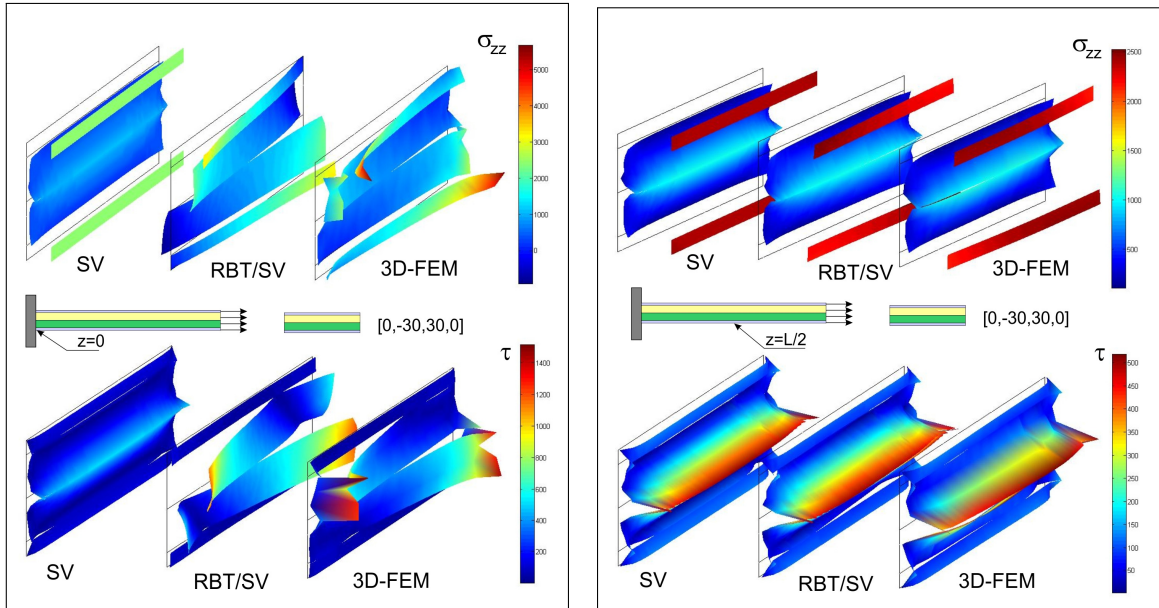
Figure 26. σ_{zz} and τ fields at $z0$ and midspan. Comparison of SV, RBT/SV and 3D-FEM results.
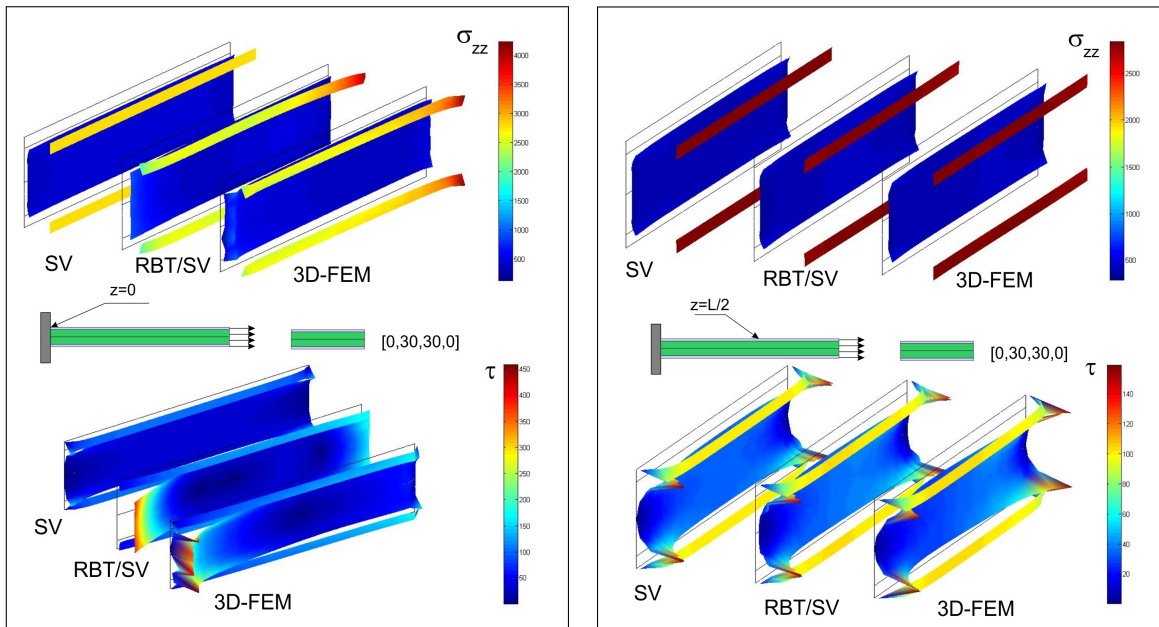
Figure 27. σ_{zz} and τ fields at $z0$ and midspan. Comparison of SV, RBT/SV and 3D-FEM results.

The enrichment of the displacement model uses the main deformation modes of the section (Poisson's effects, out-of plane warpings and distortions). For a given section, these sectional modes being extracted from the correspondent 3D SV's solution, they lead to a beam theory that really fits the section nature (shape and materials).

From the significant set of cross-sections and beam problems presented in this paper, it is clear that RBT/SV is able to describe not only the elastic structural behavior of the beam but also the 3D solution in terms of displacements and stresses in the major interior area of the beam, even if the slenderness is relatively small. Different kinds of 3D effects have been described; these are related to the shape of the section (thin/thick, walled/compact, symmetric/unsymmetric), to its composite nature (anisotropies of the materials, even strongly contrasted) and to the edge effects,[16] especially those due to a built-in section. Theoretically, any boundary condition may be treated, but for the particular case of cantilever or clamped beam, the edge effects appear to be very well described; for other cases, the results on edge effect description will depend on the boundary condition prescribed.

The present refined beam theory may be considered as *a general (1D) beam theory* not only because valid for an arbitrary cross-section (shape and material(s)) but also because it could also be seen as a refinement of SV's approach and hence the correspondent TPSV. Indeed, far from the ends, 3D-RBT/SV results (as 3D-FEM ones) tend toward those of 3D SV's solution when the beam length is sufficiently large (or the ends effects sufficiently small or confined). This result is here expected because RBT/SV is built on SV results: the enrichment in RBT/SV displacement model $\boldsymbol{\xi}_{\text{RBT/SV}}$, using the sectional modes extracted from 3D SV's solution, contains the shape of 3D SV displacement $\boldsymbol{\xi}_{\text{sv}}$ (Equation (8)).

From a practical standpoint, the application of RBT/SV, which deals with detailed results for arbitrary cross-sections, has to be obviously (or inevitably) performed through a numerical way. For that purpose, a package (CSB) of two complementary numerical tools has been developed to accompany RBT/SV: CSection & CBeam. CSection computes by 2D-FEM the sectional characteristics of the cross-section and CBeam uses these characteristics to solve by 1D-FEM the beam problem according to RBT/SV (regardless of the number of the sectional modes available for the cross-section). Thanks to these two steps which combine 2D and 1D computations for the beam, it is possible to recover an important part of the 3D beam behavior, exhibiting detailed 3D effects in terms of displacements and stresses. These numerical tools, which are easy to use, can really help section and beam design and prevent (at least as a first step) the use of costly 3D-FEM computations, especially when working with strongly anisotropic materials and/or thin-walled open/closed profiles. The present work is currently limited to a constant cross-section along the beam axis; its extension to the case of a variable cross-section is under study and will be proposed in a very near future.

References

[Alpdogan et al. 2010] C. Alpdogan, S. B. Dong, and E. Taciroglu, "A method of analysis for end and transitional effects in anisotropic cylinders", *Int. J. Solids Struct.* **47** (2010), 947–956.

[Basaglia et al. 2011] C. Basaglia, D. Camotim, and N. Silvestre, "Non-linear GBT formulation for open-section thin-walled members with arbitrary support conditions", *Comput. Struct.* **89** (2011), 1906–1919.

---

[16]The edge effects of the free ends depend on the way the tip loads are applied; tip loading and other kinds of boundary conditions need more investigation to obtain a better description of the end-effects they generate.

[Bebiano et al. 2015] R. Bebiano, R. Gonçalves, and D. Camotim, "A cross-section analysis procedure to rationalise and automate the performance of GBT-based structural analyses", *Thin-Walled Struct.* **92** (2015), 29–47.

[Benscoter 1954] S. Benscoter, "A theory of torsion bending for multicell beams", *J. Appl. Mech.* (*ASME*) **21**:1 (1954), 25–34.

[Berdichevsky 1979] V. L. Berdichevsky, "Variational-asymptotic method of constructing a theory of shells", *Prikl. Mat. Mekh.* **43**:4 (1979), 664–687. In Russian; translated in *J. Appl. Math. Mech.* **43**:4 (1979), 711–736.

[Blasques 2012] J. P. Blasques, *User's manual for BECAS: a cross section analysis tool for anisotropic and inhomogeneous beam sections of arbitrary geometry*, v2.0, Technical University of Denmark, Roskilde, Feb. 23, 2012, Available at http://orbit.dtu.dk/files/7711204/ris_r_1785.pdf.

[Camotim et al. 2006] D. Camotim, N. Silvestre, R. Gonçalves, and P. B. Dinis, "GBT-based structural analysis of thin-walled members: overview, recent progress and future developments", pp. 187–204 in *Advances in engineering structures, mechanics & construction: proceedings of an international conference on advances in engineering structures, mechanics & construction* (Waterloo, ON, 2006), edited by M. Pandey et al., Solid Mechanics and Its Applications **140**, Springer, Dordrecht, 2006.

[Camotim et al. 2007] D. Camotim, N. Silvestre, and R. Bebiano, "GBT-based local and global vibration analysis of thin-walled members", pp. 36–76 in *Analysis and design of plated structures, I: Dynamics*, edited by N. E. Shanmugam and C. M. Wang, Woodhead, Cambridge, 2007.

[Carrera and Giunta 2010] E. Carrera and G. Giunta, "Refined beam theories based on a unified formulation", *Int. J. Appl. Mech.* **2**:1 (2010), 117–143.

[Carrera et al. 2011] E. Carrera, G. Giunta, and M. Petrolo, *Beam structures: classical and advanced theories*, Wiley, Chichester, 2011.

[Carrera et al. 2015] E. Carrera, A. Pagani, M. Petrolo, and E. Zappino, "Recent developments on refined theories for beams with applications", *Mech. Eng. Rev.* **2**:2 (2015), Article ID #14–00298.

[Chandra and Chopra 1991] R. Chandra and I. Chopra, "Experimental and theoritical analysis of composite I-beams with elastic couplings", *AIAA J.* **29**:12 (1991), 2197–2206.

[Chandra et al. 1990] R. Chandra, A. D. Stemple, and I. Chopra, "Thin-walled composite beams under bending, torsional and extensional loads", *J. Aircraft* **27**:7 (1990), 619–626.

[Dong et al. 2001] S. B. Dong, K. J., and H. Lin, "On Saint-Venant's problem for an inhomogeneous, anisotropic cylinder, I: Methodology for Saint-Venant solutions", *J. Appl. Mech.* (*ASME*) **68**:3 (2001), 376–381.

[El Fatmi 2007a] R. El Fatmi, "Non-uniform warping including the effects of torsion and shear forces, I: A general beam theory", *Int. J. Solids Struct.* **44** (2007), 5912–5929.

[El Fatmi 2007b] R. El Fatmi, "Non-uniform warping including the effects of torsion and shear forces, II: Analytical and numerical applications", *Int. J. Solids Struct.* **44** (2007), 5930–5952.

[El Fatmi 2007c] R. El Fatmi, "Non-uniform warping theory for beams", *C. R. Mécanique* **335** (2007), 467–474.

[El Fatmi 2012] R. El Fatmi, "A Matlab tool to compute the mechanical characteristics of any composite section", *Rev. Compos. Matér. Av.* **22**:3 (2012), 395–413.

[El Fatmi and Ghazouani 2011a] R. El Fatmi and N. Ghazouani, "A higher order composite beam theory built on 3D Saint Venant' solution, part-1: Theoretical developments", *Compos. Struct.* **93** (2011), 557–566.

[El Fatmi and Ghazouani 2011b] R. El Fatmi and N. Ghazouani, "A higher order composite beam theory built on 3D Saint Venant' solution, part-2: Built-in effect influence on the behavior of end-loaded cantilever beams", *Compos. Struct.* **93** (2011), 567–581.

[El Fatmi and Zenzri 2002] R. El Fatmi and H. Zenzri, "On the structural behavior and the Saint Venant solution in the exact beam theory: application to laminated composite beams", *Comput. Struct.* **80**:16-17 (2002), 1441–1456.

[El Fatmi and Zenzri 2004] R. El Fatmi and H. Zenzri, "A numerical method for the exact elastic beam theory: Applications to homogeneous and composite beams", *Int. J. Solids Struct.* **41**:9–10 (2004), 2521–2537.

[Ferrero et al. 2001] J. F. Ferrero, J. J. Barrau, J. M. Segura, B. Castanie, and M. Sudre, "Torsion of thin-walled composite beams with midplane symmetry", *Compos. Struct.* **54** (2001), 111–120.

[Genoese et al. 2014a] A. Genoese, A. Genoese, A. Bilotta, and G. Garcea, "A composite beam model including variable warping effects derived from a generalized Saint Venant solution", *Compos. Struct.* **110** (2014), 140–151.

[Genoese et al. 2014b] A. Genoese, A. Genoese, A. Bilotta, and G. Garcea, "A generalized model for heterogeneous and anisotropic beams including section distortions", *Thin-Walled Struct.* **74** (2014), 85–103.

[Giavotto et al. 1983] V. Giavotto, M. Borri, P. Mantegazza, G. Ghiringhelli, V. Carmaschi, G. C. Maffioli, and F. Mussi, "Anisotropic beam theory and applications", *Comput. Struct.* **16** (1983), 403–413.

[Horgan and Simmonds 1991] C. O. Horgan and J. G. Simmonds, "Asymptotic analysis of an end-loaded, transversely isotropic, elastic, semi-infinite strip weak in shear", *Int. J. Solids Struct.* **27**:15 (1991), 1895–1914.

[Horgan and Simmonds 1994] C. O. Horgan and J. G. Simmonds, "Saint Venant end effects in composite structures", *Compos. Eng.* **4**:3 (1994), 279–286.

[Iesan 1976] D. Iesan, "Saint-Venant's problem for inhomogeneous and anisotropic elastic bodies", *J. Elasticity* **6** (1976), 277–294.

[Jung et al. 2007] S. N. Jung, I.-J. Park, and E. S. Shin, "Theory of thin-walled composite beams with single and double cell sections", *Compos. B Eng.* **38** (2007), 182–192.

[Kim and White 1997] C. Kim and R. S. White, "Thick-walled composite beam theory including 3D elastic effects and torsional warping", *Int. J. Solids Struct.* **34**:31-32 (1997), 4237–4259.

[Kim et al. 2006] N.-I. Kim, D. K. Shin, and M.-Y. Kim, "Exact solutions for thin-walled open-section composite beams with arbitrary lamination subjected to torsional moment", *Thin-Walled Struct.* **44** (2006), 638–654.

[Ladevèze and Simmonds 1998] P. Ladevèze and J. G. Simmonds, "New concepts for linear beam theory with arbitrary geometry and loading", *Eur. J. Mech. A Solids* **17**:3 (1998), 377–402.

[Lee and Lee 2004] J. Lee and S.-h. Lee, "Flexural-torsional behavior of thin-walled composite beams", *Thin-Walled Struct.* **42** (2004), 1293–1305.

[Loughlan and Ata 1998] J. Loughlan and M. Ata, "The analysis of carbon fibre composite box beams subjected to torsion with variable twist", *Comput. Methods Appl. Mech. Eng.* **152** (1998), 373–391.

[Pluzsik and Kollar 2006] A. Pluzsik and L. Kollar, "Torsion of closed section, orthotropic, thin-walled beams", *Int. J. Solids Struct.* **43** (2006), 5307–5336.

[Polit et al. 2015] O. Polit, L. Gallimard, P. Vidal, M. D'Ottavio, G. Giunta, and S. Belouettar, "An analysis of composite beams by means of hierarchical finite elements and a variables separation method", *Comput. Struct.* **158** (2015), 15–29.

[Rand 1998] O. Rand, "Interlaminar shear stresses in solid composite beams using a complete out of plane shear deformation model", *Comput. Struct.* **66**:6 (1998), 713–723.

[Rand 2000] O. Rand, "On the importance of cross-sectional warping in solid composite beams", *Compos. Struct.* **49** (2000), 393–397.

[Rappel and Rand 2000] O. Rappel and O. Rand, "Analysis of elastically coupled thick-walled composite blades", *Int. J. Solids Struct.* **37** (2000), 1019–1043.

[Roberts and Al-Ubaidi 2001] T. M. Roberts and H. Al-Ubaidi, "Influence of shear deformation on restrained torsional warping of pultruded FRP bars of open cross-section", *Thin-Walled Struct.* **39** (2001), 395–414.

[Sapountzakis and Mokos 2007] E. J. Sapountzakis and V. G. Mokos, "3D beam element of composite cross section including warping and shear deformation effects", *Comput. Struct.* **85** (2007), 102–116.

[Schardt 1994] R. Schardt, "Generalized beam theory: An adequate method for coupled stability problems", *Thin-Walled Struct.* **19** (1994), 161–180.

[Silvestre et al. 2011] N. Silvestre, D. Camotim, and N. F. Silva, "Generalized beam theory revisited: From the kinematical assumptions to the deformation mode determination", *Int. J. Struct. Stab. Dyn.* **11**:5 (2011), 969–997.

[Toupin 1965] R. A. Toupin, "Saint-Venant's principle", *Arch. Ration. Mech. Anal.* **18** (1965), 83–96.

[Vlasov 1959] V. Z. Vlasov, Тонкостенные упругие стержни, Fizmatgiz, Moscow, 1959. Translated as *Thin-walled elastic beams*, 2nd ed., National Technical Information Service, Jerusalem, 1961.

[Volovoi et al. 1999] V. V. Volovoi, D. H. Hodges, V. L. Berdichevsky, and V. G. Sutyrin, "Asymptotic theory for static behavior of elastic anisotropic I-beams", *Int. J. Solids Struct.* **36**:7 (1999), 1017–1043.

[Volovoi et al. 2001] V. V. Volovoi, D. H. Hodges, C. E. S. Cesnik, and B. Popescu, "Assessment of beam modeling methods for rotor blade applications", *Math. Comput. Model.* **33** (2001), 1099–1112.

[Yu et al. 2005] W. Yu, D. H. Hodges, V. V. Volovoi, and E. D. Fuchs, "A generalized Vlasov theory for composite beams", *Thin-Walled Struct.* **43** (2005), 1493–1511.

[Yu et al. 2012] W. Yu, D. H. Hodges, and J. C. Ho, "Variational asymptotic beam sectional analysis—an updated version", *Int. J. Eng. Sci.* **59** (2012), 40–64.

RACHED EL FATMI: rached.elfatmi@enit.rnu.tn
Ecole Nationale d'Ingénieurs de Tunis, Université de Tunis El Manar, LGC, BP 37, Le Belvédère, 1002 Tunis, Tunisia

▪▪
▪msp

A UNIFIED THEORY FOR CONSTITUTIVE MODELING OF COMPOSITES

Wenbin Yu

A unified theory for multiscale constitutive modeling of composites is developed using the concept of structure genomes. Generalized from the concept of the representative volume element, a structure genome is defined as the smallest mathematical building block of a structure. Structure genome mechanics governs the necessary information to bridge the microstructure length scale of composites and the macroscopic length scale of structural analysis and provides a unified theory to construct constitutive models for structures including three-dimensional structures, beams, plates, and shells over multiple length scales. For illustration, this paper is restricted to construct the Euler–Bernoulli beam model, the Kirchhoff–Love plate/shell model, and the Cauchy continuum model for structures made of linear elastic materials. Geometrical nonlinearity is systematically captured for beams, plates/shells, and Cauchy continuum using a unified formulation. A general-purpose computer code called SwiftComp (accessible at https://cdmhub.org/resources/scstandard) implements this unified theory and is used in a few example cases to demonstrate its application.

1. Introduction

Structural analyses are often carried out using finite element analysis (FEA) in terms of three-dimensional (3D) solid elements, two-dimensional (2D) plate or shell elements or one-dimensional (1D) beam elements (see Figure 1). Here, the notation of 1D, 2D, or 3D refers to the number of coordinates needed to describe the analysis domain. It is not related with the dimensionality of the behavior. For example, a beam element can have three-dimensional behavior as it can deform in three directions. A constitutive relation is needed for the corresponding structural element. For isotropic homogeneous structures, material properties such as Young's modulus and Poisson's ratio are direct inputs for structural analysis using solid elements; these properties, combined with the geometry of the structure, can be used for plate/shell/beam elements. However, such straightforwardness does not exist for composite structures featuring anisotropy and/or heterogeneity. Consider a typical composite rotor blade of length 8.6 m and chord 0.72 m, with a main D-spar composed of 60 graphite/epoxy plies each with a ply thickness of 125 μm. To directly use the properties of graphite/epoxy composite plies in the blade analysis, at least one 3D solid element through the ply thickness should be used. Sometimes several layers are commonly lumped together into a single element with "smeared properties", however, this will result in approximate solutions that would negate the supposed accuracy advantage gained by the use of 3D solid elements. Suppose one uses 20-noded brick elements with a 1:10 thickness-length ratio: it is estimated that around ten billion degrees of freedom are needed for the blade analysis. Such a huge FEA model is too costly for effective blade design and analysis. An alternative is to model rotor blades as beams [Yu et al. 2012]
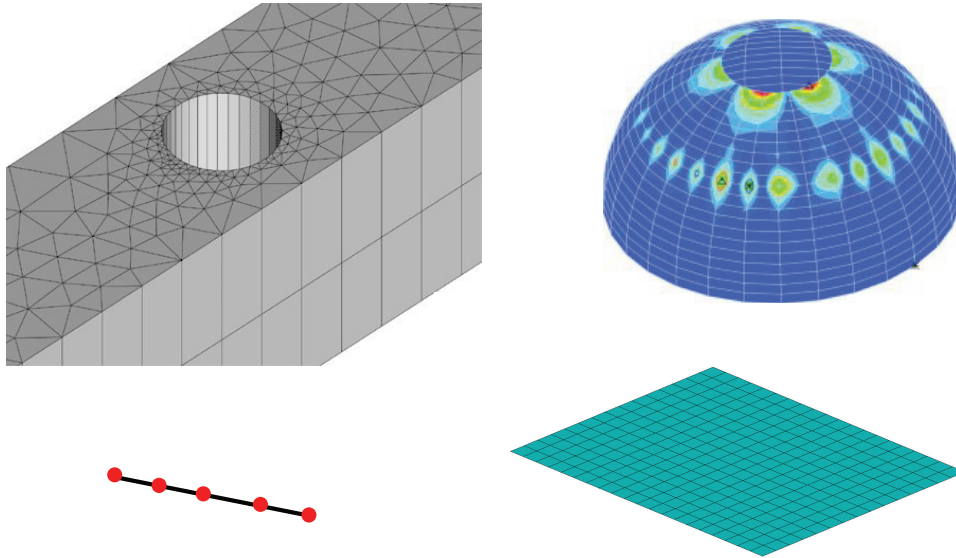
Figure 1. Typical structural elements: a) 3D solid elements; b) 2D shell elements; c) 1D beam elements; d) 2D plate elements.

with models to bridge the material properties of composite plies and the beam properties, and compute the stress fields within each layer for failure and safety predictions.

Sometimes, it is desirable to start the modeling process of composite structures from the fiber (usually the size of a few microns) and the matrix. A multiscale modeling approach is needed to link micromechanics [Li and Wang 2008; Nemat-Nasser and Hori 1998; Aboudi et al. 2012; Fish 2013] and structural mechanics [Reddy 2004; Kollár and Springer 2009; Carrera et al. 2014]. Many micromechanics models have been introduced to provide either rigorous bounds, such as the rules of mixtures [Hill 1952], Hashin–Shtrikman bounds [Hashin and Shtrikman 1962], third-order bounds [Milton 2002], and higher-order bounds [Torquato 2002]; or approximate predictions such as Mori–Tanaka method [Mori and Tanaka 1973], the method of cells [Aboudi 1982; 1989] and its variants [Paley and Aboudi 1992; Aboudi et al. 2001; 2012; Williams 2005], mathematical homogenization theories [Bensoussan et al. 1978; Murakami and Toledano 1990; Guedes and Kikuchi 1990; Michel et al. 1999; Fish 2013; Zhang and Oskay 2016], finite element approaches using conventional stress analysis of representative volume elements (RVEs) [Sun and Vaidya 1996; Berger et al. 2006], Voronoi cell finite element method [Ghosh 2011], and variational asymptotic method for unit cell homogenization [Yu and Tang 2007; Zhang and Yu 2014]. Even more structural models have been developed for composite structures which are usually based on a set of *a priori* assumptions. For composite laminates, the displacement field is usually assumed to be expressed in terms of 2D functions with known distributions through the thickness [Reddy 2004; Khandan et al. 2012]. For example, the classical laminated plate theory (CLPT) was derived based on the assumption that the transverse normal remains normal to the reference surface and is rigid. The first-order shear-deformation theory was derived based on the assumption that the transverse normal remains straight and rigid, but does not necessarily remain normal. Many assumptions have been proposed in the literature including equivalent single-layer assumptions [Reddy 1984; Mantari et al. 2012], layerwise assumptions
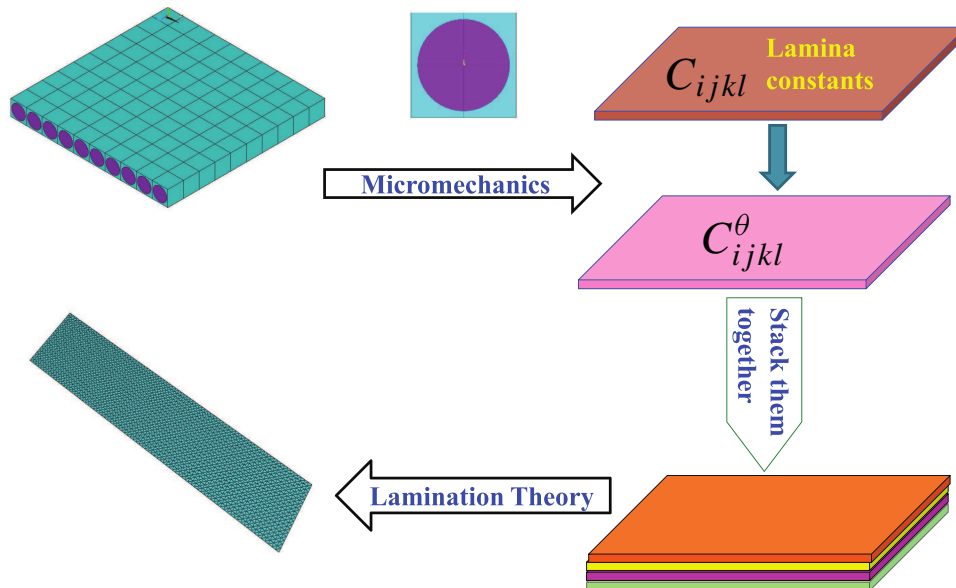
Figure 2. Traditional multiscale modeling approach illustrated for composite laminates.

[Plagianakos and Saravanos 2009; Icardi and Ferrero 2010], and zigzag assumptions [Carrera 2003; Xi-aohui et al. 2011]. Recently, Carrera [2012] developed a unified formulation to systematically construct all these models based on *a priori* assumptions [Demasi and Yu 2012]. To avoid these assumptions, asymptotic models were developed [Maugin and Attou 1990; Cheng and Batra 2000; Kalamkarov and Kolpakov 2001; Reddy and Cheng 2001; Kalamkarov et al. 2009; Kim 2009; Skoptsov and Sheshenin 2011] with the field variables expressed using a formal asymptotic series.

Common multiscale modeling approaches usually apply a two-step approach (TSA), which carry out a micromechanical analysis followed by a structural analysis. For example, for composite laminates, a micromechanics model is first used to compute the lamina constants in terms of the microstructure — commonly called the RVE or unit cell (UC) — of the composite ply, then a lamination theory is used to construct a structural model for the macroscopic analysis (see Figure 2). There are three possible issues with this approach. First, the microstructural scale is implicitly assumed to be much smaller than the structural scale which might cause significant error for structures where one of the dimensions is similar in size to the microstructure, such as thin laminates or sandwich structures with a thick core. Second, as shown in Figure 3, TSA creates artificial discontinuities at the layer interfaces because the original heterogeneous panel (Figure 3a) is effectively replaced with an imaginary panel made of homogeneous layers (Figure 3b). The real discontinuities happen at the interfaces between the fiber and matrix if perfect bonding is assumed between layers, which is normally done in lamination theories. Third, composite damage might initiate and propagate in such a way that the separation of microscale and laminate scale in TSA is not valid any more. These issues have been noticed by Pagano and Rybicki [1974]. The focus of this paper is to potentially resolve these issues by developing a unified theory to link the lowest scale of interest to the structural scale.

a) Real problem   b) Two-step approach
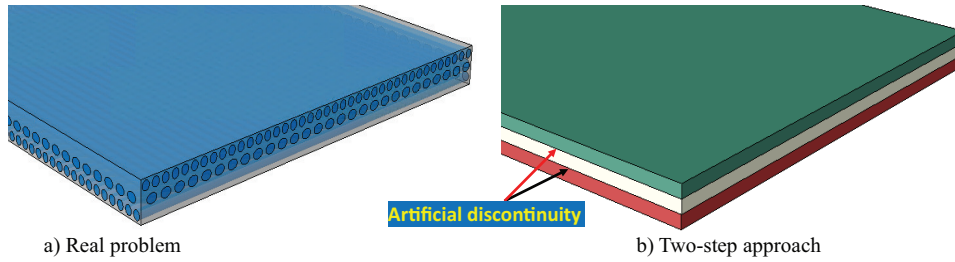
**Figure 3.** Artificial discontinuity created by the lamination theory.
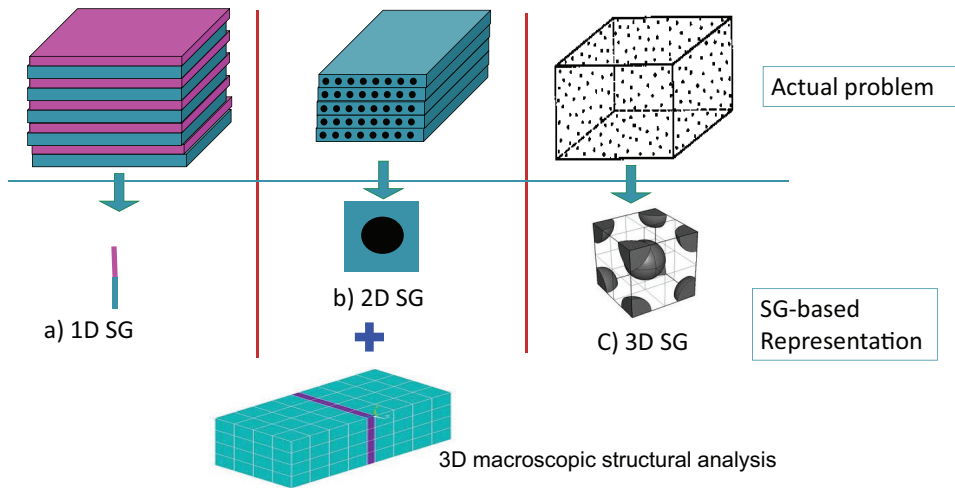
Figure 4. Analysis of 3D heterogeneous structures approximated by a constitutive modeling over SG and a corresponding 3D macroscopic structural analysis.

2. Structure Genome (SG)

A genome serves as a blueprint for an organism's growth and development. We can extrapolate this word into nonbiological contexts to connote a *fundamental building block* of a system. A new concept called the Structure Genome (SG) is defined as the *smallest mathematical building block* of the structure, to emphasize the fact that it contains all the constitutive information needed for a structure in the same fashion that the genome contains all the genetic information for an organism's growth and development. It is noted that this work uses the continuum hypothesis, and scales below the continuum scale (such as the atomic scale) are not considered here.

2.1. *SG for 3D structures.* As shown in Figure 4, analyses of 3D heterogeneous structures can be approximated by a 3D macroscopic structural analysis with the material properties provided by a constitutive modeling of a SG. For 3D structures, the SG serves a similar role as the RVE in micromechanics. However, they are significantly different, so the new term (SG) is used to avoid confusion. For example, for a structure made of composites featuring 1D heterogeneity (e.g. binary composites made of two alternating layers, Figure 4a), the SG will be a straight line with two segments denoting corresponding phases. One
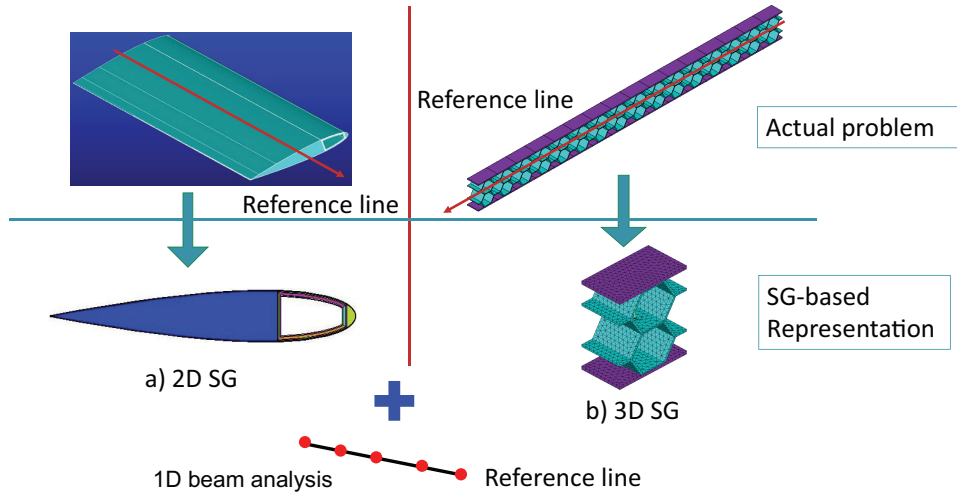
Figure 5. Analysis of beam-like structures approximated by a constitutive modeling over SG and a corresponding 1D beam analysis.

can mathematically repeat this line in-plane to build the two layers of the binary composite, and then repeat the binary composite out of plane to build the entire structure. Another possible application is to model a laminate as an equivalent homogeneous solid. The transverse normal line is the 1D SG for the laminate. The constitutive modeling over the 1D SG can compute the complete set of 3D properties and local fields. Such applications of the SG are not equivalent to the RVE. For a structure made of composites featuring 2D heterogeneity (e.g. continuous unidirectional fiber reinforced composites, Figure 4b), the SG will be 2D. Although 2D RVEs are also used in micromechanics, only in-plane properties and local fields can be obtained from common RVE-based models. If the complete set of properties are needed for a 3D structural analysis, a 3D RVE is usually required [Sun and Vaidya 1996; Fish 2013], while a 2D domain is sufficient if it is modeled using SG-based models (Figure 4b) or some semianalytical models such as GMC/HFGMC [Aboudi et al. 2012]. For a structure made of composites featuring 3D heterogeneity (e.g. particle reinforced composites, Figure 4c), the SG will be a 3D volume. Although a 3D SG for 3D structures represents the most similar case to a RVE, indispensable boundary conditions in terms of displacements and tractions in RVE-based models are not needed for SG-based models.

2.2. *SG for beams/plates/shells.* SG allows the connection of microstructure studies with beam/plate/shell analyses. For example, the structural analysis of slender (beam-like) structures can use beam elements (Figure 5). If the beam has uniform cross-sections which could be made of homogeneous materials or composites (Figure 5a), its SG is the 2D cross-sectional domain because the cross-section can be projected along the beam reference line to form the beam-like structure. This inspires a *new perspective* toward beam modeling [Yu et al. 2012], a traditional branch of structural mechanics. If the beam reference line is considered as a 1D continuum, every material point of this continuum has a cross-section as its microstructure. In other words, *constitutive modeling for beams can be effectively viewed as an application of micromechanics.* If the beam is also heterogeneous in the spanwise direction (Figure 5b), a 3D SG is needed to describe the microstructure of the 1D continuum, the behavior of which is governed
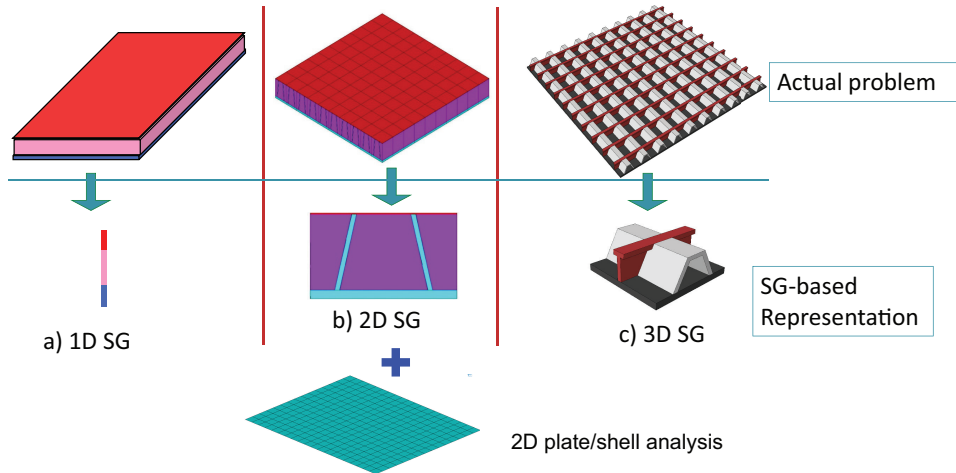
Figure 6. Analysis of plate-like structures approximated by a constitutive modeling over SG and a corresponding 2D plate analysis.

by the 1D beam analysis. Note that SG is different from the traditional notion of obtaining apparent material properties for a structure. For example, the flexural stiffness of an I-beam could be given by E^*I, such that an I-beam could be represented by a rectangular beam but with an apparent Young's modulus E^* so that $E^*I = E^* \times bd^3/12$ with b as the width and d as the height. Instead, using SG we can obtain the bending stiffness directly for the I-beam without referring to a geometry factor (reinterpreting it as a rectangular beam). No intermediate step such as E^* is needed. The concept of SG provides a unified treatment of structural modeling and micromechanics modeling and enables us to collapse the cross-section or a 3D beam segment into a material point for a beam analysis over the reference line with a possible, fully populated 4×4 stiffness matrix simultaneously accounting for extension, torsion, and bending in two directions.

If the structural analysis uses plate/shell elements, a SG can also be chosen properly. For illustrative purposes, typical SGs of plate-like structures are sketched in Figure 6. If the plate-like structures feature no in-plane heterogeneities (Figure 6a), the SG is the transverse normal line with each segment denoting the corresponding layer. For a sandwich panel with a core corrugated in one direction (Figure 6b), the SG is 2D. If the panel is heterogeneous in both in-plane directions (Figure 6c), such as a stiffened panel with stiffeners running in both directions, the SG is 3D. Despite the different dimensionalities of the SGs, the constitutive modeling should output structural properties for the corresponding structural analysis (such as the A, B, and D matrices for the Kirchhoff–Love plate model) and relations to express the original 3D fields in terms of the global behavior (e.g., moments, curvatures, etc.) obtained from the plate/shell analysis. It is known that theories of plates/shells traditionally belong to structural mechanics, but the constitutive modeling of these structures can be treated as special micromechanics applications using the SG concept. For a plate/shell-like structure, if the reference surface is considered as a 2D continuum, every material point of this continuum has an associated SG as its microstructure.

It is easy to identify SGs for periodic structures as shown in Figures 4, 5, and 6. For structures which are not globally periodic, we usually assume that the structure is at least periodic in the neighborhood of

a material point in the macroscopic structural analysis, the so-called local periodicity assumption implicit in all multiscale modeling approaches [Fish 2013]. For nonlinear behavior, it is also possible that the smallest mathematical building block of the structure is not sufficient as the characteristic length scale of the nonlinear behavior may cover several building blocks. For this case, SG should be interpreted as the smallest mathematical building block necessary to represent the nonlinear behavior.

SG serves as the link between the original structure with microscopic details and the macroscopic structural analysis. Here, the terms "microstructure" and "microscopic details" are used in a general sense: any details explicitly existing in a SG but not in the macroscopic structural analysis are termed microscopic details in this paper. Here and later in the paper, the real structure with microscopic details is termed as the original structure and the structure used in the macroscopic structural analysis is termed as the macroscopic structural model. It is also interesting to point out the relation between the SG concept and the idea of substructuring or superelement, which is commonly used in sizing software such as HyperSizer [Collier et al. 2002]. A line element in the global analysis could correspond to a box beam made of four laminated walls, and a surface element could correspond to a sandwich panel with laminated face sheets and a corrugated core. For these cases, SG and its companion mechanics presented below provide a rigorous and systematic approach based on micromechanics to compute the constitutive models for the line and surface elements and the local fields within the original structures.

3. Mechanics of structure genome (MSG)

SG serves as the fundamental building block of a structure; whether it is a 3D structure or a beam, plate, or shell. For SG to not merely remain as a concept, it must be governed by a physics-based theory, namely mechanics of structure genome (MSG), so that there is a two-way communication between microstructural details and structural analysis: microstructural information can be rigorously passed to structural analysis to predict structural performance, and structural performance can be passed back to predict the local fields within the microstructure for failure prediction and other detailed analyses.

A structural model contains kinematics, kinetics, and constitutive relations. On the one hand, kinematics deals with strain-displacement relations and compatibility equations, while on the other hand, kinetics deals with stress and equations of motion. Constitutive relations relate stress and strain. Both kinematics and kinetics can be formulated exactly within the framework of continuum mechanics and remain the same for the same structural model independent of the composition of the structure. Constitutive relations are where the difference comes from and are ultimately approximate because a hypothetical continuum is used to model the underlying atomic structure. Some criteria is needed for us to minimize the loss of information between the original model describing the microscopic details and the model used for the macroscopic structural analysis. For elastic materials, this can be achieved by minimizing the difference between the strain energy of the materials stored in SG and that stored in the macroscopic structural model.

3.1. *Kinematics.* The first step in formulating MSG is to express the kinematics, including the displacement field and the strain field, of the original structures in terms of those in the macroscopic structural model. Although the SG concept is applicable to original structures made of materials admitting general continuum descriptions such as the Cosserat continuum [Cosserat and Cosserat 1909], this work focuses on materials admitting the Cauchy continuum description.
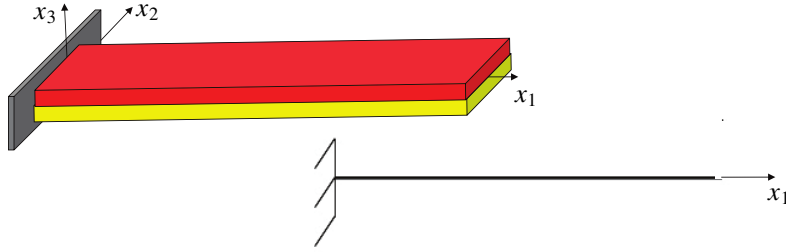
Figure 7. Macrocoordinates (x_1, x_2, x_3) and eliminated coordinates (x_2, x_3) of a beam.

3.1.1. *Coordinate systems.* Let us use x_i, called macrocoordinates here, to denote the coordinates describing the original structure. The coordinates could be general curvilinear coordinates. However, without loss of generality, we choose an orthogonal system of arc-length coordinates. If the structure is dimensionally reducible, some of the macrocoordinates x_α, called eliminated coordinates here, correspond to the dimensions eliminated in the macroscopic structural model. Here and throughout the paper, Greek indices assume values corresponding to the eliminated macrocoordinates, Latin indices k, l, m assume values corresponding to the macrocoordinates remaining in the macroscopic structural model, and other Latin indices assume 1, 2, 3. Repeated indices are summed over their range except where explicitly indicated.

For beam-like structures, only x_1, describing the beam reference line, will remain in the final beam model, while x_2, x_3, the cross-sectional coordinates, will be eliminated (see Figure 7); for plate/shell-like structures, x_1 and x_2, describing the plate/shell reference surface, will remain in the final plate/shell model, while x_3, the thickness coordinate, will be eliminated. For this reason, the beam model is called a 1D continuum model because all the unknown fields are functions of x_1 only. Similarly, the plate/shell model is called a 2D continuum model because all the unknown fields are functions of x_1 and x_2 only.

Since the size of a SG is much smaller than the wavelength of the macroscopic deformation, we introduce microcoordinates $y_i = x_i/\varepsilon$ to describe the SG, with ε being a small parameter. This basically enables a zoom-in view of the SG at a size similar to the macroscopic structure. If the SG is 1D, only y_3 is needed; if the SG is 2D, y_2 and y_3 are needed; if the SG is 3D, all three coordinates y_1, y_2, y_3 are needed. In multiscale structural modeling, a field function of the original structure can be generally written as a function of the macrocoordinates x_k which remain in the macroscopic structural model and the microcoordinates y_j. Following [Bensoussan et al. 1978], the partial derivative of a function $f(x_k, y_j)$ can be expressed as

$$\frac{\partial f(x_k, y_j)}{\partial x_i} = \frac{\partial f(x_k, y_j)}{\partial x_i}\bigg|_{y_j=\text{const}} + \frac{1}{\varepsilon}\frac{\partial f(x_k, y_j)}{\partial y_i}\bigg|_{x_k=\text{const}} \equiv f_{,i} + \frac{1}{\varepsilon}f_{|i}. \tag{1}$$

3.1.2. *Undeformed and deformed configurations.* Let $\boldsymbol{b}_k$ denote the unit vector tangent to x_k for the undeformed configuration. Note $\boldsymbol{b}_i$ chosen this way are functions of x_k only. For example, for beam-like structures, we choose $\boldsymbol{b}_1$ to be tangent to the beam reference line x_1, and $\boldsymbol{b}_2, \boldsymbol{b}_3$ as unit vectors tangent to the cross-sectional coordinates x_α. As shown in Figure 8, we can describe the position of any material point of the original structure by its position vector $\boldsymbol{r}$ relative to a point O fixed in an inertial frame such
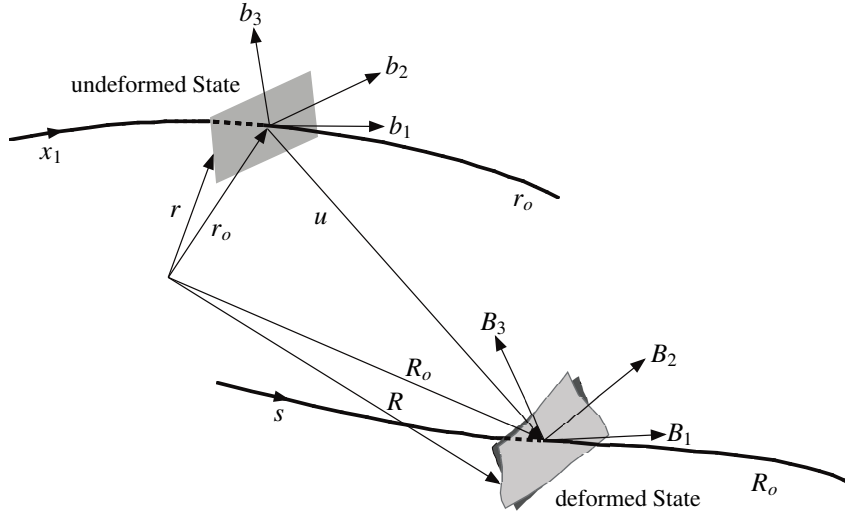
Figure 8. Deformation of a typical beam structure.

that

$$r(x_k, y_\alpha) = r_o(x_k) + \varepsilon y_\alpha b_\alpha(x_k), \tag{2}$$

where r_o is the position vector from O to a material point of the macroscopic structural model. Note here x_k denotes only those coordinates remaining in the macroscopic structural model, and y_α corresponds to eliminated coordinates x_α. Because x_k is an arc-length coordinate, we have $b_k = \partial r_o / \partial x_k$.

When the original structure deforms, the particle that had position vector r in the undeformed configuration now has position vector R in the deformed configuration, such that

$$R(x_k, y_j) = R_o(x_k) + \varepsilon y_\alpha B_\alpha(x_k) + \varepsilon w_i(x_k, y_j) B_i(x_k), \tag{3}$$

where R_o denotes the position vector of the deformed structural model, B_i forms a new orthonormal triad for the deformed configuration, and εw_i are fluctuating functions introduced to accommodate all possible deformations other than those described by R_o and B_i. B_i can be related with b_i through a direction cosine matrix, $C_{ij} = B_i \cdot b_j$, subject to the requirement that these two triads are the same in the undeformed configuration. R is expressed in terms of R_o, B_i, and w_i in (3), resulting in six times redundancy. Six constraints are needed to ensure a unique mapping. These constraints can be directly related with how we define R_o and B_i in terms of R. For example, it is natural for us to define

$$R_o = \langle\langle R \rangle\rangle - \langle\langle \varepsilon y_\alpha \rangle\rangle B_\alpha(x_k), \tag{4}$$

where $\langle\langle \cdot \rangle\rangle$ indicates averaging over the SG. If y_α is chosen such that $\langle\langle \varepsilon y_\alpha \rangle\rangle = 0$, R_o is defined as the average of the position vector of the original structure. Then (3) implies the following constraint on the fluctuating functions:

$$\langle\langle w_i \rangle\rangle = 0. \tag{5}$$

Note that for 3D structures y_α disappears and no requirement for $\langle\langle \varepsilon y_\alpha \rangle\rangle = 0$ is needed but the constraint in (5) remains.

The other three constraints can be used to specify $\boldsymbol{B}_i$. For plate/shell-like structures, we can select $\boldsymbol{B}_3$ in such a way that

$$\boldsymbol{B}_3 \cdot \boldsymbol{R}_{o,1} = 0, \quad \boldsymbol{B}_3 \cdot \boldsymbol{R}_{o,2} = 0, \tag{6}$$

which provides two constraints implying that we choose $\boldsymbol{B}_3$ normal to the reference surface of the deformed plate/shell. It should be noted that this choice has nothing to do with the well-known Kirchhoff hypothesis. In the Kirchhoff assumption, the transverse normal can only rotate rigidly without any local deformation. However, in the present formulation, we allow all possible deformations, classifying all deformations other than those described by $\boldsymbol{R}_o$ and $\boldsymbol{B}_i$ in terms of the fluctuating function $w_i \boldsymbol{B}_i$. The last constraint can be specified by the rotation of $\boldsymbol{B}_\alpha$ around $\boldsymbol{B}_3$ such that

$$\boldsymbol{B}_1 \cdot \boldsymbol{R}_{o,2} = \boldsymbol{B}_2 \cdot \boldsymbol{R}_{o,1}. \tag{7}$$

This constraint symmetrizes the macrostrains for a plate/shell model as defined in (19) later.

For beam-like structures, we can select $\boldsymbol{B}_\alpha$ in such a way that

$$\boldsymbol{B}_2 \cdot \boldsymbol{R}_{o,1} = 0, \quad \boldsymbol{B}_3 \cdot \boldsymbol{R}_{o,1} = 0, \tag{8}$$

which provides two constraints implying that we choose $\boldsymbol{B}_1$ to be tangent to the reference line of the deformed beam. Note that this choice is not the well-known Euler–Bernoulli assumption as the present formulation can describe all deformations of the cross-section. We can also prescribe the rotation of $\boldsymbol{B}_\alpha$ around $\boldsymbol{B}_1$ such that

$$\boldsymbol{B}_3 \cdot \frac{\partial \boldsymbol{R}}{\partial x_2} - \boldsymbol{B}_2 \cdot \frac{\partial \boldsymbol{R}}{\partial x_3} = 0, \tag{9}$$

which implies the following constraint on the fluctuating functions:

$$\langle\langle w_{2|3} - w_{3|2} \rangle\rangle = 0. \tag{10}$$

This constraint actually defines the twist angle of the macroscopic beam model in terms of the original position vector as pointed out in [Yu et al. 2012].

Thus the fluctuating functions are constrained according to (5). For beam structures, they are additionally constrained according to (10). Other constraints for the fluctuating functions can be introduced naturally into the formulation. For example, for periodic structures, fluctuating functions should be equal on periodic boundaries.

3.1.3. *Strain field.* If the local rotation (the rotation of a material point of the original structure subtracting the rotation needed for bringing $\boldsymbol{b}_i$ to $\boldsymbol{B}_i$) is small, it is convenient to use the Jauman–Biot–Cauchy strain according to the decomposition of the rotation tensor [Danielson and Hodges 1987]

$$\Gamma_{ij} = 1/2(F_{ij} + F_{ji}) - \delta_{ij}, \tag{11}$$

where δ_{ij} is the Kronecker symbol and F_{ij} is the mixed-basis component of the deformation gradient tensor defined as

$$F_{ij} = \boldsymbol{B}_i \cdot \boldsymbol{G}_a \boldsymbol{g}^a \cdot \boldsymbol{b}_j = \boldsymbol{B}_i \cdot (\boldsymbol{G}_k \boldsymbol{g}^k + \boldsymbol{G}_\alpha \boldsymbol{g}^\alpha) \cdot \boldsymbol{b}_j. \tag{12}$$

Here $\boldsymbol{g}^a$ are the 3D contravariant base vectors of the undeformed configuration and $\boldsymbol{G}_a$ are the 3D covariant basis vectors of the deformed configuration.

The contravariant base vector $\boldsymbol{g}^a$ is defined as

$$\boldsymbol{g}^a = \frac{1}{2\sqrt{g}} e_{aij} \boldsymbol{g}_i \times \boldsymbol{g}_j, \tag{13}$$

with e_{aij} as the 3D permutation symbol and $\boldsymbol{g}_i$ as the covariant base vector of undeformed configuration and $g = \det(\boldsymbol{g}_i \cdot \boldsymbol{g}_j)$.

From the undeformed configuration in (2), corresponding to the remaining macrocoordinate x_k, we obtain the covariant base vector as

$$\boldsymbol{g}_k = \frac{\partial \boldsymbol{r}}{\partial x_k} = \boldsymbol{b}_k + \varepsilon y_\alpha \frac{\partial \boldsymbol{b}_\alpha}{\partial x_k} = \boldsymbol{b}_k + \varepsilon y_\alpha \boldsymbol{k}_k \times \boldsymbol{b}_\alpha = \boldsymbol{b}_k + e_{i\alpha j} \varepsilon y_\alpha k_{ki} \boldsymbol{b}_j. \tag{14}$$

Here $\boldsymbol{k}_k = k_{ki} \boldsymbol{b}_i$ is the initial curvature vector corresponding to the remaining macrocoordinate x_k. This definition is consistent with k_{kl}^{2D} for initial curvatures of shells in [Yu and Hodges 2004a], if we let

$$k_{kl}^{2D} = \alpha_{lm} k_{km}, \quad k_{k3}^{2D} = k_{k3}, \tag{15}$$

with α_{lm} as the 2D permutation symbol: $\alpha_{11} = \alpha_{22} = 0$, $\alpha_{12} = -\alpha_{21} = 1$.

From the undeformed configuration in (2), corresponding to the eliminated macrocoordinate x_α, we obtain the covariant base vector as

$$\boldsymbol{g}_\alpha = \frac{\partial \boldsymbol{r}}{x_\alpha} = \frac{\partial \varepsilon y_\alpha}{x_\alpha} \boldsymbol{b}_\alpha = \boldsymbol{b}_\alpha. \tag{16}$$

From the deformed configuration in (3), corresponding to the remaining macrocoordinate x_k, we obtain the covariant base vector $\boldsymbol{G}_k$ as

$$\boldsymbol{G}_k = \frac{\partial \boldsymbol{R}}{\partial x_k} = \frac{\partial \boldsymbol{R}_o}{\partial x_k} + \varepsilon y_\alpha \frac{\partial \boldsymbol{B}_\alpha}{\partial x_k} + \varepsilon \frac{\partial w_i}{\partial x_k} \boldsymbol{B}_i + \varepsilon w_i \frac{\partial \boldsymbol{B}_i}{\partial x_k}. \tag{17}$$

From the deformed configuration in (3), corresponding to the eliminated macrocoordinate x_α, we obtain the covariant base vector as

$$\boldsymbol{G}_\alpha = \frac{\partial \boldsymbol{R}}{\partial x_\alpha} = \frac{\partial (\varepsilon y_\beta)}{\partial x_\alpha} \boldsymbol{B}_\beta + \varepsilon \frac{\partial w_i}{\partial x_\alpha} \boldsymbol{B}_i = \boldsymbol{B}_\alpha + \frac{\partial w_i}{\partial y_\alpha} \boldsymbol{B}_i. \tag{18}$$

A proper definition of the generalized strain measures for the macroscopic structural model is needed for the purpose of formulating the macroscopic structural analysis in a geometrically exact fashion. Following [Yu et al. 2012; Yu and Hodges 2004a; Pietraszkiewicz and Eremeyev 2009b], we introduce the following definitions:

$$\begin{aligned}
\epsilon_{kl} &= \boldsymbol{B}_l \cdot \frac{\partial \boldsymbol{R}_o}{\partial x_k} - \delta_{kl}, \\
\kappa_{ki} &= (1/2) e_{iaj} \boldsymbol{B}_j \cdot \frac{\partial \boldsymbol{B}_a}{\partial x_k} - k_{ki},
\end{aligned} \tag{19}$$

where ϵ_{kl} is the Lagrangian stretch tensor and κ_{ki} is the Lagrangian curvature strain tensor (or the so-called wryness tensor). This definition corresponds to the kinematics of a nonlinear Cosserat continuum [Cosserat and Cosserat 1909] which allows six degrees of freedom (three translations and three rotations) for each material point no matter whether the macroscopic structural model is 1D, 2D, or 3D. For beam-like structures, this definition reproduces the 1D generalized strain measures of the Timoshenko beam

model defined in [Hodges 2006]. If we restrict $\boldsymbol{B}_1$ to be tangent to $\boldsymbol{R}_o$, (8), this definition reproduces the 1D generalized strain measures of the Euler–Bernoulli beam model defined in the previous work. For plate/shell-like structures, if we use (7), we will have the symmetry $\epsilon_{12} = \epsilon_{21}$ as a constraint for the kinematics of the final plate/shell model. This definition reproduces the 2D generalized strain measures of the Reissner–Mindlin model defined in [Yu and Hodges 2004a]. If we further restrain $\boldsymbol{B}_3$ to be normal to the reference surface, (6), this definition reproduces the 2D generalized strain measures of the Kirchhoff–Love plate/shell model defined in [Yu et al. 2002]. For 3D structures, this definition corresponds to the natural strain measures defined in [Pietraszkiewicz and Eremeyev 2009b] for a nonlinear Cosserat continuum. Although the SG kinematics formulated this way has the potential to construct a Cosserat continuum model for the 3D macroscopic structural model even if the material of the original heterogeneous structure is described using a Cauchy continuum, we will restrict ourselves to the Cauchy continuum model for the 3D macroscopic structural model in this paper. In other words, we are seeking a symmetric Lagrangian stretch tensor ϵ_{kl} and negligible curvature strain tensor κ_{ki}. This can be achieved by constraining the global rotation needed for bringing $\boldsymbol{b}_i$ to $\boldsymbol{B}_i$ in a specific way, which can be illustrated more clearly using an invariant form of the definitions in (19). According to [Pietraszkiewicz and Eremeyev 2009a; 2009b], these definitions can be rewritten as

$$
\begin{aligned}
\epsilon &= \boldsymbol{C}^T \cdot \boldsymbol{F} - \boldsymbol{I}, \\
\kappa^T &= -(1/2)\boldsymbol{e} : \left(\boldsymbol{C}^T \cdot \frac{\partial \boldsymbol{C}}{\partial x_k} \boldsymbol{b}_k \right),
\end{aligned}
\tag{20}
$$

where ϵ is the Lagrangian stretch tensor, κ the Lagrangian curvature strain tensor, $\boldsymbol{C} = \boldsymbol{B}_i \boldsymbol{b}_i$ is the global rotation tensor bringing $\boldsymbol{b}_i$ to $\boldsymbol{B}_i$, $\boldsymbol{F}$ is the deformation gradient tensor, $\boldsymbol{I} = \boldsymbol{b}_i \boldsymbol{b}_i$ is the second-order identity tensor, and $\boldsymbol{e} = -\boldsymbol{I} \times \boldsymbol{I}$ is the third-order skew Ricci tensor. If the global rotation tensor $\boldsymbol{C}$ is constrained to be decomposed from $\boldsymbol{F}$ according to the polar decomposition theorem,

$$
\boldsymbol{F} = \boldsymbol{C} \cdot \boldsymbol{U},
\tag{21}
$$

where $\boldsymbol{U}$ is a second-order positive symmetric tensor, then the definitions in (20) become

$$
\begin{aligned}
\epsilon &= \boldsymbol{C}^T \cdot (\boldsymbol{C} \cdot \boldsymbol{U}) - \boldsymbol{I} = \boldsymbol{U} - \boldsymbol{I}, \\
\kappa^T &= -(1/2)\boldsymbol{e} : \left(\boldsymbol{C}^T \cdot \frac{\partial \boldsymbol{C}}{\partial x_k} \boldsymbol{b}_k \right).
\end{aligned}
\tag{22}
$$

Clearly, the Lagrangian stretch tensor ϵ becomes symmetric and is the definition of Jauman–Biot–Cauchy strain tensor. The Lagrangian curvature strain tensor κ corresponds to higher-order terms (gradient of the deformation gradient) which are commonly neglected in the Cauchy continuum model. This derivation is significant because it provides a geometrically exact description for the 3D solid and has demonstrated that the Cauchy continuum description can be actually reduced from the Cosserat continuum description. It is noted that restraining the global rotation tensor according to (21) is equivalent to introducing three constraints for $\boldsymbol{B}_i$ needed for 3D structures. With this derivation, the nonlinear kinematics of beams, plates/shells, and 3D structures can be described using a single, unified formulation.

To facilitate the derivation of the covariant vectors $\boldsymbol{G}_i$, we can rewrite the definitions in (19) as

$$
\begin{aligned}
\frac{\partial \boldsymbol{R}_o}{\partial x_k} &= \boldsymbol{B}_k + \epsilon_{kl} \boldsymbol{B}_l, \\
\frac{\partial \boldsymbol{B}_i}{\partial x_k} &= (\kappa_{kj} + k_{kj}) \boldsymbol{B}_j \times \boldsymbol{B}_i.
\end{aligned}
\tag{23}
$$

Note $\epsilon_{13} = \epsilon_{23} = 0$ for plate/shell-like structures due to (6) and $\epsilon_{12} = \epsilon_{13} = 0$ for beam-like structures due to (8).

Substituting (23) into (17), we can obtain more detailed expressions for the covariant base vectors of the deformed configuration $\boldsymbol{G}_k$ as follows:

$$
\begin{aligned}
\boldsymbol{G}_k &= \boldsymbol{B}_k + \varepsilon_{kl}\boldsymbol{B}_l + \varepsilon y_\alpha \frac{\partial \boldsymbol{B}_\alpha}{\partial x_k} + \varepsilon \frac{\partial w_l}{\partial x_k}\boldsymbol{B}_l + \varepsilon \frac{\partial w_\alpha}{\partial x_k}\boldsymbol{B}_\alpha + \varepsilon w_l \frac{\partial \boldsymbol{B}_l}{\partial x_k} + \varepsilon w_\alpha \frac{\partial \boldsymbol{B}_\alpha}{\partial x_k} \\
&= \left(\delta_{kl} + \epsilon_{kl} + \varepsilon \frac{\partial w_l}{\partial x_k}\right)\boldsymbol{B}_l + \varepsilon(y_\alpha + w_\alpha)\frac{\partial \boldsymbol{B}_\alpha}{\partial x_k} + \varepsilon \frac{\partial w_\alpha}{\partial x_k}\boldsymbol{B}_\alpha + \varepsilon w_l \frac{\partial \boldsymbol{B}_l}{\partial x_k} \\
&= \left(\delta_{kl} + \epsilon_{kl} + \varepsilon \frac{\partial w_l}{\partial x_k}\right)\boldsymbol{B}_l + \varepsilon\left[e_{ij\alpha}(y_\alpha + w_\alpha)(\kappa_{kj} + k_{kj}) + \frac{\partial w_\alpha}{\partial x_k}\delta_{\alpha i} + e_{ijl}w_l(\kappa_{kj} + k_{kj})\right]\boldsymbol{B}_i.
\end{aligned}
\tag{24}
$$

Using the expressions for g^a and $\boldsymbol{G}_a$, and dropping nonlinear terms due to the product of the curvature strains and the fluctuating functions, the 3D strain field defined in (11) can be written in the following matrix form:

$$
\Gamma = \Gamma_h w + \Gamma_\epsilon \bar{\epsilon} + \varepsilon \Gamma_l w + \varepsilon \Gamma_R w,
\tag{25}
$$

where $\Gamma = \lfloor \Gamma_{11}\ \Gamma_{22}\ \Gamma_{33}\ 2\Gamma_{23}\ 2\Gamma_{13}\ 2\Gamma_{12} \rfloor^T$ denotes the strain field of the original structure, $w = \lfloor w_1\ w_2\ w_3 \rfloor^T$ the fluctuating functions, and $\bar{\epsilon}$ is a column matrix containing the generalized strain measures for the macroscopic structural model. For example, if the macroscopic structural model is a beam model, we have $\bar{\epsilon} = \lfloor \epsilon_{11}\ \kappa_{11}\ \kappa_{12}\ \kappa_{13} \rfloor^T$ with ϵ_{11} denoting the extensional strain, κ_{11} the twist, and κ_{12} and κ_{13} the bending curvatures. If the macroscopic structural model is a plate/shell model, we have $\bar{\epsilon} = \lfloor \epsilon_{11}\ \epsilon_{22}\ 2\epsilon_{12}\ \kappa_{11}^{2D}\ \kappa_{22}^{2D}\ \kappa_{12}^{2D} + \kappa_{21}^{2D} \rfloor^T$ with $\epsilon_{\alpha\beta}$ denoting the in-plane strains and $\kappa_{\alpha\beta}^{2D}$ denoting the curvature strains. If the macroscopic structural model is a 3D continuum model, we have $\bar{\epsilon} = \lfloor \epsilon_{11}\ \epsilon_{22}\ \epsilon_{33}\ 2\epsilon_{23}\ 2\epsilon_{13}\ 2\epsilon_{12} \rfloor^T$ with ϵ_{ij} denoting the Biot strain measures in a Cauchy continuum. Γ_h is an operator matrix which depends on the dimensionality of the SG. Γ_ϵ and Γ_l are two operator matrices, the form of which depends on the macroscopic structural model. Γ_R is an operator matrix existing only for those original structures featuring initial curvatures. The explicit expressions for these operators are given in the appendix for completeness.

3.2. *Variational statement for SG.*

Although the SG concept can be used to analyze structures made of various types of materials, in this paper, we illustrate its use by focusing on structures made of elastic materials. These structures are governed by the variational statement

$$
\delta U = \overline{\delta W},
\tag{26}
$$

where δ is the usual Lagrangean variation, U is the strain energy, and $\overline{\delta W}$ is the virtual work of the applied loads. The over bar indicates that the virtual work needs not be the variation of a functional. For

a linear elastic material characterized using a 6×6 stiffness matrix D, the strain energy can be written as

$$U = \frac{1}{2} \int \frac{1}{\omega} \langle \Gamma^T D \Gamma \rangle \, d\Omega, \tag{27}$$

where Ω is the volume of the domain spanned by x_k remaining in the macroscopic structural model. The notation $\langle \bullet \rangle = \int \bullet \sqrt{g} \, d\omega$ is used to denote a weighted integration over the domain of the SG and ω denotes the volume of the domain spanned by y_k corresponding to the coordinates x_k remaining in the macroscopic structural model. If none of y_k is needed in the SG, then $\omega = 1$. For example, if a heterogeneous beam-like structure features a 3D SG, ω is the length of the SG in the y_1 direction, corresponding to x_1 remaining in the macroscopic beam model. If the heterogeneous beam-like structure features a 2D SG (uniform cross-section), y_1 is not needed for the SG and $\omega = 1$. ω for plate/shell-like structures or 3D structures can be obtained similarly.

For a Cauchy continuum, there may exist applied loads from tractions and body forces. The virtual work done by these applied loads can be calculated as

$$\overline{\delta W} = \int \frac{1}{\omega} \left(\langle p \rangle \cdot \delta R + \int_s Q \cdot \delta R \sqrt{c} \, ds \right) d\Omega, \tag{28}$$

where s denotes the boundary surfaces of the SG with applied traction force per unit area $Q = Q_i B_i$ and applied body force per unit volume $p = p_i B_i$. $\sqrt{c}$ is equal to 1 except for some degenerated cases where s is only a boundary curve of the SG and one of coordinates x_k is required to form the physical surfaces on which the load is applied. In this case, the differential area of the physical surface is equal to $\sqrt{c} \, ds \, dx_k$ with ds as the differential arc length along the boundary curve of SG. For example, for beam-like structures featuring a 2D SG, the SG boundary is the curve encircling the cross-section and $\sqrt{c} = \sqrt{g + (y_2(dy_2/ds) + y_3(dy_3/ds))^2 k_{11}^2}$.

Here δR is the Lagrangian variation of the displacement field in (3), such that

$$\delta R = \overline{\delta q_i} B_i + \varepsilon y_\alpha \delta B_\alpha + \varepsilon \delta w_i B_i + \varepsilon w_i \delta B_i. \tag{29}$$

We may safely ignore products of the fluctuating functions and virtual rotations in δR, because the fluctuating functions are small. The last term of the above equation is then dropped so that

$$\delta R = \overline{\delta q_i} B_i + \varepsilon y_\alpha \delta B_\alpha + \varepsilon \delta w_i B_i. \tag{30}$$

The virtual displacements and rotations of the macroscopic structural model are defined as

$$\overline{\delta q_i} = \delta R_o \cdot B_i, \quad \delta B_\alpha = \overline{\delta \psi}_j B_j \times B_\alpha, \tag{31}$$

where $\overline{\delta q_i}$ and $\overline{\delta \psi_i}$ contain the components of the virtual displacement and rotation in the B_i system, respectively. They are functions of x_k only. Note $\overline{\delta \psi}_j$ are restrained to be derivable from $\overline{\delta q_i}$ and are higher-order terms that are neglected in a 3D structure described using the Cauchy continuum.

Then we can rewrite (30) as

$$\delta R = \left(\overline{\delta q_i} + \varepsilon e_{j\alpha i} y_\alpha \overline{\delta \psi}_j + \varepsilon \delta w_i \right) B_i. \tag{32}$$

Finally, we express the virtual work due to applied loads as

$$\overline{\delta W} = \overline{\delta W}_H + \varepsilon \overline{\delta W}^*, \tag{33}$$

where $\overline{\delta W}_H$ is the virtual work not related to the fluctuating functions w_i and $\overline{\delta W}^*$ is the virtual work related to the fluctuating functions. Specifically,

$$\overline{\delta W}_H = \int \left(f_i \overline{\delta q_i} + m_i \overline{\delta \psi_i} \right) d\Omega, \quad \overline{\delta W}^* = \int \frac{1}{\omega} \left(\langle p_i \delta w_i \rangle + \oint Q_i \delta w_i \sqrt{c}\, ds \right) d\Omega, \tag{34}$$

with the generalized forces f_i and moments m_i defined as

$$f_i = \frac{1}{\omega} \left(\langle p_i \rangle + \int Q_i \sqrt{c}\, ds \right), \quad m_i = \frac{e_{i\alpha j}}{\omega} \left(\langle \varepsilon y_\alpha p_j \rangle + \int \varepsilon y_\alpha Q_j \sqrt{c}\, ds \right). \tag{35}$$

If we assume that p_i and Q_i are independent of the fluctuating functions, then we can rewrite $\overline{\delta W}^*$ as

$$\overline{\delta W}^* = \delta \int \frac{1}{\omega} \left(\langle p_i w_i \rangle + \int Q_i w_i \sqrt{c}\, ds \right) d\Omega. \tag{36}$$

In view of the strain energy in (27) and virtual work in (33) along with (34), the variational statement in (26) can be rewritten as

$$\int \frac{1}{\omega} \delta \left[\frac{1}{2} \langle \Gamma^T D \Gamma \rangle - \varepsilon \left(\langle p_i w_i \rangle + \int Q_i w_i \sqrt{c}\, ds \right) \right] - \left(f_i \overline{\delta q_i} + m_i \overline{\delta \psi_i} \right) d\Omega = 0. \tag{37}$$

If we attempt to solve this variational statement directly, we will encounter the same difficulty as in a direct analysis of the original structure. The main complexity comes from the fluctuating functions w_i, which are unknown functions of both micro- and macrocoordinates. To reduce the original continuum model to a macroscopic structural model, the common practice in structural modeling is to assume the fluctuating functions, *a priori*, in terms of some unknown functions (displacements, rotations, and/or strains) of x_k and some known functions of y_k. However, for arbitrary structures made with general composites, use of such *a priori* assumptions may introduce significant errors. Fortunately, the variational asymptotic method (VAM) [Berdichevsky 2009] provides a useful technique to obtain the fluctuating functions through an asymptotical analysis of the variational statement in (37). It does so in terms of the small parameter ε which is inherent in the composite structure to construct asymptotically correct macroscopic structural models. As the last two terms in (37) are not functions of w_i, we can conclude that the fluctuating function is governed by the following variational statement instead:

$$\delta \left[\frac{1}{2} \langle \Gamma^T D \Gamma \rangle - \varepsilon \left(\langle p_i w_i \rangle + \int Q_i w_i \sqrt{c}\, ds \right) \right] = 0, \tag{38}$$

which can be considered as a variational statement for the SG as it is posed over the SG domain only. According to VAM, we can neglect the terms in the order of ε to construct the first approximation of the variational statement in (38) as

$$\delta (1/2) \langle (\Gamma_h w + \Gamma_\epsilon \bar{\epsilon})^T D (\Gamma_h w + \Gamma_\epsilon \bar{\epsilon}) \rangle = 0. \tag{39}$$

It is noted here that only small geometry parameters are considered in this work. For structures made of materials featuring significantly different properties, small material parameters should also be introduced for the asymptotic analysis using VAM. It is also pointed out that VAM is used to discard energetically small terms which might cause difficulty in capturing some higher order local stresses. However, such

loss of information is mainly governed by the macroscopic structural model. In this work, only the classical structural models including the Euler–Bernoulli beam model, Kirchhoff–Love plate/shell model, and the Cauchy continuum model are constructed using MSG. It is our future plan to derive refined models such as the Reissner–Mindlin plate/shell model, Timoshenko beam model, and Cosserat continuum model using the unified MSG framework.

For very simple cases such as isotropic beams [Yu and Hodges 2004b], laminated plates [Yu 2005], and binary composites [Yu 2012], the variational statement in (39) can be solved exactly and analytically, while for general cases we need to turn to numerical techniques such as the finite element method for solutions. To this end, we need to express w using shape functions defined over SG as

$$w(x_k, y_j) = S(y_j)V(x_k). \tag{40}$$

Equation (40) is a standard way to solve (39) using the finite element method. Equation (39) is a variational statement used to solve for w given $\bar{\epsilon}$ with V as a function of x_k because of $\bar{\epsilon}$. Such a separation of variables is inherent in multiscale modeling and structural modeling approaches. S are the standard shape functions depending on the type of elements one uses, and can be found in typical finite element textbooks. V is what we need to solve for as the nodal values for the influence function based on the discretization.

Substituting (40) into (39), we obtain the following discretized version of the strain energy functional:

$$U = (1/2)(V^T E V + 2 V^T D_{h\epsilon} \bar{\epsilon} + \bar{\epsilon}^T D_{\epsilon\epsilon} \bar{\epsilon}), \tag{41}$$

where

$$E = \langle (\Gamma_h S)^T D (\Gamma_h S) \rangle, \quad D_{h\epsilon} = \langle (\Gamma_h S)^T D \Gamma_\epsilon \rangle, \quad D_{\epsilon\epsilon} = \langle \Gamma_\epsilon^T D \Gamma_\epsilon \rangle. \tag{42}$$

Minimizing U in (41), subject to the constraints, gives us the linear system

$$E V = -D_{h\epsilon} \bar{\epsilon}. \tag{43}$$

It is clear that V linearly depends on $\bar{\epsilon}$, and the solution can be symbolically written as

$$V = V_0 \bar{\epsilon}. \tag{44}$$

Substituting (44) back into (41), we can calculate the strain energy stored in the SG as the first approximation as

$$U = (1/2)\bar{\epsilon}^T (V_0^T D_{h\epsilon} + D_{\epsilon\epsilon})\bar{\epsilon} \equiv (\omega/2)\bar{\epsilon}^T \bar{D} \bar{\epsilon}, \tag{45}$$

where $\bar{D}$ is the effective stiffness to be used in the macroscopic structural model. For the Euler–Bernoulli beam model, $\bar{D}$ could be a fully populated 4×4 stiffness matrix; for the Kirchhoff–Love plate/shell model and Cauchy continuum model, $\bar{D}$ could be a fully populated 6×6 stiffness matrix.

Substituting the solved strain energy stored in the SG into (37), we can rewrite the variational statement governing the original structure as

$$\int \left[\delta(1/2)\bar{\epsilon}^T \bar{D} \bar{\epsilon} - f_i \overline{\delta q_i} - m_i \overline{\delta \psi_i} \right] d\Omega = 0. \tag{46}$$

This variational statement governs the macroscopic structural model as it involves only fields which are unknown functions of the macrocoordinates x_k. The first term is the variation of the strain energy of

the macroscopic structural model and the rest of the terms are the virtual work done by generalized forces and moments. This variational statement governs the linear elastic behavior of structural elements (3D solid elements, 2D plate/shell elements, 1D beam elements) implemented in most commercial FEA software packages.

Often, we are also interested in computing the local fields within the original structure. With $\bar{\epsilon}$ obtained from the macroscopic structural analysis, the fluctuating function can be obtained as

$$w = SV_0\bar{\epsilon}. \tag{47}$$

The local displacement field can be obtained as

$$u_i = \bar{u}_i + x_\alpha(C_{\alpha i} - \delta_{\alpha i}) + \varepsilon w_j C_{ji}, \tag{48}$$

where u_i is the local displacement and $\bar{u}_i$ is the macroscopic displacement. For SGs having coordinates y_k with corresponding x_k existing in the macroscopic structural model, $\bar{u}_i$ should be interpreted as

$$\bar{u}_i = \bar{u}_i(x_{k_0}) + x_k\bar{u}_{i,k}, \tag{49}$$

where x_{k_0} is the center of the SG and $\bar{u}_{i,k}$ is the gradient along x_k evaluated at x_{k_0}.

The local strain field can be obtained as

$$\Gamma = (\Gamma_h SV_0 + \Gamma_\epsilon)\bar{\epsilon}. \tag{50}$$

The local stress field can be obtained directly using the Hooke's law as

$$\sigma = D\Gamma. \tag{51}$$

4. An analytical example: deriving the Kirchhoff–Love model for composite laminates

MSG presented above is very general so that it can handle a geometrically exact analysis for all types of structures with arbitrary heterogeneity. For the sake of simplicity, the above formulation will be specialized to derive the linear elastic Kirchhoff–Love model for composite laminates.

If we assume that the composite laminate is made of anisotropic homogeneous layers, the linear elastic behavior is governed by 3D elasticity in terms of 3D displacements u_i, strains ε_{ij}, and stresses σ_{ij}. To construct a plate model, we need to first express the 3D displacements in terms of 2D plate displacements:

$$
\begin{aligned}
u_1(x_1, x_2, y_3) &= \bar{u}_1(x_1, x_2) - y_3\bar{u}_{3,1} + w_1(x_1, x_2, y_3) \\
u_2(x_1, x_2, y_3) &= \bar{u}_2(x_1, x_2) - y_3\bar{u}_{3,2} + w_2(x_1, x_2, y_3) \\
u_3(x_1, x_2, y_3) &= \bar{u}_3(x_1, x_2) + w_3(x_1, x_2, y_3)
\end{aligned}
\tag{52}
$$

Here $u_i(x_1, x_2, y_3)$ are 3D displacements, while $\bar{u}_i(x_1, x_2)$ are plate displacements which are functions of x_1, x_2 only. We also introduce 3D unknown fluctuating functions $w_i(x_1, x_2, y_3)$ to describe the information of 3D displacements which cannot be described by the simpler Kirchhoff–Love plate kinematics. Note that the displacement expressions in (52) have nothing to do with the celebrated Kirchhoff–Love assumptions. It can be considered as a change of variables to express the 3D displacements in terms of the displacement variables of the Kirchhoff–Love plate model and fluctuating functions. The Kirchhoff–Love assumptions are equivalent to assuming $w_i = 0$. Since we consider that the original 3D model is

our true model, we construct the plate model as an approximation to the true model. To this end, we need to define the plate displacements in terms of 3D displacements. A natural choice is

$$h\bar{u}_3(x_1, x_2) = \langle u_3 \rangle, \quad h\bar{u}_\alpha(x_1, x_2) = \langle u_\alpha(x_1, x_2, y_3) \rangle + \langle y_3 \rangle \bar{u}_{3,\alpha}, \tag{53}$$

which implies the following constraint on the fluctuating functions:

$$\langle w_i \rangle = 0. \tag{54}$$

Note if the origin of the thickness coordinate is at the middle of the plate thickness, (53) actually defines the plate displacements to be the average of the 3D displacements.

Then the 3D strain field can be obtained as

$$\Gamma_{11} = \epsilon_{11} + x_3 \kappa_{11} + w_{1,1},$$
$$2\Gamma_{12} = 2\epsilon_{12} + 2x_3 \kappa_{12} + w_{1,2} + w_{2,1},$$
$$\Gamma_{22} = \epsilon_{22} + x_3 \kappa_{22} + w_{2,2},$$
$$2\Gamma_{13} = w_{1,3} + w_{3,1},$$
$$2\Gamma_{23} = w_{2,3} + w_{3,2},$$
$$\Gamma_{33} = w_{3,3},$$

with the linear plate strains defined as

$$\epsilon_{\alpha\beta}(x_1, x_2) = \tfrac{1}{2}(\bar{u}_{\alpha,\beta} + \bar{u}_{\beta,\alpha}), \quad \kappa_{\alpha\beta}^{2D}(x_1, x_2) = -\bar{u}_{3,\alpha\beta}. \tag{55}$$

Here α, β denote subscript 1 or 2.

The 3D strain field can also be written in the following matrix form:

$$\varepsilon_e = \epsilon + x_3 \kappa + I_\alpha w_{\parallel,\alpha}, \quad 2\varepsilon_s = w_\parallel' + e_\alpha w_{3,\alpha}, \quad \varepsilon_t = w_3', \tag{56}$$

with

$$\varepsilon_e = \lfloor \Gamma_{11} \ \Gamma_{22} \ 2\Gamma_{12} \rfloor^T,$$
$$2\varepsilon_s = \lfloor 2\Gamma_{13} \ 2\Gamma_{23} \rfloor^T,$$
$$\varepsilon_t = \Gamma_{33},$$
$$\epsilon = \lfloor \epsilon_{11} \ \epsilon_{22} \ 2\epsilon_{12} \rfloor^T,$$
$$\kappa = \lfloor \kappa_{11}^{2D} \ \kappa_{22}^{2D} \ \kappa_{12}^{2D} + \kappa_{21}^{2D} \rfloor^T,$$

and

$$I_1 = \begin{bmatrix} 1 & 0 \\ 0 & 1 \\ 0 & 0 \end{bmatrix}, \quad I_2 = \begin{bmatrix} 0 & 0 \\ 1 & 0 \\ 0 & 1 \end{bmatrix}, \quad e_1 = \begin{Bmatrix} 1 \\ 0 \end{Bmatrix}, \quad e_2 = \begin{Bmatrix} 0 \\ 1 \end{Bmatrix}. \tag{57}$$

The strain energy can be used as a natural measure for information governing the linear elastic behavior. Twice of the strain energy can be written as

$$2U = \left\langle \begin{Bmatrix} \varepsilon_e \\ 2\varepsilon_s \\ \varepsilon_t \end{Bmatrix}^T \begin{bmatrix} C_e & C_{es} & C_{et} \\ C_{es}^T & C_s & C_{st} \\ C_{et}^T & C_{st}^T & C_t \end{bmatrix} \begin{Bmatrix} \varepsilon_e \\ 2\varepsilon_s \\ \varepsilon_t \end{Bmatrix} \right\rangle. \tag{58}$$

The explicit expression after dropping smaller energy contributions due to $w_{i,\alpha}$ according to VAM is

$$2U_0 = \langle (\epsilon + x_3\kappa)^{\mathrm{T}}C_e(\epsilon + x_3\kappa) + w_\parallel'^{\mathrm{T}}C_s w_\parallel' + w_3'^{\mathrm{T}}C_t w_3'$$
$$+ 2(\epsilon + x_3\kappa)^{\mathrm{T}}C_{es}w_\parallel' + 2(\epsilon + x_3\kappa)^{\mathrm{T}}C_{et}w_3' + 2w_\parallel'^{\mathrm{T}}C_{st}w_3'\rangle. \quad (59)$$

Minimizing this energy with respect to the fluctuating function w_i along with the constraints in (54), we reach the following Euler–Lagrange equations:

$$((\epsilon + x_3\kappa)^{\mathrm{T}}C_{es} + w_\parallel'^{\mathrm{T}}C_s + w_3'C_{st}^{\mathrm{T}})' = \lambda_\parallel, \quad (60)$$

$$((\epsilon + x_3\kappa)^{\mathrm{T}}C_{et} + w_\parallel'^{\mathrm{T}}C_{st} + w_3'C_t)' = \lambda_3, \quad (61)$$

where $\lambda_\parallel = \lfloor \lambda_1 \lambda_2 \rfloor^T$ and λ_3 denote the Lagrange multipliers enforcing the constraints in (54). The boundary conditions on the top and bottom surfaces are

$$(\epsilon + x_3\kappa)^{\mathrm{T}}C_{es} + w_\parallel'^{\mathrm{T}}C_s + w_3'C_{st}^{\mathrm{T}} = 0, \quad (62)$$

$$(\epsilon + x_3\kappa)^{\mathrm{T}}C_{et} + w_\parallel'^{\mathrm{T}}C_{st} + w_3'C_t = 0. \quad (63)$$

We can conclude that the above two equations should be satisfied at every point through the thickness and solve for $w_\parallel'^{\mathrm{T}}$ and w_3' as

$$w_\parallel'^{\mathrm{T}} = -(\epsilon + x_3\kappa)C_{es}^* C_s^{-1}, \quad (64)$$

$$w_3' = -(\epsilon + x_3\kappa)C_{et}^* C_t^{*-1}, \quad (65)$$

with

$$C_t^* = C_t - C_{st}^{\mathrm{T}}C_s^{-1}C_{st}, \quad C_{et}^* = C_{et} - C_{es}C_s^{-1}C_{st}, \quad C_{es}^* = C_{es} - C_{et}^* C_{st}^{\mathrm{T}}/C_t^*. \quad (66)$$

w_i can be solved by simply integrating through the thickness along with the interlaminar continuity.

Substituting the solved fluctuating functions into (59), we have

$$2U_0 = \langle (\epsilon + x_3\kappa)^{\mathrm{T}}C_e^*(\epsilon + x_3\kappa)\rangle = \begin{Bmatrix} \epsilon \\ \kappa \end{Bmatrix}^{\mathrm{T}} \begin{bmatrix} A & B \\ B & D \end{bmatrix} \begin{Bmatrix} \epsilon \\ \kappa \end{Bmatrix}, \quad (67)$$

with

$$C_e^* = C_e - C_{es}^* C_s^{-1}C_{es}^{\mathrm{T}} - C_{et}^* C_{et}^{\mathrm{T}}/C_t^*, \quad A = \langle C_e^* \rangle, \quad B = \langle x_3 C_e^* \rangle, \quad D = \langle x_3^2 C_e^* \rangle. \quad (68)$$

This strain energy along with the work done by applied loads can be used to solve the 2D plate problem to obtain $\bar{u}_i, \epsilon, \kappa$. 3D displacements can be obtained after we have solved for w_i:

$$u_1(x_1, x_2, x_3) = \bar{u}_1(x_1, x_2) - x_3\bar{u}_{3,1} + w_1(x_1, x_2, y_3),$$
$$u_2(x_1, x_2, x_3) = \bar{u}_2(x_1, x_2) - x_3\bar{u}_{3,2} + w_2(x_1, x_2, y_3), \quad (69)$$
$$u_3(x_1, x_2, x_3) = \bar{u}_3(x_1, x_2) + w_3(x_1, x_2, y_3).$$

It is clear that the transverse normal does not remain rigid and normal according to Kirchhoff–Love assumptions in CLPT. Instead, the transverse normal can be deformed according to w_i.

3D strains can be obtained after neglecting the higher order terms $w_{i,\alpha}$, which are not contributing to the approximation of the plate energy. That is,

$$\varepsilon_e = \epsilon + x_3\kappa, \quad 2\varepsilon_s = -(\epsilon + x_3\kappa)C_{es}^* C_s^{-1}, \quad \varepsilon_{33} = -(\epsilon + x_3\kappa)C_{et}^* C_t^{*-1}. \quad (70)$$

Clearly, the strain field is not in-plane as what is traditionally assumed using Kirchhoff–Love assumptions in CLPT. Instead, transverse shear and normal strains both could exist.

By directly using the above strain field along with the Hooke's law in the original 3D elasticity theory, 3D stresses can be obtained as

$$\sigma_e = C_e^*(\epsilon + x_3 \kappa,) \quad \sigma_s = 0, \quad \sigma_{33} = 0 \tag{71}$$

It can be observed that the Kirchhoff–Love model derived using MSG satisfies the plane-stress assumption invoked in CLPT. However, this is not assumed *a priori* but derived by using MSG.

5. Numerical examples

The MSG developed in this paper was implemented into a computer code called SwiftComp. A few examples are used here to demonstrate the application and validity of MSG and its companion code SwiftComp. It can be theoretically shown that one can specialize MSG to reproduce the well established theory of composite beams known as Variational Asymptotic Beam Sectional analysis (VABS) [Cesnik and Hodges 1997; Yu et al. 2012], the theory of composite plates/shells known as Variational Asymptotic Plate And Shell analysis (VAPAS) [Yu 2005] and the micromechanics theories known as Variational Asymptotic Method for Unit Cell Homogenization (VAMUCH) [Yu and Tang 2007] and theories of heterogeneous plates and beams [Lee and Yu 2011a; 2011b]. We have verified that the current version of SwiftComp can reproduce all the results of VAMUCH, and the classical models of VABS and VAPAS. Particularly, an extensively benchmark study for micromechanics theories and codes has been recently carried out by cdmHUB (Composites Design and Manufacturing HUB) and the results have shown that MSG and SwiftComp can achieve the versatility and accuracy of 3D FEA with much less computational time, which clearly demonstrates the advantage of MSG in micromechanics. Interested readers are directed to the report and database of the Micromechanics Simulation Challenge available at https://cdmhub.org/projects/mmsimulationchalleng. Here, a few examples which cannot be handled by current versions of VAMUCH, VABS, and VAPAS are used to demonstrate the application of MSG and SwiftComp.

5.1. *A cross-ply laminate.* First, we will use a simple cross-ply laminate example to demonstrate the application of MSG. As shown in Figure 9, a four-layer cross-ply [90°/0°/90°/0°] laminate with length
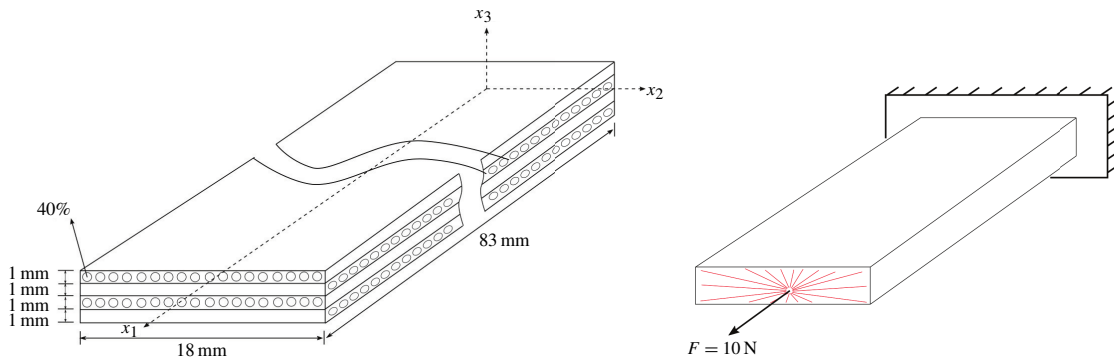

**Figure 9.** Sketch of the four-layer cross-ply laminate.
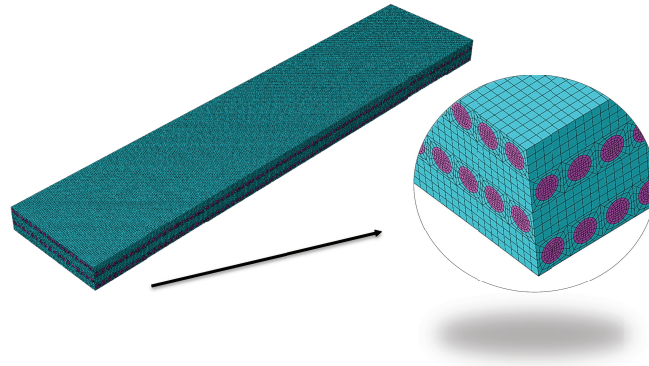
Figure 10. 3D finite element mesh of the four-layer cross-ply laminate.

83 mm, width 18 mm, and height 4 mm is clamped at one end and loaded at the other end with a 10 N tensile force at the center of the cross-section. The composite prepreg is assumed to have square packing with 40% fiber volume fraction. The fiber and matrix are assumed to be isotropic, with a Young's modulus of 276 GPa and a Poisson's ratio of 0.28 for the fiber and a Young's modulus of 4.76 GPa and a Poisson's ratio of 0.37 for the matrix.

It is noted here that this example is not representative of a typical fiber reinforced composite laminate, as usually each layer could contain many more fibers instead of one fiber per layer thickness as assumed here for simplicity. The purpose of this example is not to question CLPT's modeling capability for conventional laminates, which could be the subject of a future publication. Instead, this example is used to demonstrate the accuracy and efficiency of alternative analysis options provided by MSG. There are two common approaches to analyze this type of structure: 3D FEA using solid elements to mesh all of the microstructural details (see Figure 10) and lamination theory with lamina constants computed by a micromechanics approach (see Figure 2). Using 3D FEA, the laminate is meshed with 2,294,784 C3D20R elements with a total of 9,319,562 nodes in ABAQUS to achieve a fair convergence of stress predictions. Using MSG, we can also analyze the structure as a plate with the constitutive relations provided through an analysis of the corresponding SG as shown in Figure 11, where the SG is meshed in ABAQUS using 1,536 20-noded brick elements with 7,585 total nodes, and the reference surface is meshed with 2,988 STRI3 elements containing 1,596 nodes. Because the length is much larger than both the height and width, the structure can also be analyzed as a beam with the constitutive relations provided
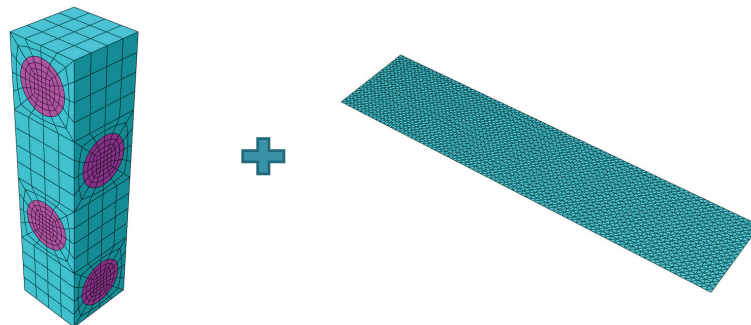
Figure 11. SwiftComp-based plate analysis.
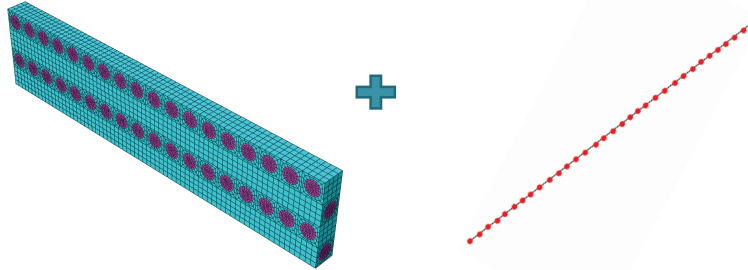
Figure 12. SwiftComp-based beam analysis.

through an analysis of the corresponding SG as shown in Figure 12. The SG is meshed with 27,648 20-noded brick elements with 124,409 nodes total, and the reference line is meshed with 83 two-noded line elements with 84 nodes total.

Different analysis approaches require different computing resources and time. Using 3D FEA, we used a computer with 48 cores and it took ABAQUS 7 days 11 hours and 37 minutes to finish the analysis. For the lamination theory, we used the composite layup analysis in ABAQUS with the same surface mesh as shown in Figure 11. To compute the lamina constants, SwiftComp only requires a 2D SG which is much more efficient than other computational homogenization approaches which usually require a 3D domain to obtain the complete set of properties [Fish 2013]. The micromechanics analysis and the laminate analysis are finished within 30 seconds. For SwiftComp-based plate analysis, homogenization of the SG to compute the plate stiffness takes 6 seconds, the surface analysis takes 28 seconds, and dehomogenization to obtain 3D local fields takes 6 seconds. For SwiftComp-based beam analysis, homogenization of SG to compute the beam stiffness takes 3 minutes and 14 seconds, the beam analysis takes 0.02 second, and dehomogenization to obtain 3D local fields takes 1 minute 21 seconds. Except for the 3D FEA, all the other analyses were done in the same computer using only 1 core. The other analyses are several orders of magnitude more efficient than 3D FEA. SwiftComp adds small overhead for the constitutive modeling including both the homogenization and dehomogenization processes in comparison to the traditional lamination theory for this simple static analysis. However, constitutive modeling is usually done once, while many global structural analyses using beam elements or plate elements are needed in the real design and analysis of composite structures. In other words, the small overhead added by SwiftComp could be negligible for most cases.

Different analysis approaches result in different predictions. The displacements at the center of the loaded tip are shown in Table 1. SwiftComp-based plate and beam analyses achieve excellent agreement

| Analysis methods	Deflection (mm)	Extension (mm)
3D FEA	$2.7124 \cdot 10^{-3}$	$2.0849 \cdot 10^{-4}$
SwiftComp beam analysis	$2.7146 \cdot 10^{-3}$	$2.0873 \cdot 10^{-4}$
SwiftComp plate analysis	$2.7084 \cdot 10^{-3}$	$2.0832 \cdot 10^{-4}$
ABAQUS Composite layup	$2.5264 \cdot 10^{-3}$	$2.0804 \cdot 10^{-4}$

Table 1. Displacements predicted by different analyses.

with 3D FEA. Lamination theory using ABAQUS layup analysis provides an excellent prediction for the minor displacement (extension), but introduces about 7% error for the major displacement (deflection) in comparison to 3D FEA. The prediction of the detailed stress distribution within composites is also very important, as these quantities could be directly related with the failure of the structure. Consider the stress distribution through the thickness at $x_1 = 41.5$ mm, $x_2 = 0.5$ mm. Note at this point x_3 is passing through the diameter of one of the fibers. As shown in Figures 13, 14, and 15, both SwiftComp-based plate analysis and beam analysis achieve excellent agreement with 3D FEA for all the nontrivial stress components while the ABAQUS composite layup analysis shows significant discrepancies from 3D FEA. It is clear that the composite layup analysis predicts stress discontinuities happening at the wrong locations and the maximum stresses predicted by the composite layup analysis are also very different from 3D FEA. The composite layup analysis cannot predict the transverse normal stress (σ_{33}) due to its inherent plane-stress assumption, while SwiftComp-based plate and beam analyses still remain in very good agreement with 3D FEA, although the magnitude is small compared to the other two in-plane stress components. It can be observed that for this problem, SwiftComp can achieve similar accuracy as 3D FEA but with orders of magnitude savings in computing time and resources. Regarding the relatively larger discrepancy between SwiftComp and 3D FEA for σ_{33}, it is mainly because we could not further refine the 3D FEA model due to the limitation of the workstation we can access (56 CPUs with 256 GB RAM). We have verified that for simpler cases such as a two-layer plate of the same example, we can get a perfect match with 3D FEA. We have done mesh convergence studies for many problems and MSG consistently converges faster than 3D FEA due to the semianalytical nature of MSG.

5.2. _Sandwich beam with periodically varying cross-sections._ The next example is used to demonstrate the application of MSG to analyze beams with spanwise heterogeneities which can be commonly found in civil engineering applications. It is a sandwich beam with periodically variable cross-section studied
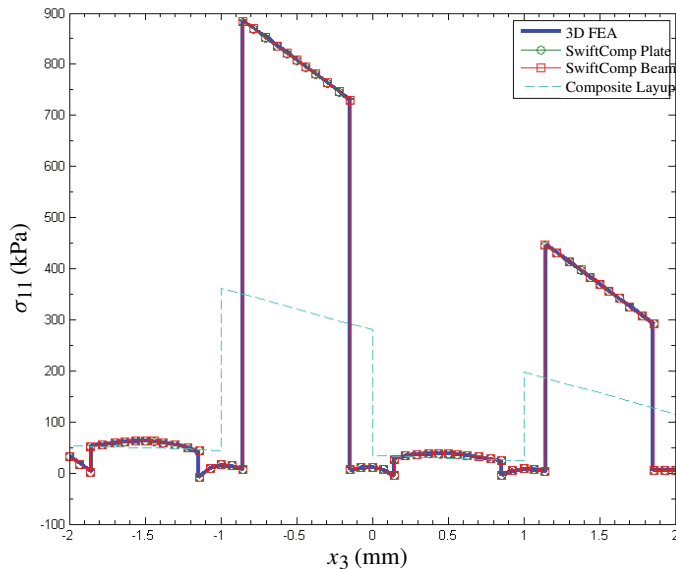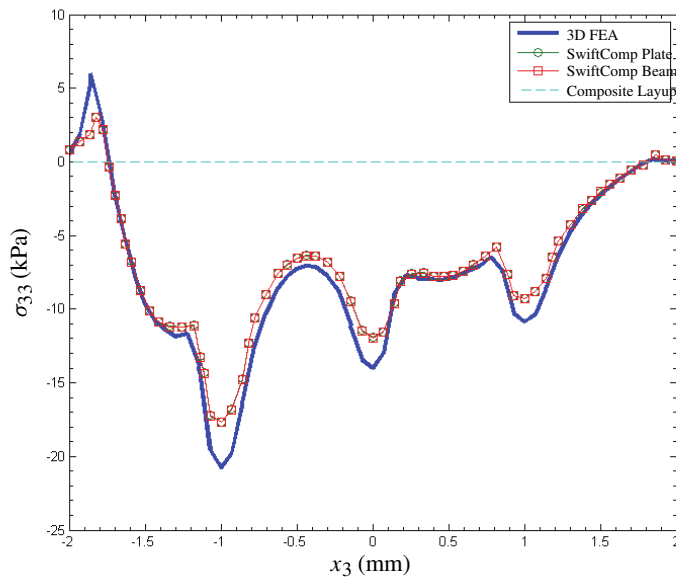

**Figure 13.** σ_{11} distribution through the thickness ($x_1 = 41.5$ mm, $x_2 = 0.5$ mm).
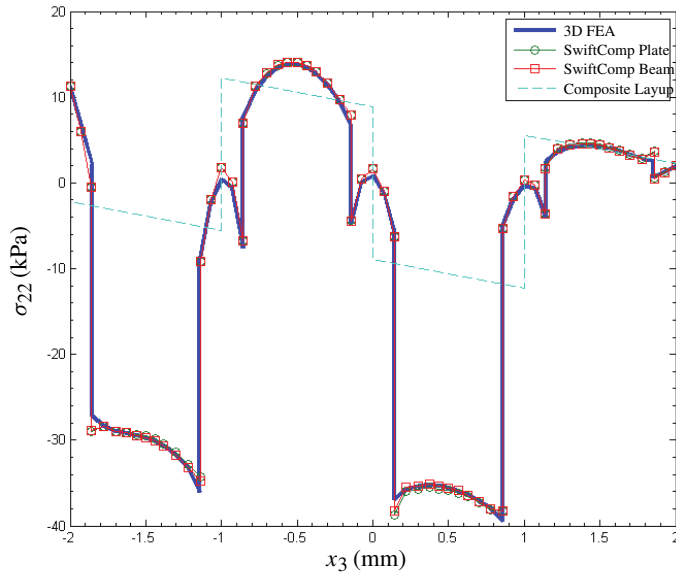
Figure 14. σ_{22} distribution through the thickness ($x_1 = 41.5\,\text{mm}$, $x_2 = 0.5\,\text{mm}$).

in [Dai and Zhang 2008]. The geometric parameters for each configuration are given in Figure 16. Note that although all the SGs in Figure 16 are uniform along y_2, the SG must be 3D because they are used to form a beam structure and y_2 is one of the cross-sectional coordinates (Figure 17). All sandwich beams in the above cases have the same core material properties (material indicated by blue color in the figure) of $E_c = 3.5\,\text{GPa}$, $v_c = 0.34$ and face sheet material properties (indicated by purple color in the figure) of $E_f = 70\,\text{GPa}$, $v_c = 0.34$. Also note that although these beams are studied in [Dai and Zhang 2008],

Figure 15. σ_{33} distribution through the thickness ($x_1 = 41.5\,\text{mm}$, $x_2 = 0.5\,\text{mm}$).
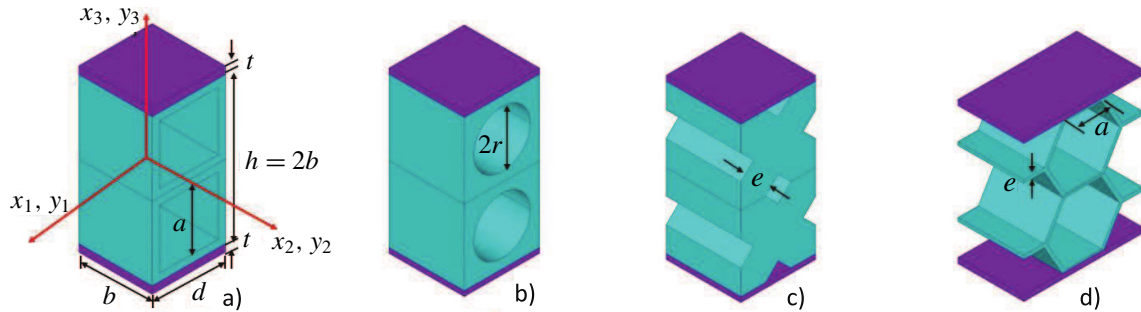
Figure 16. The structure genome for sandwich beams with different cross-sections: a) square holes ($b = d = 1.5$ m, $t = 0.1$ m, $a = 1$ m); b) circular holes ($b = d = 1.5$ m, $t = 0.1$ m, $r = 0.5614$ m); c) cross-shaped holes ($b = d = 1.5$ m, $t = 0.1$ m, $e = 0.7071$ m); d) hexagonal holes ($b = 1.23745$ m, $d = 2b$, $t = 0.1$ m, $a = 0.7887$ m, $e = 0.6431$ m).

	[Dai and Zhang 2008]	SwiftComp	NIAH
square holes	5.669	5.576	5.576
circular holes	5.176	5.537	5.554
cross-shaped holes	5.486	5.805	5.891
hexagonal holes	2.875	2.888	2.886

Table 2. Effective beam bending stiffness of sandwich beams predicted by different methods (all units are 10^{10} N·m^2).

only bending stiffnesses are given. In fact, the effective stiffness for the classical beam model in general should be represented by a fully populated 4×4 matrix. This example is also studied in [Yi et al. 2015] using a novel finite implementation of the asymptotic homogenization theory applied to beams. The effective bending stiffnesses predicted by the analytical formulas in [Dai and Zhang 2008], those of [Yi et al. 2015] denoted as NIAH standing for Novel Implementation of Asymptotic Homogenization, and SwiftComp are listed in Table 2. The details of these approaches can be found in the cited references.

As can be observed, SwiftComp predictions have an excellent agreement with NIAH and are slightly different from those in [Dai and Zhang 2008]. However, the present approach is more versatile than that in the previous work because that paper only provides analytic formulas for the bending stiffness of beams made of materials characterized only by one material constant, the Young's modulus, while SwiftComp can estimate all the engineering beam constants represented by a 4×4 stiffness matrix (possibly fully populated) for the most general anisotropic materials by factorizing the coefficient matrix in the linear system (Equation (43)) only once. NIAH results are obtained using multiple runs of a commercial finite element code, which requires much more computing time than SwiftComp.

5.3. *Sandwich panel with a corrugated core.* The last example is to demonstrate the application of MSG to model plates with in-plane heterogeneities. It is a corrugated-core sandwich panel, a concept used for Integrated Thermal Protection Systems (ITPS) studied in [Sharma et al. 2010]. The ITPS panel along with the details of the SG is sketched in Figure 18. Both materials are isotropic with $E_1 = 109.36$
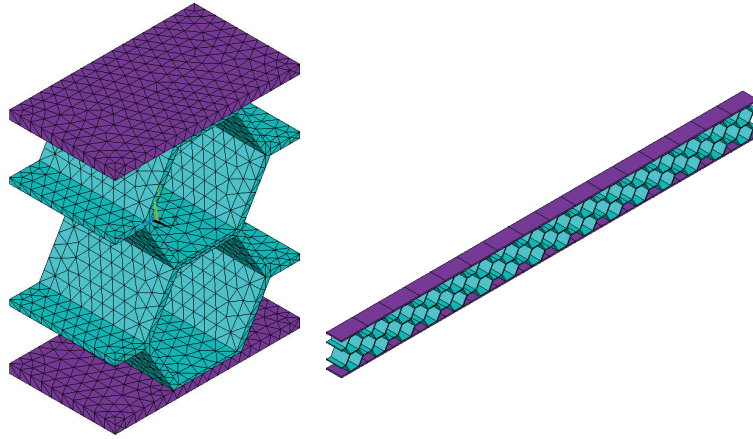
Figure 17. A sandwich beam with hexagonal holes.

GPa, $\nu_1 = 0.3$ for material 1, and $E_2 = 209.482$ GPa, $\nu_2 = 0.063$ for material 2. Although 3D unit cells are needed for the study in the previous reference, only a 2D SG is necessary for SwiftComp as it is uniform along one of the in-plane directions. The effective stiffness for the Kirchhoff–Love plate model can be represented using the A, B and D matrices known in CLPT. Results obtained in the previous reference are compared with SwiftComp in Tables 3, 4 and 5. SwiftComp predictions agree very well when compared to those results with the biggest difference (around 1%) appearing for the extension-bending coupling stiffness (B_{11}). However, the present approach is much more efficient because using the approach in [Sharma et al. 2010] one needs to carry out six analyses of a 3D unit cell under six different sets of boundary conditions and load conditions and postprocess the 3D stresses to compute the

	A_{11}	A_{12}	A_{22}	A_{33}
[Sharma et al. 2010]	2.83	0.18	2.33	1.07
SwiftComp	2.80	0.18	2.33	1.08

Table 3. Effective extension stiffness of ITPS (all units in 10^9 N/m).

	D_{11}	D_{12}	D_{22}	D_{33}
[Sharma et al. 2010]	3.06	0.22	2.85	1.32
SwiftComp	3.03	0.22	2.87	1.32

Table 4. Effective bending stiffness of ITPS (all units in 10^6 N·m).

	B_{11}	B_{13}	B_{22}	B_{33}
[Sharma et al. 2010]	-71.45	-3.36	-34.05	-71.45
SwiftComp	-70.67	-3.31	-34.06	-71.42

Table 5. Effective coupling stiffness of ITPS (all units in 10^6 N).
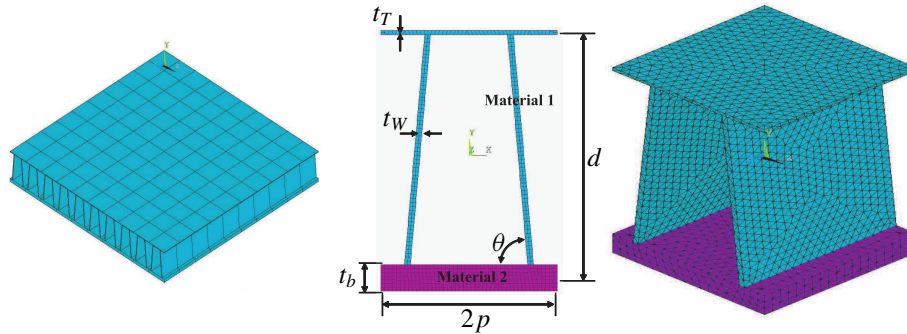
Figure 18. Sketch of the ITPS panel (left) and its SG ($t_T = 1.2$ mm, $t_B = 7.49$ mm, $t_W = 1.63$ mm, $p = 25$ mm, $d = 70$ mm, and $\theta = 85°$).

plate stress resultants. Using the present approach, one only needs to carry out one analysis of a 2D SG without applying carefully crafted boundary conditions and postprocessing.

6. Conclusion

This paper developed a unified theory for multiscale constitutive modeling of composites based on the concept of SG. The SG facilitates a mathematical decoupling of the original complex analysis of composite structures into a constitutive modeling over the SG and a macroscopic structural analysis. The MSG presented in this paper enables a multiscale constitutive modeling approach with the following unique features:

- Use of SG to connect microstructures and macroscopic structural analyses. Intellectually, SG enables us to view constitutive modeling for structures as applications of micromechanics. Technically, SG empowers us to systematically model complex build-up structures with heterogeneities.

- Use of VAM to avoid *a priori* assumptions commonly invoked in other approaches, providing the rigor needed to construct mathematical models with excellent tradeoffs between efficiency and accuracy.

- Decouple the original problem into two sets of analyses: a constitutive modeling and a structural analysis. This allows the structural analysis to be formulated exactly as a general (1D, 2D, or 3D) continuum, the analysis of which is readily available in commercial FEA software packages. This also confines all approximations to the constitutive modeling, the accuracy of which is guaranteed to be the best by the VAM.

A general-purpose computer code, called SwiftComp, was developed to implement MSG along with several examples to demonstrate its application. This code can be used as a plug-in for commercial FEA software packages to accurately model structures made of anisotropic heterogeneous materials using traditional structural elements.

Although only theoretical details and implementation have been worked out for linear elastic behavior of periodic structures for which a SG can be easily identified, the basic framework is also applicable to nonlinear behavior of aperiodic heterogeneous structures, which are topics for future work.

Appendix

Γ_h is an operator matrix which depends on the dimensionality of the SG. If the SG is 3D, we have

$$
\Gamma_h = \begin{bmatrix}
1/\sqrt{g_1}(\partial/\partial y_1) & 0 & 0 \\
0 & 1/\sqrt{g_2}(\partial/\partial y_2) & 0 \\
0 & 0 & (\partial/\partial y_3) \\
0 & (\partial/\partial y_3) & 1/\sqrt{g_2}(\partial/\partial y_2) \\
(\partial/\partial y_3) & 0 & 1/\sqrt{g_1}(\partial/\partial y_1) \\
1/\sqrt{g_2}(\partial/\partial y_2) & 1/\sqrt{g_1}(\partial/\partial y_1) & 0
\end{bmatrix},
\tag{72}
$$

where $\sqrt{g_1} = \sqrt{g_2} = 1$ for plate-like structures or 3D structures; $\sqrt{g_1} = 1 - \varepsilon y_2 k_{13} + \varepsilon y_3 k_{12}$, $\sqrt{g_2} = 1$ for beam-like structures; and $\sqrt{g_1} = 1 + \varepsilon y_3 k_{12}$, $\sqrt{g_2} = 1 - \varepsilon y_3 k_{21}$ for shell-like structures.

If the SG is a lower-dimensional one, one just needs to vanish the corresponding term corresponding to the microcoordinates which are not used in describing the SG. For example, if the SG is 2D, we have

$$
\Gamma_h = \begin{bmatrix}
0 & 0 & 0 \\
0 & 1/\sqrt{g_2}(\partial/\partial y_2) & 0 \\
0 & 0 & (\partial/\partial y_3) \\
0 & (\partial/\partial y_3) & 1/\sqrt{g_2}(\partial/\partial y_2) \\
(\partial/\partial y_3) & 0 & 0 \\
1/\sqrt{g_2}(\partial/\partial y_2) & 0 & 0
\end{bmatrix}.
\tag{73}
$$

If the SG is 1D, we have

$$
\Gamma_h = \begin{bmatrix}
0 & 0 & 0 \\
0 & 0 & 0 \\
0 & 0 & (\partial/\partial y_3) \\
0 & (\partial/\partial y_3) & 0 \\
(\partial/\partial y_3) & 0 & 0 \\
0 & 0 & 0
\end{bmatrix}.
\tag{74}
$$

Γ_ϵ is an operator matrix, the form of which depends on the macroscopic structural model. If the macroscopic structural model is the 3D Cauchy continuum model, Γ_ϵ is the 6×6 identity matrix. If the macroscopic structural model is a beam model, we have

$$
\Gamma_\epsilon = \frac{1}{\sqrt{g_1}} \begin{bmatrix}
1 & 0 & \varepsilon y_3 & -\varepsilon y_2 \\
0 & 0 & 0 & 0 \\
0 & 0 & 0 & 0 \\
0 & 0 & 0 & 0 \\
0 & \varepsilon y_2 & 0 & 0 \\
0 & -\varepsilon y_3 & 0 & 0
\end{bmatrix}.
\tag{75}
$$

If the macroscopic structural model is a plate/shell model, we have

$$
\Gamma_\epsilon =
\begin{bmatrix}
1/\sqrt{g_1} & 0 & 0 & \varepsilon y_3/\sqrt{g_1} & 0 & 0 \\
0 & 1/\sqrt{g_2} & 0 & 0 & \varepsilon y_3/\sqrt{g_2} & 0 \\
0 & 0 & 0 & 0 & 0 & 0 \\
0 & 0 & 0 & 0 & 0 & 0 \\
0 & 0 & 0 & 0 & 0 & 0 \\
0 & 0 & \frac{1}{2}\left(\frac{1}{\sqrt{g_1}}+\frac{1}{\sqrt{g_2}}\right) & 0 & 0 & \frac{1}{2}\left(\frac{\varepsilon y_3}{\sqrt{g_1}}+\frac{\varepsilon y_3}{\sqrt{g_2}}\right)
\end{bmatrix}.
\tag{76}
$$

Note the above expression is obtained with the understanding that the difference between κ_{12} and κ_{21} is of higher order and negligible if we are not seeking a higher-order approximation of the initial curvatures.

Γ_l is an operator matrix, the form of which depends on the macroscopic structural model. If the macroscopic structural model is 3D, Γ_l has the same form as Γ_h in (72) with $\partial/\partial y_k$ replaced with $\partial/\partial x_k$, that is

$$
\Gamma_l =
\begin{bmatrix}
1/\sqrt{g_1}(\partial/\partial x_1) & 0 & 0 \\
0 & 1/\sqrt{g_2}(\partial/\partial x_2) & 0 \\
0 & 0 & (\partial/\partial x_3) \\
0 & (\partial/\partial x_3) & 1/\sqrt{g_2}(\partial/\partial x_2) \\
(\partial/\partial x_3) & 0 & 1/\sqrt{g_1}(\partial/\partial x_1) \\
1/\sqrt{g_2}(\partial/\partial x_2) & 1/\sqrt{g_1}(\partial/\partial x_1) & 0
\end{bmatrix}.
\tag{77}
$$

Of course for 3D structures, we have $\sqrt{g_1}=\sqrt{g_2}=1$.

If the macroscopic structural model is a lower-dimensional one, one just needs to vanish the corresponding term corresponding to the macrocoordinates which are not used in describing the macroscopic structural model. For example, if the macroscopic structural model is a 2D plate/shell model, we have

$$
\Gamma_l =
\begin{bmatrix}
1/\sqrt{g_1}(\partial/\partial x_1) & 0 & 0 \\
0 & 1/\sqrt{g_2}(\partial/\partial x_2) & 0 \\
0 & 0 & 0 \\
0 & 0 & 1/\sqrt{g_2}(\partial/\partial x_2) \\
0 & 0 & 1/\sqrt{g_1}(\partial/\partial x_1) \\
1/\sqrt{g_2}(\partial/\partial x_2) & 1/\sqrt{g_1}(\partial/\partial x_1) & 0
\end{bmatrix}.
\tag{78}
$$

If the macroscopic structural model is the 1D beam model, we have

$$
\Gamma_l =
\begin{bmatrix}
1/\sqrt{g_1}(\partial/\partial x_1) & 0 & 0 \\
0 & 0 & 0 \\
0 & 0 & 0 \\
0 & 0 & 0 \\
0 & 0 & 1/\sqrt{g_1}(\partial/\partial x_1) \\
0 & 1/\sqrt{g_1}(\partial/\partial x_1) & 0
\end{bmatrix}.
\tag{79}
$$

Γ_R is an operator matrix existing only for those heterogeneous structures featuring initial curvatures. For prismatic beams, plates or 3D structures, Γ_R vanishes. For those structures having initial curvatures

such as initially twisted/curved beams or shells, the form of Γ_R depends on the macroscopic structural model. If the macroscopic structural model is a 1D beam model,

$$\Gamma_R = \frac{1}{\sqrt{g_1}} \begin{bmatrix} k_{11}\left(y_3\dfrac{\partial}{\partial y_2} - y_2\dfrac{\partial}{\partial y_3}\right) & -k_{13} & k_{12} \\ 0 & 0 & 0 \\ 0 & 0 & 0 \\ 0 & 0 & 0 \\ -k_{12} & k_{11} & k_{11}\left(y_3\dfrac{\partial}{\partial y_2} - y_2\dfrac{\partial}{\partial y_3}\right) \\ k_{13} & k_{11}\left(y_3\dfrac{\partial}{\partial y_2} - y_2\dfrac{\partial}{\partial y_3}\right) & -k_{11} \end{bmatrix}. \tag{80}$$

If the macroscopic structural model is a 2D shell model,

$$\Gamma_R = \begin{bmatrix} 0 & -k_{13}/\sqrt{g_1} & k_{12}/\sqrt{g_1} \\ k_{23}/\sqrt{g_2} & 0 & -k_{21}/\sqrt{g_2} \\ 0 & 0 & 0 \\ 0 & k_{21}/\sqrt{g_2} & 0 \\ -k_{12}/\sqrt{g_1} & 0 & 0 \\ k_{13}/\sqrt{g_1} & -k_{23}/\sqrt{g_2} & 0 \end{bmatrix}. \tag{81}$$

Acknowledgments

References

[Aboudi 1982] J. Aboudi, "A continuum theory for fiber-reinforced elastic-viscoplastic composites", *Int. J. Eng. Sci.* **20**:5 (1982), 605–621.

[Aboudi 1989] J. Aboudi, "Micromechanical analysis of composites by the method of cells", *Appl. Mech. Rev.* **42**:7 (1989), 193–221.

[Aboudi et al. 2001] J. Aboudi, M. J. Pindera, and S. Arnold, "Linear thermoelastic higher-order theory for periodic multiphase materials", *J. Appl. Mech.* **68**:5 (2001), 697–707.

[Aboudi et al. 2012] J. Aboudi, S. Arnold, and B. Bednarcyk, *Micromechanics of composite materials: a generalized multiscale analysis approach*, Elsevier, Amsterdam, 2012.

[Bensoussan et al. 1978] A. Bensoussan, J.-L. Lions, and G. Papanicolaou, *Asymptotic analysis for periodic structures*, Studies in Mathematics and its Applications **5**, North-Holland, Amsterdam, 1978.

[Berdichevsky 2009] V. Berdichevsky, *Variational principles of continuum mechanics I: Fundamentals*, Springer, Berlin, 2009.

[Berger et al. 2006] H. Berger, S. Kari, U. Gabbert, R. Rodriguez-Ramos, J. Bravo-Castillero, R. Guinovart-Diaz, F. Sabina, and G. Maugin, "Unit cell models of piezoelectric fiber composites for numerical and analytical calculation of effective properties", *Smart Mater. Struct.* **15**:2 (2006), 451–458.

[Carrera 2003] E. Carrera, "Historical review of zig-zag theories for multilayered plates and shells", *Appl. Mech. Rev.* **56**:3 (2003), 287–308.

[Carrera et al. 2012] E. Carrera, M. Maiarú, and M. Petrolo, "Component-wise analysis of laminated anisotropic composites", *Int. J. Solids Struct.* **49**:13 (2012), 1839–1851.

[Carrera et al. 2014] E. Carrera, M. Cinefra, M. Petrolo, and E. Zappino, *Finite element analysis of structures through unified formulation*, Wiley, Hoboken, NJ, 2014.

[Cesnik and Hodges 1997] C. Cesnik and D. Hodges, "VABS: a new concept for composite rotor blade cross-sectional modeling", *J. Amer. Helicopter Soc.* **42**:1 (1997), 27–38.

[Cheng and Batra 2000] Z.-Q. Cheng and R. Batra, "Three-dimensional asymptotic analysis of multiple-electroded piezoelectric laminates", *AIAA Journal* **38**:2 (2000), 317–324.

[Collier et al. 2002] C. Collier, P. Yarrington, and B. V. West, "Composite, grid-stiffened panel design for post buckling using HyperSizer", in *Proceedings of the 43rd AIAA/ASME/ASCE/AHS/ASC Structures, Structural Dynamics and Materials Conference* (Denver, 2002), AIAA, 2002.

[Cosserat and Cosserat 1909] E. Cosserat and F. Cosserat, *Théorie des corps déformables*, Hermann, Paris, 1909.

[Dai and Zhang 2008] G. Dai and W. Zhang, "Size effects of basic cell in static analysis of sandwich beams", *Int. J. Solids Struct.* **45**:9 (2008), 2512–2533.

[Danielson and Hodges 1987] D. Danielson and D. Hodges, "Nonlinear beam kinematics by decomposition of the rotation tensor", *J. Appl. Mech.* **54** (1987), 258–262.

[Demasi and Yu 2012] L. Demasi and W. Yu, "Assess the accuracy of the variational asymptotic plate and shell analysis (VAPAS) using the generalized unified formulation (GUF)", *Mech. Adv. Mater. Struct.* **20**:3 (2012), 227–241.

[Fish 2013] J. Fish, *Practical multiscaling*, Wiley, Hoboken, NJ, 2013.

[Ghosh 2011] S. Ghosh, *Micromechanical analysis and multi-scale modeling using the Voronoi cell finite element method*, CRC Press, Boca Raton, FL, 2011.

[Guedes and Kikuchi 1990] J. M. Guedes and N. Kikuchi, "Preprocessing and postprocessing for materials based on the homogenization method with adaptive finite element methods", *Comput. Methods Appl. Mech. Engrg.* **83**:2 (1990), 143–198.

[Hashin and Shtrikman 1962] Z. Hashin and S. Shtrikman, "A variational approach to the theory of the elastic behaviour of polycrystals", *J. Mech. Phys. Solids* **10** (1962), 343–352.

[Hill 1952] R. Hill, "The elastic behaviour of a crystalline aggregate", *Proc. Phys. Soc. Sec. A* **65** (1952), 349–354.

[Hodges 2006] D. Hodges, *Nonlinear composite beam theory*, AIAA, Washington, DC, 2006.

[Icardi and Ferrero 2010] U. Icardi and L. Ferrero, "Layerwise zig-zag model with selective refinement across the thickness", *Int. J. Numer. Methods Eng.* **84**:9 (2010), 1085–1114.

[Kalamkarov and Kolpakov 2001] A. L. Kalamkarov and A. G. Kolpakov, "A new asymptotic model for a composite piezoelastic plate", *Int. J. Solids Struct.* **38**:34-35 (2001), 6027–6044.

[Kalamkarov et al. 2009] A. Kalamkarov, I. Andrianov, and V. Danishevs'kyy, "Asymptotic homogenization of composite materials and structures", *Appl. Mech. Rev.* **62**:3 (2009), 030802.

[Khandan et al. 2012] R. Khandan, S. Noroozi, P. Sewell, and J. Vinney, "The development of laminated composite plate theories: a review", *J. Mater. Sci.* **47**:16 (2012), 5901–5910.

[Kim 2009] J. Kim, "An asymptotic analysis of anisotropic heterogeneous plates with consideration of end effects", *J. Mech. Mater. Struct.* **4**:9 (2009), 1535–1553.

[Kollár and Springer 2009] L. P. Kollár and G. S. Springer, *Mechanics of composite structures*, Cambridge University Press, 2009.

[Lee and Yu 2011a] C.-Y. Lee and W. Yu, "Homogenization and dimensional reduction of composite plates with in-plane heterogeneity", *Int. J. Solids Struct.* **48**:10 (2011), 1474–1484.

[Lee and Yu 2011b] C.-Y. Lee and W. Yu, "Variational asymptotic modeling of composite beams with spanwise heterogeneity", *Comput. Struct.* **89**:15–16 (2011), 1503–1511.

[Li and Wang 2008] S. Li and G. Wang, *Introduction to micromechanics and nanomechanics*, World Scientific, Hackensack, NJ, 2008.

[Mantari et al. 2012] J. Mantari, A. Oktem, and C. G. Soares, "A new trigonometric shear deformation theory for isotropic, laminated composite and sandwich plates", *Int. J. Solids Struct.* **49**:1 (2012), 43–53.

[Maugin and Attou 1990] G. A. Maugin and D. Attou, "An asymptotic theory of thin piezoelectric plates", *Quart. J. Mech. Appl. Math.* **43**:3 (1990), 347–362.

[Michel et al. 1999] J. C. Michel, H. Moulinec, and P. Suquet, "Effective properties of composite materials with periodic microstructure: a computational approach", *Comput. Methods Appl. Mech. Engrg.* **172**:1-4 (1999), 109–143.

[Milton 2002] G. W. Milton, *The theory of composites*, Cambridge Monographs on Applied and Computational Mathematics **6**, Cambridge University Press, 2002.

[Mori and Tanaka 1973] T. Mori and K. Tanaka, "Average stress in matrix and average elastic energy of materials with misfitting inclusions", *Acta Metallurgica* **21**:5 (1973), 571–574.

[Murakami and Toledano 1990] H. Murakami and A. Toledano, "A higher-order mixture homogenization of bi-laminated composites", *J. Appl. Mech.* **57** (1990), 388–296.

[Nemat-Nasser and Hori 1998] S. Nemat-Nasser and M. Hori, *Micromechanics: overall properties of heterogeneous materials*, 2nd ed., North-Holland Series in Applied Mathematics and Mechanics **37**, North-Holland, Amsterdam, 1998.

[Pagano and Rybicki 1974] N. Pagano and E. Rybicki, "On the significance of effective modulus solutions for fibrous composites", *J. Compos. Mater.* **8**:3 (1974), 214–228.

[Paley and Aboudi 1992] M. Paley and J. Aboudi, "Micromechanical analysis of composites by the generalized cells model", *Mech. Mater.* **14**:2 (1992), 127–139.

[Pietraszkiewicz and Eremeyev 2009a] W. Pietraszkiewicz and V. Eremeyev, "On vectorially parameterized natural strain measures of the nonlinear Cosserat continuum", *Int. J. Solids Struct.* **46**:11-12 (2009), 2477–2480.

[Pietraszkiewicz and Eremeyev 2009b] W. Pietraszkiewicz and V. A. Eremeyev, "On natural strain measures of the non-linear micropolar continuum", *Int. J. Solids Struct.* **46**:3-4 (2009), 774–787.

[Plagianakos and Saravanos 2009] T. S. Plagianakos and D. A. Saravanos, "Higher-order layerwise laminate theory for the prediction of interlaminar shear stresses in thick composite and sandwich composite plates", *Compos. Struct.* **87**:1 (2009), 23–35.

[Reddy 1984] J. Reddy, "A simple higher-order theory for laminated composite plates", *J. Appl. Mech.* **51**:4 (1984), 745–752.

[Reddy 2004] J. N. Reddy, *Mechanics of laminated composite plates and shells: theory and analysis*, CRC Press, Boca Raton, FL, 2004.

[Reddy and Cheng 2001] J. Reddy and Z.-Q. Cheng, "Three-dimensional solutions of smart functionally graded plates", *J. Appl. Mech.* **68**:2 (2001), 234–241.

[Sharma et al. 2010] A. Sharma, B. V. Sankar, and R. Haftka, "Homogenization of plates with microstructure and application to corrugated core sandwich panels", in *Proceedings of the 51st AIAA/ASME/ASCE/AHS/ASC Structures, Structural Dynamics, and Materials Conference* (Orlando, 2010), AIAA, 2010.

[Skoptsov and Sheshenin 2011] K. A. Skoptsov and S. V. Sheshenin, "Asymptotic analysis of laminated plates and shallow shells", *Mech. Solids* **46**:1 (2011), 129–138.

[Sun and Vaidya 1996] C. Sun and R. Vaidya, "Prediction of composite properties from a representative volume element", *Compos. Sci. Technol.* **56**:2 (1996), 171 – 179.

[Torquato 2002] S. Torquato, *Random heterogeneous materials*, Interdisciplinary Applied Mathematics **16**, Springer, New York, 2002.

[Williams 2005] T. O. Williams, "A two-dimensional, higher-order, elasticity-based micromechanics model", *Int. J. Solids Struct.* **42**:3-4 (2005), 1009–1038.

[Xiaohui et al. 2011] R. Xiaohui, C. Wanji, and W. Zhen, "A new zig-zag theory and C^0 plate bending element for composite and sandwich plates", *Arch. Appl. Mech.* **81**:2 (2011), 185–197.

[Yi et al. 2015] S. Yi, L. Xu, G. Cheng, and Y. Cai, "FEM formulation of homogenization method for effective properties of periodic heterogeneous beam and size effect of basic cell in thickness direction", *Comput. Struct.* **156** (2015), 1–11.

[Yu 2005] W. Yu, "Mathematical construction of a Reissner–Mindlin plate theory for composite laminates", *Int. J. Solids Struct.* **42**:26 (2005), 6680–6699.

[Yu 2012] W. Yu, "An exact solution for micromechanical analysis of periodically layered composites", *Mech. Res. Commun.* **46** (2012), 71–75.

[Yu and Hodges 2004a] W. Yu and D. H. Hodges, "A geometrically nonlinear shear deformation theory for composite shells", *J. Appl. Mech.* **71**:1 (2004), 1–9.

[Yu and Hodges 2004b] W. Yu and D. H. Hodges, "Elasticity solutions versus asymptotic sectional analysis of homogeneous, isotropic, prismatic beams", *J. Appl. Mech.* **71**:1 (2004), 15–23.

[Yu and Tang 2007] W. Yu and T. Tang, "Variational asymptotic method for unit cell homogenization of periodically heterogeneous materials", *Int. J. Solids Structures* **44**:11-12 (2007), 3738–3755.

[Yu et al. 2002] W. Yu, D. H. Hodges, and V. V. Volovoi, "Asymptotic generalization of Reissner–Mindlin theory: accurate three-dimensional recovery for composite shells", *Comput. Methods Appl. Mech. Eng.* **191**:44 (2002), 5087–5109.

[Yu et al. 2012] W. Yu, D. H. Hodges, and J. C. Ho, "Variational asymptotic beam sectional analysis—an updated version", *Int. J. Eng. Sci.* **59** (2012), 40–64.

[Zhang and Oskay 2016] S. Zhang and C. Oskay, "Reduced order variational multiscale enrichment method for elasto-viscoplastic problems", *Comput. Methods Appl. Mech. Engrg.* **300** (2016), 199–224.

[Zhang and Yu 2014] L. Zhang and W. Yu, "A micromechanics approach to homogenizing elasto-viscoplastic heterogeneous materials", *Int. J. Solids Struct.* **51**:23–24 (2014), 3878–3888.

WENBIN YU: wenbinyu@purdue.edu
Purdue University, 704 W Stadium Ave., West Lafayette, IN 47907, United States

■msp

MODELING AND EXPERIMENTATION OF A VISCOELASTIC MICROVIBRATION DAMPER BASED ON A CHAIN NETWORK MODEL

CHAO XU, ZHAO-DONG XU, TENG GE AND YA-XIN LIAO

Viscoelastic (VE) dampers are widely used to attenuate structural vibration. Studies have mainly focused on the employment of VE dampers for reducing structural vibration in normal conditions, and only a few studies have considered the microvibration condition. In this paper, theoretical and experimental studies on the VE microvibration damper are conducted. First, the damping mechanism of the VE microvibration damper is analyzed from microperspectives and a mathematical model based on the chain network model is proposed. The contributions of cross-link and free-chain network chains to the damping characteristics of VE material are considered in this model. Second, an experimental study of the VE microvibration damper is conducted to verify the proposed model and to reveal the dynamic properties of the VE microvibration damper. The experimental results show that the dynamic properties of VE material are influenced by excitation frequency and insignificantly affected by displacement amplitude, and the VE material has good energy dissipation capacity. The proposed model is verified by comparing the experimental data and the numerical results. The results indicate that the proposed model can accurately describe the dynamic properties of the VE microvibration damper at different frequencies.

1. Introduction

Viscoelastic (VE) dampers are among the earliest types of passive control devices that have been successfully utilized to reduce the structural dynamic responses induced by types of vibration excitations, including earthquakes, wind, mechanical vibrations, human activity, etc. Owing to their advantages of simple construction, easy manufacturing process, low cost and excellent energy dissipation capacity, VE dampers have been widely used as vibration control devices in the fields of civil buildings, bridges, spacecraft and machinery by researchers and engineers in recent decades [Soong and Spencer 2002; Webster and Semke 2005; Rao 2003; Marko et al. 2006; Rashid and Nicolescu 2008].

Extensive theoretical and experimental investigations have been conducted to study the properties of VE dampers and the effects of VE dampers on structural dynamic responses. Bergman and Hanson [1993] tested the dynamic properties of VE dampers with different VE materials at real earthquake excitations. Min et al. [2004] experimentally investigated the mechanical properties of VE dampers and dynamic characteristics of a full-scale model structure with VE dampers. Xu et al. [2014] fabricated and experimentally studied a new multidimensional high-damping earthquake isolation device with a VE core bearing and several VE dampers. All investigations have shown that VE dampers have high energy dissipation capacity and their dynamic properties are influenced by excitation frequency, displacement and temperature. Thus, how to describe the dynamic properties of VE dampers at different frequencies,

temperatures and amplitudes is an important issue. Papoulia and Kelly [1997] employed the fractional method and additive stress decomposition to describe viscoelastic response of damping rubber materials. Park [2001] investigated the standard mathematical model and determined that it can be efficiently used. Lewandowski and Pawlak [2011] employed the fractional Kelvin model and the fractional Maxwell model to describe the behavior of a VE damping structure. Xu et al. [2011] proposed the equivalent standard solid model, which can reflect the effects of ambient temperature and excitation frequency on VE dampers simultaneously. The mathematical models of VE dampers presented in the previous studies can describe the dynamic behavior of VE dampers in normal conditions. Tan and Ko [2004] designed a beam-column connection incorporated with VE dampers to suppress the vertical vibrations of long-span beam structures induced by human activity or machinery and developed an analytical method to predict structural behavior with the designed VE device. Moliner et al. [2012] adopted VE dampers to reduce the resonant vibrations of simply supported high-speed railway bridges and analyzed the reduction effect of VE dampers numerically. Saidi et al. [2011] proposed an innovative VE damper to reduce floor vibrations caused by human activity. Previous studies have indicated that VE dampers can effectively reduce the structural responses in normal conditions.

However, it can be found from the previous studies that the VE dampers are mainly used and investigated in the normal vibration conditions excited by earthquakes, human activity, etc. The vibration amplitudes in these cases are larger than the microvibration displacements that will be studied in this paper. Studies on the dynamic properties and damping effects of VE dampers under microvibration conditions are rare and have not been reported. Microvibration is defined as the low-level mechanical vibration created by working machinery, environmental change, etc. [Wacker et al. 2005; Zhang et al. 2011]. Microvibration downgrades the precision and lifespan of equipment and the quality of products. Therefore, suppressing microvibration of high-technology instruments and manufacturing facilities with severe environmental performance requirements has drawn increasing interest from scientists and engineers since the rapid development of technologies such as the production of semiconductors, optical microscopes and laser research systems. Several devices and methods including passive control, active control, active-passive hybrid control and semiactive control systems are improved to protect high-precision payloads from the effects of microvibration [Liu et al. 2014; 2015]. However, how to control structural microvibration remains a crucial issue and needs to be further investigated. Owing to the excellent performance of VE dampers in normal conditions, employing the VE microvibration damper to reduce structural microvibration is a good prospective application.

In order to promote application of VE microvibration dampers, the damping mechanism, mathematical model and mechanical properties of the VE microvibration damper, which may be different from those under normal vibration amplitude, should be investigated. The micro-macro approach to investigate or model material properties is currently a hot topic. Li et al. [2012] proposed a predictive multiscale computational framework to study the viscoelastic properties of polymeric materials. In their study, the scale from nano to meso was bridged by a coarse-grained model, whereas the scale from micro to macro was bridged by a developed continuum constitutive law. Tang et al. [2012] presented a two-scale theory for the nonlinear viscoelasticity of elastomeric materials and used this theory to describe the physical phenomena of materials from microperspectives. Tomita et al. [2006] developed a computational model to represent the behavior of carbon-black-filled rubber by using the homogenization method, which can consider the changes of the chain entanglement. Miehe and Göktepe [2005] proposed a new constitutive

framework of finite viscoelasticity for rubber-like materials by introducing two key microkinematics associated with the free-chain motion and its network constraints. The aforementioned studies considered the effects of material microstructures on the mechanical properties of VE materials and implied that the macromechanical properties of VE materials depend on the material microstructures. Nevertheless, the aforementioned investigations mainly focused on the material static mechanical properties and are complex for engineers to understand and use. Thus, investigating the connection of the macroscopic dynamic properties of materials with material microstructures is important.

Consequently, in this study, the damping mechanism of VE microvibration dampers is analyzed from microperspectives. A mathematical model based on the chain network model of VE material is proposed to describe the dynamic properties of VE microvibration dampers under microvibration excitations. This model can reflect the effects of cross-link and free-chain network chains on the dynamic behavior of VE material, and the model parameters have clear physical meaning. Tests on VE microvibration dampers are carried out under different excitation amplitudes and frequencies to reveal the dynamic behavior of VE microvibration dampers and to verify the proposed model. The experimental results show that the VE microvibration damper has good energy dissipation capacity and the dynamic properties of VE microvibration dampers are significantly influenced by excitation frequency under microvibration conditions. Comparison between the experimental data and the numerical results indicates that the proposed model can accurately describe the dynamic properties of VE microvibration damper.

2. Damping mechanism and mathematical model of the VE microvibration damper

An accurate mathematical model is always essential to describe the dynamic characteristics of the VE microvibration damper and to analyze the structural dynamic responses of structures with VE microvibration dampers. In this section, the damping mechanism of the VE damper is first analyzed from microperspectives and a mathematical model based on the chain network model of VE material is then proposed.

2.1. *Damping mechanism of the VE microvibration damper.* The macroscopic mechanical behavior of materials mainly depends on the material microstructure characteristics, including the quantity, properties and spatial distribution of the microstructures [Ward and Hadley 1993; Gabriel and Münstedt 2002]. For VE material, the elastic properties, viscoelastic properties and other properties are dependent on the properties of the molecular chain structures within the VE material. The present work focuses on the dynamic viscoelastic properties of VE material and their relationship with material microstructures.

The deformations of elastomeric materials can be decomposed into two parts, namely, the deformations of cross-link network chains and the deformations of free-chain network chains, when static viscoelastic properties of VE solids are investigated [Tang et al. 2012; Miehe and Göktepe 2005]. Analogous to this method, VE material microstructure can be abstracted as molecular chain structure, as shown in Figure 1. Two different molecular chain structures can be observed: one is the chain network caused by the cross-linking effect, and the other is the superimposed free chains that exist in VE material. The former is mainly considered to contribute to the elastic properties of the VE material, which can transmit the stress induced by material deformation. The latter contributes to the viscous properties that will dissipate energy. The molecular chain structures of polymer materials are complex, and the real structure of the materials is difficult to describe by using an accurate mathematical model. The hyperelastic properties of
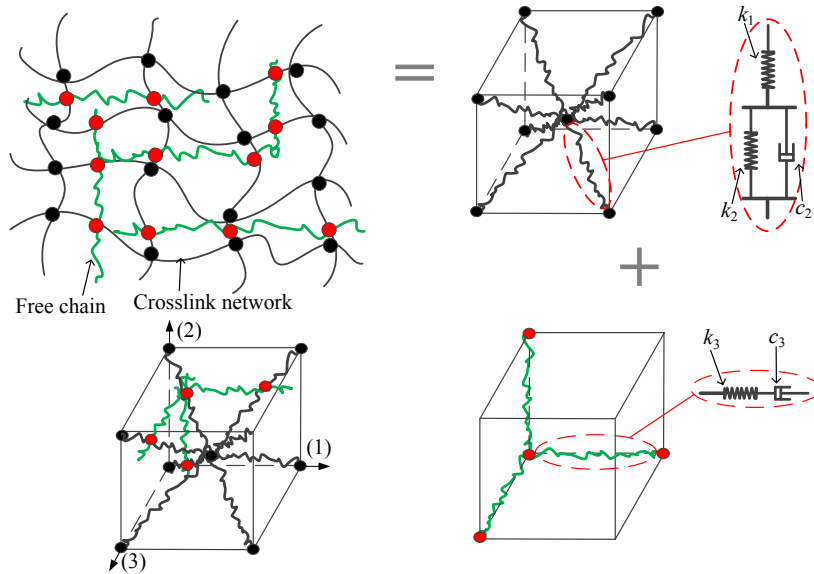
Figure 1. Microstructure and the model of VE material. Top left: microstructure. Top right: eight-chain network model. Bottom left: chain structure model. Bottom right: three-chain network model.

rubber-like materials have been investigated in the past decades, and several mathematical models based on molecular chain structures have been proposed. Among these mathematical models are the Gaussian chain network model and the non-Gaussian chain network model based on the statistical properties of molecular chains [Marckmann and Verron 2006]. The properties of the two molecular chain structures are detailed and analyzed below.

Chain network structure of VE material. Molecular chains can form a chain network by entanglement or cross-linking effects [Svaneborg et al. 2004]. This part of molecular chains can transmit stress under an external load and can restore to the original state by thermal motion when the external excitations unload. The VE material will present elastic properties and restores its original shape in the macroscopic view. Additionally, the main chain motions can also be impeded by the adjacent molecular chains and molecular chain segments. In other words, this part of molecular chains of VE material can also exhibit viscous properties. Thus, molecular chains of this part contribute not only to the elastic property but also the viscous property of VE material. However, the contribution to the viscous property is far less than the contribution to the elastic property. Hence, the elastic property of the chain network is mainly considered in this part.

The eight-chain network model is employed to study the chain network structure, as shown in Figure 1, top right. The eight molecular chains link at the cube center and extend to the eight corners. The structure has a strong symmetry, and the cross-linking point is always at the center location during deformation. Hence, each molecular chain has the same elongation ratio during deformation. The eight-chain network model can better depict the superelastic properties of VE materials in several deformation patterns. Therefore, the eight-chain network model is employed in this part.

As mentioned previously, a single molecular chain of the chain network represents strong elastic properties and weak viscous properties. In short, it exhibits viscoelastic properties. At present, the

models that can describe the viscoelastic properties mainly including the Maxwell model, Kelvin model, standard linear solid model, etc. The linear viscoelastic solid model is employed to characterize the mechanical properties of a single molecular chain in the eight-chain network model, as shown in Figure 1, top right. This model can represent the asymptotic and transient elastic responses of the material, which is in accordance with the performance of the molecular chains studied in the eight-chain network model.

According to the standard linear solid model shown in Figure 1, top right, the force-displacement relationship of a single molecular chain in the model can be directly written as

$$F_{s1} = \frac{k_1\left(k_2 + c_2\frac{d}{dt}\right)}{(k_1 + k_2) + c_2\frac{d}{dt}}\Delta x. \tag{1}$$

We can assume that the deformation is a periodic dynamic variable to simplify the formula and compare it with test data that are in frequency domain. Then let $\frac{d}{dt} = j\omega$ and substitute it into (1), which results in

$$F_{s1} = \frac{k_1(k_2 + j\omega c_2)}{(k_1 + k_2) + j\omega c_2}\Delta x = E_{s1}\Delta x, \tag{2}$$

where k_1, k_2 and c_2 are the elastic and viscous coefficients of the chain and are determined by the test data, Δx is the deformation of the single chain, F_{s1} is the force of the single chain corresponding to the deformation and ω is the angular frequency of the alternating stress (or strain) applied on VE material.

According to the polymer thermodynamic theory, the conformations of molecular chain structure are in random spatial distribution due to the thermal motion of polymer chains. In other words, the length distributions and end-to-end distances of the chains cannot be accurately represented. Therefore, Gaussian chains and non-Gaussian chains are proposed based on the statistical properties of the molecular chain when analyzing the hyperelastic properties of rubber-like materials. In this study, the end-to-end distance of the molecular chain is considered as a parameter fitted by the test data to simply the formula derivation.

By introducing the concept of end-to-end distance of a molecular chain, the force-displacement relationship of a single molecular chain can be rewritten as

$$F_{s1} = \frac{k_1(k_2 + j\omega c_2)}{(k_1 + k_2) + j\omega c_2}(r - r_{0s}) = E_{s1}(r - r_{0s}), \tag{3}$$

where r and r_{0s} denote the end-to-end distances of the molecule chain after and before the deformation, respectively. Thus, the strain energy of a single chain during deformation can be determined by

$$\varphi_{s1} = F_{s1}(r - r_{0s}) = \tfrac{1}{2}E_{s1}(r - r_{0s})^2. \tag{4}$$

For the eight-chain network model, the cube volume before and after the deformation can be considered the same in the microvibration condition. Accordingly, the cube volume shown in Figure 1, top right, can be written as $V = \frac{8}{9}\sqrt{3}r_{0s}^3$ and the mechanical energy of a single chain per volume can be written as

$$\phi_{s1} = \frac{\varphi_{s1}}{V} = \frac{3\sqrt{3}}{2r_{0s}^3} \cdot \tfrac{1}{8}E_{s1} \cdot (r - r_{0s})^2. \tag{5}$$

Free chain structure of VE material. In addition to the chain network structure, there is a part of chains of VE material that do not involve the formation of the network structure. This part of chains is called the free chain, which includes the superimposed free chains and the side chains of the main molecular

chains. This portion of the molecule chains represents viscous properties with weak elastic properties since these chains lack constraint from the other chains.

The three-chain network model is employed to describe the effect of this part of molecular chains on characteristics of VE material. The three-chain network model is also based on statistical properties of molecular chains. The three chains linked at one corner of the cube extend to three mutually orthogonal edges, and affine deformation occurs during the deformation of VE material. This model can also represent the superelastic properties of VE material at certain deformation patterns. Moreover, we adopt the three-chain network model since it is convenient to connect with the above-mentioned eight-chain network model to establish the final mathematical model of the VE microvibration damper, as shown in Figure 1, bottom left.

The Maxwell model is adopted to represent the mechanical properties of a single molecular chain of the three-chain network model. The Maxwell model can capture well the rheological properties of the material, which is in accordance with the properties of the molecular chains in the three-chain network model, as shown in Figure 1, bottom right. The force-displacement relationship of a single molecular chain can be directly written as

$$F_{c1} = \frac{k_3 \cdot j\omega c_3}{k_3 + j\omega c_3}(r - r_{0c}) = E_{c1}(r - r_{0c}),$$ (6)

where k_3 and c_3 are the elastic and viscous coefficients, respectively, of the chain and are determined by the test data, ω is the angular frequency of the alternating stress (or strain) and r and r_{0c} denote the end-to-end distances of chains after and before the deformation, respectively. Hence, the strain energy of a single chain during deformation can be determined by

$$\varphi_{c1} = F_{c1}(r - r_{0c}) = \tfrac{1}{2}E_{c1}(r - r_{0c})^2.$$ (7)

For this three-chain network model, the cube volume, as shown in Figure 1, bottom right, is $V = r_{0c}^3$, the deformation of the three chains of the model is not the same and the average mechanical energy of a single chain of the model is $\bar{\varphi}_{c1} = \tfrac{1}{2} \cdot \tfrac{1}{3} \sum_{i=1}^{3} E_{c1} \cdot (r_i - r_{0c})^2$; therefore, the mechanical energy of a single chain per volume can be written as

$$\phi_{c1} = \frac{\bar{\varphi}_{c1}}{V} = \frac{1}{2r_{0c}^3} \cdot \frac{1}{3} \sum_{i=1}^{3} E_{c1} \cdot (r_i - r_{0c})^2.$$ (8)

2.2. Chain structure model of the VE microvibration damper.
The preceding discussion indicated that the mechanical properties of VE material or dampers are determined by the two types of microscopic chain structures, namely, the network chains and the free chains. Based on the mechanical properties of the microscopic chain structure and the multiscale analysis method, a mathematical model based on the material chain network model is proposed to describe the dynamic characteristics of the VE microvibration damper.

The total energy of the VE material per volume can be considered the sum of the energy of the two parts of chain structures and can be expressed as

$$\phi = n_{s1}\phi_{s1} + n_{c1}\phi_{c1},$$ (9)

where n_{s1} and n_{c1} are the numbers of the network chains and free chains per volume, respectively. Then the true stress can be expressed as

$$\sigma_i = \lambda_i \frac{\partial \phi}{\partial \lambda_i} \quad (i = 1, 2, 3), \tag{10}$$

where λ_i is the stretch ratio of the material in the i-th direction ($i = 1, 2, 3$), as shown in Figure 1, bottom left.

The deformations of the molecular chains of the material are assumed to comply with the law of affine deformation. Therefore, the macroscopic deformations of material and the deformations of molecular chain conformations can be connected by

$$\boldsymbol{r} = \boldsymbol{F} \cdot \boldsymbol{r}_0, \tag{11}$$

where $\boldsymbol{F}$ is the deformation gradient corresponding to the deformation pattern. In this study, the simple deformation pattern, uniaxial deformation, is considered. For the uniaxial deformation (in the 1-axis), the deformation gradient can be expressed as

$$\boldsymbol{F} = \lambda_1 \boldsymbol{e}_1 \otimes \boldsymbol{e}_1 + \lambda_1^{-1/2} \boldsymbol{e}_2 \otimes \boldsymbol{e}_2 + \lambda_1^{-1/2} \boldsymbol{e}_3 \otimes \boldsymbol{e}_3. \tag{12}$$

So the following expression can be derived with the combination of (11) and (12):

$$|r - r_0|^2 = [(\lambda_1 - 1)^2 + (\lambda_2 - 1)^2 + (\lambda_3 - 1)^2] r_0^2. \tag{13}$$

Therefore, the true stress-strain formula can be gained from (10) as

$$\sigma_i = \lambda_i \frac{n_{s1} 3\sqrt{3}}{8 r_{0s}} E_{s1} (\lambda_i - 1) + \lambda_i \frac{n_{c1}}{3 r_{0c}} E_{c1} (\lambda_i - 1) \quad (i = 1, 2, 3). \tag{14}$$

Assuming that the alternating strain $\varepsilon_1 = \varepsilon_0 \sin(\omega t)$ is along the 1-axis, (14) can be rewritten as

$$\begin{aligned}
\sigma_1 &= \lambda_1 \frac{n_{s1} 3\sqrt{3}}{8 r_{0s}} E_{s1} (\lambda_1 - 1) + \lambda_1 \frac{n_{c1}}{3 r_{0c}} E_{c1} (\lambda_1 - 1) \\
&= \varepsilon_1 \frac{n_{s1} 3\sqrt{3}}{8 r_{0s}} E_{s1} (\varepsilon_1 + 1) + \varepsilon_1 \frac{n_{c1}}{3 r_{0c}} E_{c1} (\varepsilon_1 + 1) \\
&= \varepsilon_1^2 \left(\frac{n_{s1} 3\sqrt{3}}{8 r_{0s}} E_{s1} + \frac{n_{c1}}{3 r_{0c}} E_{c1} \right) + \varepsilon_1 \left(\frac{n_{s1} 3\sqrt{3}}{8 r_{0s}} E_{s1} + \frac{n_{c1}}{3 r_{0c}} E_{c1} \right).
\end{aligned} \tag{15}$$

In this study, the dynamic properties of VE microvibration dampers are only considered in the microvibration condition, and the strain amplitude is small during the deformation. Hence, the square of the strain ε_1^2 is small and can be ignored without affecting the accuracy of the formula. Equation (15) can be transformed into

$$\sigma_1 = \varepsilon_1 \left(\frac{n_{s1} 3\sqrt{3}}{8 r_{0s}} E_{s1} + \frac{n_{c1}}{3 r_{0c}} E_{c1} \right) = E \varepsilon_1. \tag{16}$$

The VE material always undergoes shear deformation when the VE damper works under external vibration excitation. The relationship between shear stress and shear strain is expressed as

$$\tau = G\gamma, \tag{17}$$

where G is the shear modulus of the VE material, τ is the shear stress and γ is the shear strain. The relationship between shear modulus G and elasticity modulus E can be expressed as $G = E/2(1 + \mu)$, where μ is the Poisson ratio of the VE material and is approximately 0.5 for the incompressible materials, such as rubber-like materials. Hence, the shear modulus can be gained from elasticity modulus E. The shear modulus G has a complex form and can be decomposed into two parts: imaginary part $\text{Im}\, G$ and real part $\text{Re}\, G$. The real part denotes the storage modulus of VE material, and the ratio of the imaginary part and real part is defined as the loss factor of VE material. The complex modulus G can be written as

$$
\begin{aligned}
G &= \tfrac{1}{3}E = \frac{1}{3}\left(\frac{n_{s1}3\sqrt{3}}{8r_{0s}}E_{s1} + \frac{n_{c1}}{3r_{0c}}E_{c1}\right) \\
&= \frac{n_{s1}\sqrt{3}}{8r_{0s}}\left(\frac{k_1^2 k_2 + k_1 k_2^2 + k_1\omega^2 c_2^2}{(k_1+k_2)^2 + \omega^2 c_2^2} + j\frac{k_1^2\omega c_2}{(k_1+k_2)^2 + \omega^2 c_2^2}\right) + \frac{n_{c1}}{9r_{0c}}\left(\frac{k_3\omega^2 c_3^2}{k_3^2 + \omega^2 c_3^2} + j\frac{k_3^2\omega c_3}{k_3^2 + \omega^2 c_3^2}\right). \quad (18)
\end{aligned}
$$

Hence, the storage modulus and loss factor can be expressed as

$$
\begin{aligned}
G_1 &= \text{Re}\, G = \frac{n_{s1}\sqrt{3}}{8r_{0s}}\left(\frac{k_1^2 k_2 + k_1 k_2^2 + k_1\omega^2 c_2^2}{(k_1+k_2)^2 + \omega^2 c_2^2}\right) + \frac{n_{c1}}{9r_{0c}}\left(\frac{k_3\omega^2 c_3^2}{k_3^2 + \omega^2 c_3^2}\right), \\
G_2 &= \text{Im}\, G = \frac{n_{s1}\sqrt{3}}{8r_{0s}}\left(\frac{k_1^2\omega c_2}{(k_1+k_2)^2 + \omega^2 c_2^2}\right) + \frac{n_{c1}}{9r_{0c}}\left(\frac{k_3^2\omega c_3}{k_3^2 + \omega^2 c_3^2}\right), \\
\eta &= \frac{G_2}{G_1}.
\end{aligned}
\qquad (19)
$$

Equation (19) is the proposed model, which can describe the storage modulus and loss factor of the VE microvibration damper. The parameters of this model have been interpreted in the previous parts. The proposed model can describe the dynamic properties of VE microvibration dampers from micro-perspectives, and the model parameters have clearly physical meanings, which are related to the material microstructures. Additionally, the effect of displacement amplitude on properties of VE microvibration dampers is not considered under microvibration from the model-establishing process.

3. Experimental study and model verification of the VE microvibration damper

In order to verify the proposed model and investigate the dynamic properties of VE microvibration dampers, tests on VE microvibration dampers are carried out at different excitation frequencies and displacement amplitudes. The test results are analyzed and compared with the numerical results calculated by the proposed model in this section.
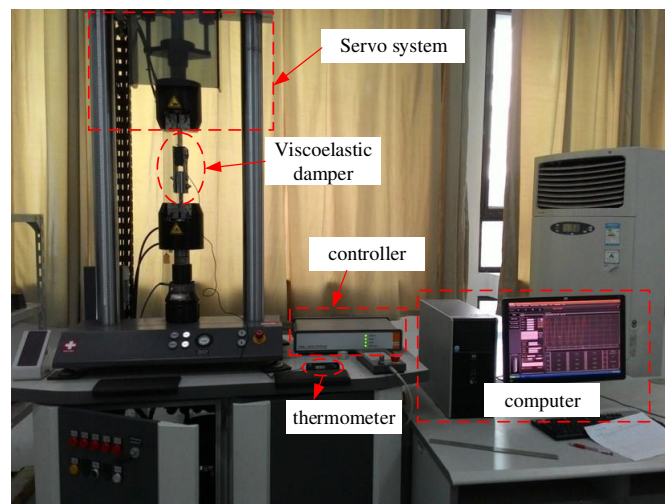
3.1. *Test procedure.* The VE microvibration damper tested in this paper is a kind of double-sandwich damper, as shown in Figure 2, which is manufactured by vulcanization bonding of two VE layers among three parallel steel plates. The VE layers undergo nearly pure shear deformation while the middle steel plate and the two lateral steel plates move in the opposite direction during the tests. Then, the VE material can dissipate the vibration energy by converting the energy into heat and dispersing it into air. The key dimension information of the tested VE microvibration damper is provided in Figure 2.
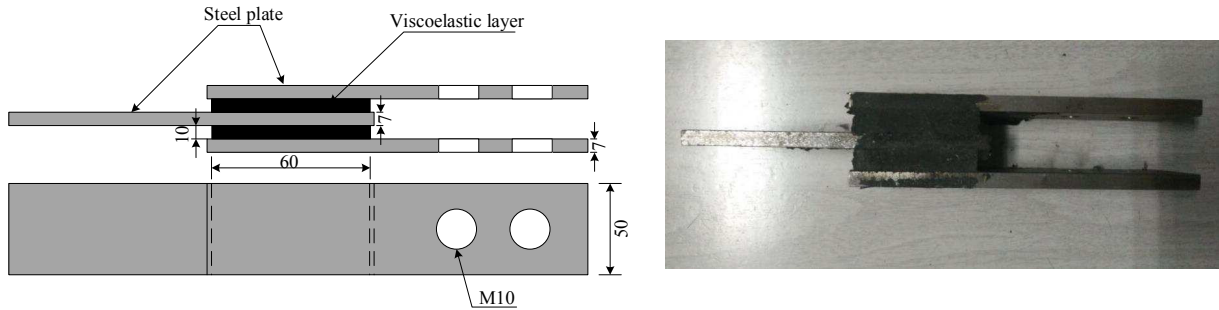
Figure 2. VE microvibration damper. Left: configuration schematic (mm units). Right: specimen photo.

The performance tests on the VE microvibration damper have been conducted in a 10 kN servo-hydraulic testing machine in the Center of Mechanics Experiment, Nanjing University of Science and Technology, as shown in Figure 3. The test machine is manufactured by the Walter+Bai Testing Machines Corporation and is sufficiently accurate to test the VE microvibration damper at microvibration amplitudes. During the tests, the machine is controlled through the displacement control mode. The tests are conducted under the ambient temperature of 12 °C.

In each condition, the test on the VE damper is carried out with serial cycles of sinusoidal excitation with fixed displacement amplitude and excitation frequency. The displacement excitation and loading data are recorded by the computer and the control system. The cycle number of the excitation is selected to obtain steady hysteresis curves and would vary at different conditions. The excitation displacements and frequencies are selected with comprehensive consideration of the equipment capacity and the working conditions of the VE microvibration damper. The loading conditions are given in the first two columns of Table 1. Enough cycles were used to gain the stable single force-displacement hysteresis curve data.

Figure 3. Performance tests on the VE microvibration damper.

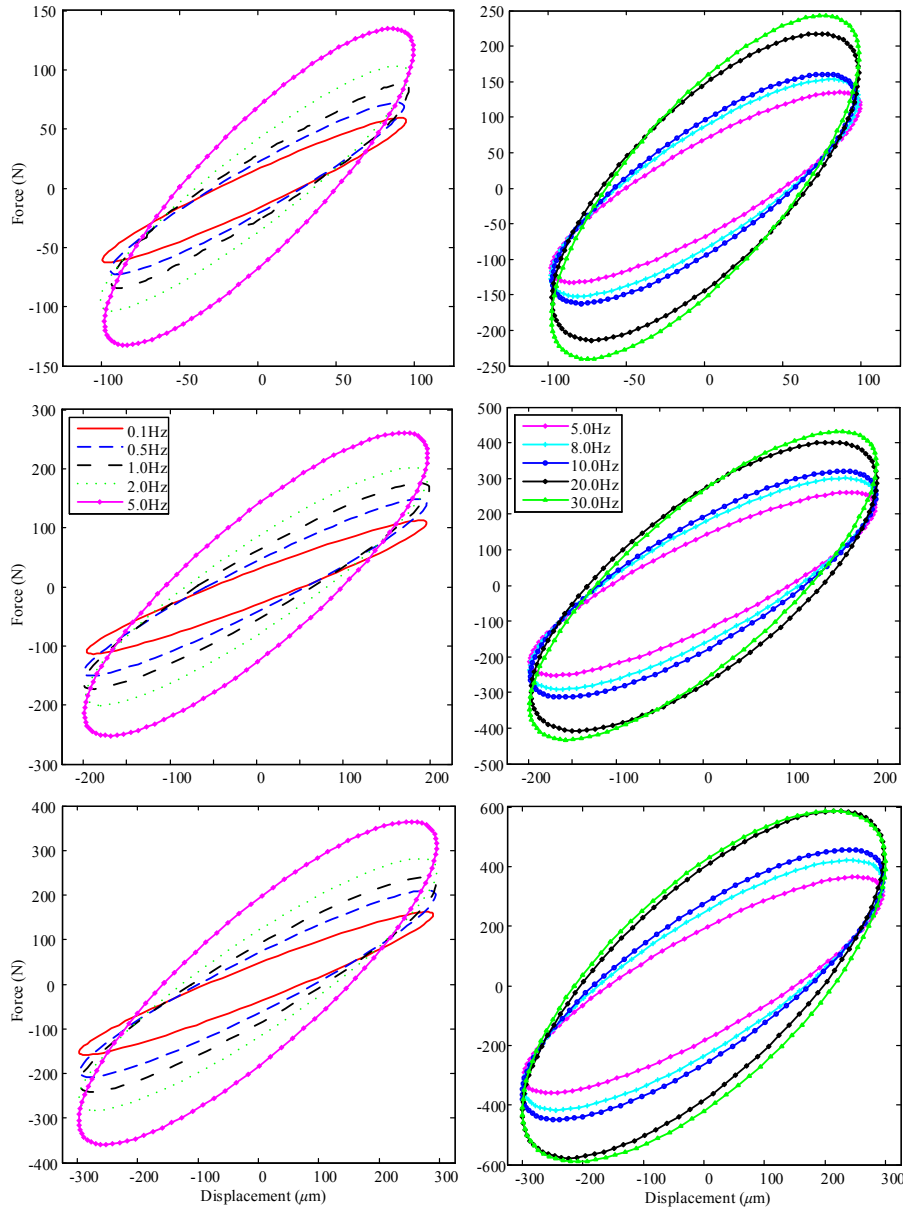| Frequency (Hz)	Displacement amplitude (μm)	Storage modulus G_1 (MPa)	Loss factor η	Equivalent stiffness K_e (KN/m)	Equivalent damping C_e (N·s/m)	Energy dissipation E_d (N·m)
	100	1.0000	0.2667	600.00	254647.91	0.0050
	150	0.9778	0.2727	586.67	254647.91	0.0113
0.1	200	0.9417	0.2655	565.00	238732.42	0.0188
	250	0.8733	0.2672	524.00	222816.92	0.0275
	300	0.8667	0.2692	520.00	222816.92	0.0396
	100	1.1833	0.3099	710.00	70028.18	0.0069
	150	1.1889	0.2897	713.33	65784.04	0.0146
0.5	200	1.2333	0.2973	740.00	70028.18	0.0276
	250	1.0733	0.3478	644.00	71301.42	0.0440
	300	1.1167	0.3383	670.00	72150.24	0.0641
	100	1.3500	0.3333	810.00	42971.84	0.0085
	150	1.4222	0.3281	853.33	44563.38	0.0198
1.0	200	1.3750	0.3636	825.00	47746.48	0.0377
	250	1.2600	0.3915	756.00	47109.86	0.0581
	300	1.2556	0.3938	753.33	47215.97	0.0839
	100	1.5667	0.4149	940.00	31035.21	0.0123
	150	1.5333	0.4420	920.00	32361.51	0.0287
2.0	200	1.5333	0.4457	920.00	32626.76	0.0515
	250	1.4200	0.4695	852.00	31830.99	0.0785
	300	1.4222	0.4609	853.33	31300.47	0.1112
	100	1.8667	0.6071	1120.00	21645.07	0.0214
	150	1.8667	0.5952	1120.00	21220.66	0.0471
5.0	200	1.8167	0.6055	1090.00	21008.45	0.0829
	250	1.7200	0.6008	1032.00	19735.21	0.1217
	300	1.7556	0.5981	1053.33	20053.52	0.1781
	100	2.0833	0.6880	1250.00	17109.16	0.0270
	150	2.1667	0.6462	1300.00	16711.27	0.0594
8.0	200	1.9833	0.7101	1190.00	16810.74	0.1062
	250	1.9733	0.6858	1184.00	16154.23	0.1594
	300	1.9333	0.6954	1160.00	16048.12	0.2281
	100	2.1333	0.7422	1280.00	15119.72	0.0298
	150	2.1667	0.7333	1300.00	15172.77	0.0674
10.0	200	2.0917	0.7570	1255.00	15119.72	0.1194
	250	2.0800	0.7244	1248.00	14387.61	0.1775
	300	2.0667	0.7339	1240.00	14483.10	0.2573
	100	2.6833	0.9068	1610.00	11618.31	0.0459
	150	2.6444	0.9034	1586.67	11406.10	0.1013
20.0	200	2.5917	0.8778	1555.00	10862.33	0.1715
	250	2.5267	0.8760	1516.00	10567.89	0.2608
	300	2.4389	0.9066	1463.33	10557.28	0.3751
	100	2.9333	0.9125	1760.00	8063.85	0.0478
	150	2.9222	0.9137	1753.33	7568.70	0.1008
30.0	200	2.8983	0.9185	1680.00	7055.87	0.1671
	250	2.9012	0.9235	1579.00	7108.92	0.2631
	300	2.9120	0.9320	1530.67	7427.23	0.3958

Table 1. Characteristic parameters of the VE microvibration damper.
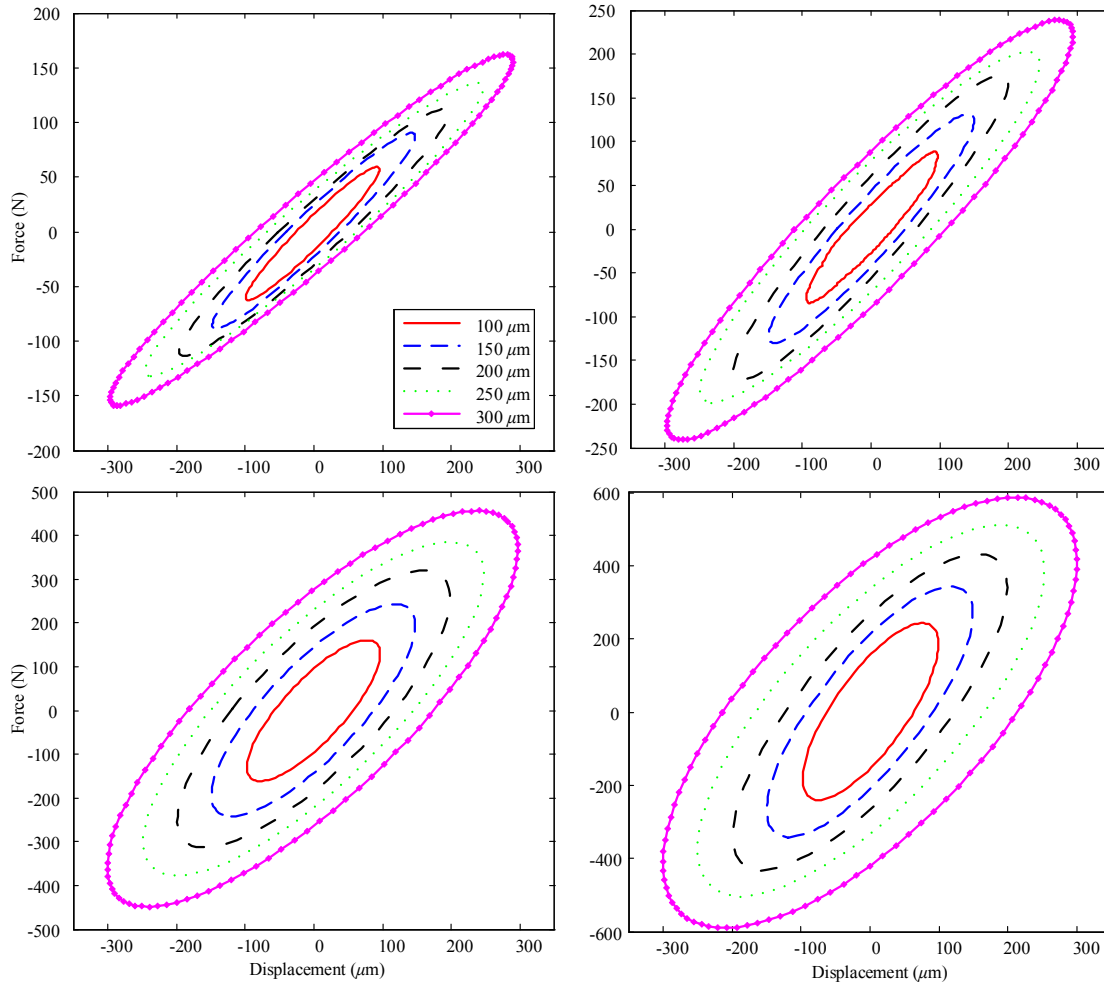
Figure 4. The hysteresis curves at the same frequency with different displacement amplitudes for $f = 0.1$ Hz (top left), 1.0 Hz (top right), 10.0 Hz (bottom left) and 30.0 Hz (bottom right).

3.2. *Experimental results and analysis.* Force-displacement hysteresis curves of the VE microvibration damper can be plotted with the data recorded at different excitation frequencies and amplitudes. A single steady cycle force-displacement hysteresis curve is selected from raw force-displacement hysteresis curves for each case, as shown in Figures 4 and 5, to distinguish force-displacement hysteresis curves clearly and to determine the VE microvibration damper characteristics at different conditions. It can be seen from Figures 4 and 5 that the VE microvibration damper has good energy dissipation capacity, and the energy dissipation capacity is influenced by the excitation conditions.

Figure 4 shows the force-displacement hysteresis curves under different excitation amplitudes at the excitation frequencies of 0.1 Hz, 1.0 Hz, 10.0 Hz and 30.0 Hz, and Figure 5 shows the force-displacement hysteresis curves under different excitation frequencies at the excitation amplitudes of 100 μm, 150 μm, 200 μm and 300 μm. It can be clearly seen from Figures 4 and 5 that the slope and width of the

Figure 5. The hysteresis curves at the same displacement amplitude with different frequencies for $d = 100\,\mu\text{m}$ (top), $200\,\mu\text{m}$ (middle) and $300\,\mu\text{m}$ (bottom).

hysteresis curves increase obviously with increasing excitation frequency, whereas they slightly vary with the excitation amplitude. The area of the hysteresis curves increases with increasing frequency and amplitude. The slope, the width and the area of the hysteresis curves are considered to be correlated with the stiffness and the energy dissipation capacity of the VE microvibration damper, which are affected by excitation frequency and amplitude. The effects of excitation conditions on VE microvibration damper characteristics will be discussed in detail in the following.
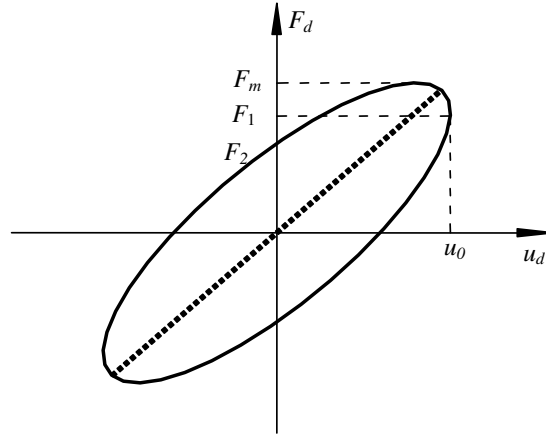
Figure 6. Force-displacement hysteresis curve.

The dynamic characteristics of the VE microvibration damper, including the storage modulus G_1, the loss factor η, the equivalent stiffness K_e, the equivalent damping C_e and the energy dissipation E_d, can be determined by force-displacement hysteresis curves. Figures 4 and 5 show that the force-displacement hysteresis curves are elliptical. This phenomenon can be illustrated by the following procedure, and the dynamic characteristics of the VE microvibration damper are obtained from the test data.

In the tests, the input displacement signal is sinusoidal excitation displacement $u_d = u_0 \sin \omega t$ (u_0 and ω are the amplitude and circular frequency of excitations, respectively). The relationship between the force and displacement of the VE damper under sinusoidal excitation can be expressed as

$$\left(\frac{F_d - K_d u_d}{\eta K_{d1} u_0}\right)^2 + \left(\frac{u_d}{u_0}\right)^2 = 1, \tag{20}$$

where F_d and u_d are the force and displacement of the VE damper, respectively, as shown in Figure 6. F_m and u_0 are the maximum force and maximum displacement of the damper, respectively. F_1 is the corresponding force at the maximum displacement u_0, and F_2 is the corresponding force at zero displacement and $F_2 = \eta K_{d1} u_0$. K_{d1} is the storage stiffness, and $K_{d1} = F_1/u_0$. In accordance with vibration mitigation theory of VE devices [Xu et al. 2011], the storage modulus G_1, the loss factor η and the energy dissipation E_d can be obtained by

$$G_1 = \frac{F_1 h_v}{n_v A_v u_0}, \tag{21}$$

$$\eta = \frac{F_2}{F_1}, \tag{22}$$

$$E_d = \frac{\pi n_v \eta G_1 A_v u_0^2}{h_v}, \tag{23}$$

where F_1 and F_2 can be gained from the force-displacement hysteresis curves, n_v is the number of VE layers and A_v and h_v are the shear area and thickness of each VE layer, respectively. A_v, h_v and n_v can be determined from the construction of the VE damper, as shown in Figure 2. Further, the equivalent

stiffness K_e and the equivalent damping C_e of the VE damper can be calculated by

$$K_e = \frac{n_v G_1 A_v}{h_v} = \frac{F_1}{u_0}, \tag{24}$$

$$C_e = \frac{n_v \eta G_1 A_v}{\omega h_v} = \frac{F_2}{\omega u_0}. \tag{25}$$

Then the storage modulus G_1, the loss factor η, the energy dissipation E_d, the equivalent stiffness K_e and the equivalent damping C_e of the VE damper in each test can be obtained through expressions (21)–(25). The detailed results are listed in Table 1, which indicates that the dynamic characteristics of the VE damper vary with excitation frequency and displacement amplitude. Therefore, these characteristics are affected by excitation frequency and displacement amplitude. The details are provided below.

Effect of excitation frequency. In order to vividly analyze the effect of excitation frequency on the dynamic characteristics of the VE microvibration damper, the storage modulus G_1, the loss factor η, the equivalent stiffness K_e, the equivalent damping C_e and the energy dissipation E_d of the VE microvibration damper under different frequencies at the fixed displacement are plotted in Figure 7.

With increasing frequency, the storage modulus G_1 and the loss factor η, which are the most important dynamic properties of the VE microvibration damper, rise as shown in Figure 7, top. The properties increase dramatically at low frequency range while slowly at high frequency range. Take the displacement amplitude of 250 μm for example; at the low frequency range, the storage modulus G_1 increases from 0.8733 MPa to 1.0733 MPa by 22.90% and 1.0733 MPa to 1.2600 MPa by 17.39% when the frequency increases from 0.1 Hz to 0.5 Hz and 0.5 Hz to 1.0 Hz, respectively. While at the high frequency range, the storage modulus G_1 increases from 2.0800 MPa to 2.5267 MPa by 21.48% and 2.5267 MPa to 2.9012 MPa by 14.82% when the frequency increases from 10 Hz to 20 Hz and 20 Hz to 30 Hz. The same phenomena can be observed for the loss factor η; at the low frequency range, it increases from 0.2672 to 0.3478 by 30.16% and 0.3478 to 0.3915 by 12.56% when the frequency increases from 0.1 Hz to 0.5 Hz and 0.5 Hz to 1.0 Hz. While at the high frequency range, it increases from 0.7244 to 0.8760 by 20.93% and 0.8760 to 0.9235 by 5.42% when the frequency increases from 10 Hz to 20 Hz and 20 Hz to 30 Hz.

The equivalent stiffness K_e and the equivalent damping C_e are also important properties of the VE microvibration damper and are directly utilized in the dynamic response analysis of VE damping structures. It can be clearly seen from Figure 7, middle, that the equivalent stiffness K_e and the equivalent damping C_e are significantly affected by excitation frequency, especially for the equivalent damping C_e, which sharply varies with excitation frequency. As shown in Figure 7, middle left, the equivalent stiffness K_e increases with the increase of frequency at the fixed displacement amplitude. The variation of the equivalent stiffness K_e is almost the same as that of the storage modulus G_1. Similarly, take the displacement amplitude of 250 μm for example; the equivalent stiffness K_e increases by 22.91%, 17.38%, 21.48% and 14.72% when the frequency increases from 0.1 Hz to 0.5 Hz, from 0.5 Hz to 1.0 Hz, from 10 Hz to 20 Hz and from 20 Hz to 30 Hz, respectively. Obviously, it can be seen that the change percentages are nearly the same as those of the storage modulus G_1. This similarity can be easily illustrated by using (24), which indicates that the equivalent stiffness is proportional to the storage modulus while other parameters are constant for a given VE damper. However, the equivalent damping C_e sharply decreases with increasing frequency, as shown in Figure 7, middle right. These variation laws of the equivalent damping with frequency can be explained by using (25). From (25), the equivalent damping
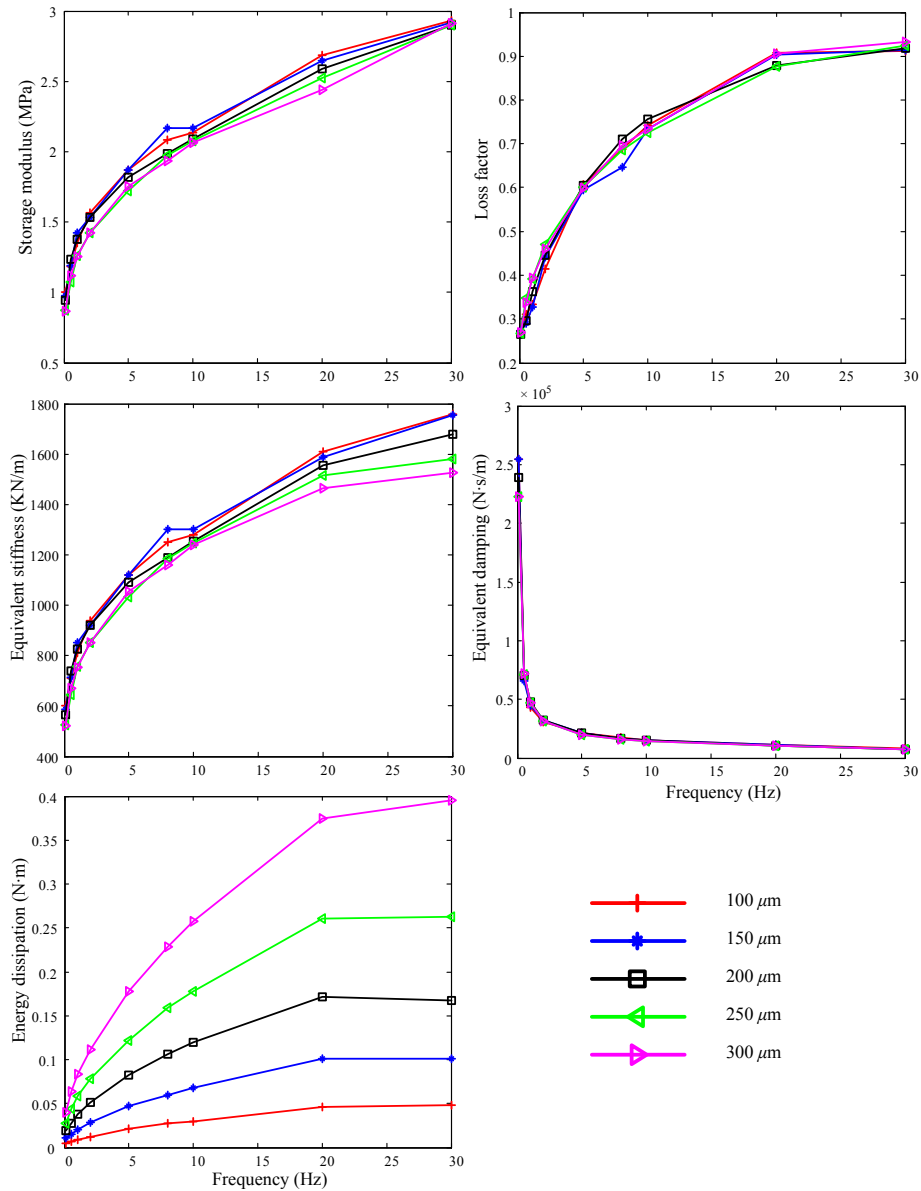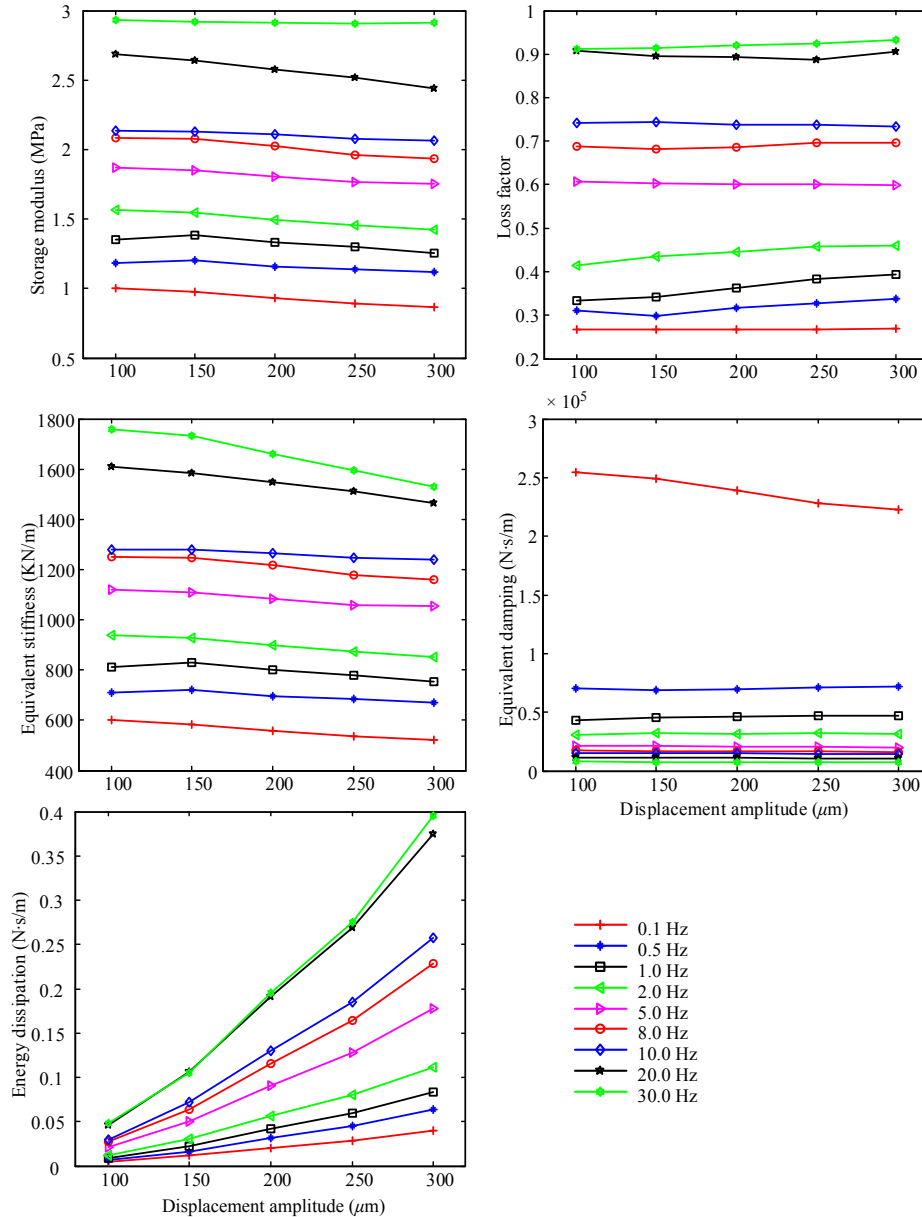
Figure 7. Dynamic parameters vary with frequency.

is proportional to ω^{-1} ($\omega = 2\pi f$), which means that the equivalent damping will decrease exponentially with increasing frequency.

The energy dissipation E_d, which is referred to as the energy dissipated by the VE microvibration damper at a single cycle during the test, is the direct index that represents the energy dissipation capacity of the VE microvibration damper. Figure 7, bottom, shows that the energy dissipation E_d rises with increasing frequency similar to the storage modulus G_1 and the loss factor η. At the low frequency range, the energy dissipation E_d increases rapidly, whereas it increases gently at the high frequency range.

Figure 8. Dynamic parameters vary with displacement amplitude.

Effect of displacement amplitude. Similarly, the effects of excitation displacement amplitude on the dynamic characteristics of the VE microvibration damper are also vividly analyzed by depicting the storage modulus G_1, the loss factor η, the equivalent stiffness K_e, the equivalent damping C_e and the energy dissipation E_d under different excitation amplitudes in Figure 8.

The characteristics of the VE microvibration damper, except for the energy dissipation E_d, slightly change with increasing excitation displacement amplitude. Figure 8, top left, shows that the storage

Frequency (Hz)	Experimental value		Model calculation		Errors	
	G_1 (MPa)	η	G_1 (MPa)	η	G_1	η
0.1	0.9417	0.2655	0.8603	0.2032	8.64%	23.45%
0.5	1.2333	0.2973	1.0550	0.2565	14.46%	13.70%
1.0	1.375	0.3636	1.1839	0.4112	13.90%	13.10%
2.0	1.5333	0.4457	1.3916	0.5256	10.11%	16.95%
5.0	1.8167	0.6055	1.9774	0.6597	8.85%	8.97%
8.0	1.9833	0.7101	2.1768	0.6747	9.76%	4.98%
10.0	2.0917	0.757	2.4172	0.6800	15.56%	10.16%
20.0	2.5917	0.8778	2.5203	0.8251	2.75%	6.00%
30.0	2.8983	0.9185	2.6226	1.0845	9.51%	18.08%

Table 2. Comparison between experimental and numerical results.

modulus G_1 slightly reduces with increasing displacement amplitude within the test frequency ranges while the loss factor η almost keeps constant with the increasing displacement amplitude, as shown in Figure 8, top right. The experimental data of frequency of 8 Hz are employed for the following analyses. The maximum changes are approximately 8.46% and 6.08% for the storage modulus and the loss factor when the displacement amplitude increases from 150 μm to 200 μm, respectively. In addition, the equivalent stiffness K_e and the equivalent damping C_e gently change with the increasing displacement amplitude, as shown in Figure 8, middle. The maximum changes of the equivalent stiffness and the equivalent damping are 8.46% and 4.08%, respectively. However, the energy dissipation E_d obviously increases with the increase of amplitude, as shown in Figure 8, bottom. This phenomenon can easily be explained by (23), which demonstrates that the energy dissipation is proportional to the square of displacement. Hence, the displacement amplitude has a significant effect on the energy dissipation. It can be concluded from the analyses that the displacement amplitude has an insignificant effect on the properties of the VE microvibration damper except for the energy dissipation.

The above analyses indicate that the storage modulus G_1 and the loss factor η are the basic characteristics of the VE microvibration damper and the other characteristics depend on these characteristics. The excitation frequency has a significant effect on the characteristics of the VE microvibration damper while the excitation displacement amplitude does not have such an effect. Overall, the analysis results are in accordance with the results shown in force-displacement hysteresis curves.

3.3. Model verification. The experimental data of the VE microvibration damper are compared with the numerical results to verify the accuracy of the model proposed in the previous section. Firstly, the parameters of the mathematical model are determined by using part of the experimental data. And then the storage modulus G_1 and the loss factor η of the VE microvibration damper are calculated by the model with determined parameters and compared with the experimental data. The conclusion that the displacement amplitude has only a slight effect on the dynamic properties of VE material has been gained from the test results and the derivation of the mathematical model. Hence, the experimental data at the displacement of 200 μm are used in this section. The nonlinear least squares method is used to determine the parameters. By optimizing min $F(x)$ in (26) with the storage modulus G_1 and the loss factor η at five different frequencies (randomly selected), the parameters of the mathematical model are determined as $k_1 = 2.82 \times 10^{-4}$, $k_2 = 1.35 \times 10^{-5}$, $c_2 = 5.71 \times 10^{-9}$, $k_3 = 3.31 \times 10^{-8}$, $c_3 = 1.25 \times 10^{-4}$, $n_{s1} = 2.53 \times 10^{14}$, $n_{c1} = 1.76 \times 10^9$ and $r_{0s} = r_{0c} = 1.71 \times 10^{-4}$. The experimental and numerical results
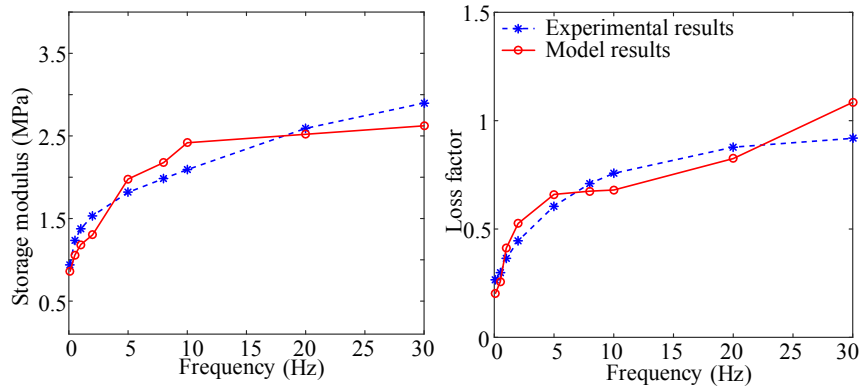
Figure 9. Experimental and numerical results comparison under different frequencies.

are listed in Table 2. Additionally, the absolute errors of the experimental and numerical results are also calculated and listed in Table 2. Here

$$F(\omega) = [\alpha((G_1(\omega) - G_1^0(\omega))/G_1(\omega))^2 + \beta((\eta(\omega) - \eta^0(\omega))/\eta(\omega))^2], \qquad (26)$$

where α and β are the weighting factors, $\alpha + \beta = 1$, $G_1(\omega)$ and $\eta(\omega)$ are the experimental storage modulus and loss factor, respectively and $G_1^0(\omega)$ and $\eta^0(\omega)$ are the numerical results.

To clearly analyze the availability of the proposed model, the storage modulus G_1 and the loss factor η of the experimental data and the numerical results of the VE microvibration damper at different frequencies are shown in Figure 9. The proposed model can describe the characteristics of VE microvibration dampers well. Figure 9, left, shows that the numerical results are in good agreement with the experimental results for the storage modulus and the error is less than 15.56%. As for the loss factor, the numerical results are in agreement with experimental results and the maximum error is less than 20% as shown in Figure 9, right. The microstructures of VE material are complex, and the chain network models are simplified models to describe the molecular chain structure of VE material. In this study, the mathematical model is proposed based on the chain network model and cannot exactly capture the effect of the real microstructure of VE material on mechanical behavior. For instance, the molecular chains interaction is not considered in this model. The effects of other constituents on VE material are also not considered. In addition, the servo-hydraulic testing machine used in the test may not be precise enough and the effects of other factors, such as environmental vibration, during the test are not considered. However, the errors between the numerical results and the test data are within the acceptable region. Therefore, this model is precise enough to describe the dynamic properties of the VE microvibration damper within the test frequency ranges.

4. Conclusions

In the present paper, the damping mechanism of VE microvibration dampers is analyzed from micro-perspectives and a mathematical model based on the chain network model is proposed to describe the dynamic behavior of the VE microvibration damper. The dynamic properties of the VE microvibration

damper are tested and analyzed. Comparison between experimental data and model numerical results is carried out to verify the proposed model. Several conclusions can be obtained through the investigation:

- The mathematical model proposed in this paper can describe the dynamic properties of VE microvibration damper well. Additionally, the model parameters have clear physical meaning and are related to the material microstructures.

- The force-displacement hysteretic loops of the VE microvibration damper are fully elliptical, and it demonstrates that the VE microvibration damper has good energy dissipation capabilities.

- The excitation frequency has a significant effect on the dynamic properties of the VE microvibration damper, whereas the displacement amplitude has only a slight influence. The storage modulus G_1, the loss factor η, the equivalent stiffness K_e and the energy dissipation E_d increase with increasing frequency while the equivalent damping C_e decreases.

5. Acknowledgments

References

[Bergman and Hanson 1993] D. M. Bergman and R. D. Hanson, "Viscoelastic mechanical damping devices tested at real earthquake displacements", *Earthq. Spectra* **9**:3 (1993), 389–417.

[Gabriel and Münstedt 2002] C. Gabriel and H. Münstedt, "Influence of long-chain branches in polyethylenes on linear viscoelastic flow properties in shear", *Rheol. Acta* **41**:3 (2002), 232–244.

[Lewandowski and Pawlak 2011] R. Lewandowski and Z. Pawlak, "Dynamic analysis of frames with viscoelastic dampers modelled by rheological models with fractional derivatives", *J. Sound Vib.* **330**:5 (2011), 923–936.

[Li et al. 2012] Y. Li, S. Tang, B. C. Abberton, M. Kröger, C. Burkhart, B. Jiang, G. J. Papakonstantopoulos, M. Poldneff, and W. K. Liu, "A predictive multiscale computational framework for viscoelastic properties of linear polymers", *Polymer* **53**:25 (2012), 5935–5952.

[Liu et al. 2014] J. Liu, Y. Li, Y. Zhang, Q. Gao, and B. Zuo, "Dynamics and control of a parallel mechanism for active vibration isolation in space station", *Nonlinear Dynam.* **76**:3 (2014), 1737–1751.

[Liu et al. 2015] C. Liu, X. Jing, S. Daley, and F. Li, "Recent advances in micro-vibration isolation", *Mech. Syst. Signal Pr.* **56–57** (2015), 55–80.

[Marckmann and Verron 2006] G. Marckmann and E. Verron, "Comparison of hyperelastic models for rubber-like materials", *Rubber Chem. Technol.* **79**:5 (2006), 835–858.

[Marko et al. 2006] J. Marko, D. Thambiratnam, and N. Perera, "Study of viscoelastic and friction damper configurations in the seismic mitigation of medium-rise structures", *J. Mech. Mater. Struct.* **1**:6 (2006), 1001–1039.

[Miehe and Göktepe 2005] C. Miehe and S. Göktepe, "A micro-macro approach to rubber-like materials, II: The micro-sphere model of finite rubber viscoelasticity", *J. Mech. Phys. Solids* **53**:10 (2005), 2231–2258.

[Min et al. 2004] K.-W. Min, J. Kim, and S.-H. Lee, "Vibration tests of 5-storey steel frame with viscoelastic dampers", *Eng. Struct.* **26**:6 (2004), 831–839.

[Moliner et al. 2012] E. Moliner, P. Museros, and M. D. Martínez-Rodrigo, "Retrofit of existing railway bridges of short to medium spans for high-speed traffic using viscoelastic dampers", *Eng. Struct.* **40** (2012), 519–528.

[Papoulia and Kelly 1997] K.-D. Papoulia and J. M. Kelly, "Visco-hyperelastic model for filled rubbers used in vibration isolation", *J. Eng. Mater. ASME* **119**:3 (1997), 292–297.

[Park 2001] S. W. Park, "Analytical modeling of viscoelastic dampers for structural and vibration control", *Int. J. Solids Struct.* **38**:44–45 (2001), 8065–8092.

[Rao 2003] M. D. Rao, "Recent applications of viscoelastic damping for noise control in automobiles and commercial airplanes", *J. Sound Vib.* **262**:3 (2003), 457–474.

[Rashid and Nicolescu 2008] A. Rashid and C. M. Nicolescu, "Design and implementation of tuned viscoelastic dampers for vibration control in milling", *Int. J. Mach. Tool. Manu.* **48**:9 (2008), 1036–1053.

[Saidi et al. 2011] I. Saidi, E. F. Gad, J. L. Wilson, and N. Haritos, "Development of passive viscoelastic damper to attenuate excessive floor vibrations", *Eng. Struct.* **33**:12 (2011), 3317–3328.

[Soong and Spencer 2002] T. T. Soong and B. F. Spencer, Jr., "Supplemental energy dissipation: state-of-the-art and state-of-the-practice", *Eng. Struct.* **24**:3 (2002), 243–259.

[Svaneborg et al. 2004] C. Svaneborg, G. S. Grest, and R. Everaers, "Strain-dependent localization, microscopic deformations, and macroscopic normal tensions in model polymer networks", *Phys. Rev. Lett.* **93** (2004), 257801.

[Tan and Ko 2004] X. M. Tan and J. M. Ko, "Vibration control of long-span beams: experimental and analytical study of beam structures incorporated with connection dampers", *J. Vib. Control* **10**:5 (2004), 707–730.

[Tang et al. 2012] S. Tang, M. S. Greene, and W. K. Liu, "Two-scale mechanism-based theory of nonlinear viscoelasticity", *J. Mech. Phys. Solids* **60**:2 (2012), 199–226.

[Tomita et al. 2006] Y. Tomita, W. Lu, M. Naito, and Y. Furutani, "Numerical evaluation of micro- to macroscopic mechanical behavior of carbon-black-filled rubber", *Int. J. Mech. Sci.* **48**:2 (2006), 108–116.

[Wacker et al. 2005] T. Wacker, L. Weimer, and K. Eckert, "GOCE platform micro-vibration verification by test and analysis", in *Proceedings of the European Conference on Spacecraft Structures, Materials and Mechanical Testing* (Noordwijk, 2005), ESA Special Publication **581**, Noordwijk, 2005.

[Ward and Hadley 1993] I. M. Ward and D. W. Hadley, *An introduction to the mechanical properties of solid polymers*, Wiley, New York, 1993.

[Webster and Semke 2005] A. L. Webster and W. H. Semke, "Broad-band viscoelastic rotational vibration control for remote sensing applications", *J. Vib. Control* **11**:11 (2005), 1339–1356.

[Xu et al. 2011] Z.-D. Xu, D.-X. Wang, and C.-F. Shi, "Model, tests and application design for viscoelastic dampers", *J. Vib. Control* **17**:9 (2011), 1359–1370.

[Xu et al. 2014] Z.-D. Xu, S.-A. Wang, and C. Xu, "Experimental and numerical study on long-span reticulate structure with multidimensional high-damping earthquake isolation devices", *J. Sound Vib.* **333**:14 (2014), 3044–3057.

[Zhang et al. 2011] Z. Zhang, G. S. Aglietti, and W. Zhou, "Microvibrations induced by a cantilevered wheel assembly with a soft-suspension system", *AIAA J.* **49**:5 (2011), 1067–1079.

CHAO XU: xuchaolove11@126.com
Key Laboratory of C&PC Structures of the Ministry of Education, Southeast University, Nanjing, 210096, China

ZHAO-DONG XU: zhdxu@163.com
Key Laboratory of C&PC Structures of the Ministry of Education, Southeast University, Nanjing, 210096, China

TENG GE: seuergeteng@163.com
Key Laboratory of C&PC Structures of the Ministry of Education, Southeast University, Nanjing, 210096, China

YA-XIN LIAO: lyxviras@163.com
Changjiang Institute of Survey, Planning, Design and Research, Wuhan, 430010, China

AN ANISOTROPIC PIEZOELECTRIC HALF-PLANE CONTAINING AN ELLIPTICAL HOLE OR CRACK SUBJECTED TO UNIFORM IN-PLANE ELECTROMECHANICAL LOADING

MING DAI, PETER SCHIAVONE AND CUN-FA GAO

We derive a series solution for the electro-elastic field inside an anisotropic piezoelectric half-plane containing an elliptical hole or a crack when the half-plane is subjected to in-plane mechanical and electric loadings. Our solution is based on a specific type of conformal map which allows for the mapping of a complete half-plane (without a hole) onto the interior of the unit circle in the imaginary plane. We illustrate our solution with several examples. We show that with decreasing distance between the hole and the edge of the half-plane, the maximum hoop stress around the hole increases rapidly under mechanical loading but slowly in the presence of electric loading. In particular, for a crack with particular orientation in a piezoelectric half-plane subjected to pure shear, we find that the mode-II stress intensity factor at the crack tip farthest from the edge of the half-plane may decrease as the crack approaches the edge. Moreover, if the distance between the crack or the elliptical hole and the edge of the half-plane exceeds four times the size of the hole or semi-length of the crack, the half-plane can be treated essentially as a whole plane without inducing significant errors in the stress concentration around the hole or in the stress and electric displacement intensity factors at the crack tips.

1. Introduction

Piezoelectric materials have been used widely in electronic and mechatronic devices due to their pronounced electromechanical coupling properties. However, since various defects (e.g. pores, micro-cracks or inclusions) often arise in the manufacture of piezoelectric materials, high stress and/or electric field concentrations may be induced near defects when the material is subjected to mechanical and/or electric loading. This, in turn, may cause crack initialization/growth, dielectric breakdown, fracture and ultimately failure [Zhang and Gao 2004]. In an effort to predict the reliability of piezoelectric devices, problems involving the prediction of electro-elastic fields (including stress and electric field concentrations) in piezoelectric materials containing holes or inclusions have attracted tremendous attention in the literature. In the context of two-dimensional deformations, researchers have examined problems involving the anti-plane shear of an isotropic plane of the piezoelectric material subjected to out-of-plane shear loading and in-plane electric loading as well as plane strain or plane stress problems corresponding to an anisotropic plane of the piezoelectric material subjected to both in-plane mechanical and electric loading. In the case of anti-plane shear, analytical results have been obtained not only for the case of an elliptical hole/inclusion [Pak 2010; Guo et al. 2010] but also for an arbitrarily-shaped hole/inclusion [Shen et al. 2010; Wang and Zhou 2013; Wang et al. 2015]. Problems involving plane strain or plane stress are rather more challenging with analytical methods available only when the hole/inclusion is

elliptical [Sosa 1991; Sosa and Khutoryansky 1996; Chung and Ting 1996; Qin 1998; Gao and Fan 1999; Wang and Gao 2012] (see, in particular, the explanation in [Ting 2000]) with most studies resorting to approximate methods to deal with cases of non-elliptical holes/inclusions [Dai and Gao 2014].

In many piezoelectric systems (structures or composites), it is common for holes or inclusions to appear near an edge. This suggests that the system could be adequately modelled as a half-plane (rather than a whole plane) containing holes or inclusions. In this context, Ru [2000] and Pan [2004] have obtained exact solutions for a piezoelectric half-plane containing an arbitrarily-shaped inclusion and a polygonal inclusion with uniform eigenstrains, respectively. However, in both of [Ru 2000; Pan 2004], the solutions require that the inclusion has the same material constants as those of its surrounding piezo-electric matrix (this essentially prevents the inclusion from degenerating into a hole). Kaloerov and Glushchenko [2001] derived an approximate solution for a piezoelectric half-plane with holes or cracks using a collocation method to deal with the boundary conditions on the holes/cracks. It is well-known, however, that collocation methods often produce unsatisfactory and imprecise results with convergence often becoming unstable with an increasing number of collocation points resulting in the possibility that the corresponding boundary conditions are not well-satisfied. Based on the fundamental solution for a dislocation in a piezoelectric half-plane, Yang et al. [2007] obtained a general solution for a crack in a piezoelectric half-plane with a traction-induction free surface by modeling the crack using continuously distributed dislocations. However, it is extremely difficult to extend the method in [Yang et al. 2007] to deal with the equally significant case of a hole in a half-plane. In particular, we mention that, despite the fact that an internal electric field inside the hole or crack may induce a significant impact on the surrounding electro-elastic field and subsequently on the fracture behavior of the corresponding materials (see [Sosa and Khutoryansky 1996; Gao and Fan 1999]), the contribution of any internal electric field remains absent from both aforementioned papers [Kaloerov and Glushchenko 2001; Yang et al. 2007]. In this paper, recognizing the above-mentioned deficiencies in the methods used previously, we develop a new efficient method, completely distinct from those used in [Kaloerov and Glushchenko 2001; Yang et al. 2007] to address the problem of plane strain deformations of a piezoelectric half-plane containing an elliptical hole or crack. In particular, we incorporate the contribution of electromechanical loadings applied on surface of the half-plane and assume that the elliptical hole is permeable to an electric field. This further requires that we take into consideration the electric field inside the hole: an issue hitherto absent in the problem of a general anisotropic half-plane containing an elliptical hole.

The paper is organized as follows. Basic formula and boundary conditions of the problem are presented in Section 2. The details of a novel solution procedure are given in Section 3. In Section 4, we calculate the stress concentration around the elliptical hole and the electro-elastic intensity factors at the crack tips. Finally, the main results are summarized in Section 5.

2. Basic formula and boundary conditions

We refer to the standard Cartesian xy-coordinate system and consider the plane strain deformation of a piezoelectric lower half-plane containing an elliptical hole (see Figure 1 which includes the geometrical parameters of the hole) whose poling direction is along the positive y-axis. The elliptical hole degenerates into a crack when the minor axis of the elliptical hole tends towards zero. It is assumed that uniform mechanical loadings ($\sigma_{xx}^\infty, \sigma_{yy}^\infty, \sigma_{xy}^\infty$) and uniform electric displacement loadings (D_x^∞, D_y^∞) are applied
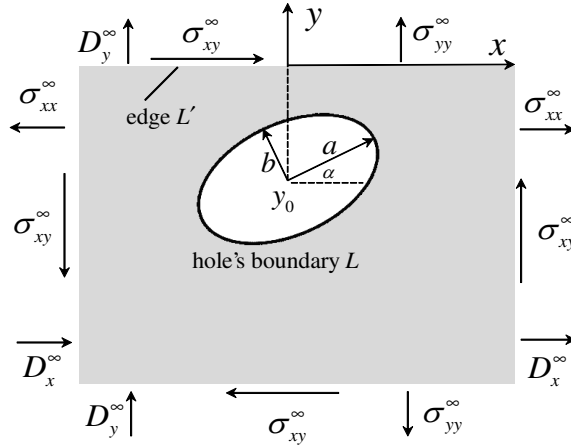
Figure 1. A piezoelectric half-plane with an elliptical hole.

both at infinity and on the edge L' of the half-plane and that the elliptical hole has a traction-free boundary and is filled with a homogeneous gas or liquid with dielectric constant ϵ_0. The stress components $(\sigma_{xx}, \sigma_{yy}, \sigma_{xy})$, the electric displacement components (D_x, D_y) and the electric potential ϕ of the piezoelectric half-plane can be described in terms of three complex functions $\varphi_i(z_i)$ ($z_i = x + \mu_i y$, $i = 1, 2, 3$) as [Sosa 1991]

$$\langle \sigma_{xx}, \sigma_{yy}, \sigma_{xy} \rangle = 2\text{Re}\left\{ \sum_{i=1}^{3} \langle \mu_i^2, 1, -\mu_i \rangle \varphi_i'(z_i) \right\}, \tag{1}$$

$$\langle D_x, D_y \rangle = 2\text{Re}\left\{ \sum_{i=1}^{3} \lambda_i \langle \mu_i, -1 \rangle \varphi_i'(z_i) \right\}, \tag{2}$$

$$\phi = -2\text{Re}\left\{ \sum_{i=1}^{3} \kappa_i \varphi_i'(z_i) \right\} \tag{3}$$

where the angled brackets represent vectors and the related constants $(\mu_i, \lambda_i, \kappa_i)$ are determined by the elastic constants a_{ij}, piezoelectric constants b_{ij} and dielectric constants c_{ij} of the piezoelectric material occupying the half-plane, as [Sosa 1991]

$$a_{11}c_{11}\mu_i^6 + (a_{11}c_{22} + 2a_{12}c_{11} + a_{33}c_{11} + b_{21}^2 + b_{13}^2 + 2b_{21}b_{13})\mu_i^4 +$$
$$(a_{22}c_{11} + 2a_{12}c_{22} + a_{33}c_{22} + 2b_{21}b_{22} + 2b_{13}b_{22})\mu_i^2 + a_{22}c_{22} + b_{22}^2 = 0, \tag{4}$$

$$\lambda_i = -\frac{(b_{21} + b_{13})\mu_i^2 + b_{22}}{c_{11}\mu_i^2 + c_{22}}, \quad \kappa_i = (b_{13} + c_{11}\lambda_i)\mu_i. \tag{5}$$

Here, μ_i ($i = 1, 2, 3$) are three distinct complex roots with positive imaginary parts each determined from Equation (4). Figure 2 shows the domains of definition of the functions $\varphi_i(z_i)$ ($i = 1, 2, 3$), respectively, in which the curves L_i in the z_i-planes ($i = 1, 2, 3$) correspond to the hole's boundary L in the xy-plane while the edges L_i' in the z_i-planes ($i = 1, 2, 3$) correspond to the edge L' in the xy-plane.
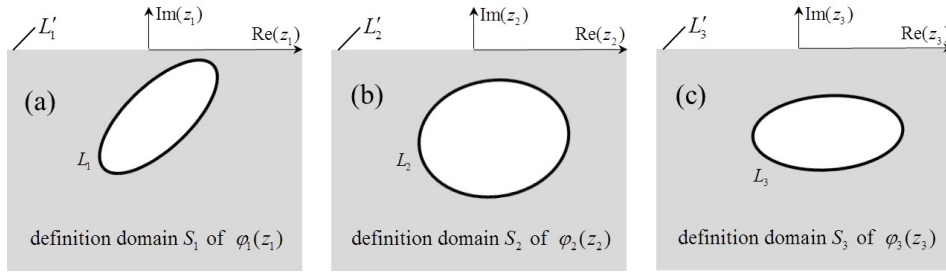
Figure 2. Domain of definition of the complex functions $\varphi_i(z_i)$ $(i = 1, 2, 3)$.

The electric displacement components $(D_x^{(0)}, D_y^{(0)})$ and electric potential $\phi^{(0)}$ of the medium inside the elliptical hole can be expressed in terms of a holomorphic function $f(z)$ $(z = x + Iy$ with I denoting the imaginary unit) by

$$\phi^{(0)} = \text{Re}[f(z)], \tag{6}$$

$$D_x^{(0)} - I D_y^{(0)} = -\epsilon_0 f'(z). \tag{7}$$

Using the functions $\varphi_i(z_i)$ $(i = 1, 2, 3)$ and $f(z)$, the electro-elastic conditions on the hole's boundary L and on the edge L' of the half-plane are then described as [Sosa 1991; Sosa and Khutoryansky 1996]

$$\left.\begin{aligned}
2\text{Re}\left\{ \sum_{i=1}^{3} \varphi_i(z_i) \right\} &= B \\
2\text{Re}\left\{ \sum_{i=1}^{3} \mu_i \varphi_i(z_i) \right\} &= C \\
2\text{Re}\left\{ \sum_{i=1}^{3} \lambda_i \varphi_i(z_i) \right\} &= D - \epsilon_0 \text{Im}[f(z)] \\
-2\text{Re}\left\{ \sum_{i=1}^{3} \kappa_i \varphi_i(z_i) \right\} &= E + \text{Re}[f(z)]
\end{aligned}\right\} (z_i \in L_i, z \in L), \tag{8}$$

$$\left.\begin{aligned}
2\text{Re}\left\{ \sum_{i=1}^{3} \varphi_i(z_i) \right\} &= B' + \sigma_{yy}^\infty x \\
2\text{Re}\left\{ \sum_{i=1}^{3} \mu_i \varphi_i(z_i) \right\} &= C' - \sigma_{xy}^\infty x \\
2\text{Re}\left\{ \sum_{i=1}^{3} \lambda_i \varphi_i(z_i) \right\} &= D' - D_y^\infty x
\end{aligned}\right\} (z_i \in L_i', x \in L'), \tag{9}$$

where B, C, D, E, B', C' and D' are real constants to be determined (although they do not influence the final electro-elastic field of the half-plane). In what follows, we determine the four complex functions

$\varphi_i(z_i)$ ($i = 1, 2, 3$) and $f(z)$ in their respective domains of definition from the boundary conditions (8) and (9).

3. Solution process

3.1. *Series representations of the complex functions.* Noting that uniform electro-elastic loadings are imposed at infinity and on the edge of the half-plane, the complex functions $\varphi_i(z_i)$ ($i = 1, 2, 3$) can take the form

$$\varphi_i(z_i) = A_i z_i + \varphi_{i0}(z_i), \quad i = 1, 2, 3; \tag{10}$$

where $\varphi_{i0}(z_i)$ ($i = 1, 2, 3$) are holomorphic in the regions S_i ($i = 1, 2, 3$; see Figure 2), respectively, while the complex constants A_i ($i = 1, 2, 3$) are specified by the imposed electro-elastic loadings (according to Equations (1) and (2)) as

$$\langle \sigma_{xx}^\infty, \sigma_{yy}^\infty, \sigma_{xy}^\infty \rangle = 2\mathrm{Re}\left\{ \sum_{i=1}^3 \langle \mu_i^2, 1, -\mu_i \rangle A_i \right\},$$

$$\langle D_x^\infty, D_y^\infty \rangle = 2\mathrm{Re}\left\{ \sum_{i=1}^3 \lambda_i \langle \mu_i, -1 \rangle A_i \right\}. \tag{11}$$

Here, since Equation (11) is insufficient to determine all three complex constants A_i ($i = 1, 2, 3$), we can prescribe, for example, $\mathrm{Im}(A_1) = 0$. Note that the domain of definition S_i ($i = 1, 2, 3$) of each complex function $\varphi_{i0}(z_i)$ ($i = 1, 2, 3$) can be interpreted as the intersection of an infinite region outside the hole bounded by L_i ($i = 1, 2, 3$) in the entire z_i-plane ($i = 1, 2, 3$) and a complete lower z_i-half-plane ($i = 1, 2, 3$) (without a hole), so that based on the principle of superposition [Dai and Gao 2014; Dai and Sun 2013], $\varphi_{i0}(z_i)$ ($i = 1, 2, 3$) can be expressed as

$$\varphi_{i0}(z_i) = \sum_{j=1}^{+\infty} a_{i,j} \xi_i^{-j} + \sum_{j=1}^{+\infty} b_{i,j} \eta_i^j, \quad i = 1, 2, 3; \tag{12}$$

where $a_{i,j}$ and $b_{i,j}$ are some constant coefficients to be determined. We note that the ξ_i-plane and η_i-plane ($i = 1, 2, 3$) are associated with the z_i-plane ($i = 1, 2, 3$) by the following conformal mappings [Lekhnitskii 1950; Copson 1935],

$$z_i = \omega_i(\xi_i) = \mu_i y_0 + \frac{a_0 - I\mu_i b_0}{2} \xi_i + \frac{\bar{a}_0 + I\mu_i \bar{b}_0}{2} \xi_i^{-1}, \quad |\xi_i| \geq 1,$$

$$a_0 = a\cos\alpha + Ib\sin\alpha, \quad b_0 = b\cos\alpha + Ia\sin\alpha, \quad i = 1, 2, 3; \tag{13}$$

$$z_i = \rho(\eta_i) = -Iy_0 \frac{\eta_i + 1}{\eta_i - 1}, \quad |\eta_i| \leq 1, \quad i = 1, 2, 3. \tag{14}$$

Note that (13) maps the infinite region outside the curve L_i ($i = 1, 2, 3$) in the entire z_i-plane ($i = 1, 2, 3$)

onto the exterior of the unit circle in the ξ_i-plane ($i = 1, 2, 3$), respectively, while (14) maps the complete lower z_i-half-plane ($i = 1, 2, 3$) onto the interior of the unit circle in the η_i-plane ($i = 1, 2, 3$), respectively. In particular, when point (x, y) is located on the hole's boundary L or on the edge L' in the physical xy-plane, the arguments z_i, ξ_i and η_i ($i = 1, 2, 3$) in their respective planes take the values

$$z_i = \begin{cases} \omega_i(\sigma), \ (z_i \in L_i) \\ \rho(\sigma') = x, \ (x \in L, z_i \in L_i') \end{cases}, i = 1, 2, 3; \tag{15}$$

$$\xi_i = \begin{cases} \sigma, \ (z_i \in L_i) \\ \omega_i^{-1}(\rho(\sigma')), \ (|\omega_i^{-1}(\rho(\sigma'))| > 1, z_i \in L_i') \end{cases}, i = 1, 2, 3; \tag{16}$$

$$\eta_i = \begin{cases} \rho^{-1}(\omega_i(\sigma)), \ (z_i \in L_i) \\ \sigma', \ (z_i \in L_i') \end{cases}, i = 1, 2, 3; \tag{17}$$

with

$$\sigma = e^{I\theta}, \quad 0 \le \theta \le 2\pi,$$
$$\sigma' = e^{I\theta'}, \quad 0 \le \theta' \le 2\pi. \tag{18}$$

Consequently on the curves L_i ($i = 1, 2, 3$) and L_i' ($i = 1, 2, 3$) in the z_i-plane ($i = 1, 2, 3$), the complex functions $\varphi_i(z_i)$ ($i = 1, 2, 3$) can be expressed completely with respect to the arguments σ and σ', respectively, as

$$\varphi_i(z_i) = A_i \omega_i(\sigma) + \sum_{j=1}^{+\infty} a_{i,j} \sigma^{-j} + \sum_{j=1}^{+\infty} b_{i,j} [\rho^{-1}(\omega_i(\sigma))]^j, \quad z_i \in L_i, \quad i = 1, 2, 3; \tag{19}$$

$$\varphi_i(z_i) = A_i \rho(\sigma') + \sum_{j=1}^{+\infty} a_{i,j} [\omega_i^{-1}(\rho(\sigma'))]^{-j} + \sum_{j=1}^{+\infty} b_{i,j} (\sigma')^j, \quad z_i \in L_i', \quad i = 1, 2, 3. \tag{20}$$

On the other hand, since the function $f(z)$ is defined in the region occupied by the elliptical hole in the physical xy-plane, it can be expanded into a Faber series such as [Dai and Sun 2013]

$$f(z) = \sum_{j=1}^{+\infty} c_j (a+b)^{-j} \left[\left(P + \sqrt{P^2 - a^2 + b^2} \right)^j + \left(P - \sqrt{P^2 - a^2 + b^2} \right)^j \right],$$
$$P = (z - I y_0) e^{-I\alpha}, \tag{21}$$

where the c_j are constant coefficients to be determined. Specifically, the boundary value of $f(z)$ on the curve L in the xy-plane turns out to be

$$f(z) = \sum_{j=1}^{+\infty} c_j \left[\sigma^j + \left(\frac{a-b}{a+b} \right)^j \sigma^{-j} \right], \quad \sigma = e^{I\theta}, \quad z \in L \tag{22}$$

where σ is given in Equation (18).

3.2. *Fourier expansion method.* Substituting (19), (20) and (22) into the boundary conditions (8) and (9) we obtain

$$2\text{Re}\left\{\sum_{i=1}^{3}\left[A_i\omega_i(\sigma)+\sum_{j=1}^{+\infty}a_{i,j}\sigma^{-j}+\sum_{j=1}^{+\infty}b_{i,j}[\rho^{-1}(\omega_i(\sigma))]^j\right]\right\}=B,$$

$$2\text{Re}\left\{\sum_{i=1}^{3}\mu_i\left[A_i\omega_i(\sigma)+\sum_{j=1}^{+\infty}a_{i,j}\sigma^{-j}+\sum_{j=1}^{+\infty}b_{i,j}[\rho^{-1}(\omega_i(\sigma))]^j\right]\right\}=C,$$

$$2\text{Re}\left\{\sum_{i=1}^{3}\lambda_i\left[A_i\omega_i(\sigma)+\sum_{j=1}^{+\infty}a_{i,j}\sigma^{-j}+\sum_{j=1}^{+\infty}b_{i,j}[\rho^{-1}(\omega_i(\sigma))]^j\right]\right\}$$

$$=D-\epsilon_0\text{Im}\left\{\sum_{j=1}^{+\infty}c_j\left[\sigma^j+\left(\frac{a-b}{a+b}\right)^j\sigma^{-j}\right]\right\},\tag{23}$$

$$-2\text{Re}\left\{\sum_{i=1}^{3}\kappa_i\left[A_i\omega_i(\sigma)+\sum_{j=1}^{+\infty}a_{i,j}\sigma^{-j}+\sum_{j=1}^{+\infty}b_{i,j}[\rho^{-1}(\omega_i(\sigma))]^j\right]\right\}$$

$$=E+\text{Re}\left\{\sum_{j=1}^{+\infty}c_j\left[\sigma^j+\left(\frac{a-b}{a+b}\right)^j\sigma^{-j}\right]\right\},$$

and

$$2\text{Re}\left\{\sum_{i=1}^{3}\left[\sum_{j=1}^{+\infty}a_{i,j}[\omega_i^{-1}(\rho(\sigma'))]^{-j}+\sum_{j=1}^{+\infty}b_{i,j}(\sigma')^j\right]\right\}=B',$$

$$2\text{Re}\left\{\sum_{i=1}^{3}\mu_i\left[\sum_{j=1}^{+\infty}a_{i,j}[\omega_i^{-1}(\rho(\sigma'))]^{-j}+\sum_{j=1}^{+\infty}b_{i,j}(\sigma')^j\right]\right\}=C',\tag{24}$$

$$2\text{Re}\left\{\sum_{i=1}^{3}\lambda_i\left[\sum_{j=1}^{+\infty}a_{i,j}[\omega_i^{-1}(\rho(\sigma'))]^{-j}+\sum_{j=1}^{+\infty}b_{i,j}(\sigma')^j\right]\right\}=D'.$$

Note that both sides of Equations (23) and (24) can be expanded into Fourier series in σ, and σ', respectively. Consequently, if we truncate the series in Equations (12) and (21) so that we seek only the unknown coefficients $a_{i,j}$ $(i=1,2,3; j=1\dots N)$, $b_{i,j}$ $(i=1,2,3; j=1\dots M)$ and c_j $(j=1\dots N)$, equating the coefficients of σ^k $(k=1\dots N)$ and $(\sigma')^k$ $(k=1\dots M)$ on both sides of Equations (23) and (24), respectively, we obtain a system of linear equations with respect to the unknown coefficients $a_{i,j}$ $(i=1,2,3; j=1\dots N)$, c_j $(j=1\dots N)$ and $b_{i,j}$ $(i=1,2,3; j=1\dots M)$, namely

$$\sum_{i=1}^{3}\left[A_i C_{i,k}^{(2)} + \bar{A}_i \bar{C}_{i,-k}^{(2)} + \sum_{j=1}^{M} b_{i,j} C_{i,j,k}^{(1)} + \sum_{j=1}^{M} \bar{b}_{i,j} \bar{C}_{i,j,-k}^{(1)} + \bar{a}_{i,k}\right] = 0,$$

$$\sum_{i=1}^{3}\mu_i\left[A_i C_{i,k}^{(2)} + \bar{A}_i \bar{C}_{i,-k}^{(2)} + \sum_{j=1}^{M} b_{i,j} C_{i,j,k}^{(1)} + \sum_{j=1}^{M} \bar{b}_{i,j} \bar{C}_{i,j,-k}^{(1)} + \bar{a}_{i,k}\right] = 0,$$

$$\sum_{i=1}^{3}\lambda_i\left[A_i C_{i,k}^{(2)} + \bar{A}_i \bar{C}_{i,-k}^{(2)} + \sum_{j=1}^{M} b_{i,j} C_{i,j,k}^{(1)} + \sum_{j=1}^{M} \bar{b}_{i,j} \bar{C}_{i,j,-k}^{(1)} + \bar{a}_{i,k}\right]$$

$$= 0.5 I \epsilon_0\left[c_k - \left(\frac{a-b}{a+b}\right)^k \bar{c}_k\right],$$

$$-\sum_{i=1}^{3}\kappa_i\left[A_i C_{i,k}^{(2)} + \bar{A}_i \bar{C}_{i,-k}^{(2)} + \sum_{j=1}^{M} b_{i,j} C_{i,j,k}^{(1)} + \sum_{j=1}^{M} \bar{b}_{i,j} \bar{C}_{i,j,-k}^{(1)} + \bar{a}_{i,k}\right]$$

$$= 0.5\left[c_k + \left(\frac{a-b}{a+b}\right)^k \bar{c}_k\right],$$

$$\left. \right\} \quad (k = 1 \ldots N), \qquad (25)$$

$$\sum_{i=1}^{3}\left[\sum_{j=1}^{M} a_{i,j} C_{i,j,k}^{(3)} + \sum_{j=1}^{M} \bar{a}_{i,j} \bar{C}_{i,j,-k}^{(3)} + b_{i,k}\right] = 0$$

$$\sum_{i=1}^{3}\mu_i\left[\sum_{j=1}^{M} a_{i,j} C_{i,j,k}^{(3)} + \sum_{j=1}^{M} \bar{a}_{i,j} \bar{C}_{i,j,-k}^{(3)} + b_{i,k}\right] = 0$$

$$\sum_{i=1}^{3}\lambda_i\left[\sum_{j=1}^{M} a_{i,j} C_{i,j,k}^{(3)} + \sum_{j=1}^{M} \bar{a}_{i,j} \bar{C}_{i,j,-k}^{(3)} + b_{i,k}\right] = 0$$

$$\left. \right\} \quad (k = 1 \ldots M), \qquad (26)$$

where

$$C_{i,j,k}^{(1)} = \frac{1}{2\pi} \int_0^{2\pi} [\rho^{-1}(\omega_i(\sigma))]^j \sigma^{-k} \, d\theta, \qquad i = 1, 2, 3; \ j = 1 \ldots M, \ k = \pm 1 \cdots \pm N, \qquad (27)$$

$$C_{i,k}^{(2)} = \begin{cases} (a_0 - I\mu_i b_0)/2, \, k = 1, \\ (\bar{a}_0 + I\mu_i \bar{b}_0)/2, \, k = -1, \\ 0, \, k = \pm 2, \pm 3, \ldots, \pm N, \end{cases} \qquad i = 1, 2, 3; \qquad (28)$$

$$C_{i,j,k}^{(3)} = \frac{1}{2\pi} \int_0^{2\pi} [\omega_i^{-1}(\rho(\sigma'))]^{-j} (\sigma')^{-k} \, d\theta', \qquad i = 1, 2, 3; \ j = 1 \ldots N, \ k = \pm 1 \cdots \pm M. \qquad (29)$$

Here, the definite integrals in Equations (27) and (29) can be evaluated numerically, for example, by Gaussian quadrature. Finally, the $(4N + 3M)$ unknown coefficients $a_{i,j}$ ($i = 1, 2, 3; \ j = 1 \ldots N$), c_j ($j = 1 \ldots N$) and $b_{i,j}$ ($i = 1, 2, 3; \ j = 1 \ldots M$) are determined from Equations (25) and (26), following which we can obtain the electro-elastic field in the piezoelectric half-plane and the electric field inside the elliptical hole.

4. Numerical examples

In the following examples, the material constants of the piezoelectric half-plane are taken as those of PZT-4 ceramic [Berlincourt et al. 1964],

$$a_{11} = 8.205 \times 10^{-12}, \ a_{12} = -3.144 \times 10^{-12}, \quad a_{22} = 7.495 \times 10^{-12}, \quad a_{33} = 19.3 \times 10^{-12} (\text{Pa}^{-1});$$
$$b_{13} = 39.4 \times 10^{-3}, \qquad b_{21} = -16.62 \times 10^{-3}, \quad b_{22} = 23.96 \times 10^{-3} (\text{m}^2/\text{C});$$
$$c_{11} = 7.66 \times 10^{7}, \qquad c_{22} = 9.82 \times 10^{7} (\text{m/F});$$

$$(30)$$

and the related complex parameters μ_i, λ_i and κ_i $(i = 1, 2, 3)$ in Equations (4) and (5) are calculated as

$$\mu_1 = 1.218I, \qquad\qquad -\bar{\mu}_2 = \mu_3 = 0.201 + 1.070I;$$
$$\lambda_1 = -6.351 \times 10^{-10}, \quad \lambda_2 = \bar{\lambda}_3 = (-2.411 + 1.362I) \times 10^{-10} (\text{m} \cdot \text{F/C}); \qquad (31)$$
$$\kappa_1 = -0.0113I, \qquad -\bar{\kappa}_2 = \kappa_3 = 0.0154 + 0.0203I (\text{m}^2/\text{C});$$

while the medium inside the elliptical hole is assumed to be homogeneous air with an approximate dielectric constant $\epsilon_0 = 8.85 \times 10^{-12}$ F/m. The convergence of the present solution is verified by the fact that the relative error between the calculated electro-elastic field corresponding to two adjacent values of N and M is less than 10^{-4}.

4.1. *Verification of the method.* Our solution for a piezoelectric half-plane degenerates quite simply into that for an elastic half-plane without piezoelectricity when all of the piezoelectric constants b_{ij} in Equations (4) and (5) tend towards zero. Comparisons between our present solutions and known results [Dejoie et al. 2006; Kushch et al. 2006] for stress distributions in an isotropic half-plane with circular or elliptical hole are presented in Figures 3 and 4 which indicated good agreement between the two.
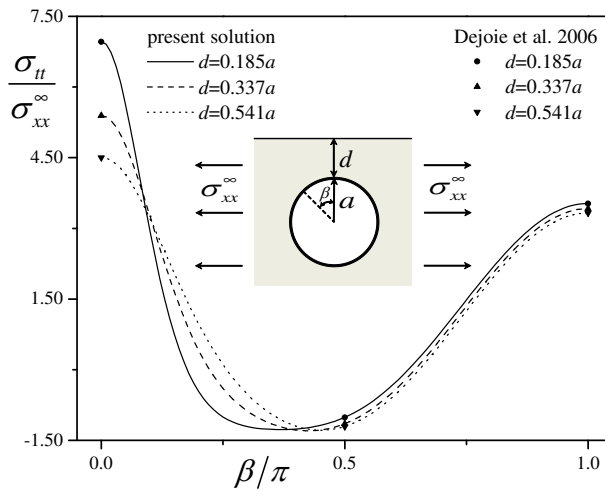

Figure 3. Hoop stress around a circular hole in an isotropic half-plane under uniform uniaxial tensile loading parallel to the edge of the half-plane.
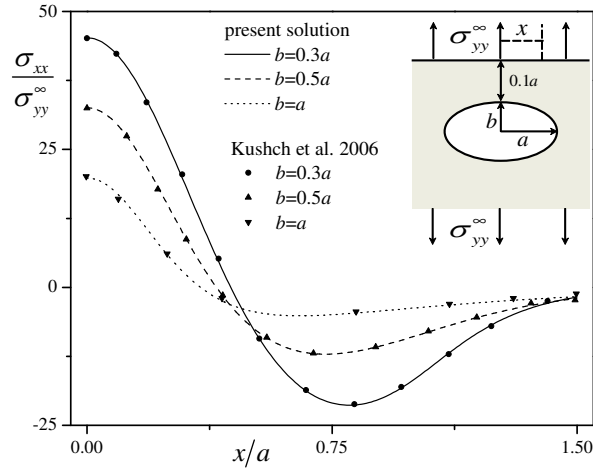
Figure 4. Stress concentration along the edge of an isotropic half-plane with an elliptical hole under uniform uniaxial tensile loading perpendicular to the edge.
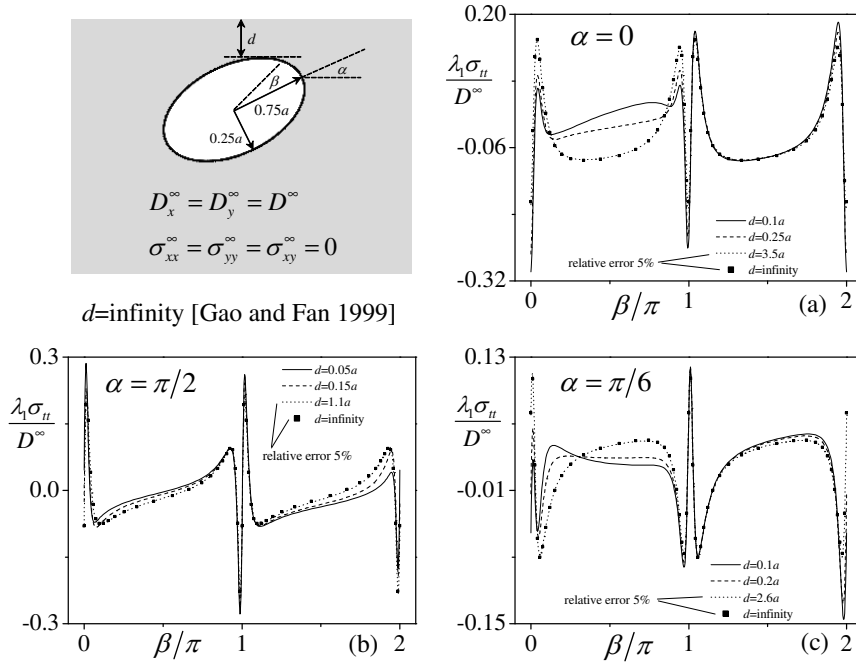
4.2. *An elliptical hole in a piezoelectric half-plane.* Figures 5 and 6 show the hoop stresses around an elliptical hole in a piezoelectric half-plane under mechanical and electric loadings, respectively, with increasing distance between the hole and the edge of the half-plane.

In Figures 5 and 6 we see that, as the distance between the hole and the edge of the half-plane
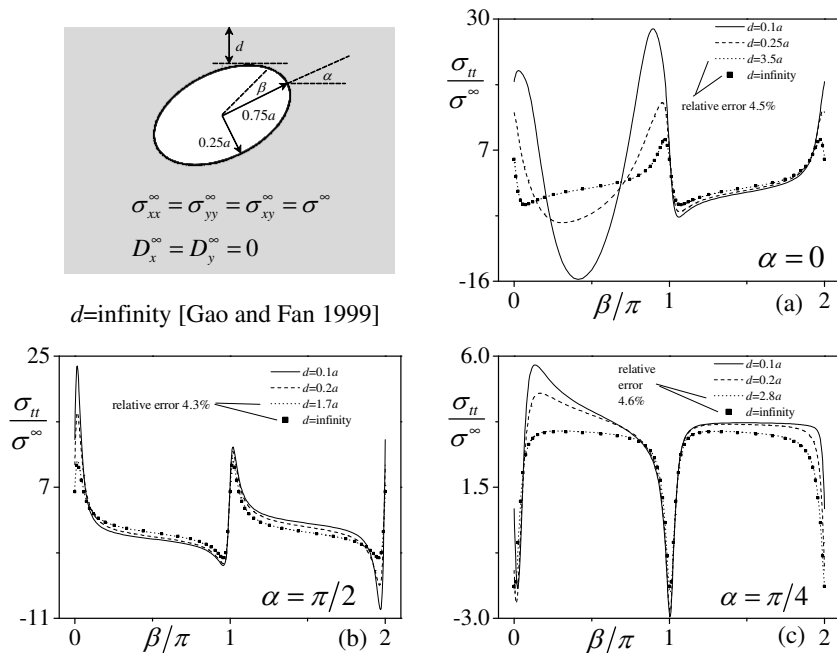
Figure 5. Hoop stress around an elliptical hole in a piezoelectric half-plane under mechanical loadings.

**Figure 6.** Hoop stress around an elliptical hole in a piezoelectric half-plane under electric loadings.

decreases, the maximum hoop stress around the hole increases rapidly under the influence of mechanical loadings but much slower when subjected to electric loading. On the other hand, for an arbitrarily-oriented elliptical hole in a piezoelectric half-plane under either mechanical or electric loading, when the distance between the hole and the edge exceeds, for example, four times the size of the hole, the effect of the edge on the stress concentration around the hole is negligible so that the half-plane can be modeled approximately as a whole plane.

4.3. *A crack in a piezoelectric half-plane.* Since the crack face is permeable to an electric field, electric loading alone does not induce stress or electric field concentrations at the crack tips. As a result, here we consider only mechanical loading. Stress and electric displacement intensity factors at the crack tips in a piezoelectric half-plane subjected to mechanical loading are given in Figures 7–12.

It is shown in Figures 7–12 that both stress and electric displacement intensity factors at the crack tip closest to the edge of the half-plane always increase with decreasing distance between the crack and the edge. However, as shown in Figure 11(b), for a crack with particular orientation in a piezoelectric half-plane under pure shear loading, the mode-II stress intensity factor at the crack tip farthest from the edge of the half-plane, may decrease with decreasing distance between the crack and the edge. Moreover, as shown in Figures 7–12, for a crack with an arbitrary orientation in a piezoelectric half-plane under mechanical loading, if the distance between the crack and the edge of the half-plane is larger than, for example, twice the length of the crack, the influence of the edge on the stress and electric displacement intensity factors at the crack tips is negligible so that the half-plane can again be treated approximately as a whole plane.
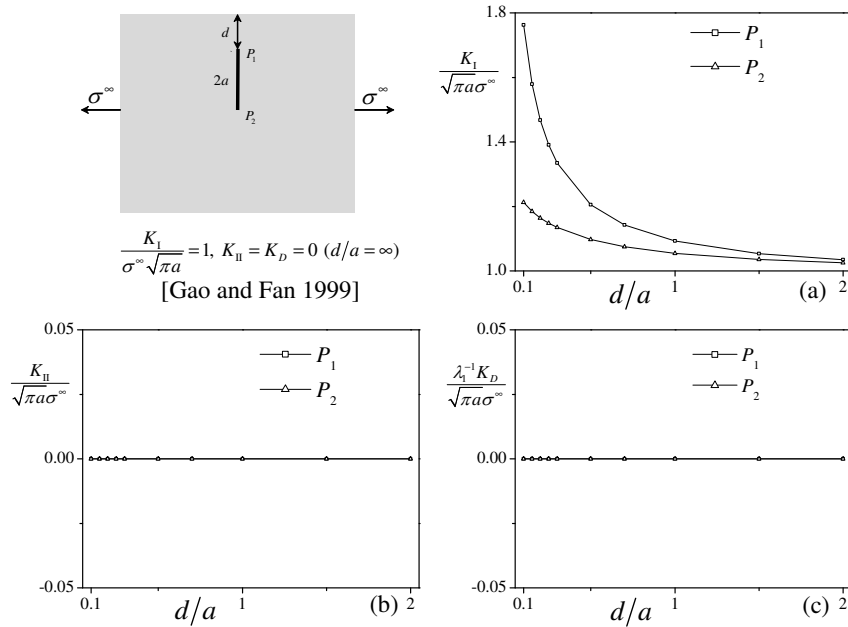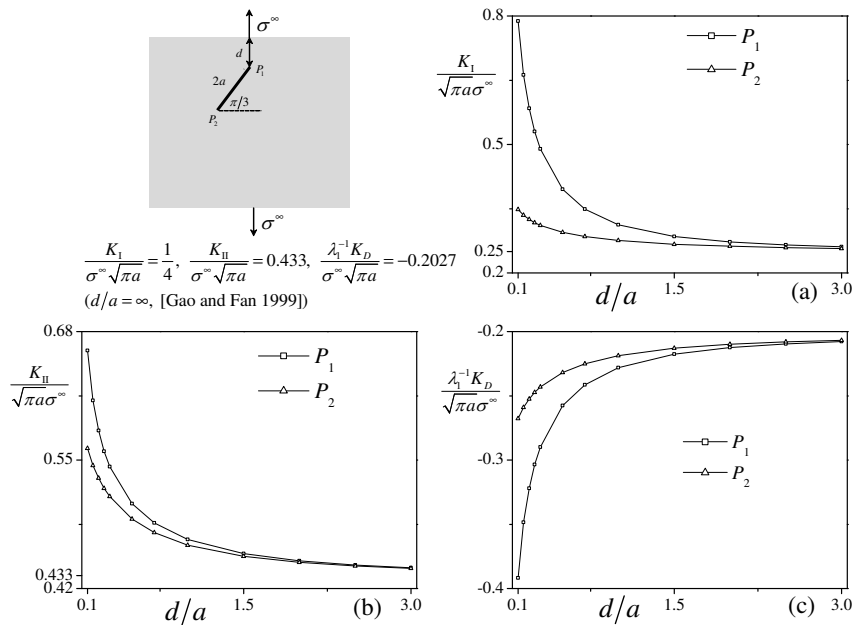
Figure 7. Intensity factors of stress and electric displacement at the tips of a crack perpendicular to the edge of the piezoelectric half-plane under uniaxial tensile loading parallel to the edge.
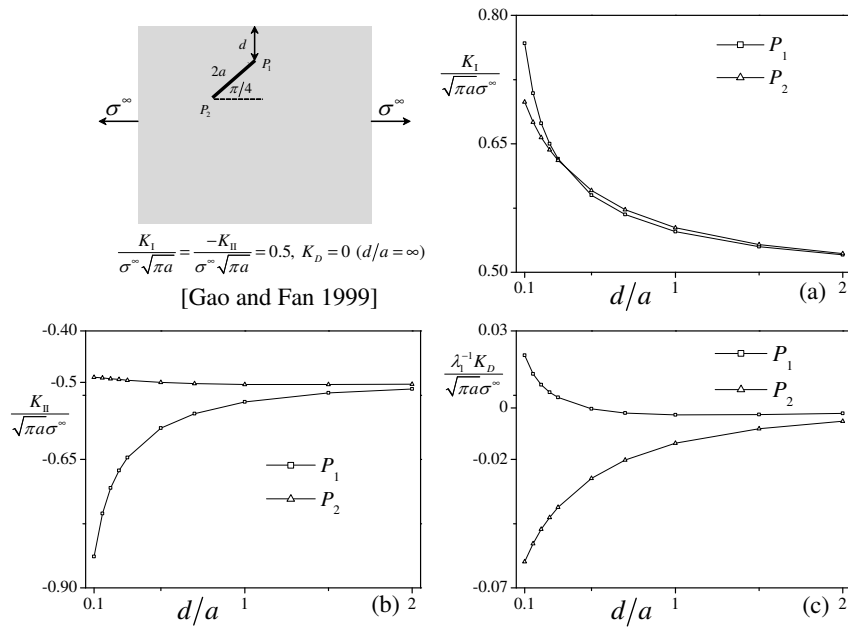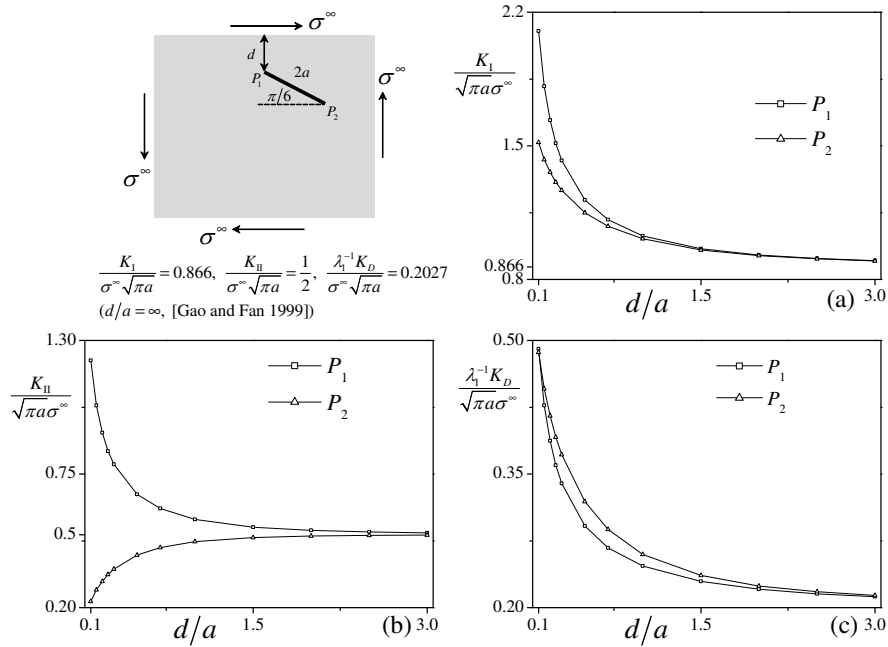

Figure 8. Intensity factors of stress and electric displacement at the tips of a crack inclined from the edge of the piezoelectric half-plane under uniaxial tensile loading parallel to the edge.
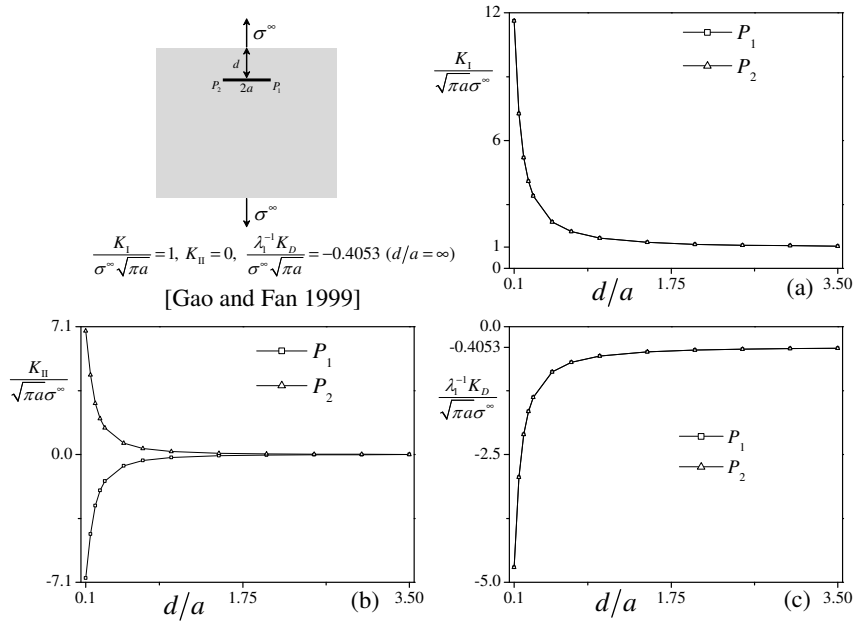
Figure 9. Intensity factors of stress and electric displacement at the tips of a crack parallel to the edge of the piezoelectric half-plane under uniaxial tensile loading perpendicular to the edge.

Figure 10. Intensity factors of stress and electric displacement at the tips of a crack inclined from the edge of the piezoelectric half-plane under uniaxial tensile loading perpendicular to the edge.
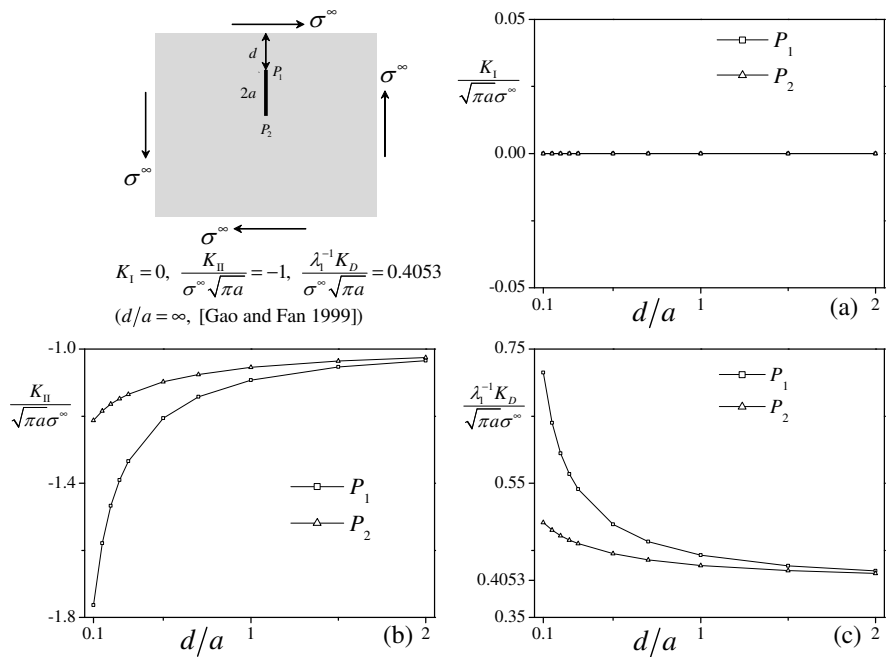
Figure 11. Intensity factors of stress and electric displacement at the tips of a crack inclined from the edge of the piezoelectric half-plane under pure shear loading.

Figure 12. Intensity factors of stress and electric displacement at the tips of a crack perpendicular to the edge of the piezoelectric half-plane under pure shear loading.

5. Conclusions

The electro-elastic field in a piezoelectric half-plane containing an elliptical hole or a crack under in-plane electromechanical loadings is obtained using conformal mapping and Fourier expansion techniques. Numerical results are given to verify the feasibility of the present solution and to demonstrate the effect of the edge of the half-plane on the stress concentration around the hole and on the electro-elastic intensity factors at the crack tips. For an elliptical hole or a crack in a piezoelectric half-plane with an edge perpendicular to the poling direction of the half-plane with mechanical or electric loading imposed on the edge and remotely, our main conclusions are as follows:

(1) The maximum hoop stress around the elliptical hole increases with decreasing distance between the hole and the edge of the half-plane under either mechanical or electric loading. However, the hoop stress around the hole is much more sensitive to the distance between the hole and the edge of the half-plane when subjected to mechanical as opposed to electric loading.

(2) In general, all stress and electric displacement intensity factors at the two crack tips increase with decreasing distance between the crack and the edge of the half-plane. However, for a crack with particular orientations in a piezoelectric half-plane subjected to pure shear loading, the mode-II stress intensity factor at one of the crack tips (that farthest from the edge) may decrease with decreasing distance between the crack and the edge.

(3) When the distance between the elliptical hole or the crack and the edge of the half-plane is more than four times the size of the hole or the semi-length of the crack, the half-plane can be treated approximately as a whole plane.

Acknowledgement

References

[Berlincourt et al. 1964] D. A. Berlincourt, D. R. Curran, and H. Jaffe, "Piezoelectric and piezomagnetic materials and their function in transducers", pp. 169–270 in *Physical acoustics: principles and methods*, vol. 1A, edited by W. P. Mason, Academic Press, New York, NY, 1964.

[Chung and Ting 1996] M. Y. Chung and T. C. T. Ting, "Piezoelectric solid with an elliptic inclusion or hole", *Int. J. Solids Struct.* **33**:23 (1996), 3343–3361.

[Copson 1935] E. T. Copson, *An introduction to the theory of functions of a complex variable*, Oxford, London, 1935.

[Dai and Gao 2014] M. Dai and C.-F. Gao, "Perturbation solution of two arbitrarily-shaped holes in a piezoelectric solid", *Int. J. Mech. Sci.* **88** (2014), 37–45.

[Dai and Sun 2013] M. Dai and H. Sun, "Thermo-elastic analysis of a finite plate containing multiple elliptical inclusions", *Int. J. Mech. Sci.* **75** (2013), 337–344.

[Dejoie et al. 2006] A. Dejoie, S. G. Mogilevskaya, and S. L. Crouch, "A boundary integral method for multiple circular holes in an elastic half-plane", *Eng. Anal. Bound. Elem.* **30**:6 (2006), 450–464.

[Gao and Fan 1999] C.-F. Gao and W.-X. Fan, "Exact solutions for the plane problem in piezoelectric materials with an elliptic [sic] or a crack", *Int. J. Solids Struct.* **36**:17 (1999), 2527–2540.

[Guo et al. 2010] J.-H. Guo, Z.-X. Lu, H.-T. Han, and Z. Yang, "The behavior of two non-symmetrical permeable cracks emanating from an elliptical hole in a piezoelectric solid", *Eur. J. Mech. A Solids* **29**:4 (2010), 654–663.

[Kaloerov and Glushchenko 2001] S. A. Kaloerov and Y. A. Glushchenko, "Electroelastic state of a multiply connected piezoelectric half plane with holes and cracks", *J. Math. Sci. (NY)* **107**:6 (2001), 4416–4424.

[Kushch et al. 2006] V. I. Kushch, S. V. Shmegera, and V. A. Buryachenko, "Elastic equilibrium of a half plane containing a finite array of elliptic inclusions", *Int. J. Solids Struct.* **43**:11–12 (2006), 3459–3483.

[Lekhnitskii 1950] S. G. Lekhnitskii, *Теория упругости анизотропного тела*, Gostekhizdat, Moscow, 1950. Translated as *Theory of elasticity of an anisotropic elastic body*, Holden Day, San Francisco, CA, 1963. 2nd ed. in Russian published by Nauka, Moscow, 1977; translated by Mir, Moscow, 1981.

[Pak 2010] Y. E. Pak, "Elliptical inclusion problem in antiplane piezoelectricity: implications for fracture mechanics", *Int. J. Eng. Sci.* **48**:2 (2010), 209–222.

[Pan 2004] E. Pan, "Eshelby problem of polygonal inclusions in anisotropic piezoelectric full- and half-planes", *J. Mech. Phys. Solids* **52**:3 (2004), 567–589.

[Qin 1998] Q.-H. Qin, "Thermoelectroelastic Green's function for a piezoelectric plate containing an elliptic hole", *Mech. Mater.* **30**:1 (1998), 21–29.

[Ru 2000] C. Q. Ru, "Eshelby's problem for two-dimensional piezoelectric inclusions of arbitrary shape", *Proc. R. Soc. Lond. A* **456**:1997 (2000), 1051–1068.

[Shen et al. 2010] M. H. Shen, F. M. Chen, and S. Y. Hung, "Piezoelectric study for a three-phase composite containing arbitrary inclusion", *Int. J. Mech. Sci.* **52**:4 (2010), 561–571.

[Sosa 1991] H. Sosa, "Plane problems in piezoelectric media with defects", *Int. J. Solids Struct.* **28**:4 (1991), 491–505.

[Sosa and Khutoryansky 1996] H. Sosa and N. Khutoryansky, "New developments concerning piezoelectric materials with defects", *Int. J. Solids Struct.* **33**:23 (1996), 3399–3414.

[Ting 2000] T. C. T. Ting, "Common errors on mapping of nonelliptic curves in anisotropic elasticity", *J. Appl. Mech. (ASME)* **67**:4 (2000), 655–657.

[Wang and Gao 2012] Y.-J. Wang and C.-F. Gao, "Thermoelectroelastic solution for edge cracks originating from an elliptical hole in a piezoelectric solid", *J. Therm. Stresses* **35**:1–3 (2012), 138–156.

[Wang and Zhou 2013] X. Wang and K. Zhou, "Three-phase piezoelectric inclusions of arbitrary shape with internal uniform electroelastic field", *Int. J. Eng. Sci.* **63** (2013), 23–29.

[Wang et al. 2015] Y.-J. Wang, C.-F. Gao, and H. Song, "The anti-plane solution for the edge cracks originating from an arbitrary hole in a piezoelectric material", *Mech. Res. Commun.* **65** (2015), 17–23.

[Yang et al. 2007] P. S. Yang, J. Y. Liou, and J. C. Sung, "Analysis of a crack in a half-plane piezoelectric solid with traction-induction free boundary", *Int. J. Solids Struct.* **44**:25–26 (2007), 8556–8578.

[Zhang and Gao 2004] T.-Y. Zhang and C.-F. Gao, "Fracture behaviors of piezoelectric materials", *Theor. Appl. Fract. Mech.* **41**:1–3 (2004), 339–379.

MING DAI: mdai1@ualberta.ca
State Key Laboratory of Mechanics and Control of Mechanical Structures, Nanjing University of Aeronautics and Astronautics, Nanjing, 210016, China

and

Department of Mechanical Engineering, University of Alberta, Edmonton, Alberta T6G 2G8, Canada

PETER SCHIAVONE: p.schiavone@ualberta.ca
Department of Mechanical Engineering, University of Alberta, Edmonton, Alberta T6G 2G8, Canada

CUN-FA GAO: cfgao@nuaa.edu.cn
State Key Laboratory of Mechanics and Control of Mechanical Structures, Nanjing University of Aeronautics and Astronautics, Nanjing, 210016, China

msp

ON THE CAUSALITY OF THE RAYLEIGH WAVE

BARIŞ ERBAŞ AND ONUR ŞAHIN

An explicit hyperbolic-elliptic formulation for surface Rayleigh waves is analysed with an emphasis on the causality of obtained results. As an example, a 3D moving load problem for a distributed vertical load is considered. A simple approximate solution is derived for a near-resonant regime, and the related point load solution is recast as a limiting case. It is shown that causality is characteristic only for the longitudinal wave potential along the surface, where it is governed by a hyperbolic equation modelling the small dilatation disturbances propagating at the Rayleigh wave speed.

1. Introduction

Propagation of surface waves has been investigated in numerous papers since the original contribution of Rayleigh [1885]. In his well-known work, Chadwick [1976] presented a general formulation of the Rayleigh wave field in terms of a single harmonic function. His results have been recently generalised to 3D by Kiselev and Parker [2010]. Parker [2012] later generalised their results for evanescent Schölte waves with an arbitrary profile. Surface waves in layered structures [Kiselev and Rogerson 2009; Kiselev et al. 2007] have also attracted considerable attention. Among other contributions, we note the approach of Rousseau and Maugin [2011] associating the quasiparticles with the Rayleigh wave, along with papers developing the mathematical theory of surface waves in anisotropic media, e.g., [Achenbach 1998; Prikazchikov 2013; Parker 2013].

The issue of causality of the Rayleigh wave does not usually arise in linear elasticity governed by hyperbolic equations with the characteristics corresponding to longitudinal and transverse wave speeds; see, e.g., [Achenbach 1973; Poruchikov 1993]. This is only a feature of the specialised hyperbolic-elliptic model oriented to the Rayleigh wave and neglecting bulk waves [Kaplunov et al. 2006; Erbaş et al. 2013; Kaplunov and Prikazchikov 2013]. The advantages of this model are illustrated by investigation of the near-resonant regimes of moving loads on an elastic half-space [Kaplunov et al. 2010; 2013; Erbaş et al. 2014].

In the case of a vertical load, the implementation of the aforementioned model begins with solving a scalar hyperbolic equation for the longitudinal wave potential on the surface. The characteristics of this equation are associated with the Rayleigh wave speed. Then the variation of the longitudinal potential over the interior is found from a Dirichlet problem for a pseudostatic elliptic equation with the boundary condition coming from the solution of the wave equation on the surface. Finally, the transverse wave potential is determined. In particular, in the plane-strain setup, it is recovered as the harmonic conjugate of the longitudinal wave potential; see also [Chadwick 1976].

It is obvious that we may only expect causality of the longitudinal wave potential along the surface, where it is governed by a hyperbolic equation. The causality concept is not applicable to the transverse
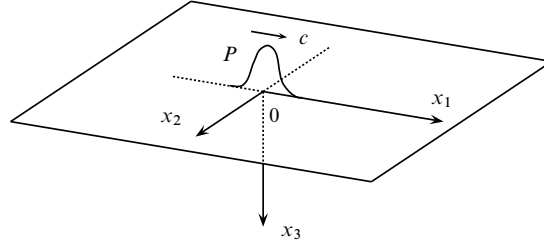
Figure 1. Distributed load moving along the x_1 axis.

wave potential and the longitudinal wave potential over the interior, where both of them satisfy elliptic equations. Fortunately, this only means that the considered surface wave formulation is valid only behind bulk wave fronts. However, the presence of bulk waves ignored within this formulation may also hypothetically result in formally noncausal solutions of the wave equation on the surface; see the discussion of the Mach cones associated with a super-Rayleigh moving load in [Erbaş et al. 2014].

In this paper, we revisit the 3D steady-state moving load problem for an elastic half-space studied earlier in [Kaplunov et al. 2013], with a special focus on the causality of the Rayleigh wave, including analysis of the associated Mach cones. In contrast to [Erbaş et al. 2014] dealing with a point force, we are mainly concerned with the case a distributed load, which is seemingly more relevant to modern engineering applications, motivated by modelling of high-speed trains; see, e.g., [Cao et al. 2012; Galvín and Domínguez 2007; El Kacimi et al. 2013; Gupta et al. 2010; Agostinacchio et al. 2013; Dieterman and Metrikine 1997; Celebi 2006].

The paper is organised as follows. In Section 2, we formulate the problem in terms of the aforementioned hyperbolic-elliptic model. In Section 3, the super-Rayleigh solution on the surface is analysed, with the causality concept embedded. Then the solution over the interior is constructed via the Poisson formula, and the components of the transverse wave potentials are determined with the help of the relevant differential relations on the surface. In Section 4, the steady-state solution for a *distributed load* over the interior of the half-space is obtained. Finally, in Section 5, comparisons of solutions for point and distributed forces are illustrated numerically.

2. Statement of the problem

We consider the dynamic response of a 3D elastic isotropic half-space ($-\infty < x_1, x_2 < \infty, 0 \leq x_3 < \infty$) under the influence of a vertical load of magnitude P distributed along the x_1 axis and moving along its positive direction on the surface $x_3 = 0$ of the half-space at a constant speed c; see Figure 1.

In this paper, we employ a hyperbolic-elliptic approximate model for the surface wave field [Kaplunov et al. 2006; Erbaş et al. 2013]. Within the framework of this model, the Lamé potentials φ and ψ_i, $i = 1, 2$, satisfy the pseudostatic elliptic equations over the interior

$$\frac{\partial^2 \varphi}{\partial x_3^2} + k_1^2 \Delta_2 \varphi = 0, \qquad \frac{\partial^2 \psi_i}{\partial x_3^2} + k_2^2 \Delta_2 \psi_i = 0, \quad i = 1, 2, \tag{2-1}$$

where $\Delta_2 = \partial^2/\partial x_1^2 + \partial^2/\partial x_2^2$ is a 2D Laplacian, $k_i^2 = 1 - c_R^2/c_i^2$, $i = 1, 2$, and c_1, c_2 and c_R are the longitudinal, transverse and Rayleigh wave speeds, respectively. The components of the displacement

vector may be written in terms of the Lamé potentials as

$$u_1 = \frac{\partial \varphi}{\partial x_1} - \frac{\partial \psi_1}{\partial x_3}, \qquad u_2 = \frac{\partial \varphi}{\partial x_2} - \frac{\partial \psi_2}{\partial x_3}, \qquad u_3 = \frac{\partial \varphi}{\partial x_3} + \frac{\partial \psi_1}{\partial x_1} + \frac{\partial \psi_2}{\partial x_2}; \qquad (2\text{-}2)$$

for more details, see [Kaplunov and Prikazchikov 2013]. The boundary conditions on the surface $x_3 = 0$ include the hyperbolic equation

$$\Delta_2 \varphi - \frac{1}{c_R^2} \frac{\partial^2 \varphi}{\partial t^2} = AP \frac{a}{\pi[(x_1 - ct)^2 + a^2]} \delta(x_2), \qquad (2\text{-}3)$$

together with the relations between the potentials

$$\frac{\partial \varphi}{\partial x_i} = \frac{2}{1 + k_2^2} \frac{\partial \psi_i}{\partial x_3}, \quad i = 1, 2. \qquad (2\text{-}4)$$

In (2-3), A is a constant depending on the material properties of a half-space given by

$$A = \frac{k_1 k_2 (1 + k_2^2)}{2\mu[k_2(1 - k_1^2) + k_1(1 - k_2^2) - k_1 k_2(1 - k_2^4)]}. \qquad (2\text{-}5)$$

Throughout the paper, we are mainly concerned with the steady-state regime in the moving frame related to the coordinate $\lambda = x_1 - ct$. Rewriting (2-3) in the new coordinates, we get for the sub-Rayleigh ($c < c_R$) and super-Rayleigh ($c > c_R$) cases, respectively,

$$\frac{\partial^2 \varphi}{\partial x_2^2} + \varepsilon^2 \frac{\partial^2 \varphi}{\partial \lambda^2} = AP \frac{a}{\pi[\lambda^2 + a^2]} \delta(x_2), \qquad (2\text{-}6)$$

$$\frac{\partial^2 \varphi}{\partial x_2^2} - \varepsilon^2 \frac{\partial^2 \varphi}{\partial \lambda^2} = AP \frac{a}{\pi[\lambda^2 + a^2]} \delta(x_2), \qquad (2\text{-}7)$$

where

$$\varepsilon = \left| 1 - \frac{c^2}{c_R^2} \right|^{1/2}. \qquad (2\text{-}8)$$

The adopted approximate formulation is valid when the load speed is close to the Rayleigh wave speed, i.e., when $\varepsilon \ll 1$, which enables investigation of the near-resonant response dominated by the Rayleigh wave contribution [Kaplunov et al. 2010; 2013]. Introducing the scaled variables

$$\xi_1 = \frac{\lambda}{\varepsilon}, \qquad \xi_2 = x_2, \qquad \xi_3 = \frac{x_3}{\varepsilon}, \qquad (2\text{-}9)$$

the elliptic equations (2-1) become

$$\frac{\partial^2 \varphi}{\partial \xi_3^2} + k_1^2 \frac{\partial^2 \varphi}{\partial \xi_1^2} + \varepsilon^2 k_1^2 \frac{\partial^2 \varphi}{\partial \xi_2^2} = 0,$$

$$\frac{\partial^2 \psi_i}{\partial \xi_3^2} + k_2^2 \frac{\partial^2 \psi_i}{\partial \xi_1^2} + \varepsilon^2 k_2^2 \frac{\partial^2 \psi_i}{\partial \xi_2^2} = 0, \quad i = 1, 2,$$

$$(2\text{-}10)$$

along with boundary conditions (2-6) and (2-7) on the surface $\xi_3 = 0$ rewritten as

$$\frac{\partial^2 \varphi}{\partial \xi_2^2} + \frac{\partial^2 \varphi}{\partial \xi_1^2} = AP \frac{a}{\pi[\varepsilon^2 \xi_1^2 + a^2]} \delta(\xi_2), \tag{2-11}$$

$$\frac{\partial^2 \varphi}{\partial \xi_2^2} - \frac{\partial^2 \varphi}{\partial \xi_1^2} = AP \frac{a}{\pi[\varepsilon^2 \xi_1^2 + a^2]} \delta(\xi_2). \tag{2-12}$$

The relations (2-4) for the potentials φ, ψ_1 and ψ_2 now take the form

$$\frac{\partial \varphi}{\partial \xi_1} = \frac{2}{1 + k_2^2} \frac{\partial \psi_1}{\partial \xi_3}, \qquad \frac{\partial \varphi}{\partial \xi_2} = \frac{2}{\varepsilon(1 + k_2^2)} \frac{\partial \psi_2}{\partial \xi_3}. \tag{2-13}$$

3. Revisit of the moving point force problem

Before considering the problem (2-10)–(2-13) for a distributed load, let us discuss the solution for a point force for the super-Rayleigh regime ($c > c_R$) earlier treated in [Kaplunov et al. 2013]. In the limit $a \to 0$, the hyperbolic equation on the surface (2-3) becomes

$$\Delta_2 \varphi - \frac{1}{c_R^2} \frac{\partial^2 \varphi}{\partial t^2} = AP \delta(x_1 - ct) \delta(x_2). \tag{3-1}$$

The fundamental solution of the 2D wave equation is given by

$$\mathscr{F}(x_1, x_2, t) = -\frac{c_R H\left(c_R t - \sqrt{x_1^2 + x_2^2}\right)}{2\pi \sqrt{c_R^2 t^2 - x_1^2 - x_2^2}} \tag{3-2}$$

[Zauderer 2006], where $H(x)$ is the Heaviside function. As might be expected, it is causal in the variables x_1, x_2 and t. Then the solution of (3-1) may be expressed as a convolution, i.e.,

$$\begin{aligned}
\varphi(x_1, x_2, 0, t) &= \int_0^t \mathscr{F}(x_1 - ct, x_2, t - \tau) \, d\tau \\
&= -\frac{APc_R}{2\pi} \int_0^t \frac{H\left(c_R(t - \tau) - \sqrt{(x_1 - c\tau)^2 + x_2^2}\right)}{\sqrt{c_R^2(t - \tau)^2 - (x_1 - c\tau)^2 - x_2^2}} \, d\tau,
\end{aligned} \tag{3-3}$$

or in the form

$$\varphi(\lambda, x_2, 0) = -\frac{APc_R}{2\pi} \int_0^t \frac{H\left(c_R s - \sqrt{(\lambda + cs)^2 + x_2^2}\right)}{\sqrt{(c_R^2 - c^2)s^2 - 2sc\lambda - \lambda^2 - x_2^2}} \, ds, \tag{3-4}$$

where $s = t - \tau$. The argument of the Heaviside function in the numerator of (3-4) is positive when $\lambda < 0$ in the considered super-Rayleigh case and $s_1 \le s \le s_2$, where

$$s_1 = n + \sqrt{n^2 - m}, \qquad s_2 = n - \sqrt{n^2 - m}, \tag{3-5}$$

with

$$n = -\frac{\lambda c}{c^2 - c_R^2}, \qquad m = \frac{\lambda^2 + x_2^2}{(c^2 - c_R^2)^2}. \tag{3-6}$$
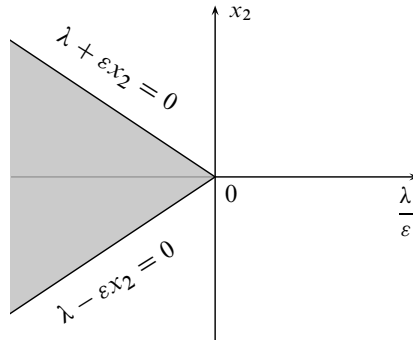
Figure 2. Mach cone.

As $t \to \infty$,

$$\varphi(\lambda, x_2, 0) = -\frac{AP c_R}{2\pi} \int_{s_1}^{s_2} \frac{1}{\sqrt{(c_R^2 - c^2)s^2 - 2sc\lambda - \lambda^2 - x_2^2}}\, ds = -\frac{AP}{2\varepsilon}. \tag{3-7}$$

We note that the roots s_1 and s_2 are real, provided that $n^2 - m \geq 0$; hence, $\varepsilon^2 x_2^2 - \lambda^2 \leq 0$. Therefore, since $\lambda < 0$,

$$\varphi(\lambda, x_2, 0) = \frac{AP}{2\varepsilon}\left[H\left(x_2 - \frac{\lambda}{\varepsilon}\right) - H\left(x_2 + \frac{\lambda}{\varepsilon}\right) \right] H(-\lambda). \tag{3-8}$$

The obtained solution (3-8) does not violate the causality concept and predicts the Mach cone shown in Figure 2. At the same time, we could immediately arrive at the same result by introducing the moving coordinate λ into (3-1) to get

$$\frac{\partial^2 \varphi}{\partial x_2^2} - \varepsilon^2 \frac{\partial^2 \varphi}{\partial \lambda^2} = A\delta(\lambda)\delta(x_2). \tag{3-9}$$

It is interesting that making use of the conventional fundamental noncausal solution in the variables λ and x_2 in (3-9) results in (3-8) without the factor $H(-\lambda)$ enabling the causality [Kaplunov et al. 2013]. Similar to [Kaplunov et al. 2013], the potential φ may now be recovered over the interior, $x_3 > 0$, through the Poisson formula [Courant and Hilbert 1962], resulting in

$$\varphi(\lambda, x_2, x_3) = \frac{AP}{2\pi\varepsilon} k_1 \eta_3 \int_{-\infty}^{0} \frac{H(x_2 - \eta/\varepsilon) - H(x_2 + \eta/\varepsilon)}{(\eta - \lambda)^2 + k_1 x_3^2}\, d\eta = \frac{AP}{2\pi\varepsilon} \cot^{-1}\left(\frac{\lambda + \varepsilon|x_2|}{k_1 x_3} \right). \tag{3-10}$$

It is now a simple matter to get the potentials ψ_1 and ψ_2 using the relations (2-4). The result is

$$\psi_1(\lambda, x_2, x_3) = -\frac{AP k_1(1 + k_2^2)}{8\pi\varepsilon k_2^2} \ln(k_2^2 x_3^2 + (\lambda + \varepsilon|x_2|)^2), \tag{3-11}$$

$$\psi_2(\lambda, x_2, x_3) = -\frac{AP k_1(1 + k_2^2)\, \mathrm{sgn}(x_2)}{8\pi k_2^2} \ln(k_2^2 x_3^2 + (\lambda + \varepsilon|x_2|)^2). \tag{3-12}$$

In what follows, we illustrate the behaviour of potentials for different values of the depth x_3 — specif-
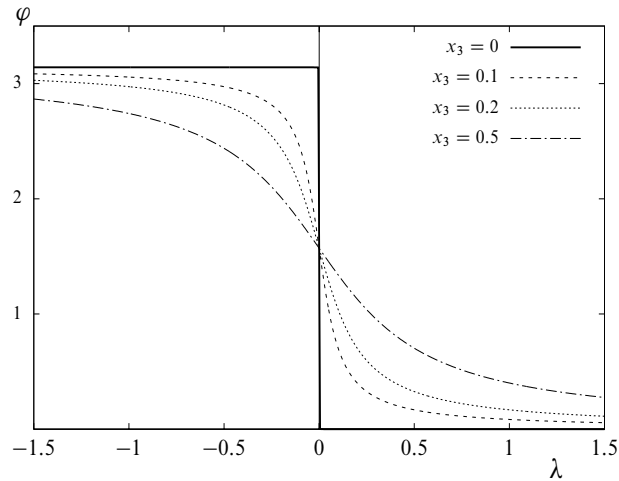
Figure 3. Potential φ versus λ at $x_2 = 0$.

ically, in Figure 3 we consider $x_3 = 0, 0.1, 0.2$ and 0.5. It is seen that on the surface $x_3 = 0$ the causality principle holds true, that is, there is no contribution of the longitudinal wave potential φ appearing in front of the load. However, as the depth increases ($x_3 > 0$), it is observed that in the interior of the half-space there appear some disturbances in front of the moving load. Figure 4 illustrates variation of the potentials ψ_1 and ψ_2 for different depths. It is clear from Figure 4 and also from (3-11) and (3-12) that the causality principle is not applicable to potentials ψ_1 and ψ_2, i.e., they may be treated as nonwave potentials.

Thus, within the framework of the approximate formulation of the Rayleigh wave, the causality principle is only valid on the surface and only for the longitudinal wave potential φ.
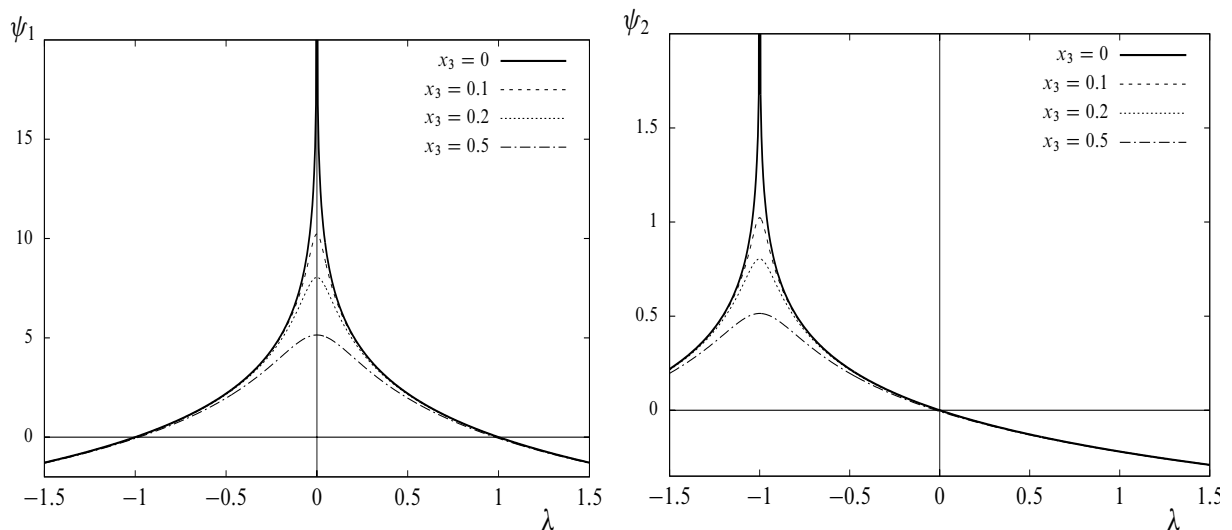
Figure 4. Potentials ψ_1 and ψ_2 versus λ at $x_2 = 0$ and $x_2 = 1$, respectively.

4. Solution for distributed force

We may now derive the steady-state solution of (2-10)–(2-13) employing the adopted hyperbolic-elliptic model. Consider first the super-Rayleigh regime. At leading order, elliptic equations (2-10) give

$$\frac{\partial^2 \varphi}{\partial \xi_3^2} + k_1^2 \frac{\partial^2 \varphi}{\partial \xi_1^2} = 0, \qquad \frac{\partial^2 \psi_i}{\partial \xi_3^2} + k_2^2 \frac{\partial^2 \psi_i}{\partial \xi_1^2} = 0, \quad i = 1, 2, \tag{4-1}$$

which should be solved together with the hyperbolic equation (2-7) and relations (2-4). Using the fundamental solution of the wave operator

$$F(\xi_1, \xi_2) = \tfrac{1}{2}[H(\xi_2 - \xi_1) - H(\xi_2 + \xi_1)], \tag{4-2}$$

for $\xi_1 < 0$, from the causality, the longitudinal wave potential on the surface may easily be obtained in the form

$$\varphi(\xi_1, \xi_2, 0) = \frac{AP}{2\pi\varepsilon}\left[\frac{\pi}{2} - \tan^{-1}(\alpha(\xi_1 + |\xi_2|))\right], \tag{4-3}$$

where the notation $\alpha = \varepsilon/a$ is introduced. The sought-after solution for the Dirichlet problem for elliptic equation (4-1) may be written using the 2D Poisson integral formula giving

$$\begin{aligned}
\varphi(\xi_1, \xi_2, \xi_3) &= \frac{AP}{2\pi^2\varepsilon}k_1\xi_3\left\{\frac{\pi}{2}\int_{-\infty}^{\infty}\frac{1}{(\eta - \xi_1)^2 + k_1^2\xi_3^2}\,d\eta - \int_{-\infty}^{\infty}\frac{\tan^{-1}(\alpha(\eta + |\xi_2|))}{(\eta - \xi_1)^2 + k_1^2\xi_3^2}\,d\eta\right\} \\
&= \frac{AP}{2\pi\varepsilon}\cot^{-1}\left(\frac{\alpha(\xi_1 + |\xi_2|)}{1 + \alpha k_1\xi_3}\right).
\end{aligned} \tag{4-4}$$

In order to obtain the transverse wave potentials ψ_1 and ψ_2, we employ relations (2-13). Differentiation of (4-4) gives

$$\frac{\partial \varphi(\xi_1, \xi_2, \xi_3)}{\partial \xi_1} = -\frac{AP}{2\pi a}\frac{1 + \alpha k_1\xi_3}{(1 + \alpha k_1\xi_3)^2 + \alpha^2(\xi_1 + |\xi_2|)^2}. \tag{4-5}$$

Taking into account (4-1)$_2$ and (2-13)$_1$, we get

$$\frac{\partial \psi_1(\xi_1, \xi_2, \xi_3)}{\partial \xi_3} = -\frac{AP(1 + k_2^2)}{4\pi a}\frac{1 + \alpha k_2\xi_3}{(1 + \alpha k_2\xi_3)^2 + \alpha^2(\xi_1 + |\xi_2|)^2}; \tag{4-6}$$

hence,

$$\psi_1(\xi_1, \xi_2, \xi_3) = -\frac{AP(1 + k_2^2)}{8\pi\varepsilon k_2}\ln((1 + \alpha k_2\xi_3)^2 + \alpha^2(\xi_1 + |\xi_2|)^2). \tag{4-7}$$

Using (2-13)$_2$ and following the same procedure as above, we obtain

$$\psi_2(\xi_1, \xi_2, \xi_3) = -\frac{AP\,\mathrm{sgn}(\xi_2)(1 + k_2^2)}{8\pi k_2}\ln((1 + \alpha k_2\xi_3)^2 + \alpha^2(\xi_1 + |\xi_2|)^2). \tag{4-8}$$
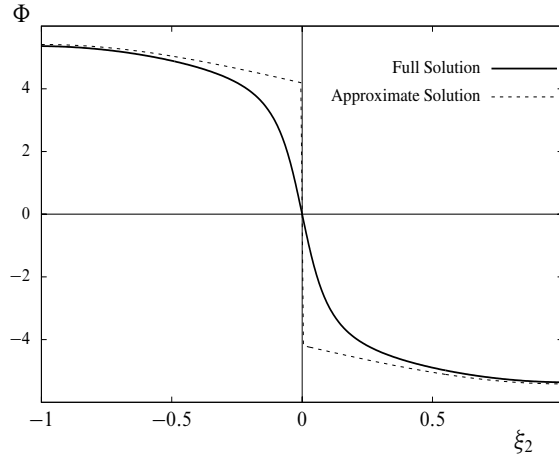
Figure 5. Derivatives of super-Rayleigh full and approximate solutions, for $\nu = 0.25$, $a = 0.1$, $\varepsilon = 0.1$, $\xi_1 = -1$ and $\xi_3 = 1$.

Rewriting (2-2) in terms of scaled variables (2-9) and using the results (4-4), (4-7) and (4-8), we get for the displacement components

$$u_1 = \frac{\alpha}{\varepsilon^2} \frac{AP}{2\pi} \left[\frac{1+k_2^2}{2} \frac{1+\alpha k_2 \xi_3}{(1+\alpha k_2 \xi_3)^2 + \alpha^2 (\xi_1 + |\xi_2|)^2} - \frac{1+\alpha k_1 \xi_3}{(1+\alpha k_1 \xi_3)^2 + \alpha^2 (\xi_1 + |\xi_2|)^2} \right], \tag{4-9}$$

$$u_2 = \frac{AP\alpha \operatorname{sgn}(\xi_2)}{2\pi \varepsilon} \left[\frac{1+k_2^2}{2} \frac{1+\alpha k_2 \xi_3}{(1+\alpha k_2 \xi_3)^2 + \alpha^2 (\xi_1 + |\xi_2|)^2} - -\frac{1+\alpha k_1 \xi_3}{(1+\alpha k_1 \xi_3)^2 + \alpha^2 (\xi_1 + |\xi_2|)^2} \right], \tag{4-10}$$

$$u_3 = -\frac{AP\alpha^2(1+k_2^2)}{4\pi k_2} \frac{\xi_1 + |\xi_2|}{(1+\alpha k_2 \xi_3)^2 + \alpha^2 (\xi_1 + |\xi_2|)^2}$$
$$- \frac{AP\alpha^2}{2\pi \varepsilon^2} \left[\frac{(1+k_2^2)}{2k_2} \frac{\xi_1 + |\xi_2|}{(1+\alpha k_2 \xi_3)^2 + \alpha^2 (\xi_1 + |\xi_2|)^2} - k_1 \frac{\xi_1 + |\xi_2|}{(1+\alpha k_1 \xi_3)^2 + \alpha^2 (\xi_1 + |\xi_2|)^2} \right]. \tag{4-11}$$

We remark that keeping the $O(\varepsilon^2)$ terms in the elliptic equations (4-1), the full solution for the potential φ may be obtained via Poisson's formula for a half-space, giving

$$\varphi(\xi_1, \xi_2, \xi_3) = \frac{AP\xi_3}{4\pi^2 \varepsilon} \int_{-\infty}^{\infty} \int_{-\infty}^{\infty} \frac{\cot^{-1}(\alpha k_1(\eta_1 + \varepsilon|\eta_2|))}{[(\eta_1 - \xi_1/k_1)^2 + (\eta_2 - \xi_2/(\varepsilon k_1))^2 + \xi_3^2]^{3/2}} \, d\eta_1 \, d\eta_2. \tag{4-12}$$

We may now compare the approximate solution (4-4) with its full counterpart (4-12) for the longitudinal wave potential φ. We compare the normalised derivative $\Phi = (2\pi/AP)\partial\varphi/\partial\xi_2$ in Figure 5.

Let us now present the results for the sub-Rayleigh regime ($c < c_R$). The solution of (2-11) on the surface $x_3 = 0$ may be written as

$$\varphi(\xi_1, \xi_2, 0) = \frac{AP}{4\pi \varepsilon} \ln(\xi_1^2 + (\alpha^{-1} + |\xi_2|)^2). \tag{4-13}$$

The approximate solution over the interior follows, again, from the 2D Poisson formula giving

$$\varphi(\xi_1, \xi_2, \xi_3) = \frac{AP}{4\pi \varepsilon} \ln(\xi_1^2 + (|\xi_2| + k_1\xi_3 + \alpha^{-1})^2). \tag{4-14}$$

Figure 6. Derivatives of sub-Rayleigh full and approximate solutions for $a = 0.1$, $\varepsilon = 0.1$, $\xi_1 = -1$ and $\xi_3 = 1$.

The full solution of the sub-Rayleigh case may be expressed in an integral form as

$$\varphi(\xi_1, \xi_2, \xi_3) = \frac{AP\xi_3}{8\pi^2\varepsilon} \int_{-\infty}^{\infty} \int_{-\infty}^{\infty} \frac{\ln((\eta_1/\varepsilon)^2 + ((\varepsilon\alpha k_1)^{-1} + |\eta_2|)^2)}{[(\eta_1 - \xi_1/k_1)^2 + (\eta_2 - \xi_2/(\varepsilon k_1))^2 + \xi_3^2]^{3/2}} \, d\eta_1 \, d\eta_2. \tag{4-15}$$
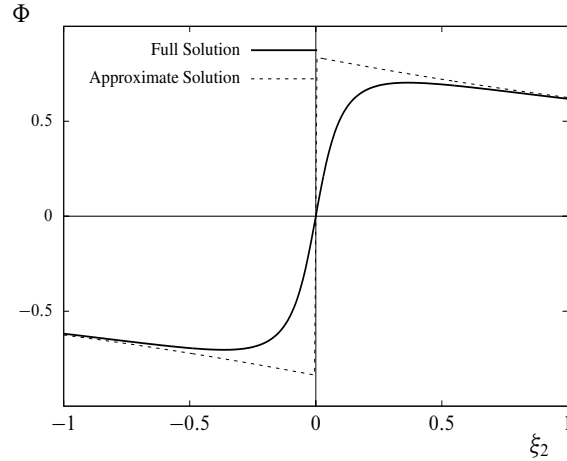
The numerical comparison of the normalised derivative of the full and approximate solutions, $\Phi = (4\pi\varepsilon/AP)\partial\varphi/\partial\xi_2$, is presented in Figure 6.

Following the procedure presented in detail for the super-Rayleigh case, potentials ψ_1 and ψ_2 are found to be

$$\psi_1(\xi_1, \xi_2, \xi_3) = \frac{AP(1 + k_2^2)}{4\pi\varepsilon k_2} \tan^{-1}\left(\frac{|\xi_2| + k_2\xi_3 + \alpha^{-1}}{\xi_1}\right), \tag{4-16}$$

$$\psi_2(\xi_1, \xi_2, \xi_3) = \frac{AP \operatorname{sgn}(\xi_2)(1 + k_2^2)}{8\pi k_2} \ln(\xi_1^2 + (|\xi_2| + k_2\xi_3 + \alpha^{-1})^2). \tag{4-17}$$

The resulting displacement components are

$$u_1 = \frac{1}{\varepsilon^2}\frac{AP}{2\pi}\left[\frac{\xi_1}{\xi_1^2 + (|\xi_2| + k_1\xi_3 + \alpha^{-1})^2} - \frac{1 + k_2^2}{2}\frac{\xi_1}{\xi_1^2 + (|\xi_2| + k_2\xi_3 + \alpha^{-1})^2}\right], \tag{4-18}$$

$$u_2 = \frac{1}{\varepsilon}\frac{AP \operatorname{sgn}(\xi_2)}{2\pi}\left[\frac{|\xi_2| + k_1\xi_3 + \alpha^{-1}}{\xi_1^2 + (|\xi_2| + k_1\xi_3 + \alpha^{-1})^2} - \frac{1 + k_2^2}{2}\frac{|\xi_2| + k_2\xi_3 + \alpha^{-1}}{\xi_1^2 + (|\xi_2| + k_2\xi_3 + \alpha^{-1})^2}\right], \tag{4-19}$$

$$u_3 = \frac{AP(1 + k_2^2)}{4\pi k_2}\frac{|\xi_2| + k_2\xi_3 + \alpha^{-1}}{\xi_1^2 + (|\xi_2| + k_2\xi_3 + \alpha^{-1})^2}$$
$$+ \frac{1}{\varepsilon^2}\frac{AP}{2\pi}\left[k_1\frac{|\xi_2| + k_1\xi_3 + \alpha^{-1}}{\xi_1^2 + (|\xi_2| + k_1\xi_3 + \alpha^{-1})^2} - \frac{1 + k_2^2}{2k_2}\frac{|\xi_2| + k_2\xi_3 + \alpha^{-1}}{\xi_1^2 + (|\xi_2| + k_2\xi_3 + \alpha^{-1})^2}\right]. \tag{4-20}$$
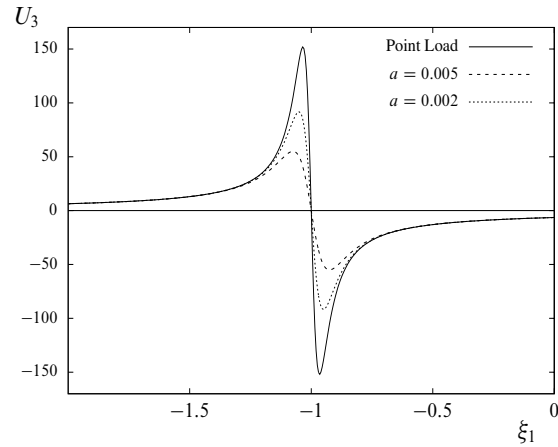
Figure 7. Super-Rayleigh vertical displacement versus ξ_1 for $a = 0.005$, $a = 0.002$ and the point load ($a = 0$).

5. Numerical comparison of solutions for point and distributed forces

In this section, we illustrate numerically the comparisons of the results for distributed load against those for point load discussed in [Kaplunov et al. 2013]. To this end, we set Poisson's ratio to $\nu = 0.25$ corresponding to the value $c_R = 0.9194c_2$. In the present problem, the load exhibits a gaussian-like profile, and as the parameter a approaches zero, the profile becomes a delta function moving along the x_1 axis. It is reasonable to expect, as a gets smaller, a considerable agreement between the displacements of both problems. We employ the same normalisation for the displacements presented in Section 5 of [Kaplunov et al. 2013], namely

$$U_i(\xi_1, \xi_2, \xi_3) = \frac{2\pi}{AP} u_i(\xi_1, \xi_2, \xi_3).$$
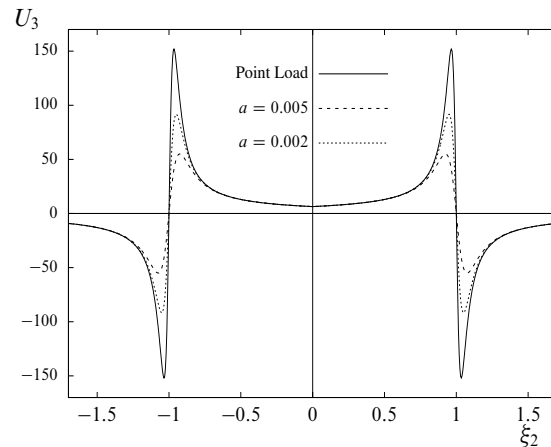

Figure 8. Super-Rayleigh vertical displacement versus ξ_2 for $a = 0.005$, $a = 0.002$ and the point load ($a = 0$).
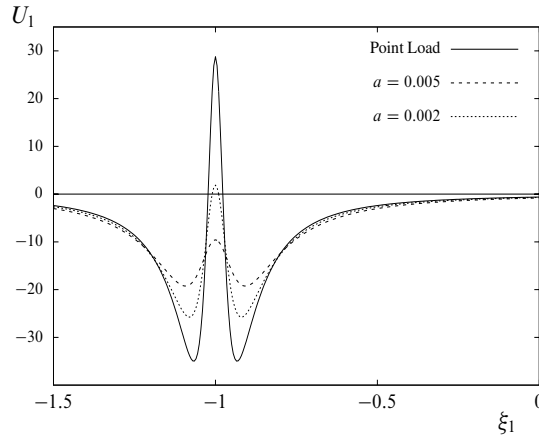
Figure 9. Super-Rayleigh horizontal displacement versus ξ_1 for $a = 0.005$, $a = 0.002$ and the point load ($a = 0$).

We first consider the super-Rayleigh case for which the load speed is taken as $c = 0.924c_2$ corresponding to $\varepsilon = 0.1$. Figure 7 displays comparisons of vertical displacements U_3 plotted against the moving coordinate ξ_1, with the depth being $\xi_3 = 0.1$. As expected, the singular behaviour under the point load corresponding to the coordinate $\xi_1 = -1$ is smoothed out by the distributed load, and it is clear that in the limit as $a \to 0$ we recover the solution for the point load problem. Figure 8 demonstrates the variation of the vertical displacement U_3 against the other horizontal variable ξ_2. Here, we take $\xi_1 = -1$ at depth $\xi_3 = 0.1$. A similar surface discontinuity is also evident here, which is again flattened for large values of a. Figure 9 presents a cross-section of displacement U_1. We observe that the delta-like profile near the singularity for the point load has been smoothed by the inclusion of the parameter a. Finally, numerical illustration for the sub-Rayleigh case is presented in Figure 10, which shows variation of the vertical displacement U_3 along the horizontal variable ξ_2. In the sub-Rayleigh case, the speed of the load is taken as $c = 0.9148c_2$, corresponding again to $\varepsilon = 0.1$.

Figure 10. Sub-Rayleigh vertical displacement versus ξ_2 for $a = 0.05$, $a = 0.01$ and the point load ($a = 0$).
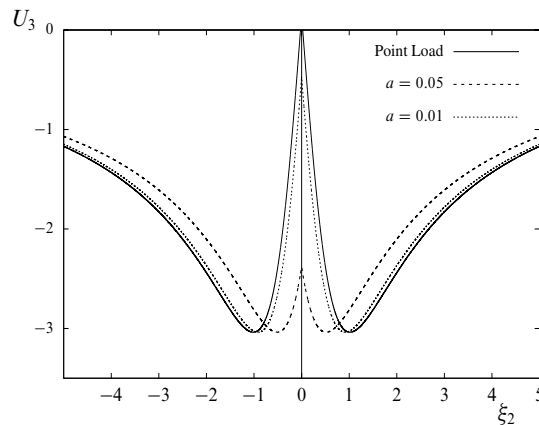
6. Concluding remarks

In this paper, a 3D problem for a distributional load of a gaussian-like profile moving along the surface of an elastic half-space is investigated. The hyperbolic-elliptic model in [Kaplunov and Prikazchikov 2013; Kaplunov et al. 2013] is specialised to tackle near-resonant behaviour ignoring the effect of longitudinal and transverse bulk waves. The presence of a small parameter expressing the proximity of the load speed to the Rayleigh wave speed enables us to reduce the 3D elliptic problems for the interior to 2D ones for the vertical cross-section along the load trajectory.

Various aspects of the Rayleigh wave causality are addressed. In contrast to the consideration in [Kaplunov et al. 2013], the steady-state location of the Mach cones, characteristic of the super-Rayleigh regime, is evaluated at a large time limit of the associated transient solution. Noncausality of the transverse wave potential, as well as the longitudinal wave potential over the interior, is due to the approximate nature of the adopted mathematical model.

The transition from the distributed load solution to the point load one is analysed numerically. As might be expected (see Figure 8), a distributed load smooths the singularities typical for a point load, e.g., those at Mach cones. We also mention that the effect of a distributed load is similar, in a sense, to that of an elastic coating [Erbaş et al. 2014].

A similar approach considered in this work may be readily extended to interfacial waves, e.g., Stoneley, Schölte, etc., and also to the media where the effects of prestress, layered structure and anisotropy are rather essential.

Acknowledgements

References

[Achenbach 1973] J. D. Achenbach, *Wave propagation in elastic solids*, Applied Mathematics and Mechanics **16**, North-Holland, Amsterdam, 1973.

[Achenbach 1998] J. D. Achenbach, "Explicit solutions for carrier waves supporting surface waves and plate waves", *Wave Motion* **28**:1 (1998), 89–97.

[Agostinacchio et al. 2013] M. Agostinacchio, D. Ciampa, M. Diomedi, and S. Olita, "Parametrical analysis of the railways dynamic response at high speed moving loads", *J. Mod. Transp.* **21**:3 (2013), 169–181.

[Cao et al. 2012] Y. Cao, H. Xia, and Z. Li, "A semi-analytical/FEM model for predicting ground vibrations induced by high-speed train through continuous girder bridge", *J. Mech. Sci. Technol.* **26**:8 (2012), 2485–2496.

[Celebi 2006] E. Celebi, "Three-dimensional modelling of train-track and sub-soil analysis for surface vibrations due to moving loads", *Appl. Math. Comput.* **179**:1 (2006), 209–230.

[Chadwick 1976] P. Chadwick, "Surface and interfacial waves of arbitrary form in isotropic elastic media", *J. Elasticity* **6**:1 (1976), 73–80.

[Courant and Hilbert 1962] R. Courant and D. Hilbert, *Methods of mathematical physics, II: Partial differential equations*, Wiley, New York, NY, 1962.

[Dieterman and Metrikine 1997] H. A. Dieterman and A. V. Metrikine, "Steady-state displacements of a beam on an elastic half-space due to a uniformly moving constant load", *Eur. J. Mech. A Solids* **16**:2 (1997), 295–306.

[El Kacimi et al. 2013] A. El Kacimi, P. K. Woodward, O. Laghrouche, and G. Medero, "Time domain 3D finite element modelling of train-induced vibration at high speed", *Comput. Struct.* **118** (2013), 66–73.

[Erbaş et al. 2013] B. Erbaş, J. D. Kaplunov, and D. A. Prikazchikov, "The Rayleigh wave field in mixed problems for a half-plane", *IMA J. Appl. Math.* **78**:5 (2013), 1078–1086.

[Erbaş et al. 2014] B. Erbaş, J. D. Kaplunov, D. A. Prikazchikov, and O. Şahin, "The near-resonant regimes of a moving load in a three-dimensional problem for a coated elastic half-space", *Math. Mech. Solids* (online publication October 2014).

[Galvín and Domínguez 2007] P. Galvín and J. Domínguez, "Analysis of ground motion due to moving surface loads induced by high-speed trains", *Eng. Anal. Bound. Elem.* **31**:11 (2007), 931–941.

[Gupta et al. 2010] S. Gupta, H. Van den Berghe, G. Lombaert, and G. Degrande, "Numerical modelling of vibrations from a Thalys high speed train in the Groene Hart tunnel", *Soil Dyn. Earthq. Eng.* **30**:3 (2010), 82–97.

[Kaplunov and Prikazchikov 2013] J. D. Kaplunov and D. A. Prikazchikov, "Explicit models for surface, interfacial and edge waves", pp. 73–114 in *Dynamic localization phenomena in elasticity, acoustics and electromagnetism*, edited by R. Craster and J. D. Kaplunov, International Centre for Mechanical Sciences Courses and Lectures **547**, Springer, Vienna, 2013.

[Kaplunov et al. 2006] J. D. Kaplunov, A. Zakharov, and D. A. Prikazchikov, "Explicit models for elastic and piezoelastic surface waves", *IMA J. Appl. Math.* **71**:5 (2006), 768–782.

[Kaplunov et al. 2010] J. D. Kaplunov, E. Nolde, and D. A. Prikazchikov, "A revisit to the moving load problem using an asymptotic model for the Rayleigh wave", *Wave Motion* **47**:7 (2010), 440–451.

[Kaplunov et al. 2013] J. D. Kaplunov, D. A. Prikazchikov, B. Erbaş, and O. Şahin, "On a 3D moving load problem for an elastic half space", *Wave Motion* **50**:8 (2013), 1229–1238.

[Kiselev and Parker 2010] A. P. Kiselev and D. F. Parker, "Omni-directional Rayleigh, Stoneley and Schölte waves with general time dependence", *Proc. R. Soc. Lond. A* **466**:2120 (2010), 2241–2258.

[Kiselev and Rogerson 2009] A. P. Kiselev and G. A. Rogerson, "Laterally dependent surface waves in an elastic medium with a general depth dependence", *Wave Motion* **46**:8 (2009), 539–547.

[Kiselev et al. 2007] A. P. Kiselev, E. Ducasse, M. Deschamps, and A. Darinskii, "Novel exact surface wave solutions for layered structures", *C. R. Mécanique* **335**:8 (2007), 419–422.

[Parker 2012] D. F. Parker, "Evanescent Schölte waves of arbitrary profile and direction", *Eur. J. Appl. Math.* **23**:2 (2012), 267–287.

[Parker 2013] D. F. Parker, "The Stroh formalism for elastic surface waves of general profile", *Proc. R. Soc. Lond. A* **469**:2160 (2013), Article ID #20130301.

[Poruchikov 1993] V. B. Poruchikov, *Methods of the classical theory of elastodynamics*, Springer, Berlin, 1993.

[Prikazchikov 2013] D. A. Prikazchikov, "Rayleigh waves of arbitrary profile in anisotropic media", *Mech. Res. Commun.* **50** (2013), 83–86.

[Rayleigh 1885] J. W. S. Rayleigh, "On waves propagated along the plane surface of an elastic solid", *Proc. Lond. Math. Soc.* **17** (1885), 4–11.

[Rousseau and Maugin 2011] M. Rousseau and G. A. Maugin, "Rayleigh surface waves and their canonically associated quasi-particles", *Proc. R. Soc. Lond. A* **467**:2126 (2011), 495–507.

[Zauderer 2006] E. Zauderer, *Partial differential equations of applied mathematics*, 3rd ed., Wiley, Hoboken, NJ, 2006.

BARIŞ ERBAŞ: berbas@anadolu.edu.tr
Department of Mathematics, Anadolu University, Yunusemre Campus, 26470 Eskişehir, Turkey

ONUR ŞAHIN: onur.sahin@anadolu.edu.tr
Department of Mathematics, Anadolu University, Yunusemre Campus, 26470 Eskişehir, Turkey

ON THE MODELING OF DISSIPATIVE MECHANISMS IN A
DUCTILE SOFTENING BAR

JACINTO ULLOA, PATRICIO RODRÍGUEZ AND ESTEBAN SAMANIEGO

The computational modeling of softening materials is still a challenging subject. An interesting way to deal with this problem is to adopt a variational framework. However, there are appealing features in using a classical approach. We explore the possibilities of both frameworks to include dissipative mechanisms. We start with a one-dimensional variational plastic-damage model rewritten in a classical framework, where regularization through viscoplasticity is applied. We highlight the appearance of an implicit internal length in the plastic strain field during the damage phase, allowing plasticity to evolve over a region before concentrating. Then, a consistent variational approach is adopted. A plastic strain gradient term is added to the global energy functional, with variable internal length coupled to the damage level. This model is further enriched by the addition of a hardening variable to the plastic evolution. A comparative analysis of the computational implementation of the different alternatives is performed.

1. Introduction

Classical fracture mechanics models are noteworthy for the description of existing cracks; however, the precursory state of the material is not provided by these theories [Lemaitre and Lippmann 1996]. Hence, the introduction of damage mechanics plays a major role in the representation of the evolution previous to the eventual macroscopic crack. According to Krajcinovic [1989], the deterioration of a material can be described in at least three levels of scale. The treatment of the first, corresponding to the atomic level, requires noncontinuum mechanics. The second level is related to the formation of microcracks and microvoids and is treated via continuum damage mechanics. On the other hand, the third scale corresponds to the macroscopic level and is treated by classical fracture models. In this work, the second level of scale is considered, and the softening mechanism of damage is coupled to plasticity to capture ductile failure. Furthermore, the thermodynamics of internal variables is applied to build the model in a physically consistent manner, which stems out from [Maugin 1992; Maugin and Muschik 1994]. Representing ductile behavior in a softening regime is a challenging task that has not been widely explored in past efforts in a variational setting [Ambati et al. 2015]. For a comprehensive account of material failure, the reader is referred to [Bigoni 2012].

The capacity to simulate the strain localization phenomenon and hence, the appearance of discontinuities in the displacement field that characterizes fracture, is an attractive feature of local softening models [Oliver et al. 2002]. However, its use has been known to result in ill-posed problems, returning mesh-dependent solutions and spurious localization, which are meaningless material responses [De Borst and Mühlhaus 1992]. This problem has been widely treated and several methods have been employed.

Keywords: material modeling, dissipative materials, plasticity, damage, classical approach, variational formulation.

Relying on the introduction of discontinuous functions in the description of the displacement field, several techniques have shown fruitful results. The strong discontinuity approach and the extended finite element method discussed in [Oliver et al. 2002; 2003; Moës et al. 1999] have been applied to the modeling of fracture and strain concentration in [Oliver et al. 2004; Chen et al. 2011; Samaniego and Belytschko 2005]. Another interesting treatment can be seen in the multiple scale analytical approach found in [Garikipati and Hughes 1998]. The concept is applied in an adaptive-mesh strategy for a local plastic-damage model in [Venini and Morana 2001].

In other approaches, modifications to the constitutive equations are made to include nonlocal effects, ranging from rate-dependent viscoplastic regularization (see [Needleman 1988]) to gradient-enhanced models, where nonlocal treatments furnish fruitful results (see [Bažant and Jirásek 2002] for nonlocal formulations). All of these are, to some degree, based on the introduction of an internal length scale as a material's characteristic property [Borst et al. 1993].

The application of regularization to simulate fracture is of great interest and has been treated in several works. The introduction of a gradient term was first proposed in [Triantafyllidis and Aifantis 1986], and has been widely applied to nonlocal energy functionals. The derivation of a gradient regularization for a phase-field fracture model can be seen in [Miehe et al. 2010]. A phase-field model for ductile fracture is proposed in [Ambati et al. 2015]. Softening gradient-dependent plasticity models are analyzed in [Jirásek and Rolshoven 2009a; 2009b], and with verification of experimental results in [Lancioni 2015]. Both gradient-dependent plasticity and gradient-dependent damage models are analyzed in [de Borst et al. 1999]. Furthermore, gradient-dependent variational models are proven to converge to the Griffith fracture model in [Bourdin et al. 2008] through Γ convergence. Thus, regularization via the internal length represents the transition between discontinuous fracture models and regularized models [Ambati et al. 2015]. On the other hand, a viscoplastic regularization of local damage can be seen in [Niazi et al. 2013] and a study of a model that includes rate-dependent perturbations and gradient terms is carried out in [Dal Corso and Willis 2011].

This work picks up from the variational gradient damage model coupled to perfect plasticity proposed by Alessi [2013; 2014], which was initially developed in [Pham and Marigo 2010a; 2010b] for brittle fracture. The variational approach follows the regularization of [Bourdin et al. 2008] for the energy minimization approach of the Griffith model that was proposed in [Francfort and Marigo 1998]. The energetic formulation that is applied comes from [Mainik and Mielke 2005; Mielke 2006] for rate-independent systems. As pointed out in [de Borst et al. 1999], the coupling of plasticity to damage is physically appealing due to the capability of representing a wide range of materials that deteriorate with a combination of void nucleation and plastic strains. The model in [Alessi 2013; Alessi et al. 2014] is capable of capturing different behaviors, from where we highlight the following evolution:

(1) An initial elastic phase.

(2) A homogeneous perfect plasticity phase.

(3) A plasticity and damage coupled phase with a strain localization region, where a jump in the displacement field appears with nonvanishing stress. Then, a cohesive crack forms at the center of the localization zone.

The variational formulation furnishes a natural numerical implementation that results in an *alternate minimization algorithm*, which is applied to minimize a global energy functional [Mumford and Shah

1989]. However, the use of global energy functionals could lead to nonphysical results [Bourdin et al. 2008]. For instance, a homogeneous damage evolution, which is possible in this context, would be a clearly nonphysical response for a deteriorating material. Despite this, several advantages of this treatment are observed in this work. For example, plasticity is able to evolve uniformly during the perfect plasticity phase, without a regularization method [Alessi 2013]. Contrary to the classical approach, the variational model conserves the local constitutive equations without the necessity of introducing nonlocal effects in this stage.

In this work, this model is rewritten in a classical framework, where the evolution of the system is defined using the algorithm discussed in [Simo and Hughes 1998]. Here, the balance of the linear momentum equation is solved to determine the displacement field over the body. In this approach, it becomes evident that the perfect plasticity model lacks uniqueness and requires local regularization. In order to conserve the structure of the algorithm in [Simo and Hughes 1998] and to maintain a local definition of the plastic variables (see [Borja 2013] and [Runesson 2006] for local plasticity and damage formulations), the viscoplasticity model, also discussed in [Simo and Hughes 1998], is adopted instead of the perfect plasticity model. Although rate-dependence is introduced in the evolution of the system with this regularization, it is shown numerically that as the loading rate tends to zero, the response converges to the variational model in [Alessi 2013]. One feature observed in the simulations of the viscoplastic regularized evolution is worth highlighting: the appearance of an implicit internal length scale in the plastic strain field that varies with the loading rate. As we will see in Section 4, this allows plasticity to evolve over a determined region during the plasticity-damage phase.

To develop this feature in a more consistent manner, and taking advantage of the capacity of the variational approach to incorporate new characteristics in the model by (eventually) adding new terms to the global energy functional, the following original contributions are incorporated in this work:

(1) The addition of a hardening variable coupled to damage to capture additional material responses and the analysis of the resulting local evolution.

(2) The addition of a plastic strain gradient term to the global model.

(3) The application of a variable plastic strain internal length depending on the damage variable. A threshold damage level is introduced to control when the plastic internal length drops to zero.

(4) The numeric solution of the complete gradient-dependent damage and gradient-dependent hardening plasticity model.

The first new feature enables the model to capture material behaviors with a hardening plastic phase, which is common in metals. Then, the incorporation of the plastic strain gradient term allows plasticity to evolve in a controlled region via the internal length. If Neumann boundary conditions are imposed on the plastic strain field, plasticity will first evolve homogeneously, and Dirichlet boundary conditions are necessary on the damage field to trigger a nonhomogeneous evolution. As pointed out in [Bigoni 2012], several material evolutions initially present a homogeneous deformation, until bifurcation and instabilities appear. Then, only after extreme loading, strain localizations take place. In this case, these are due to plasticity and damage and a localized response is not induced until softening occurs in the damage phase. In the case of Neumann bounded plasticity, the distribution of plastic strains remains homogeneous until softening. Similar results have been obtained in [Dal Corso and Willis 2011] for

an approach involving perturbations, where plastic strains begin to localize in the defects during the softening regime. Then, the plastic strain internal length is allowed to vary as a decreasing function of the damage level, simulating the necking phenomenon of a deteriorating material with strain localization. Moreover, the damage threshold value deactivates the effect of the plastic internal length when desired, changing the jump in the displacement field from a relatively smooth behavior to an abrupt evolution and localizing the plastic strains at the center of the bar. It is worth mentioning that the plastic strain gradient does not replace the damage gradient and both terms are used. This is because a local damage evolution will cause an abrupt localization of damage and an instantaneous rupture as soon as the damage phase begins.

The main novelty of this work lies in the fact that the mechanisms described above have been carefully added within a thermodynamically consistent variational framework, enriching the model presented in [Alessi 2013], which only considers local perfect plasticity and gradient damage. A similar effort can be found in [Ambati et al. 2015], which builds over [Duda et al. 2015]. There, gradient damage is coupled to hardening plasticity by heuristically modifying the original energy functional. By contrast, in our contribution, new coupling terms and a new gradient term (gradient plasticity with a variable internal length) are consistently added within the same rigorous framework used to build the model in [Alessi 2013]. Additionally, the problem has been treated in a classical setting with viscoplasticity, and the numerical solution for both frameworks is presented. The results of the time-dependent model are qualitatively compared to the variational model with gradient-enhanced plasticity.

The first section of this work consists of the classical formulation of the elastic-plastic-damage problem. The standard local models for perfect plasticity and viscoplasticity, as well as the numeric implementation of the global response are briefly explored. Then, the gradient-dependent damage model is coupled to the elastic-plastic evolution, and the computational implementation is presented, where the finite element method is used with linear approximations on the displacement and damage fields. The next section is devoted to the explicit enrichment of the variational model. First, the hardening variable is added to the local evolution and the resulting response is analyzed. Then, the plastic strain gradient term is added to the nonlocal functional. The resulting formulation is solved through the finite element method with quadratic approximations on the displacement field, and the computational implementation is presented. For both approaches, the model is implemented in a one-dimensional fashion for a bar with Dirichlet boundary conditions: one end is constrained and displacements are imposed on the other. For simplicity and without losing generality, an initially virgin material is considered and only monotonic loading is applied. The small strain theory is applied, and the decomposition of the total strain,

$$\epsilon = \epsilon_e + \epsilon_p,$$

is considered, where ϵ_e and ϵ_p are the elastic and plastic strains, respectively.

2. Classical approach

This section is devoted to the classical formulation of the plastic-damage model in [Alessi 2013]. Although mathematically equivalent to the energetic formulation for the plastic-damage response, the classical approach leads to a different numerical model. While the damage field is still given by the nonlocal

gradient criterion, both the displacement field and the plastic strain field are found simultaneously by the standard Newton–Raphson method, which can be found in [Simo and Hughes 1998; Borja 2013].

As mentioned, the problem of perfect plasticity in a classical approach requires regularization. The Newton–Raphson method distributes the displacements along the bar by obtaining the plastic strain field locally via a standard *return mapping algorithm* and verifying equilibrium. Thus, once the yield stress is reached, there is an infinite number of admissible solutions. Specifically, strains localize in the element where the displacement is imposed. Because of this, a viscoplastic model is used as a regularization to approximate the perfect plasticity phase.

2.1. *Perfect plasticity model and viscoplastic regularization.*

2.1.1. *Governing equations.* The perfect plasticity and viscoplastic models that are briefly explored can be seen in [Simo and Hughes 1998; Runesson 2006], and the numeric implementation is developed in [Simo and Hughes 1998]. The free energy is defined locally as

$$\Psi(\epsilon, \epsilon_{\mathrm{p}}) = \frac{1}{2} E (\epsilon - \epsilon_{\mathrm{p}})^2, \tag{2-1}$$

with E as the elastic modulus, from where the constitutive equations

$$\sigma = \frac{\partial \Psi}{\partial \epsilon} = E(\epsilon - \epsilon_{\mathrm{p}}), \quad \sigma_{\mathrm{p}} = -\frac{\partial \Psi}{\partial \epsilon_{\mathrm{p}}} = E(\epsilon - \epsilon_{\mathrm{p}}) \equiv \sigma,$$

are obtained. The quasistatic yield criterion is defined as

$$f(\epsilon, \epsilon_{\mathrm{p}}) = f(\sigma) = |\sigma| - \sigma_{\mathrm{p}}, \tag{2-2}$$

where σ_{p} is the initial yield stress. In the case of rate-independent plasticity, one has $f(\epsilon, \epsilon_{\mathrm{p}}) \leq 0$. Hence, after defining the plastic multiplier $\lambda = |\dot{\epsilon}_{\mathrm{p}}|$, the Kuhn–Tucker conditions

$$\lambda \geq 0, \quad f(\sigma) \leq 0, \quad \lambda f(\sigma) = 0, \tag{2-3}$$

follow. The actual value of the plastic multiplier λ is found via the consistency conditions and the plastic flow rule, which reads as

$$\dot{\epsilon}_{\mathrm{p}} = \lambda \frac{\partial}{\partial \sigma} f(\sigma) = \lambda \operatorname{sign} \sigma. \tag{2-4}$$

The consistency conditions are a function of $\dot{f}(\sigma)$, where one has

$$\dot{f}(\sigma) \leq 0, \quad \lambda \geq 0, \quad \dot{f}(\sigma) \lambda = 0. \tag{2-5}$$

The plastic response is then given by equations (2-3), (2-4) and (2-5).

On the other hand, the yield criterion defined in (2-2) is allowed to exceed the yield surface for the viscoplastic model, where $|\sigma| > \sigma_{\mathrm{p}}$. The additional stress is accounted for by the *overstress*, defined as

$$\sigma_{\mathrm{ex}} = (|\sigma| - \sigma_{\mathrm{p}}) \operatorname{sign}(\sigma) = f(\sigma) \operatorname{sign}(\sigma).$$

Defining the viscous relationship $\sigma_{\mathrm{ex}} = \upsilon \dot{\epsilon}_{\mathrm{p}}$, where υ is the viscosity constant, the evolution of the plastic strain is given by

$$\dot{\epsilon}_{\mathrm{p}} = (\sigma - \sigma_{\mathrm{p}})/(E\tau),$$

where $\tau = \upsilon / E$ is the relaxation time, which can be interpreted as a factor that determines the rate at which the overstress tends to zero and the stress tends to the yield stress, recovering the plastic rate-independent response.

These models are solved computationally in a discrete fashion, where the state of the system is given at time n by the set of variables $(\sigma_n, \epsilon_{p_n})$, and the goal is to determine the updated variables $(\sigma_{n+1}, \epsilon_{p_{n+1}})$ at time $n + 1$ via standard *return mapping algorithms*. The steps are summarized in the local algorithms found in [Simo and Hughes 1998].

2.1.2. *Energy dissipation.* From the Clausius–Duhem inequality, one has

$$\sigma \dot{\epsilon} - \dot{\Psi} \geq 0$$

which, for the viscoplastic model, leads to

$$\Phi = |\dot{\epsilon_p}|(\sigma_p + \sigma_{ex}) = |\dot{\epsilon_p}|\sigma_p(1 + \upsilon|\dot{\epsilon_p}|/\sigma_p) \geq 0.$$

Again, note that as υ tends to zero, the dissipation potential tends to the rate-independent plastic potential, which reads as

$$\Phi = |\dot{\epsilon_p}|\sigma_p.$$

2.1.3. *Global iterative solution.* Once the local evolution is defined, the global response is obtained through the finite element method in a Newton–Raphson iterative procedure.

Consider a one-dimensional body occupying a space $\Omega = [0, L]$. The initial boundary-value problem is defined by the boundary conditions, which are only imposed in the displacement field:

$$u(0, t) = 0, \quad u(L, t) = \bar{u}(t) \, \forall \, t \in [0, T],$$

where $\bar{u}(t)$ is the imposed displacement and $t \in [0, T]$ is an arbitrary time in the interval where displacements are imposed.

The initial boundary-value problem stems out from the balance of linear momentum, and reads as

$$\rho \frac{\partial v}{\partial t} - b_f - \frac{\partial \sigma}{\partial x} = 0.$$

The first term is eliminated once the dynamic effects have been neglected and the second term equals zero once the absence of external loads has been considered. Then, after introducing the test function w, with $w\big|_0^L = 0$, the weak form is

$$\int_0^L \sigma \frac{\partial w}{\partial x} dx = 0. \tag{2-6}$$

The approximation functions $w^h(x) = \sum_{i=1}^n w_i N_i(x)$ and $\sigma^h(x, t)$ are considered, with shape functions contained in vectors $\boldsymbol{N}$ and $\boldsymbol{B} = d\boldsymbol{N}/dx$. Then, from (2-6), the matrix form of the problem is

$$\int_0^L \boldsymbol{w}^T \sigma^h \boldsymbol{B}^T dx = \boldsymbol{w}^T \int_0^L \sigma^h \boldsymbol{B}^T dx = \boldsymbol{w}^T [\boldsymbol{F}^{int}] = 0$$

which, because of the boundary conditions in w, results in

$$\boldsymbol{R} = \begin{bmatrix} F_2^{\text{int}} \\ \vdots \\ F_{n-1}^{\text{int}} \end{bmatrix} = 0. \tag{2-7}$$

In the case of a linear elastic response, the stress field is simply given by $\sigma = E\epsilon$. On the other hand, a nonlinear behavior is given by nonlinear local models, such as the constitutive models explored in the previous section. The global response is then obtained through the iterative Newton–Raphson procedure, which can be found in [Simo and Hughes 1998; Borja 2013]. Essentially, a displacement vector is found that results in a convergence vector given by (2-7) and meets a certain tolerance.

2.2. *Damage coupling.* In this section, the damage criterion is presented in a classical framework, where the evolution of the damage variable $\alpha \in [0, 1)$ is coupled to the plastic evolution. The damage criterion can be expressed as

$$f_{\text{d}} = a(\hat{\sigma}) - g(\alpha, p, \alpha'') \leq 0,$$

where a is the dissipative force of the damage variable, $\hat{\sigma}$ is the effective stress, which stems out from the equivalent strain principle, and $p = \int_0^t |\dot{\epsilon}_{\text{p}}(x, \tau)| d\tau$ is the accumulated plastic strain. The criterion is expressed as

$$f_{\text{d}} = a(\hat{\sigma}) - w'(\alpha) + pm(\alpha) + \eta_{\text{d}}^2 \alpha'' \leq 0, \tag{2-8}$$

where $w(\alpha)$ is related to the damage dissipation and η_{d} corresponds to the internal length. The term $m(\alpha)$ allows the coupling between damage and plasticity, where $m(\alpha) > 0 \, \forall \, \alpha \in [0, 1)$ is defined. Equation (2-8) has been adopted from [Alessi 2013] and represents the nonlocal damage criterion that is solved through the finite element method. As in [Alessi 2013], the constitutive functions

$$E(\alpha) = E_0(1-\alpha)^2, \quad w(\alpha) = w_0\alpha, \quad m(\alpha) = -\sigma_{\text{p}_0}'(\alpha), \quad \sigma_{\text{p}}(\alpha) = \sigma_{\text{p}_0}(1-\alpha)^2, \tag{2-9}$$

are applied, where E_0 is the initial elastic modulus and σ_{p_0} is the initial plastic yield stress. Replacing in (2-8),

$$f_{\text{d}} = E_o(\epsilon - \epsilon_{\text{p}})^2(1-\alpha) - w_o + 2\sigma_{y_o}(1-\alpha)p + \eta_{\text{d}}^2\alpha'' \leq 0.$$

The first term in the previous expression corresponds to the dissipative force $a(\hat{\sigma})$. It is the result of taking the derivative of the free energy with respect to the damage variable once the damage effect $(1-\alpha)^2$ has been multiplied by the elastic modulus in (2-1). The effective stress takes the form $\hat{\sigma} = \sigma/(1-\alpha)^2$. In order to break the homogeneity of the bar, the Dirichlet boundary conditions

$$\alpha(0, t) = \alpha(L, t) = 0$$

are applied. Additionally, a response capable of recovering stiffness is not considered; hence, the irreversibility condition

$$\alpha(t_i) \leq \alpha(t_j) \, \forall \, i \leq j \tag{2-10}$$

is applied. The weak form of the damage criterion reads as

$$\int_0^L E_o(1-\alpha)(\epsilon - \epsilon_{\text{p}})^2 w \, dx - \int_0^L w_o w \, dx + \int_0^L 2\sigma_{y_o}(1-\alpha)pw \, dx + \int_0^L \eta_{\text{d}}^2 \frac{\partial^2 \alpha}{\partial x^2} w \, dx = 0,$$

which leads to the following matrix form:

$$
\boldsymbol{w}^T \int_0^L \boldsymbol{N}^T E_o (\epsilon - \epsilon_{\mathrm{p}})^2 \, \mathrm{d}x - \boldsymbol{w}^T \int_0^L \boldsymbol{N}^T E_o (\epsilon - \epsilon_{\mathrm{p}})^2 \boldsymbol{N} \, \mathrm{d}x \boldsymbol{\alpha} - \boldsymbol{w}^T \int_0^L \boldsymbol{N}^T w_o \, \mathrm{d}x
$$
$$
+ \boldsymbol{w}^T \int_0^L 2\sigma_{y_o} p \boldsymbol{N}^T \, \mathrm{d}x - \boldsymbol{w}^T \int_0^L 2\sigma_{y_o} p \boldsymbol{N}^T \boldsymbol{N} \, \mathrm{d}x \boldsymbol{\alpha} - \boldsymbol{w}^T \int_0^L \boldsymbol{B}^T \eta_{\mathrm{d}}^2 \boldsymbol{B} \boldsymbol{\alpha} \, \mathrm{d}x = 0.
$$

The following vectors and matrices are obtained:

$$
\boldsymbol{E}_{\mathrm{d}} = \int_0^L \boldsymbol{N}^T E_o (\epsilon - \epsilon_{\mathrm{p}})^2 \, \mathrm{d}x, \quad \boldsymbol{L}_{\mathrm{d}} = \int_0^L \boldsymbol{N}^T E_o (\epsilon - \epsilon_{\mathrm{p}})^2 \boldsymbol{N} \, \mathrm{d}x,
$$
$$
\boldsymbol{W}_{\mathrm{d}} = \int_0^L \boldsymbol{N}^T w_o \, \mathrm{d}x, \qquad\quad \boldsymbol{S}_{\mathrm{d}} = \int_0^L 2\sigma_{y_o} p \boldsymbol{N}^T \, \mathrm{d}x,
$$
$$
\boldsymbol{M}_{\mathrm{d}} = \int_0^L 2\sigma_{y_o} p \boldsymbol{N}^T \boldsymbol{N} \, \mathrm{d}x, \qquad \boldsymbol{J}_{\mathrm{d}} = \int_0^L \boldsymbol{B}^T \eta_{\mathrm{d}}^2 \boldsymbol{B} \boldsymbol{\alpha} \, \mathrm{d}x,
$$

from where the nodal values of α are obtained as

$$
\boldsymbol{\alpha} = [-\boldsymbol{J}_{\mathrm{d}} - \boldsymbol{L}_{\mathrm{d}} - \boldsymbol{M}_{\mathrm{d}}]^{-1} [\boldsymbol{W}_{\mathrm{d}} - \boldsymbol{S}_{\mathrm{d}} - \boldsymbol{E}_{\mathrm{d}}]. \tag{2-11}
$$

2.3. *Computational implementation.* The elastic-plastic response in Section 2.1.3. is coupled to the damage evolution, where the plastic yield surface is now

$$
f_{\mathrm{p}} = |\sigma| - \sigma_{\mathrm{p}}(\alpha) \le 0,
$$

and the stress is $\sigma = E(\alpha)(\epsilon - \epsilon_{\mathrm{p}})$. The global elastic-plastic-damage response is obtained with the following considerations:

- The displacements are imposed gradually, where n_{desp} is the number of imposed displacements.
- Two convergence criteria are applied: the sum of the internal forces with tolerance $\mathrm{tol}_{\mathrm{p}}$ for the elastic-plastic problem and L_∞ norm with tolerance $\mathrm{tol}_{\mathrm{d}}$ for the damage problem.

The procedure is presented in Algorithm 1, which resembles the procedure used in [Almansba et al. 2010].

3. Variational approach

This section is devoted to the enrichment of the variational plastic-damage model in [Alessi 2013]. First, the hardening variable is added to the local coupled model and the resulting formulation is investigated, where the conditions for the different possible responses are explored. Because of the local treatment, no variational tools are required in this subsection. In the next subsection, as well as in the numeric implementation that follows, the variational approach is illustrated with the nonlocal gradient model that is developed with the addition of the plastic strain gradient term.

The complete material response consists of the following stages:

(1) An initial elastic phase.

(2) A homogeneous hardening plastic phase with zero Neumann boundary conditions, or a smooth distribution of plastic strains with zero Dirichlet boundary conditions.

1:   **for** $n = 1$ **to** n_{desp} **do**

2:      Initialize
     $k = 0$;

3:      **while** $||\boldsymbol{\alpha}_n^k - \boldsymbol{\alpha}_n^{k-1}||_\infty > \text{tol}_{\text{d}}$ **and** $k \leq \text{itmax}$ **do**

4:         Initialize
        $j = 0, \quad \Delta \boldsymbol{d}_n^j = \boldsymbol{0}$;

5:         **while** $||\boldsymbol{R}_n^j||_1 > \text{tol}_{\text{p}}$ **and** $k \leq \text{itmax}$ **do**

6:            Initialize the stiffness matrix and the internal force vector
           $\boldsymbol{K}_n^j = \boldsymbol{\Gamma}, \quad \boldsymbol{F}_n^{\text{int}^j} = \boldsymbol{\Gamma}$;

7:            **for** $e = 1$ **to** n_{el} **do**

8:               Obtain the average damage per element $\bar{\alpha}$

9:               Obtain $\{\sigma, \epsilon, \epsilon_{\text{p}}, p\}$ via one of the local models, as well as the corresponding tangential
              modulus introducing $E(\bar{\alpha})$ and $\sigma_y(\bar{\alpha})$

10:            Update $\boldsymbol{F}_n^{\text{int}^j}$ and $\boldsymbol{K}_n^j$

11:            **end for**

12:            **if** $||\boldsymbol{R}_n^j||_1 > \text{tol}_{\text{p}}$ **then**

13:               Obtain the incremental nodal displacements for the next iteration
              $\Delta \boldsymbol{d}_n^j = \Delta \boldsymbol{d}_n^j - [\boldsymbol{K}_n^j]^{-1}[\boldsymbol{R}_n^j]$;

14:               $j = j + 1$

15:            **end if**

16:         **end while**

17:         Obtain the nodal damage values $\boldsymbol{\alpha}$ via (2-11)

18:         **if** $||\boldsymbol{\alpha}_n^k - \boldsymbol{\alpha}_n^{k-1}||_\infty > \text{tol}_{\text{d}}$ **then**

19:            $k = k + 1$

20:         **end if**

21:      **end while**

22: **end for**

Algorithm 1. Classical approach elastic-plastic-damage algorithm.

---

(3) A coupled plastic-damage phase, with a nonhomogenous distribution of both fields. If Neumann
boundary conditions are imposed in the plastic phase, Dirichlet boundary conditions are necessary
in the damage field to break the homogeneity of the bar. Each variable will distribute according
to its own internal length with a maximum at the center of the bar, with the plastic internal length
decreasing as a function of the damage level.

(4) A localization of the plastic strain evolution at the center of the bar as soon as a threshold level of
damage has been reached in the bar.

3.1. *Local model with hardening plasticity.* In this subsection, the analytical governing equations are
presented for the local coupled model. The work carried out is adopted from [Alessi 2013] and the
hardening variable is incorporated in the procedure.

3.1.1. *General model.* The free energy is defined locally as

$$\Psi = \frac{1}{2} E(\alpha)(\epsilon - \epsilon_{\mathrm{p}})^2 + \frac{1}{2} H(\alpha) p^2, \tag{3-1}$$

where the hardening component has been added to the free energy given by (2-1) for perfect plasticity. A plastic hardening variable $\kappa = |\epsilon_{\mathrm{p}}| = p$ is considered with a plastic modulus $H(\alpha)$.
Then, the stress-strain relation becomes

$$\sigma(\epsilon_{\mathrm{p}}, \alpha) = E(\alpha)(\epsilon - \epsilon_{\mathrm{p}}). \tag{3-2}$$

The plasticity yield criterion f_{p} and the damage criterion f_{d} read as

$$f_{\mathrm{p}}(\sigma, p, \alpha) = |\sigma| - [\sigma_{\mathrm{p}}(\alpha) + H(\alpha)p] \leq 0, \tag{3-3}$$

$$f_{\mathrm{d}}(\sigma, p, \alpha) = -\frac{1}{2} E'(\alpha)(\epsilon - \epsilon_{\mathrm{p}})^2 - \frac{1}{2} H'(\alpha) p^2 - \sigma_{\mathrm{p}}'(\alpha) p - w_0 \leq 0, \tag{3-4}$$

where the following properties are defined for each term:

$$E(\alpha) > 0, \quad E'(\alpha) < 0 \,\forall\, \alpha \in [0, 1),$$
$$H(\alpha) > 0, \quad H'(\alpha) < 0 \,\forall\, \alpha \in [0, 1),$$
$$\sigma_{\mathrm{p}}(\alpha) > 0, \quad \sigma_{\mathrm{p}}'(\alpha) < 0 \,\forall\, \alpha \in [0, 1).$$

The local evolution is given by the Kuhn–Tucker conditions and the consistency conditions for each yield surface. Moreover, from (3-3) and (3-4), the yield stresses are

$$\sigma_{\mathrm{yp}}(p, \alpha) = \sigma_{\mathrm{p}}(\alpha) + H(\alpha)p, \tag{3-5}$$

$$\sigma_{\mathrm{yd}} = \sqrt{\frac{w_0 + \sigma_{\mathrm{p}}'(\alpha) p + 1/2 H'(\alpha) p^2}{-1/2 E'(\alpha) E(\alpha)^{-2}}}. \tag{3-6}$$

Then, the evaluation of the consistency conditions is required. For this, one uses

$$\dot{f}_{\mathrm{p}}(\sigma, p, \alpha) = E(\alpha)(\dot{\epsilon} - \dot{\epsilon}_{\mathrm{p}}) \operatorname{sign}(\sigma) + \big(E'(\alpha)(\epsilon - \epsilon p) - \sigma_{\mathrm{p}}'(\alpha) - H'(\alpha)p\big)\dot{\alpha} - H(\alpha)\dot{p}, \tag{3-7}$$

$$\dot{f}_{\mathrm{d}}(\sigma, p, \alpha) = E(\alpha)(\dot{\epsilon} - \dot{\epsilon}_{\mathrm{p}}) - (\sigma_{\mathrm{p}}'(\alpha) + H'(\alpha)p)\dot{p}$$
$$- \left(\frac{1}{2} E''(\alpha)(\epsilon - \epsilon_{\mathrm{p}})^2 + \frac{1}{2} H''(\alpha) p^2 + \sigma_{\mathrm{p}}''(\alpha) p\right)\dot{\alpha}. \tag{3-8}$$

The material response consists of three stages: an elastic phase, a first dissipation phase and a second dissipation phase. These are analyzed next considering increasing monotonic loading.

Elastic phase. An elastic phase is defined by $\sigma < \min(\sigma_{\mathrm{yp}}(0, 0), \sigma_{\mathrm{yd}}(0, 0))$. The next phase, which begins at a certain stress level, can consist of one of two possible evolutions:

- <u>E-P-*:</u> $\sigma = \sigma_{\mathrm{yp}}(0, 0) < \sigma_{\mathrm{yd}}(0, 0)$. From the stress-strain relation (3-2), the strain at which the plastic phase begins is

$$\epsilon = \epsilon_{\mathrm{yp}} = \sigma_{\mathrm{p}}(0)/E(0).$$

- E-D-*: $\sigma = \sigma_{\mathrm{yd}}(0,0) < \sigma_{\mathrm{yp}}(0,0)$. The damage phase begins at the strain level

$$\epsilon = \epsilon_{\mathrm{yd}} = \sqrt{w_0/-E'(0)}.$$

First dissipation. It begins with $\sigma = \min(\sigma_{\mathrm{yp}}(0,0), \sigma_{\mathrm{yd}}(0,0))$. The two possible evolutions are analyzed:

- E-P-*: $(\epsilon_{\mathrm{yp}} \leq \epsilon < \epsilon_{\mathrm{yd}})$. Therefore, one has

$$\sigma = \sigma_{\mathrm{yp}}(0,0) < \sigma_{\mathrm{yd}}(0,0),$$
$$f_{\mathrm{p}}(\sigma,0,0) = 0,$$
$$f_{\mathrm{d}}(\sigma,0,0) < 0.$$

  For a loading condition, the evolution is obtained through the consistency conditions from (3-7), where

$$\dot{f}_{\mathrm{p}}(\sigma, p, 0) = E(0)(\dot{\epsilon} - \dot{\epsilon}_{\mathrm{p}}) - H(0)\dot{p} = 0.$$

  The second dissipation phase begins at the strain level

$$\epsilon = \epsilon_{\mathrm{yd}} = \sqrt{\frac{w_0 + \sigma_{\mathrm{p}}'(0)p + 1/2 H'(0)p^2}{-1/2 E'(0)}} + \epsilon_{\mathrm{p}}.$$

- E-D-*: $(\epsilon_{\mathrm{yd}} \leq \epsilon < \epsilon_{\mathrm{yp}})$. Therefore, one has

$$\sigma = \sigma_{\mathrm{yd}}(0,0) < \sigma_{\mathrm{yp}}(0,0),$$
$$f_{\mathrm{p}}(\sigma,0,0) < 0,$$
$$f_{\mathrm{d}}(\sigma,0,0) = 0,$$

  and the consistency conditions are investigated through (3-8), which yields

$$\dot{f}_{\mathrm{d}}(\sigma, 0, \alpha) = -E'(\alpha)\epsilon\dot{\epsilon} - \frac{1}{2}E''(\alpha)\epsilon^2\dot{\alpha} = 0,$$

  which is admissible given $E''(\alpha) > 0$. The second dissipation phase begins at the strain level

$$\epsilon = \epsilon_{\mathrm{yp}} = \sigma_{\mathrm{p}}(\alpha)/E(\alpha).$$

  Notice that if $\sigma_{\mathrm{yd}}(0, \alpha) < \sigma_{\mathrm{yp}}(0, \alpha)$ for the entire evolution, this strain level is never reached, resulting in a brittle E-D response.

Second dissipation. Different evolutions can arise, regardless of the first dissipation phase. They are investigated as follows:

- E-*-P: It is required that

$$\dot{f}_{\mathrm{p}}(\sigma, p, \alpha) = E(\alpha)(\dot{\epsilon} - \dot{\epsilon}_{\mathrm{p}}) - H(\alpha)\dot{p} = 0,$$
$$\dot{f}_{\mathrm{d}}(\sigma, p, \alpha) = E'(\alpha)(\epsilon - \epsilon_{\mathrm{p}})\dot{\epsilon}\left(\frac{E(\alpha)}{E(\alpha) + H(\alpha)} - 1\right) + (-\sigma_{\mathrm{p}}'(\alpha) - H'(\alpha))\dot{p} < 0, \qquad (3\text{-}9)$$

  which is inadmissible because, given $H(\alpha) > 0$ and $H'(\alpha) < 0$, both the first and second terms are always positive. Therefore, it is impossible for plasticity to evolve by itself once damage has been triggered. It is worth noting that this no longer holds for softening plasticity, where $H(\alpha) < 0$

and $H'(\alpha) > 0$, because the terms in the inequality can eventually become negative. In this work, however, only hardening plasticity is considered.

- E-*-D: It is required that

$$\dot{f}_p(\sigma, p, \alpha) = \big(E'(\alpha)(\epsilon - \epsilon_p) - \sigma'_p(\alpha) - H'(\alpha)p\big)\dot{\alpha} + E(\alpha)\dot{\epsilon} < 0,$$

$$\dot{f}_d(\sigma, p, \alpha) = -E'(\alpha)(\epsilon - \epsilon_p) - \left(\frac{1}{2}E''(\alpha)(\epsilon\epsilon_p)^2 + \frac{1}{2}H''(\alpha)p^2 + \sigma''_p(\alpha)p\right)\dot{\alpha} = 0,$$

which results in

$$A < -E'(\alpha)(\epsilon - \epsilon_p)/E(\alpha)B, \tag{3-10}$$

where

$$A = \frac{1}{2}E''(\alpha)(\epsilon - \epsilon_p)^2 + \frac{1}{2}H''(\alpha)p^2 + \sigma''_p(\alpha)p > 0,$$

$$B = -E'(\alpha)(\epsilon - \epsilon_p) + \sigma'_p(\alpha) + H'(\alpha)p > 0.$$

Equation (3-10) defines the necessary condition for the evolution of damage without plasticity as the second dissipation phase.

- E-*-PD: It is required that

$$\dot{f}_p(\sigma, p, \alpha) = E(\alpha)(\dot{\epsilon} - \dot{\epsilon}_p) + \big(E'(\alpha)(\epsilon - \epsilon_p) - \sigma'_p(\alpha) - H'(\alpha)p\big)\dot{\alpha} - H(\alpha)\dot{p} = 0,$$

$$\dot{f}_d(\sigma, p, \alpha) = -E'(\alpha)(\epsilon - \epsilon_p) - (\sigma'_p(\alpha) + H'(\alpha)p)\dot{p}$$

$$- \left(\frac{1}{2}E''(\alpha)(\epsilon\epsilon_p)^2 + \frac{1}{2}H''(\alpha)p^2 + \sigma''_p(\alpha)p\right)\dot{\alpha} = 0,$$

which results in

$$-E'(\alpha)(\epsilon - \epsilon_p)/E(\alpha)B < A, \tag{3-11}$$

defining the necessary condition for the coupled plastic-damage second dissipation phase.

3.1.2. *Specific model.* We focus on the E-P-PD evolution. Recalling (2-9) from the classical approach, the constitutive functions

$$E(\alpha) = E_0(1-\alpha)^2, \quad H(\alpha) = H_0(1-\alpha)^2, \quad \sigma_p(\alpha) = \sigma_{p0}(1-\alpha)^2, \tag{3-12}$$

are used. where the constitutive function of the plastic modulus has been added, with H_0 as the initial plastic modulus. Then, the yield stresses become

$$\sigma_{yp}(p, \alpha) = (1-\alpha)^2(\sigma_{p0} + H_0 p), \tag{3-13}$$

$$\sigma_{yd}(p, \alpha) = \sqrt{(w_0 - (2\sigma_{p0}p + H_0 p^2)(1-\alpha))E_0(1-\alpha)^3}. \tag{3-14}$$

Both dissipation phases are analyzed:

- First dissipation: From (3-13) and (3-14), the yield stresses become

$$\sigma_{yp}(0, 0) = \sigma_{p0},$$

$$\sigma_{yd}(0, 0) = \sqrt{w_0 E_0}.$$

Therefore, if $\sigma_{p_0} < \sqrt{w_0 E_0}$ holds, a plasticity phase is ensured as the first dissipation.

- Second dissipation: With nonsoftening plasticity as the first dissipation phase, a second dissipation is phase is guaranteed. Recalling that for monotonic loading $p = \epsilon_p$, the yield strain is

$$\epsilon_{yd} = \sqrt{\frac{w_0 - 2\sigma_{p_0} p_{yd} - H_0 p_{yd}^2}{E_0}} + p_{yd}, \tag{3-15}$$

where p_{yd} is the accumulated plastic strain corresponding to ϵ_{yd}. A coupled response needs to be assured, for which $\sigma_{yd}(p_{yd}, \alpha) > \sigma_{yp}(p, \alpha)$ needs to be verified during the evolution. Using the stress-strain relation (3-2), (3-15) and (3-13) one has

$$\sqrt{\frac{w_0 - 2\sigma_{p_0} p_{yd} - H_0 p_{yd}^2}{E_0}} - \frac{\sigma_{p_0} + H_0 p_{yd}}{E_0} = 0,$$

which results in

$$(H_0^2/E_0 + H_0) p_{yd}^2 + (\sigma_{p_0} H_0/E_0 + 2\sigma_{p_0}) p_{yd} + (\sigma_{p_0}^2/E_0 - w_0) = 0.$$

With this, the value $p = p_{yd}$ is given and from equations (3-13) and (3-14), $\sigma_{yd}(p_{yd}, \alpha) > \sigma_{yp}(p, \alpha)$ must hold for a coupled evolution.

Finally, the complete evolution is explicitly given by:

- Elastic phase: $\epsilon \in [0, \epsilon_{yp})$.

$$p(t) = 0, \quad \alpha(t) = 0, \quad \sigma(t) = E_0 \epsilon.$$

- Plastic phase: $\epsilon \in [\epsilon_{yp}, \epsilon_{yd})$.

$$p(t) = (\epsilon E_0 - \sigma_{p_0})/(E_0 + H_0), \quad \alpha(t) = 0, \quad \sigma(t) = \sigma_{p_0} + H_0 p.$$

- Plastic-damage phase: $\epsilon \in [\epsilon_{yd}, \infty)$.

$$p(t) = \frac{\epsilon E_0 - \sigma_{p_0}}{E_0 + H_0}, \quad \alpha(t) = 1 - \frac{w_0}{E_0(\epsilon - p)^2 + H_0 p^2 + 2\sigma_{p_0} p}, \quad \sigma(t) = (\sigma_{p_0} + H_0 p)(1 - \alpha)^2.$$

Energy dissipation. From the Clausius–Duhem inequality, one has

$$\sigma \dot{\epsilon} - \dot{\Psi} \geq 0,$$

from where

$$\left(-\frac{1}{2} E'(\alpha)(\epsilon - \epsilon_p)^2 - \frac{1}{2} H'(\alpha) p^2\right) \dot{\alpha} + \sigma \dot{\epsilon}_p - H(\alpha) p \dot{p} \geq 0.$$

The plastic dissipation reads as

$$\begin{aligned}
\Phi_p &= \sigma \dot{\epsilon}_p - H(\alpha) p \dot{p} \\
&= \dot{p} \left[|\sigma| - H(\alpha) p\right] \\
&= (\sigma_p(\alpha)) \dot{p} \geq 0, \tag{3-16}
\end{aligned}$$

whereas the damage dissipation is

$$
\Phi_d = \left(-\frac{1}{2} E'(\alpha)(\epsilon - \epsilon_p)^2 - \frac{1}{2} H'(\alpha) p^2 \right) \dot{\alpha}
$$

$$
= (\sigma_p'(\alpha) + w_0)\dot{\alpha} \geq 0. \tag{3-17}
$$

3.2. *Global gradient model.*

3.2.1. *Energy functional.* The nonlocal model is developed with a variational treatment. First, the energy potentials have to be defined. The stored elastic energy $\mathcal{E} = \int_0^L \Psi \, dx$ is given by

$$
\mathcal{E}(u, \epsilon_p, p, \alpha) = \int_0^L \frac{1}{2} E(\alpha)(u' - \epsilon_p)^2 + \frac{1}{2} H(\alpha) p^2 \, dx, \tag{3-18}
$$

where the hardening term is considered. From (3-16) and (3-17), the total dissipation potential is defined as

$$
\Phi(p, \alpha, p', \alpha', \dot{p}, \dot{\alpha}, \dot{p}', \dot{\alpha}') = \Phi_p + \partial_t \left(\frac{1}{2} \eta_p(\alpha)^2 p'^2 \right) + \Phi_d + \partial_t \left(\frac{1}{2} \eta_d^2 \alpha'^2 \right)
$$

$$
= (\sigma_p(\alpha)) \dot{p} + \partial_t \left(\frac{1}{2} \eta_p(\alpha)^2 p'^2 \right) + w_0 \dot{\alpha} + \sigma_p'(\alpha) \dot{\alpha} + \partial_t \left(\frac{1}{2} \eta_d^2 \alpha'^2 \right), \quad (3\text{-}19)
$$

where the terms corresponding to the plastic strain gradient and the damage gradient have been added, with $\eta_p(\alpha)$ as a variable internal length scale. The damage gradient term is kept to avoid an abrupt damage localization and an instantaneous rupture as soon as damage is triggered. With (3-19), the dissipated work $\mathcal{D}$ is defined as

$$
\mathcal{D}(u, \epsilon_p, p, \alpha) = \int_0^L \frac{1}{2} E(\alpha)(u' - \epsilon_p)^2 + \frac{1}{2} H(\alpha) p^2 \, dx
$$

$$
+ \int_0^L \sigma_y(\alpha) p + \frac{1}{2} \eta_p(\alpha)^2 p'^2 \, dx + \int_0^L w_0 \alpha + \frac{1}{2} \eta_d^2 \alpha'^2 \, dx. \tag{3-20}
$$

The energy functional is defined with (3-20) and (3-18) as

$$
\mathcal{W}(u, p, \alpha) = \mathcal{E}(u, p, \alpha) + \mathcal{D}(u, p, \alpha)
$$

$$
= \int_0^L \frac{1}{2} E(\alpha)(u' - \epsilon_p)^2 + \frac{1}{2} H(\alpha) p^2 \, dx
$$

$$
+ \int_0^L \sigma_p(\alpha) p + \frac{1}{2} \eta_p(\alpha)^2 p'^2 \, dx + \int_0^L w_0 \alpha + \frac{1}{2} \eta_d^2 \alpha'^2 \, dx. \tag{3-21}
$$

3.2.2. *Energetic formulation.* The building blocks of the variational energetic formulation are the following conditions:

(1) Stability condition.

(2) Energy balance.

(3) Irreversibility condition.

The irreversibility condition is imposed on the damage variable and is given by (2-10). This condition is applied numerically by simply considering the damage value corresponding to the previous load step as the minimum level of damage for each corresponding node as

$$
\alpha_n^i = \begin{cases} \alpha_n^i, & \text{if } \alpha_n^i \geq \alpha_{n-1}^i \\ \alpha_{n-1}^i, & \text{if } \alpha_n^i < \alpha_{n-1}^i \end{cases}, \tag{3-22}
$$

where α_n^i is the damage value for the n-th load step and the i-th node. The other two conditions are explored in this section. From now on, only monotonic loading is considered, for which $\epsilon_p = p$.

Stability condition. By differentiating potentials (3-18) and (3-20), the first order stability condition yields

$$
\begin{aligned}
\mathcal{W}&(u, p, \alpha)(\tilde{u}, \tilde{p}, \tilde{\alpha}) \\
&= \mathcal{E}'(u, p, \alpha) + \mathcal{D}'(u, p, \alpha) \\
&= \int_0^L E(\alpha)(u' - p)\tilde{u}' + \left(-E(\alpha)(u' - p) + \sigma_p(\alpha) + H(\alpha)p\right)\tilde{p} + \eta_p(\alpha)^2 p'\tilde{p}' \\
&\quad + \left(\frac{1}{2}E'(\alpha)(u' - p)^2 + \frac{1}{2}H'(\alpha)p^2 + \sigma_p'(\alpha)p + w_0 + \eta_p(\alpha)\eta_p'(\alpha)p'^2\right)\tilde{\alpha} + \eta_d^2\alpha'\tilde{\alpha}' \, dx \geq 0,
\end{aligned}
$$

from where the following cases are analyzed:

- For $\tilde{p} = \tilde{\alpha} = 0$,

$$
\int_0^L E(\alpha)(u' - p)\tilde{u}' \, dx = 0, \tag{3-23}
$$

    which is the weak form of the equilibrium equation in the absence of external loads.

- For $\tilde{u} = \tilde{\alpha} = 0$,

$$
\int_0^L \left(\left(-E(\alpha)(u' - p) + \sigma_p(\alpha) + H(\alpha)p\right)\tilde{p} + \eta_p(\alpha)^2 p'\tilde{p}'\right) dx \geq 0, \tag{3-24}
$$

    which is the weak form of the plasticity yield criterion. After integrating the last term by parts, the gradient-dependent yield criterion is recovered in the local form

$$
f_p(u, p, \alpha) = \sigma - [\sigma_p(\alpha) + H(\alpha)p] + \eta_p(\alpha)^2 p'' \leq 0. \tag{3-25}
$$

- For $\tilde{u} = \tilde{p} = 0$,

$$
\int_0^L \left(\frac{1}{2}E'(\alpha)(u' - p)^2 + \sigma_p'(\alpha)p + \frac{1}{2}H'(\alpha)p^2 + w_0 + \eta_p(\alpha)\eta_p'(\alpha)p'^2\right)\tilde{\alpha} + \eta_d^2\alpha'\tilde{\alpha}' \, dx \geq 0, \tag{3-26}
$$

    obtaining the weak form of the damage criterion. Again, the last term is integrated by parts and the gradient-dependent yield criterion is recovered in the local form

$$
f_d(u, p, \alpha) = -\frac{1}{2}E'(\alpha)(u' - p)^2 - \sigma_p'(\alpha)p - \frac{1}{2}H'(\alpha)p^2 - w_0 - \eta_p(\alpha)\eta_p'(\alpha)p'^2 + \eta_d^2\alpha'' \leq 0, \tag{3-27}
$$

where the damage gradient term is observed. Also, the plastic gradient term is present due to the possible coupling of the plastic internal length to the damage variable. This problem will be treated once the constitutive functions are introduced.

Energy balance. A procedure analogous to the treatment of the stability condition is carried out. The energy balance leads to

$$\int_0^L -E(\alpha)(u'-p)\dot{u}' + \big(E(\alpha)(u'-p) - \sigma_p(\alpha) - H(\alpha) + \eta_p(\alpha)p''\big)\dot{p}$$

$$+ \Big(-\frac{1}{2}E'(\alpha)(u'-p)^2 - \frac{1}{2}H'(\alpha)p^2 - \sigma_p'(\alpha)p - w_0 - \eta_p(\alpha)\eta_p'(\alpha)p'^2 + \eta_d\alpha''\Big)\dot{\alpha}\,\mathrm{d}x = 0. \quad \text{(3-28)}$$

The following cases are analyzed:

- For $\dot{u} = \dot{\alpha} = 0$, using (3-25), the plasticity consistency conditions are obtained as

$$f_p(u, p, \alpha)\dot{p} = 0.$$

- For $\dot{u} = \dot{p} = 0$, using (3-27), the damage consistency conditions are obtained as

$$f_d(u, p, \alpha)\dot{\alpha} = 0.$$

3.2.3. *Alternate minimization.* The finite element resolution that is applied in this work is shown in this subsection. All the integrals, when necessary, are solved through Gaussian quadrature. To gain precision and a more accurate response, no average values are taken, and the state variables are approximated as follows:

- The displacement field is approximated with quadratic shape functions and three-node elements.
- Both the plastic strain field and the damage field are approximated with linear shape functions and two-node elements.

The same constitutive functions (Equation (3-12))

$$E(\alpha) = E_0(1-\alpha)^2, \quad H(\alpha) = H_0(1-\alpha)^2, \quad \sigma_p(\alpha) = \sigma_{p_0}(1-\alpha)^2,$$

are applied. Additionally, the plastic internal length is taken as

$$\eta_p(\alpha) = \begin{cases} \eta_{p_0}(\beta - \max(\alpha)), & \text{if } \max(\alpha) \leq \beta \\ 0, & \text{if } \max(\alpha) > \beta \end{cases},$$

where η_{p_0} is the initial internal length, $\beta \in [0, 1]$ is a threshold level of damage and $\max(\alpha)$ is the maximum value of damage, which will be located at the center of the bar. This choice of function for the plastic internal length avoids the dependence of the damage variable on the plastic strain gradient because the term $\eta_p(\alpha)\eta_p'(\alpha)p'^2$ disappears from the damage criterion.

The alternate minimization follows:

- Minimization with respect to the displacement field $\mathcal{W}(u, \epsilon_p, \alpha)(\tilde{u}, 0, 0){=}0$,

$$\frac{\mathrm{d}}{\mathrm{d}h}\mathcal{W}(u + h\tilde{u}, \epsilon_p, \alpha)\Big|_{h=0} = \text{(3-23)}.$$

Introducing the constitutive functions, approximation functions and shape functions, the matrix form is obtained as

$$\int_0^L E_0(1 - N\boldsymbol{\alpha}_e)^2 \boldsymbol{M}'^T \boldsymbol{M}' \, \mathrm{d}x \boldsymbol{u} - \int_0^L E_0(1 - N\boldsymbol{\alpha})^2 \boldsymbol{M}_e'^T \boldsymbol{N} \, \mathrm{d}x \, \boldsymbol{p} = 0, \qquad (3\text{-}29)$$

where $\boldsymbol{M}$ and $\boldsymbol{N}$ are the shape functions of three-node elements and two-node elements, respectively.

- Minimization with respect to the plastic strain $\mathcal{W}'(u, \epsilon_\mathrm{p}, \alpha)(0, \tilde{\epsilon}_\mathrm{p}, 0) = 0$,

$$\frac{\mathrm{d}}{\mathrm{d}h} \mathcal{W}(u, \epsilon_\mathrm{p} + h\tilde{\epsilon}_\mathrm{p}, \alpha) \Big|_{h=0} = (3\text{-}24).$$

Along with the constitutive functions, the matrix form is

$$\int_0^L -E_0(1 - N\boldsymbol{\alpha})^2 \boldsymbol{N}^T \boldsymbol{M}' \, \mathrm{d}x \boldsymbol{u} + \int_0^L E_0(1 - N\boldsymbol{\alpha})^2 \boldsymbol{N}^T \boldsymbol{N} \, \mathrm{d}x \, \boldsymbol{p}$$

$$+ \int_0^L \sigma_{\mathrm{p}_0}(1 - N\boldsymbol{\alpha})^2 \boldsymbol{N}^T \, \mathrm{d}x + \int_\Omega H_0(1 - N\boldsymbol{\alpha})^2 \boldsymbol{N}^T \boldsymbol{N} \, \mathrm{d}x \, \boldsymbol{p}$$

$$+ \int_0^L \mathrm{H}(\beta - \max(\boldsymbol{\alpha})) \eta_{\mathrm{p}_0}^2 (\beta - \max(\boldsymbol{\alpha}))^2 \boldsymbol{N}'^T \boldsymbol{N}' \, \mathrm{d}x \, \boldsymbol{p} = 0, \qquad (3\text{-}30)$$

where H is the Heaviside step function.

- Minimization with respect to the damage field $\mathcal{W}'(u, \epsilon_\mathrm{p}, \alpha)(0, 0, \tilde{\alpha}) = 0$,

$$\frac{\mathrm{d}}{\mathrm{d}h} \mathcal{W}(u, \epsilon_\mathrm{p}, \alpha + h\tilde{\alpha}) \Big|_{h=0} = (3\text{-}26).$$

Again, the corresponding matrix form is obtained as

$$\int_0^L (w_0 - R) \boldsymbol{N}^T \, \mathrm{d}x + \int_\Omega R \boldsymbol{N}^T \boldsymbol{N} \, \mathrm{d}x \boldsymbol{\alpha} + \int_\Omega \eta_\mathrm{d}^2 \boldsymbol{N}'^T \boldsymbol{N}' \, \mathrm{d}x \boldsymbol{\alpha}, \qquad (3\text{-}31)$$

where

$$R = E_0(\boldsymbol{M}'\boldsymbol{u} - \boldsymbol{N}\boldsymbol{p})^2 + 2\sigma_{\mathrm{p}_0} \boldsymbol{N} \boldsymbol{p} + H_0 \boldsymbol{N} \boldsymbol{p} \boldsymbol{N} \boldsymbol{p}. \qquad (3\text{-}32)$$

The local vector forms are solved and the global vectors are found for each variable alternatively.

3.3. *Computational implementation.* The numeric implementation leads to the *alternate minimization algorithm*. The main characteristics are:

- The displacements are imposed gradually.
- The trial elastic state is given to all the elements by verifying equilibrium and finding the elastic displacement distribution.
- The plastic state is recovered by finding the global plastic strain vector.
- The plastic-damage field is finally obtained by finding the global damage vector.
- Three convergence criteria are applied: L_2 norms for the displacement field and the plastic strain field, with tolerances tol_u and tol_p, respectively, and L_∞ norm for the damage field with tolerance tol_d.

The computational process is summarized in Algorithm 2.

1: **for** $n = 1$ **to** n_{desp} **do**
2:     Initialize
      $k = 0$;
3:     **while** $\left(||\boldsymbol{u}_n^k - \boldsymbol{u}_n^{k-1}||_2 > \text{tol}_{\text{u}} \textbf{ or } ||\boldsymbol{\epsilon}_{\textbf{p}_n}^k - \boldsymbol{\epsilon}_{\textbf{p}_n}^{k-1}||_2 > \text{tol}_{\text{p}} \textbf{ or } ||\boldsymbol{\alpha}_n^k - \boldsymbol{\alpha}_n^{k-1}||_\infty > \text{tol}_{\text{d}} \right) \textbf{ and } k \leq \text{itmax}$
      do
4:       $k = k + 1$;
5:       Obtain $\boldsymbol{u}_n^k = \text{argmin}_u \mathcal{W}(u, \epsilon_{\text{p}_n}^{k-1}, p_n^{k-1}, \alpha_n^{k-1})$ from the solution of (3-29)
6:       Obtain $\boldsymbol{\epsilon}_{\text{p}_n}^k, \boldsymbol{p}_n^k = \text{argmin}_{\epsilon_{\text{p}}} \mathcal{W}(u_n^k, \epsilon_{\text{p}}, p, \alpha_n^{k-1})$ from the solution of (3-30)
7:       Obtain $\boldsymbol{\alpha}_n^k = \text{argmin}_\alpha \mathcal{W}(u_n^k, \epsilon_{\text{p}_n}^k, p_n^k, \alpha)$ from the solution of (3-31) and apply the irreversibility
        condition with (3-22)
8:     **end while**
9: **end for**

Algorithm 2. Energetic formulation of the *alternate minimization algorithm.*

4. Numerical simulations

The results of the numerical simulations are explored in this section. First, the classical approach is analyzed. The evolution of the state variables for the viscoplastic model is first illustrated. Then, the tendency of the model towards the perfect plasticity variational model as the loading rate tends to zero is shown. The variational approach follows. The evolution of the local hardening plasticity and gradient damage model is first analyzed, and the results are, on some level, compared to the viscoplastic model. Then, the evolution of the state variables for the gradient plasticity and gradient damage model is shown and the main characteristics are described.

4.1. *Classical model.* As mentioned, the local classical approach provides a response where the strains localize in the plastic phase in the element where the displacements are imposed. This problem is solved by introducing rate-dependence in the plastic phase, by means of the viscoplastic model. Although this model is used to represent the response of materials that exhibit rate-dependence, it can be demonstrated that as the ratio $\Delta t / v \to \infty$, the viscoplastic response tends towards the rate-independent plastic model [Simo and Hughes 1998]. For the definition of the numerical model, the loading rate $v = \Delta u / \Delta t$ is introduced as the parameter used to control the rate-dependence effect that viscosity introduces in the model, given that $\Delta t / v \to \infty$ and $v \to 0$ are equivalent conditions. The constitutive parameters used in the simulations are in Table 1 and the results of the viscoplastic evolution are illustrated in Figures 1 and 2. In Figure 1 (left), the stress-displacement curve is shown. Two main phases in the material response can be observed, corresponding to the perfect plasticity phase and the plasticity-damage phase. The displacement profile shown in Figure 1 (right) shows an initially smooth evolution, leading to a jump in the displacement field as damage evolves. In Figure 2 (left) the plastic deformation profiles are shown. During the plasticity phase, the plastic deformations evolve uniformly over the bar, but after damage is triggered, the region in which plasticity evolves reduces continuously, until it concentrates in one or two elements in the middle of the bar. The size of this region is controlled by the value of the loading rate, as seen in Figure 4 (left). This behavior has been observed before in [Niazi et al. 2013; Needleman 1988], and has been attributed to an implicit internal length included in the viscoplastic regularization.

	E_0 (MPa)	σ_{y_0} (MPa)	H_0 (MPa)	η_d (MPa$^{1/2} \cdot$ m)	η_p (MPa$^{1/2} \cdot$ m)	ν (MPa $\cdot$ s)	w_0 (MPa)	β
classical viscoplasticity	71300	345	–	0.55	–	25	30	–
local hardening plasticity	71300	345	5000	0.80	–	–	30	–
grad. dependent plasticity	71300	345	250	0.55	10	–	30	0.85

Table 1. Constitutive parameters used in the simulations.
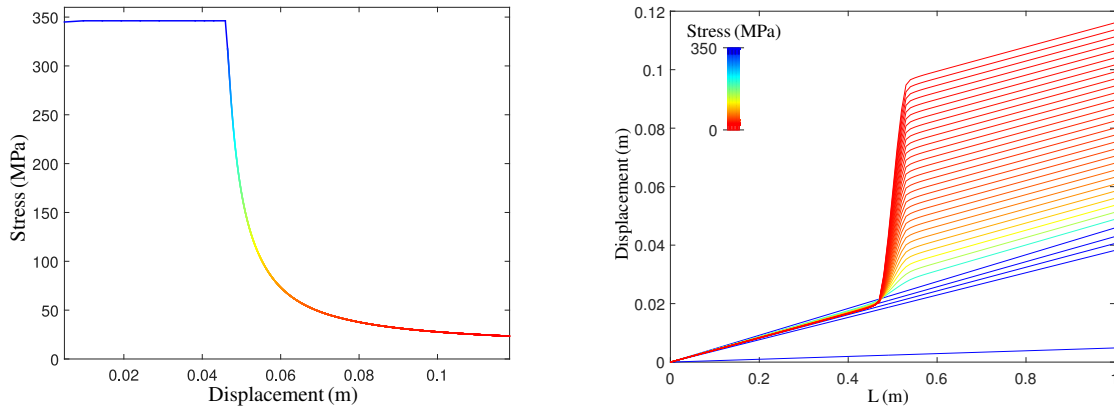
Figure 1. Stress-displacement curve (left) and displacement profiles (right) for the evolution of the classical viscoplastic and gradient damage model with 100 elements.

The damage profile observed in Figure 2 (right) shows an initially smooth distribution. As damage evolves, the spatial distribution tends to an abrupt jump in the spatial derivative of damage in the center of the bar. Another interesting result of the model is length in which the damage and plastic deformation profiles evolve during the loading process. Material damage continuously diffuses along the bar during the evolution, allowing the model to represent void coalescence during material failure. On the other hand, the size of the zone in which the plastic deformations evolve is gradually reduced, allowing the concentration of deformations at the center of the bar. This, along with the jump in the displacement field, represents the formation of a cohesive crack.

The viscoplastic model is shown to converge to the variational model in [Alessi 2013] as the loading rate tends to zero. This can be observed in Figures 3 and 4 for different loading rates $v = \Delta u / \Delta t$. In Figure 3 (left), it can be observed how the stress in the bar increases as the loading rate increases, as expected because of the hardening effect of viscoplasticity.

Additionally, a numerical disadvantage of the classical model is observed in the capacity of the algorithm to converge. For a determined loading rate, the steps at which the displacements are imposed can be too large, causing nonconvergence. Specifically, the total energy never reaches a minimum and oscillates between iterations. This effect is shown for a nonconvergence simulation in Figure 5.
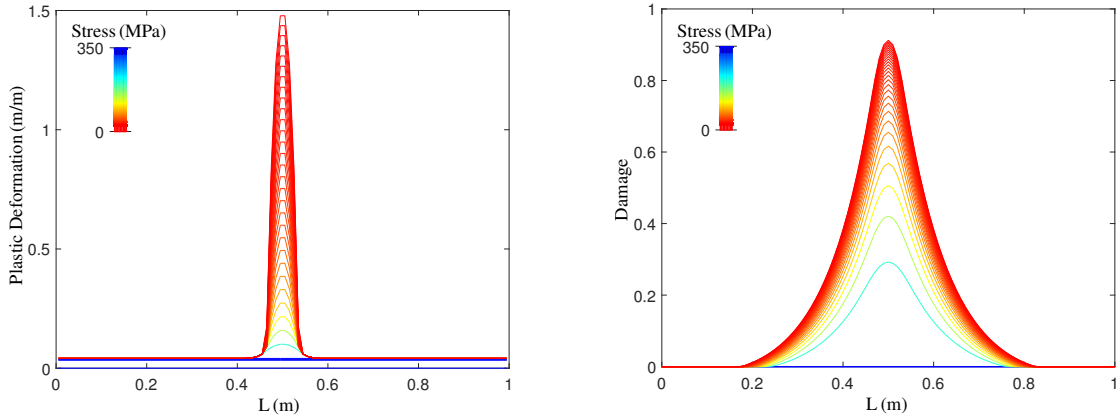
Figure 2. Plastic strain (left) and damage profiles (right) for the evolution of the classical viscoplastic and gradient damage model with 100 elements.
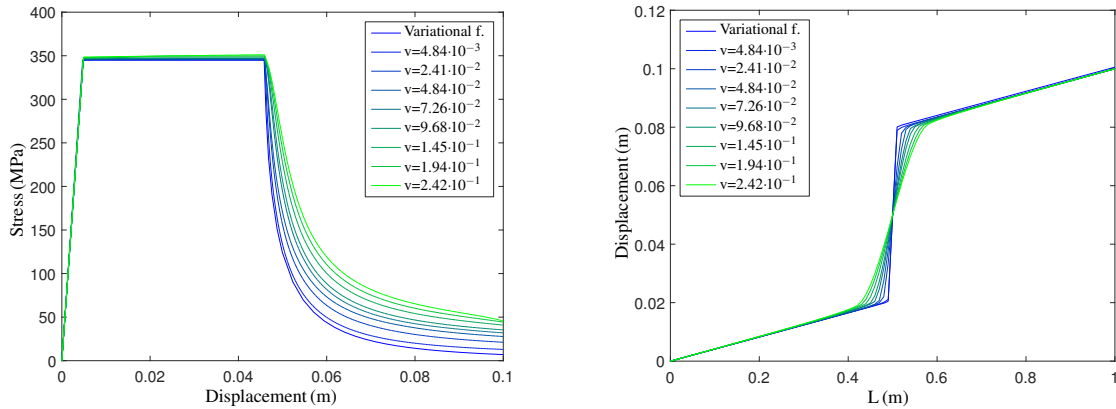

Figure 3. Stress-displacement curves (left) and displacement profiles (right) for the classical viscoplastic model using different loading rates and compared to the variational with 100 elements.
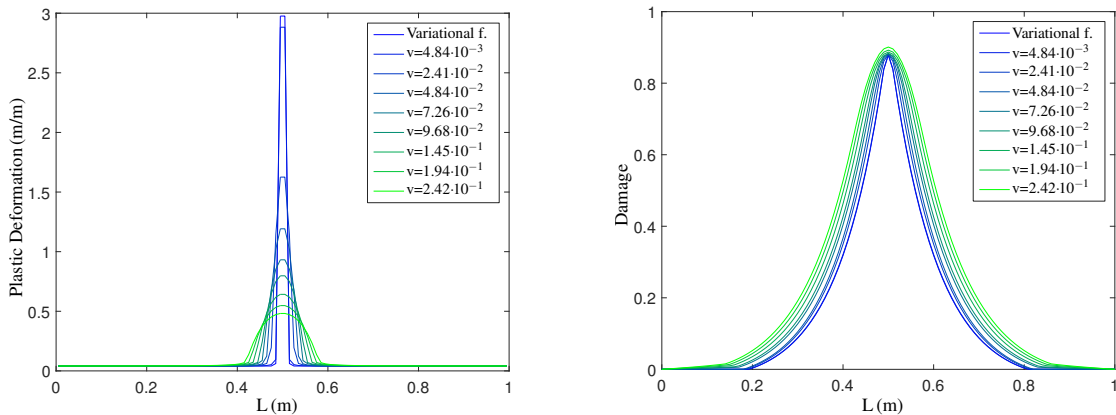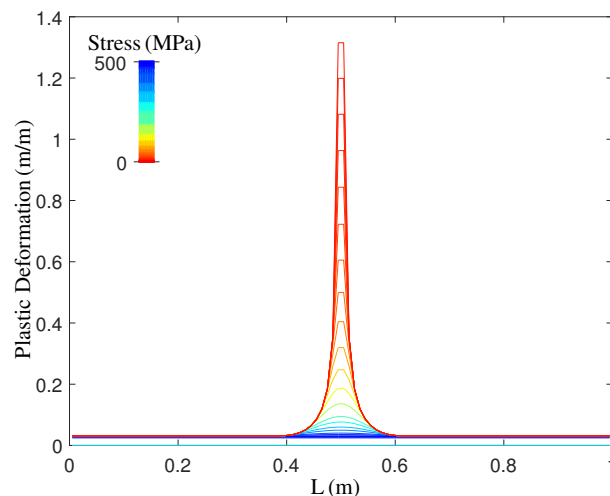

Figure 4. Plastic strain (left) and damage profiles (right) for the classical viscoplastic model using different loading rates and compared to the variational model with 100 elements.
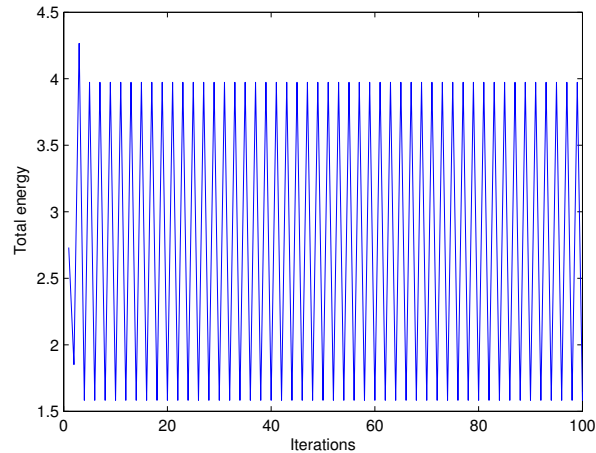
Figure 5. Nonconvergence of the classical approach.

4.2. *Variational model.*

4.2.1. *Hardening plasticity and gradient damage.* The results of the simulations of local hardening plasticity and gradient damage are illustrated. The constitutive parameters that were used are shown in Table 1.

The main feature of the local plasticity model can be appreciated in the evolution of the plastic strains shown in Figure 6. There is an initial implicit internal length caused by the hardening variable, and the evolution eventually narrows and concentrates at the center of the bar.

In Figure 7 (left), the displacement profile shows a relatively smooth evolution as the plastic modulus increases. This result is similar to the effect of increasing the loading rate in the viscoplastic model because in both cases, the material becomes stiffer. Also, the plastic strain profile shown in Figure 7

Figure 6. Plastic strain profile for the variational hardening plasticity and gradient damage model with 100 elements.
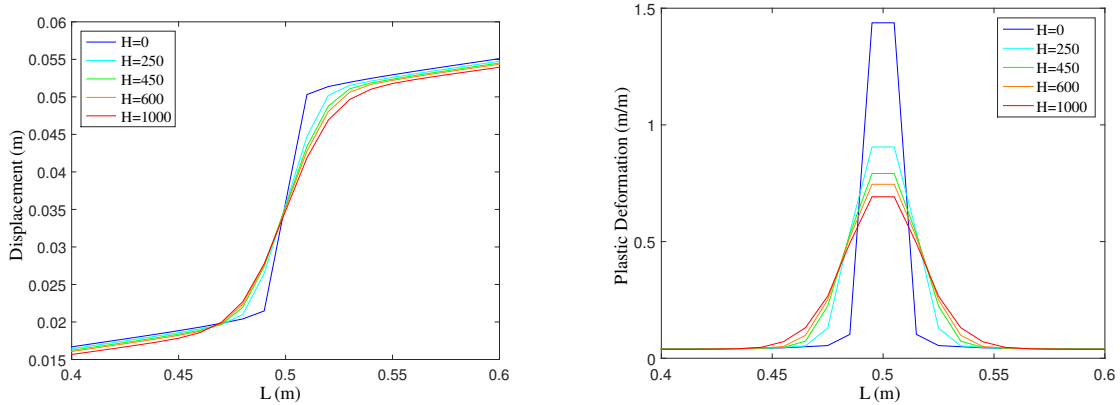
Figure 7. Displacement (left) and plastic strain profiles (right) for the variational harden-
ing plasticity and gradient damage model, varying the hardening modulus with 100 ele-
ments.
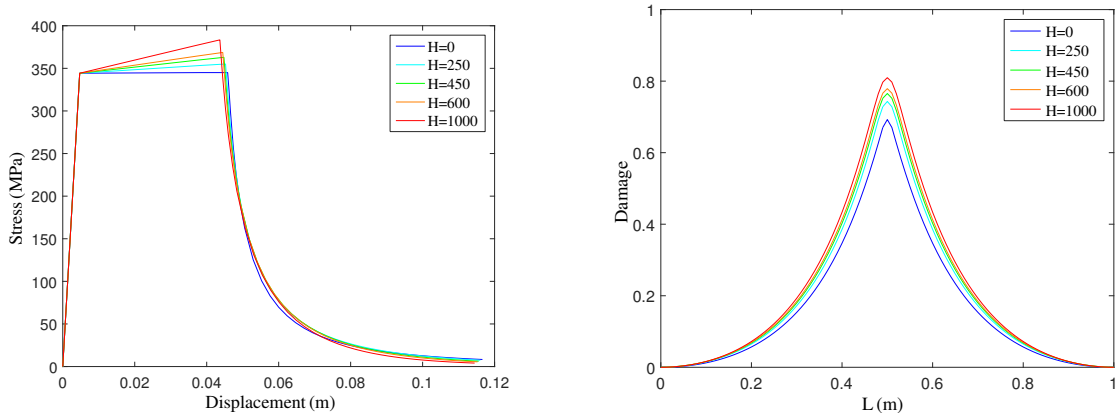
Figure 8. Stress-displacement curves (left) and damage profiles (right) for the variational
hardening plasticity and gradient damage model, varying the hardening modulus with 100
elements.

(right) shows that the plastic strains concentrate more and are higher as the plastic modulus decreases.
Clearly, $H = 0$ results in the central concentration, recovering the perfect plasticity model in [Alessi
2013]. This result also resembles the plastic strain distribution of the viscoplastic model as the loading
rates decrease.

The increase of stress in the plastic phase results in an earlier activation of damage when compared to
both the perfect plasticity model and the viscoplastic model, where the damage is triggered at the same
strain level. This result is shown in the damage yield points of Figure 8 (left). Clearly, the damage yield
stress is reached early for higher values of H. Additionally, Figure 8 (right) shows that the damage re-
sponse is significantly sensitive with respect to the hardening variable. Because of this coupled evolution,
the stress drops to zero at a higher rate as the plastic modulus increases, as shown in the damage phase
of Figure 8 (left). Physically, this result can be interpreted as the simulation of a material behavior where
hardening also implicates less ductility and a higher loss of stiffness in the softening regime.
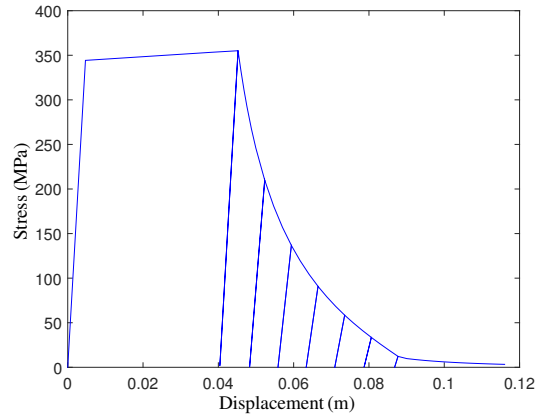
Figure 9. Unloading paths for the gradient plasticity and gradient damage model with 101 elements.

4.2.2. *Complete gradient model.* The results of the simulations of the complete gradient model are presented. The constant values that were used are shown in Table 1. Because of the nodal distribution of the plastic strains, three nodal elements are considered with quadratic approximations on the displacement field.

Figure 9 shows the unloading paths, where the loss of stiffness can be observed in the damage phase. In Figure 10 (left), the stress-displacement curve is shown in relation to the evolution of the state variables. The results are almost identical to the local hardening model with the exception of the damage phase, where initially the stress drops at a slightly slower rate. Once the damage level has reached the threshold value, the local plasticity tendency is recovered. Both the displacement profile of Figure 10 (right) and the damage profile of Figure 11 (right) also show similar results, presenting initially smooth spatial distributions. The response can be compared to the results of viscoplastic model for relatively high loading rates. On the other hand, the plastic strain profile shown in Figure 11 (left) highlights the main features of the variable plastic strain gradient term. The evolution begins with a wider localization zone then the local plasticity model for the same plastic modulus due to the effect of the gradient term. Then,
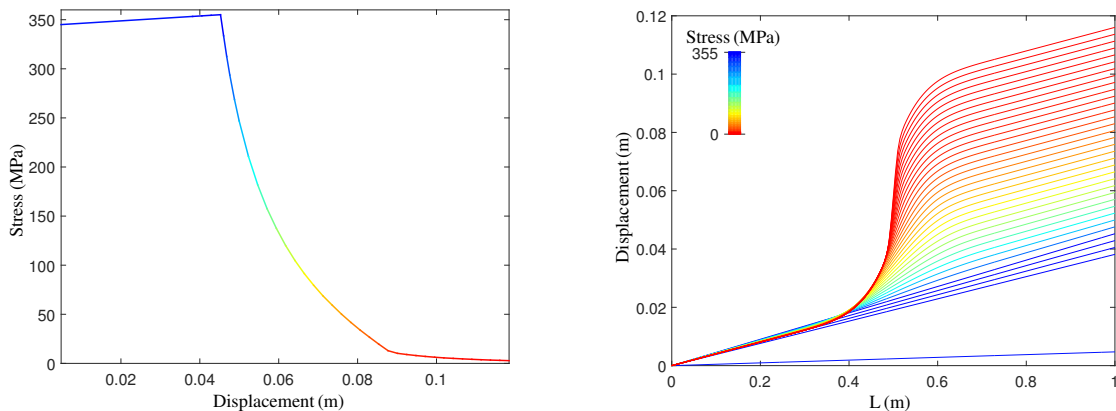
Figure 10. Stress-displacement curve (left) and displacement profile (right) for the evolution of the variational gradient plasticity and gradient damage model with 101 elements.
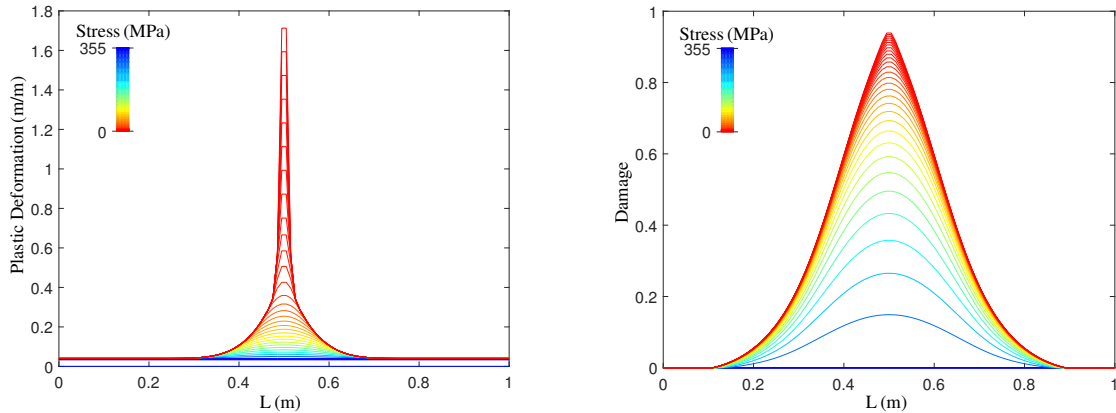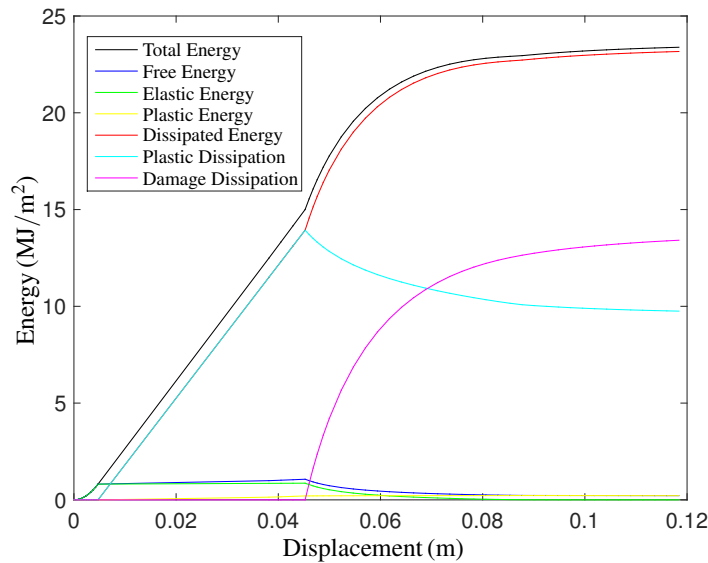
Figure 11. Plastic strain (left) and damage profiles (right) for the evolution of the variational gradient plasticity and gradient damage model with 101 elements.

the damage threshold value is reached and the evolution concentrates in the center of the bar, thereby representing the cohesive crack. Clearly, one of the advantages of this model is that the initial localization region can be controlled without changing the plastic modulus or introducing rate-dependence, which are constant properties of the material.

The energy contributions for the evolution are shown in Figure 12. It is evident that as the stored elastic energy (composed of elastic energy and plastic energy) tends to zero, the total energy becomes a sum of the different contributions of dissipative energies. The total dissipative energy of the bar evolves in the localization zone.

Figures 13 and 14 show the mesh-dependence of the model. Even for a very coarse mesh (11 elements), the tendency is well represented. Clearly, there is low sensitivity to the mesh size, and the plastic strain

Figure 12. Energy contributions for the variational gradient plasticity and gradient damage model.
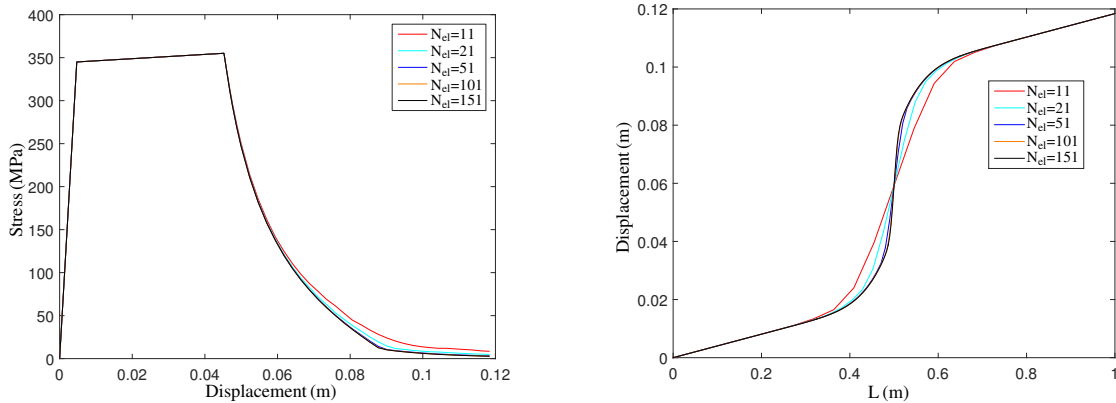
Figure 13. Stress-displacement curve (left) and displacement profiles (right) for the variational gradient plasticity and gradient damage model for different mesh sizes.
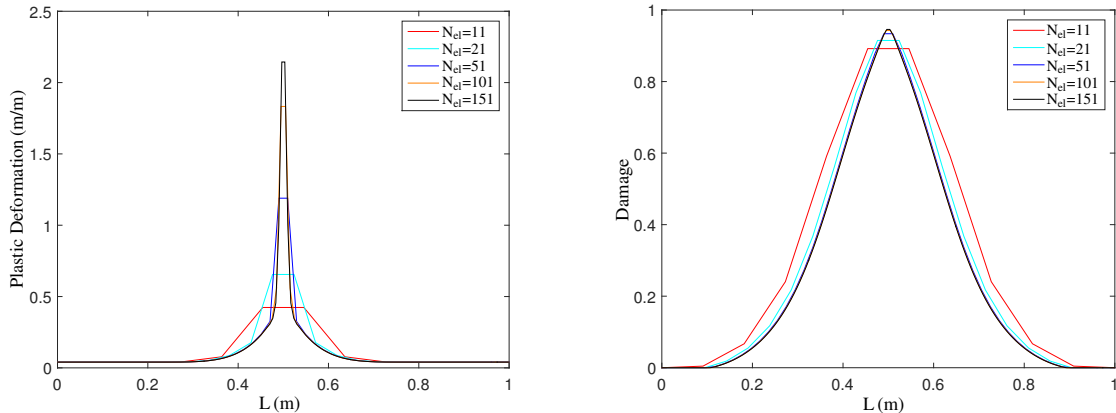
Figure 14. Plastic strain (left) and damage profiles (right) for the variational gradient plasticity and gradient damage model for different mesh sizes.

profiles show that as the mesh size decreases, the concentration of the plastic strains eventually tend to the Dirac delta, as described in [Alessi 2013].

5. Conclusions and perspectives

In this work, the behavior of nonlocal regularized plastic-damage models, in both classical and variational settings has been explored. In the classical approach, the local viscoplastic regularization was used, resulting in the introduction of an implicit internal length in the model, where the size of the localization zone is reduced during the loading process. This is triggered in the plasticity-damage phase and can be controlled through the loading rate. This feature allowed the model to represent a very interesting behavior of the plastic strain spatial distribution and evolution during the final stage of damage and beginning of fracture.

On the other hand, the variational approach in [Alessi 2013] was enriched to include hardening as well as an explicit internal length to control the size of the plastic strain localization zone. The local

evolution was investigated via the consistency conditions, and the addition of the hardening variable furnishes an interesting result, namely (3-9). Clearly, a negative value of the plastic modulus can result in softening behavior without loss of stiffness, even if damage was triggered before. Thus, condition (3-9) should be met for a physically appropriate response. In the numerical simulations, only hardening was considered. As we saw, the hardening variable introduced an implicit internal length that decreases with further loading in the plastic deformation profile, where the initial size of the localization is controlled by the plastic modulus. Similar to the viscoplastic model, the implicit internal length distributes the plastic strains in a certain region; however, the spatial distribution eventually narrows, appropriately representing a jump in the displacement field. Building over this, an explicit internal length was introduced by means of the plastic strain gradient. Taking advantage of the one-dimensional framework, a decreasing function of the maximum level of damage over the bar was used for the internal length, providing better control of the strains in the localization zone. In fact, the effect of the plastic strain gradient may eventually vanish and the local plasticity and gradient damage model in [Alessi 2013] is recovered, with concentration in the center of the bar and the eventual crack. All of this is obtained with a controllable precursory state.

The results of the viscoplastic regularization are consistent with the results obtained in [Niazi et al. 2013]. In the case of the variational model with nongradient hardening plasticity and gradient damage, the results can be qualitatively compared to [Ambati et al. 2015], where hardening plasticity is also coupled to gradient damage in a different formulation. On the other hand, the effect of the plastic strain gradient shows the same tendency observed in [Dal Corso and Willis 2011]. However, in our model, strains localize and the rest of the bar experiences unloading without introducing perturbations. In addition, the evolution can be prolonged to extreme loading with numerical stability and the narrowing of the localization zone is automatic due to the variable internal length. We think of this behavior as a representation of the necking phenomenon, where the strain localization zone eventually narrows to the fracture point (in our case, the central element of a fine mesh) with a concentration of plastic strains, successfully representing ductile failure.

References

[Alessi 2013] R. Alessi, *Variational Approach to Fracture Mechanics with Plasticity*, Ph.D. thesis, Université Pierre et Marie Curie-Paris 6, 2013.

[Alessi et al. 2014] R. Alessi, J.-J. Marigo, and S. Vidoli, "Gradient damage models coupled with plasticity and nucleation of cohesive cracks", *Arch. Ration. Mech. Anal.* **214**:2 (2014), 575–615.

[Almansba et al. 2010] M. Almansba, K. Saanouni, and N. E. Hannachi, "Isotropic elastoplasticity fully coupled with non-local damage", *Engineering* **2**:6 (2010), 420–431.

[Ambati et al. 2015] M. Ambati, T. Gerasimov, and L. De Lorenzis, "Phase-field modeling of ductile fracture", *Comput. Mech.* **55**:5 (2015), 1017–1040.

[Bažant and Jirásek 2002] Z. P. Bažant and M. Jirásek, "Nonlocal integral formulations of plasticity and damage: survey of progress", *J. Eng. Mech.-ASCE* (2002), 1119–1149.

[Bigoni 2012] D. Bigoni, *Nonlinear solid mechanics: bifurcation theory and material instability*, Cambridge University Press, 2012.

[Borja 2013] R. I. Borja, *Plasticity*, Springer, Heidelberg, Germany, 2013.

[Borst et al. 1993] R. D. Borst, L. Sluys, H. Muhlhaus, and J. Pamin, "Fundamental issues in finite element analyses of localization of deformation", *Eng. Computation* **10**:2 (1993), 99–121.

[Bourdin et al. 2008] B. Bourdin, G. A. Francfort, and J.-J. Marigo, "The variational approach to fracture", *J. Elasticity* **91**:1-3 (2008), 5–148.

[Chen et al. 2011] Q. Chen, J. E. Andrade, and E. Samaniego, "AES for multiscale localization modeling in granular media", *Comput. Methods Appl. Mech. Eng.* **200**:33-36 (2011), 2473–2482.

[Dal Corso and Willis 2011] F. Dal Corso and J. R. Willis, "Stability of strain-gradient plastic materials", *J. Mech. Phys. Solids* **59**:6 (2011), 1251–1267.

[De Borst and Mühlhaus 1992] R. De Borst and H.-B. Mühlhaus, "Gradient-dependent plasticity: Formulation and algorithmic aspects", *Int. J. Numer. Methods Eng.* **35**:3 (1992), 521–539.

[de Borst et al. 1999] R. de Borst, J. Pamin, and M. G. Geers, "On coupled gradient-dependent plasticity and damage theories with a view to localization analysis", *Eur. J. Mech., A, Solids* **18**:6 (1999), 939–962.

[Duda et al. 2015] F. P. Duda, A. Ciarbonetti, P. J. Sánchez, and A. E. Huespe, "A phase-field/gradient damage model for brittle fracture in elastic–plastic solids", *Int. J. Plasticity* **65** (2015), 269–296.

[Francfort and Marigo 1998] G. A. Francfort and J.-J. Marigo, "Revisiting brittle fracture as an energy minimization problem", *J. Mech. Phys. Solids* **46**:8 (1998), 1319–1342.

[Garikipati and Hughes 1998] K. Garikipati and T. J. R. Hughes, "A study of strain localization in a multiple scale framework– the one-dimensional problem", *Comput. Methods Appl. Mech. Eng.* **159**:3-4 (1998), 193–222.

[Jirásek and Rolshoven 2009a] M. Jirásek and S. Rolshoven, "Localization properties of strain-softening gradient plasticity models, I: Strain-gradient theories", *Int. J. Solids Struct.* **46**:11-12 (2009), 2225–2238.

[Jirásek and Rolshoven 2009b] M. Jirásek and S. Rolshoven, "Localization properties of strain-softening gradient plasticity models, II: Theories with gradients of internal variables", *Int. J. Solids Struct.* **46**:11-12 (2009), 2239–2254.

[Krajcinovic 1989] D. Krajcinovic, "Damage mechanics", *Mech. Mater.* **8**:2 (1989), 117–197.

[Lancioni 2015] G. Lancioni, "Modeling the response of tensile steel bars by means of incremental energy minimization", *J. Elasticity* **121**:1 (2015), 25–54.

[Lemaitre and Lippmann 1996] J. Lemaitre and H. Lippmann, *A course on damage mechanics*, vol. 2, Springer, Berlin, 1996.

[Mainik and Mielke 2005] A. Mainik and A. Mielke, "Existence results for energetic models for rate-independent systems", *Calc. Var. Partial Differential Equations* **22**:1 (2005), 73–99.

[Maugin 1992] G. A. Maugin, *The thermomechanics of plasticity and fracture*, Cambridge Texts in Applied Mathematics **7**, Cambridge University Press, 1992.

[Maugin and Muschik 1994] G. A. Maugin and W. Muschik, "Thermodynamics with internal variables. II: Applications", *J. Non-Equilibrium Thermodyn.* **19**:3 (1994), 250–289.

[Miehe et al. 2010] C. Miehe, F. Welschinger, and M. Hofacker, "Thermodynamically consistent phase-field models of fracture: variational principles and multi-field FE implementations", *Internat. J. Numer. Methods Eng.* **83**:10 (2010), 1273–1311.

[Mielke 2006] A. Mielke, "A mathematical framework for generalized standard materials in the rate-independent case", pp. 399–428 in *Multifield problems in solid and fluid mechanics*, edited by R. Helmig et al., Lect. Notes Appl. Comput. Mech. **28**, Springer, Berlin, 2006.

[Moës et al. 1999] N. Moës, J. Dolbow, and T. Belytschko, "A finite element method for crack growth without remeshing", *Int. J. Numer. Methods Eng.* **46**:1 (1999), 131–150.

[Mumford and Shah 1989] D. Mumford and J. Shah, "Optimal approximations by piecewise smooth functions and associated variational problems", *Comm. Pure Appl. Math.* **42**:5 (1989), 577–685.

[Needleman 1988] A. Needleman, "Material rate dependence and mesh-sensitivity in localization problems", *Comput. Methods Appl. Mech. Eng.* **67**:1 (1988), 69–85.

[Niazi et al. 2013] M. S. Niazi, H. H. Wisselink, and T. Meinders, "Viscoplastic regularization of local damage models: revisited", *Comput. Mech.* **51**:2 (2013), 203–216.

[Oliver et al. 2002] J. Oliver, A. Huespe, M. Pulido, and E. Chaves, "From continuum mechanics to fracture mechanics: the strong discontinuity approach", *Eng. Fract. Mech.* **69**:2 (2002), 113–136.

[Oliver et al. 2003] J. Oliver, A. E. Huespe, M. D. G. Pulido, and E. Samaniego, "On the strong discontinuity approach in finite deformation settings", *Internat. J. Numer. Methods Eng.* **56**:7 (2003), 1051–1082.

[Oliver et al. 2004] J. Oliver, A. Huespe, E. Samaniego, and E. Chaves, "Continuum approach to the numerical simulation of material failure in concrete", *Int. J. Numer. Anal. Methods Geomech.* **28**:7-8 (2004), 609–632.

[Pham and Marigo 2010a] K. Pham and J.-J. Marigo, "Approche variationnelle de l'endommagement. I: Les concepts fondamentaux", *C. R. Méc. Acad. Sci. Paris* **338**:4 (2010), 191–198.

[Pham and Marigo 2010b] K. Pham and J.-J. Marigo, "Approche variationnelle de l'endommagement. II: Les modèles à gradient", *C. R. Méc. Acad. Sci. Paris* **338**:4 (2010), 199–206.

[Runesson 2006] K. Runesson, "Constitutive modeling of engineering materials, theory and computation", lecture notes, 2006, http://www.am.chalmers.se/~ragnar/material_mechanics_home/literature/ThePrimer_(1).pdf.

[Samaniego and Belytschko 2005] E. Samaniego and T. Belytschko, "Continuum-discontinuum modelling of shear bands", *Internat. J. Numer. Methods Eng.* **62**:13 (2005), 1857–1872.

[Simo and Hughes 1998] J. Simo and T. Hughes, *Computational inelasticity*, Springer, Berlin, 1998.

[Triantafyllidis and Aifantis 1986] N. Triantafyllidis and E. C. Aifantis, "A gradient approach to localization of deformation, I: Hyperelastic materials", *J. Elasticity* **16**:3 (1986), 225–237.

[Venini and Morana 2001] P. Venini and P. Morana, "An adaptive wavelet-Galerkin method for an elastic-plastic-damage constitutive model: 1D problem", *Comput. Methods Appl. Mech. Eng.* **190**:42 (2001), 5619–5638.

JACINTO ULLOA: juv1991@gmail.com
Universidad de Cuenca, Av. 12 de Abril s/n, 010203, Cuenca, Ecuador

PATRICIO RODRÍGUEZ: patricio.rodriguezc@ucuenca.ec
Universidad de Cuenca, Av. 12 de Abril s/n, 010203, Cuenca, Ecuador

ESTEBAN SAMANIEGO: esteban.samaniego@ucuenca.edu.ec
Facultad de Ingenería and Departamento de Recursos Hídricos y Ciencas Ambientales, Universidad de Cuenca,
Av. 12 de Abril s/n, 010203, Cuenca, Ecuador

SUBMISSION GUIDELINES

ORIGINALITY

Authors may submit manuscripts in PDF format online at the Submissions page. Submission of a manuscript acknowledges that the manuscript is original and has neither previously, nor simultaneously, in whole or in part, been submitted elsewhere. Information regarding the preparation of manuscripts is provided below. Correspondence by email is requested for convenience and speed. For further information, write to contact@msp.org.

LANGUAGE

Manuscripts must be in English. A brief abstract of about 150 words or less must be included. The abstract should be self-contained and not make any reference to the bibliography. Also required are keywords and subject classification for the article, and, for each author, postal address, affiliation (if appropriate), and email address if available. A home-page URL is optional.

FORMAT

Authors can use their preferred manuscript-preparation software, including for example Microsoft Word or any variant of TeX. The journal itself is produced in LaTeX, so accepted articles prepared using other software will be converted to LaTeX at production time. Authors wishing to prepare their document in LaTeX can follow the example file at www.jomms.net (but the use of other class files is acceptable). At submission time only a PDF file is required. After acceptance, authors must submit all source material (see especially Figures below).

REFERENCES

Bibliographical references should be complete, including article titles and page ranges. All references in the bibliography should be cited in the text. The use of BibTeX is preferred but not required. Tags will be converted to the house format (see a current issue for examples); however, for submission you may use the format of your choice. Links will be provided to all literature with known web locations; authors can supply their own links in addition to those provided by the editorial process.

FIGURES

Figures must be of publication quality. After acceptance, you will need to submit the original source files in vector format for all diagrams and graphs in your manuscript: vector EPS or vector PDF files are the most useful. (EPS stands for Encapsulated PostScript.)

Most drawing and graphing packages—Mathematica, Adobe Illustrator, Corel Draw, MATLAB, etc.—allow the user to save files in one of these formats. Make sure that what you're saving is vector graphics and not a bitmap. If you need help, please write to graphics@msp.org with as many details as you can about how your graphics were generated.

Please also include the original data for any plots. This is particularly important if you are unable to save Excel-generated plots in vector format. Saving them as bitmaps is not useful; please send the Excel (.xls) spreadsheets instead. Bundle your figure files into a single archive (using zip, tar, rar or other format of your choice) and upload on the link you been given at acceptance time.

Each figure should be captioned and numbered so that it can float. Small figures occupying no more than three lines of vertical space can be kept in the text ("the curve looks like this:"). It is acceptable to submit a manuscript with all figures at the end, if their placement is specified in the text by means of comments such as "Place Figure 1 here". The same considerations apply to tables.

WHITE SPACE

Forced line breaks or page breaks should not be inserted in the document. There is no point in your trying to optimize line and page breaks in the original manuscript. The manuscript will be reformatted to use the journal's preferred fonts and layout.

PROOFS

Page proofs will be made available to authors (or to the designated corresponding author) at a Web site in PDF format. Failure to acknowledge the receipt of proofs or to return corrections within the requested deadline may cause publication to be postponed.